# Advanced Optical Modulation and Fast Reconfigurable En/Decoding Techniques for OCDMA Application

by

Zhensen Gao

Submitted for the Degree of Doctor of Philosophy

Heriot-Watt University

School of Engineering and Physical Sciences

October 2011

# Abstract

With the explosive growth of bandwidth requirement in optical fiber communication networks, optical code division multiple access (OCDMA) has witnessed tremendous achievements as one of the promising technologies for optical access networks over the past decades. In an OCDMA system, optical code processing is one of the key techniques. Rapid optical code reconfiguration can improve flexibility and security of the OCDMA system. This thesis focuses on advanced optical modulations and en/decoding techniques for applications in fast reconfigurable OCDMA systems and secure optical communications.

A novel time domain spectral phase encoding (SPE) scheme which can rapidly reconfigure the optical code and is compatible with conventional spectral domain phase en/decoding by using a pair of dispersive devices and a high speed phase modulator is proposed. Based on this scheme, a novel advanced modulation technique that can simultaneously generate both the optical code and the differential-phase-shift-keying (DPSK) data using a single phase modulator is experimentally demonstrated. A symmetric time domain spectral phase encoding and decoding (SPE/SPD) scheme using a similar setup for both the transmitter and receiver is further proposed, based on which a bit-by-bit optical code scrambling and DPSK data modulation technique for secure optical communications has been successfully demonstrated. By combining optical encoding and optical steganography, a novel approach for secure transmission of time domain spectral phase encoded on-off-keying (OOK)/DPSK-OCDMA signal over public wavelength-division multiplexing (WDM) network has also been proposed and demonstrated.

To enable high speed operation of the time domain SPE/SPD scheme and enhance the system security, a rapid programmable, code-length variable bit-by-bit optical code shifting technique is proposed. Based on this technique, security improvements for OOK/DPSK OCDMA systems at data rates of 10Gb/s and 40Gb/s using reconfigurable optical codes of up to 1024-chip have been achieved.

Finally, a novel tunable two-dimensional coherent optical en/decoder which can simultaneously perform wavelength hopping and spectral phase encoding based on coupled micro-ring resonator is proposed and theoretically investigated. The techniques included in this thesis could be potentially used for future fast reconfigurable and secure optical code based communication systems.

# Acknowledgement

First and foremost, I would like to express my deepest appreciation to my supervisor, Dr. Xu Wang, for providing me the opportunity to study at the optical communication and photonic network (OCPN) laboratory and his persistent support, patience, care as well as the encouragement. His enthusiasm for scientific research, research methodology and insightful physical understanding will definitely inspire my future research and work. He encouraged me to grow as not only a scientific engineer but also a professional researcher. With his invaluable guidance throughout my research, I benefit a lot of professional knowledge and skills in the fiber-optic communication research area, which makes my PhD study a memorable and valuable experience for my career.

I greatly appreciate Dr. Naoya Wada of the National Institute of Information and Communications Technology (NICT) for allowing me to access the facilities and carrying out the collaborative experiments in the photonic network group. Special thanks to Dr. Nobuyuki Kataoka, Mr. Sumimoto of NICT to teach me the experimental skill. With the generous support from them, I was able to work on different research topics in NICT. Dr. Guo-Wei Lu's helpful discussion during my stay in NICT is also greatly acknowledged.

I would like to thank Prof. Ken-ichi Kitayama of Osaka University for his kind encouragement and guidance of my research. Special thanks to Dr. Jianming Tang of University of Wales, Bangor, for the recommendation of my application for the international travel grant awarded by the Royal Academy of Engineering. I would also like to acknowledge the Royal Society International Joint Project to support the work included in the thesis.

It is my great pleasure to work with my talented colleagues from the OCPN group. I have learned a lot from them. I would like to particularly mention Mr. Bo Dai, Mr. Xuhua Wang, Mr. Mumtaz Ali and visiting PhD student Mr. Takahiro Kodama of Osaka University for their help. These friends and colleagues have made a good atmosphere in the laboratory for study and fruitful discussions with each other.

Finally and most importantly, I would like to thank my parents, Huwei Gao, YinXian Li and my wife, Shan Ba. I am extremely grateful for their endless love and support during my three years PhD study. This thesis is devoted to them!

| Name*:* | Zhensen Gao | | |
|---|---|---|---|
| School/PGI: | School of Engineering and Physical Sciences, Department of EECE | | |
| Version: *(i.e. First, Resubmission, Final)* | Final | Degree Sought (Award **and** Subject area) | Doctor of Philosophy (Optical communication) |

## Declaration

In accordance with the appropriate regulations I hereby submit my thesis and I declare that:

1) the thesis embodies the results of my own work and has been composed by myself
2) where appropriate, I have made acknowledgement of the work of others and have made reference to work carried out in collaboration with other persons
3) the thesis is the correct version of the thesis for submission and is the same version as any electronic versions submitted*.
4) my thesis for the award referred to, deposited in the Heriot-Watt University Library, should be made available for loan or photocopying and be available via the Institutional Repository, subject to such conditions as the Librarian may require
5) I understand that as a student of the University I am required to abide by the Regulations of the University and to conform to its discipline.

\*    *Please note that it is the responsibility of the candidate to ensure that the correct version of the thesis is submitted.*

| Signature of Candidate*:* | *Zhensen Gao* | Date: | |
|---|---|---|---|

## Submission

| Submitted By *(name in capitals):* | |
|---|---|
| Signature of Individual Submitting: | |
| Date Submitted: | |

## For Completion in the Student Service Centre (SSC)

| Received in the SSC by *(name in capitals):* | | | |
|---|---|---|---|
| *Method of Submission* (Handed in to SSC; posted through internal/external mail): | | | |
| *E-thesis Submitted (**mandatory for final theses**)* | | | |
| Signature: | | Date: | |

Please note this form should bound into the submitted thesis.

# Contents

# List of Publications

## Journal Publications:

1. **Z. Gao**, B. Dai, X. Wang, N. Kataoka and N. Wada, "Rapid programmable/code length variable, time domain bit-by-bit code shifting for high speed secure optical communication", *OSA Optics Letters*, vol.36, no.9, pp.1623-1625, 2011.

2. X. Wang and **Z. Gao,** "Novel reconfigurable 2-Dimensional coherent optical encoder/decoder based on coupled micro-ring reflector", *IEEE Photonics Technol. Lett.*, vol.23, no.9, pp. 591-593, 2011.

3. **Z. Gao,** B. Dai, X. Wang, N. Kataoka and N. Wada, "Transparent transmission of secure time domain spectral phase encoding DPSK-OCDM signal over DWDM network", *IEEE/OSA Journal of Optical communications and Networking,* vol.3, no.5, pp.404-410, 2011.

4. X. Wang, **Z. Gao,** X.-H.Wang, N. Kataoka and N. Wada, "Bit-by-bit Optical Code Scrambling Technique for Secure Optical Communication", *Optics Express,* vol. 19, no.4, pp.3503-3512, 2011.

5. **Z. Gao,** X. Wang, N. Kataoka and N. Wada, "Rapid reconfigurable OCDMA system based on time domain spectral phase encoding/decoding and DPSK data modulation using single phase modulator", *IEEE/OSA J. Lightwave Technol,* vol.23, no.3, pp.348-354, 2011.

6. **Z. Gao**, X. Wang, N. Kataoka and N. Wada, "Stealth transmission of time domain spectral phase encoded OCDMA signal over public WDM network", *IEEE Photonics Technol. Lett.*, Vol. 22, No.13, pp. 993~995, July, 2010.

7. **Z. Gao,** X. Wang, N. Kataoka and N. Wada, "2.5Gbps two-user OCDMA transmission based on time domain spectral phase encoding and Variable-Bandwidth Spectrum Shaper", *Microwave and Optical Technology Letter*, vol. 53, no. 8, pp. 1879-1882, 2011.

8. X. Wang, **Z. Gao**, N. Kataoka and N. Wada, "Time domain spectral phase encoding/DPSK data modulation using single phase modulator for OCDMA application", *Optics Express*, vol. 18, no.10, pp.9879-9890, 2010.

9. B. Dai, **Z. Gao**, X. Wang, N. Kataoka and N. Wada, "Demonstration of Differential Detection on Attacking Code-Shift-Keying OCDMA System", *Electronics Letters*, vol.46, no.25, pp.1680-1682, 2010.

10. B. Dai, **Z. Gao**, X. Wang, N. Kataoka and N. Wada, "Versatile waveform generation based on a single dual-drive Mach-Zehnder modulator", *Electronics Letters*, vol.47, no.5, pp.336-338, 2011.

11. B. Dai, **Z. Gao**, X. Wang, N. Kataoka and N. Wada, "Performance Comparison of $0/\pi$- and $\pm\pi/2$-Phase-Shifted Superstructured Fiber Bragg Grating En/decoder", *Optics Express*, vol. 19, no.13, pp.12248-12260, 2011.

12. B. Dai, **Z. Gao**, X. Wang, N. Kataoka and N. Wada, "A novel optical orthogonal modulation format based on differential phase shift keying and code-shift keying", *IEEE Photonics Technol. Lett.*, vol. 23, no. 17, pp. 1210-1212, 2011.

13. **Z. Gao,** B. Dai, X. Wang, N. Kataoka and N. Wada, "40-Gb/s, secure optical communication based upon fast reconfigurable time domain SPE/D with 40-Gchip/s optical code and symbol overlapping" (Accepted by *Optics Letters).*

14. **Z. Gao,** B. Dai, X. Wang, N. Kataoka and N. Wada, "10-Gbit/s, reconfigurable time domain SPE-OCDMA system with code shifting and pulse overlapping", submitted to *Microwave and Optical Technology Letter*.

15. **Z. Gao,** B. Dai, X. Wang, N. Kataoka and N. Wada, "Demonstration of a 40-Gb/s, 40-Gchip/s, high security DPSK-OCDM system using time domain equivalent bit-by-bit en/decoding", to be submitted.

**Conference Publications:**

1. X. Wang, **Z. Gao**, B. Dai, X-H. Wang, N. Kataoka, and N. Wada, "Fast optical code reconfigurable technique for secure optical communication", *13th International Conference on Transparent Optical Networks* (*ICTON* 2011), Sweden, July, 2011, Paper We. B1. 4.

2. B. Dai, **Z. Gao**, X. Wang, N. Kataoka, N. Wada, " Demonstration of Hybrid Using $\pm\pi/2$- and $0/\pi$-Phase-Shifted SSFBG En/decoders in the $4\times10$Gbit/s OCDMA system," OWV6, OFC 2011, Los Angeles, USA, Mar. 2011.

3. **Z. Gao**, B. Dai, X. Wang, N. Kataoka and N. Wada, "2D Time Domain Spectral Phase Encoding/Wavelength hopping coherent DPSK-OCDMA system Using Fiber

Bragg Gratings and Phase Modulator," ACP 2010, Shanghai, China, Dec. 2010, Paper FO7.

4. **Z. Gao**, B. Dai, X. Wang, N. Kataoka and N. Wada, "Ultrafast optical pulse repetition rate multiplication based on time domain spectral amplitude/phase filtering," ACP 2010, Shanghai, China, Dec. 2010, Paper SuG3.

5. B. Dai, **Z. Gao**, X. Wang, N. Kataoka and N. Wada, "Generation of Versatile Optical Waveforms from CW Laser using a Single-stage Dual-drive Mach-Zehnder Modulator," ACP 2010, Shanghai, China, Dec. 2010.

6. B. Dai, **Z. Gao**, X. Wang, N. Kataoka and N. Wada, "Experimental Demonstration of $\pm\pi/2$-Phase-Shifted SSFBG Encoder for Security Improvement in Time-spreading OCDMA," ACP 2010, Shanghai, China, Dec. 2010, Paper FU2.

7. B. Dai, **Z. Gao**, X. Wang, N. Kataoka and N. Wada, "Experimental Investigation on Security of Temporal Phase Coding OCDMA System with Code-Shift Keying and Differential Phase-Shift Keying," ACP 2010, Shanghai, China, Dec. 2010, Paper FO1.

8. X. Wang, **Z. Gao**, N. Kataoka and N. Wada, "Secure Optical Communication using Single Phase Modulator for bit-by-bit Code Scrambling and DPSK Data Modulation", OTuM1, Optical Fiber Communication Conference (OFC'10), San Diego, USA, 2010.

9. **Z. Gao**, X. Wang, N. Kataoka and N. Wada, "Stealth Transmission of Time Domain Spectral Phase Encoded OCDMA Signal over WDM System" OThW5, Optical Fiber Communication Conference (OFC'10), San Diego, USA, 2010.

10. **Z. Gao**, X. Wang, N. Kataoka and N. Wada, "Simultaneous time domain spectral phase encoding/DPSK data modulation with improved security for secure optical communication", The 15th OptoElectronics and Communications Conference (OECC 2010), Sapporo, Japan, July, 2010.

11. X. Wang and **Z. Gao**, "Coupled micro-ring resonator based optical en/decoder for 2-D coherent OCDMA application", 12th International Conference on Transparent Optical Networks (ICTON 2010), Munich, German, June, 2010.

12. X. Wang, **Z. Gao**, N. Kataoka, N. Wada, DPSK optical code hopping scheme using single phase modulator for secure optical communication, Th.A1.3, 12th International Conference on Transparent Optical Networks (ICTON 2010), Munich,

Germany, June 27 - July 1, 2010.

13. **Z. Gao**, X. Wang, N. Kataoka and N. Wada, "Time Domain SPE/SPD and DPSK Data Modulation Using Single Phase Modulator", CFL6, CLEO'10, San Jose, USA, 2010.

14. **Z. Gao**, X. Wang, N. Kataoka and N. Wada, "2.5Gbps Two-user OCDMA System Based on Time Domain Spectral Phase Encoding and Variable-Bandwidth Spectrum Shaper Decoding", CThC7, CLEO'10, San Jose, USA, 2010.

15. **Z. Gao**, X. Wang, "Analysis of Optical Reflector Based on Circular Coupled Microring Resonators", 11th International Conference on Transparent Optical Networks (ICTON 2009), Island of São Miguel, Azores, Portugal, July, 2009.

16. **Z. Gao,** X. Wang, N. Kataoka and N. Wada, "Demonstration of time-domain spectral phase encoding/DPSK data modulation using single phase modulator", IEEE LEOS Summer Topical 2009, TuA3. 1, New port, CA, USA, 2009.

17. **Z. Gao**, X. Wang, N. Kataoka and N. Wada "2.5Gbps SPE-OCDMA transmission using time domain spectral phase en/decoding with LCFBG", The 14th Optoelectronics and Communications Conference (OECC 2009), Hongkong, July, 2009.

# Abbreviations

| | |
|---|---|
| 2-D | Two Dimension |
| ADSL | Asymmetric Digital Subscriber Line |
| AES | Advanced Encryption Standard (AES) |
| AON | Active Optical network |
| ATM | Asynchronous Transfer Mode |
| AWG | Array Waveguide Grating |
| BER | Bit Error Rate |
| BPF | Band Pass Filter |
| BPD | Balanced Photon Detector |
| CATV | Common Antenna Television |
| CSK | Code Shift keying |
| CW | Continuum Wave |
| CWDM | Coarse Wavelength Division Multiplexing |
| CROW | Coupled Resonator Optical Waveguide |
| CRIT | Coupled Resonator Induced Transparency |
| DCF | Dispersion Compensation Fiber |
| DFF | Dispersion Flattened Fiber |
| DPSK | Differential Phase Shift Keying |
| DQPSK | Differential Quadrature Phase Shift Keying |
| DSL | Digital Subscriber Loop |
| EAM | Electron Absorption Modulator |
| EDFA | Erbium Doped Fiber Amplifier |
| FTTH | Fiber to The Home |
| FWHM | Full Width at Half Maximum |
| GVD | Group Velocity Dispersion |
| IM | Intensity Modulator |
| LCFBG | Linear Chirped Fiber Bragg Grating |
| LED | Light Emitting Diode |
| LD | Laser Diode |
| $LiNbO_3$ | Lithium Niobate |
| MAI | Multiple Access Interference |
| MLLD | Mode Locked Laser Diode |

| | |
|---|---|
| MUX | Multiplexer |
| NOLM | Nonlinear Optical Loop Mirror |
| OLT | Optical Line Terminal |
| ONU | Optical Network Unit |
| OC | Optical Code |
| OCDMA | Optical Code Division Multiple Access |
| OPS | Optical Packet Switching |
| OOK | On Off Keying |
| PON | Passive optical network |
| PLC | Planar lightwave Circuit |
| PD | Photo-Detector |
| PM | Phase Modulator |
| PRBS | Pseudo Random Binary Sequence |
| PPG | Pulse Pattern Generator |
| PS | Phase Shifter |
| QKD | Quantum Key Distribution |
| RDF | Reverse Dispersion Fiber |
| SSFBG | Superstructured Fiber Bragg Grating |
| SLPM | Spatial Light Phase Modulator |
| SPECTS | Spectral Phase Encoding Time Spreading |
| SAE | Spectral Amplitude Encoding |
| SC | Super Continuum |
| SMF | Single Mode Fiber |
| SPE/SPD | Spectral Phase Encoding/Decoding |
| SPC | Spectral Phase Code |
| SPM | Self Phase Modulation |
| OTDM | Optical Time Division Multiplexing |
| TS | Time Spreading |
| VBS | Variable Bandwidth Spectrum Shaper |
| WDM | Wavelength Division Multiplexing |
| WHTS | Wavelength Hopping Time Spreading |
| WHC | Wavelength Hopping Code |

# CHAPTER 1

# Introduction

## 1.1  Emerging fiber-optic communication

Fiber-optic communication is an important revolution in the history of telecommunication and it is now becoming one of the key information technologies in this new century. It is changing the way we work and study in an unprecedented speed. There are several milestones in the research of fiber-optic communication. In the early 1960s, Maiman invented the first stable ruby laser in the world, and later in 1970s, the semiconductor diode laser that can work continuously in room temperature for a long time was developed in Bell labs [1]. At around the same times, the proposal of using optical fiber as a transmission medium for communication by reducing the loss was proposed by Charles K. Kao, *et al* [2], which was demonstrated by Corning Company that manufactured the first optical fiber with an attenuation of 20dB/km [1, 3]. The fiber optical communication was stimulated with the breakthrough of the compact laser source and low-loss optical fiber. In 1987, the Optoelectronics Research Center at University of Southampton invented the rare erbium-doped fiber optical amplifier (EDFA) [4], which led to the rapid advances of fiber-optic communication systems. The unique advantages of enormous capacity, low electromagnetic radiation, high signal security, low weight and potential low cost make the optical fiber an ideal transmission medium and has attracted worldwide research during the past decades [3].

In fiber-optic communications, the information to be transmitted is modulated onto an optical carrier with an ultra-broad bandwidth in the order of tens of terahertz, so a major benefit of fiber-optic communications is the potential increase of information capacity, which is directly related to the carrier bandwidth. By exploiting optical fiber as the transmission medium, the fiber-optic communication systems are becoming faster and more efficient than ever before, providing a transmission speed as large as several hundreds of gigabit per second in a single fiber. Nowadays, as people's demand for high speed data exchange such as image, audio and video through the network is rapidly increasing, one of the main challenges in the fiber-optic communications is to widely exploit the broad bandwidth of the optical fiber to cope with this trend, which involves the transmission, switching and routing of high speed optical signals over a long

distance. Meanwhile, as the network expands and the internet resources increase, it is desirable to exchange the data securely between different nodes in the optical network, which could be another challenge for the fiber-optic communications.

Today's fiber-optic communication network is an extremely complicated system, but it can be mainly divided into three layers similarly as the general communication network architecture: the long haul network, the metropolitan network and the local access network, as illustrated in Figure 1.1 [5]. The long haul network is the backbone of the global optical network, which spans across different regions up to thousands of kilometers. It links with various metropolitan networks and mainly focuses on the capacity. Recently, with the development of advanced optical signal processing and multi-core optical fiber technologies, the capacity of long-haul optical network has surpassed even 100 terabits per second [6, 7]. The metropolitan network usually spans a city and interconnects with a number of local access networks. The interconnectivity, capacity and efficiency are the main concerns of metropolitan network as it connects the long haul network and local access network. The local access network also known as the "last mile" is the end edge of the whole network and the most critical segment in the telecommunication network, because it provides the direct link to the customers and generates the revenues. In recent years, although the backbone network has experienced substantial growth, the infrastructure of current access networks suffers from limited bandwidth and high network cost, and the "last mile" still remains the bottle-neck between high-capacity local access network and the backbone network [8]. The residential end-users' demand of high bit rate services to run audio, video and other
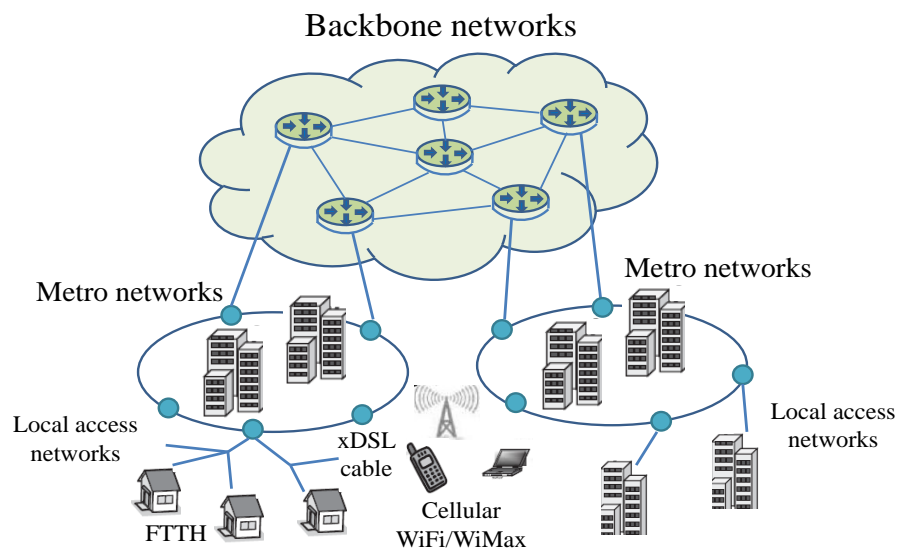


Figure 1.1 Hierarchical architecture of communication network [5].

advanced Internet applications is increasing as the broadband telecommunication develops. Various solutions for the local access network have been developed to satisfy the users' demand. Among them, the most important solutions are the digital subscriber loop (DSL), cable modem, wireless technology (Wi-Fi, WiMax) and fiber to the X (e.g. Premises, home, building) (FTTX) [5, 8]. The most dominant technologies used currently are DSL based on telephone lines and cable modem based on common antenna television (CATV). However, they are only transition solutions as they usually offer rather low data rate and cannot meet the requirements of ever-increasing symmetric bandwidth and service demand in prevalent network. Though wireless technologies can provide relatively higher bit rate (e.g. 54 Mb/s in 100 m for Wi-Fi and 28 Mb/s in 15 km for WiMAX) [5], the reach based on wireless is very limited, which has prompted the deployment of high performance local access network.

The optical fiber to the home (FTTH) is considered as an ultimate and promising solution by bringing optical fiber to the home due to its low cost, easy upgrading and potential to handle the downlink and uplink bandwidth with equal amount of ease in the last mile [9]. Many countries have made ambitious plans and deployments of FTTH network. In particular, for example, the FTTH implementation in Japan is rapidly growing in recent years [10]. Figure 1.2 shows the number of subscribers for the high speed broadband Internet access in Japan [11]. At the beginning, the asymmetric digital subscriber line (ADSL) offered the Internet services and dominated the market with more than 13 million users in 2004. CATV comes next but its growth is nearly flat. Since 2008, FTTH offering enormous bandwidth has drawn the market's attention and gradually surpassed the ADSL. The number of FTTH users is expected to approach 20 million in 2011. It has been considered that passive optical network (PON) is a promising architecture to solve the "last mile" problem in future FTTH network, and
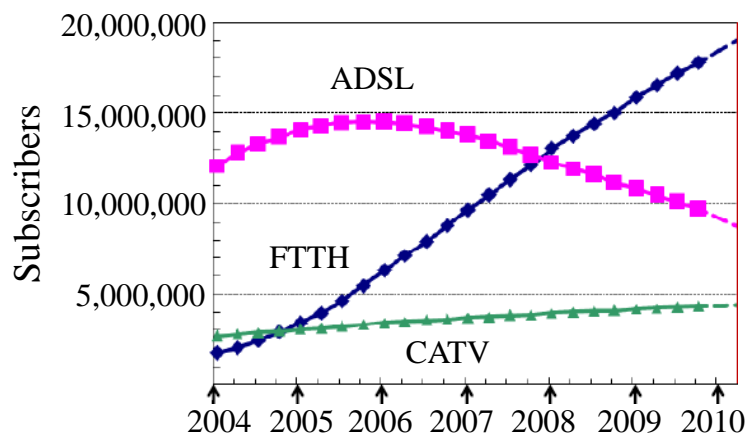


Figure 1.2 Number of broadband access network users in Japan [11].

therefore it is emerging as a crucial technology for the local access network [12]. A typical PON includes the central office or optical line terminal (OLT) and optical network unit (ONU). The OLT is connected to several ONUs via an optical distribution network consisting of optical fiber and passive splitters. Unlike active optical network (AON) that has active aggregation elements (e.g. Ethernet switch), the PON requires no any active management and no electrical power. Even a conventional EDFA is also not required in PON systems. The most notable feature of PON is that it only use inexpensive passive optical components in all points in the network, which is very easy to be operated and managed [12].

## 1.2   Multiplexing techniques in optical access network

To fully exploit the enormous bandwidth of optical fiber and satisfy the bandwidth demand in passive optical access networks, it is imperative to transmit the data at a high speed. However, the data rate for a single channel link is greatly limited by the processing speed of the transmitting and receiving electronic devices, so it is essential to multiplex low speed data streams onto an optical fiber to increase the total throughput in optical domain. Wavelength division multiplexing (WDM) and time division multiplexing (TDM) are two widely used multiplexing technologies in the passive optical access network, which are also known as WDMA and TDMA. Figure 1.3 (a) and (b) show the schematic principle of WDM and TDM technologies. In a WDM system, each user channel is assigned a unique wavelength, and multiple users can simultaneously transmit their signals over the assigned wavelengths without interfering with each other through a single optical fiber. The modulation format and speed at each wavelength channel can be independent between different channels. At the receiver, the optical signal is demultiplexed into separate wavelength channels by a WDM demux which can be an array-waveguide-grating or thin-film dielectric filter and then the demultiplexed signals are detected individually for each channel [3]. The minimum channel spacing is limited by the channel crosstalk. Typical dense WDM (DWDM) systems use a channel grid of 100 GHz or even more narrow, while coarse WDM (CWDM) operated in the range of around 1270nm to 1610nm has a wavelength spacing of 20nm [13]. In practice, the performance of WDM systems is affected by many factors such as the bandwidth of the EDFA, interchannel crosstalk, signal distortion during transmission. Therefore, in the WDM based optical access network, it requires wavelength stable laser source, broadband EDFA, sharp optical filter and so on, which will increase the system cost.

(a) WDM



(b) TDM
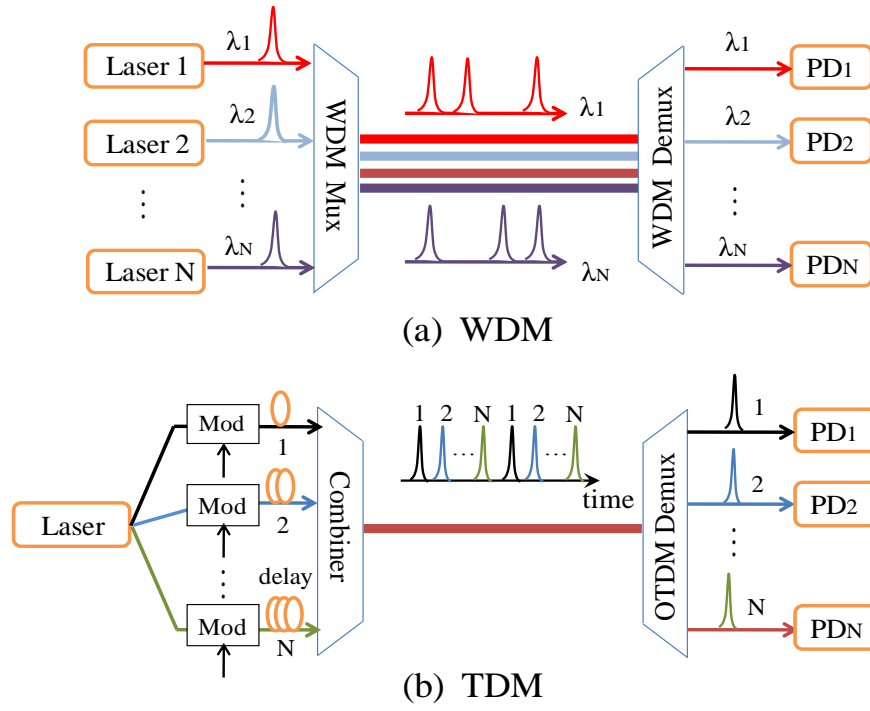
Figure 1.3 Schematic diagrams of WDM and TDM techniques.

An alternative solution is TDM technique which includes electrical and optical TDM (OTDM). Since the electrical TDM is hard to be operated beyond 100-Gb/s, the OTDM is more attractive. As shown in Fig.1.3 (b), in OTDM system, the channel is divided into several time slots *N*, and each user can transmit only during its assigned slot which interleaves with the time slots of other channels. The combined high speed *N* channel signals are demultiplexed separately into *N* low speed signals that can be detected by low speed electronic circuit individually. Unlike the WDM technique, the demultiplexing of the OTDM signal is realized in time domain. Based on the OTDM technique, TDM-PON architecture has been proposed which generally includes asynchronous transfer mode (ATM) based PON (APON), broadband-BPON, gigabit-GPON, Ethernet EPON and 10GEPON [5, 12]. APON is the standardized PON by the international telecommunication union (ITU) which supports the legacy of ATM protocols at 622 Mb/s downstream and 155Mb/s upstream bandwidth [5]. BPON is an improved solution of APON that can support gigabit rates and packet-based Internet applications. GPON is a further enhancement of BPON with maximum 2.5Gb/s downstream and 1.25Gb/s upper stream data rate [5]. Quite different from GPON, EPON are designed to carry Ethernet frames at standard Ethernet rates, which support 1.25Gb/s upper and downstream data rates [5, 12]. 10GEPON (10 gigabit PON) is a successor of GPON that provides a large data rate of 10Gb/s. Currently being installed in Asian countries such as Japan are Ethernet PON systems with gigabit transmission

capability. Meanwhile operators in the USA and Europe are focusing on gigabit-capable GPON systems [12]. The performance of OTDM system is ultimately limited by the time-serial nature [12], and thus it requires strong centralized control to allocate time slots and to maintain synchronous operation.

## 1.3   Optical code division multiple access

Besides WDMA and TDMA, optical code division multiple access (OCDMA) is another attractive solution for the broadband optical access networks [14-15]. The OCDMA originates from its electrical counterpart code division multiplexing access (CDMA) that has achieved great success in today's third generation wireless communication. The CDMA has evolved from the spread-spectrum wireless technique that is developed to resist interference for military communication. It is based on the concept of spreading the spectrum of a transmitting signal over a wider spectrum according to a signature code sequence in the radio frequency domain [14]. At the receiver, the received spectra spreading signal exhibits as a noise, and it is despread by matched filtering, so only the desired signal is retrieved. All the other interferences cannot be recovered and thus it is very robust to the environmental noise [14]. By combining the CDMA with the optical fiber medium that has a large bandwidth, a new research area OCDMA has been initiated [16]. In OCDMA system, time spreading and despreading are adopted. The optical signal is spread in the time scale after encoding with a signature code, and despread back into the original-like signal after the decoding.

Unlike WDMA or TDMA that use wavelength and time-slot channels, as shown in Figure 1.4 [17], OCDMA can provide another dimension of optical code (OC) for multiplexing, in which each user is assigned a unique optical code and distinguished by this code at the receiver, while all the users can share the same time and frequency in a fair manner. Each data bit is encoded by the OC at the transmitter. If the OC in the decoder matches with that in the encoder, an auto-correlation signal is generated but for an unmatched OC, cross-correlation signals approach to zero will be produced, which enables correct detection of the data stream with little interference. In contrast to TDMA and WDMA, where the maximum transmission capacity is determined by the total number of the time and wavelength slots, the capacity of OCDMA depends on the number of available codes [18-19]. Through the use of optical codes, the number of active users can be made much larger than the number of available time and wavelength slots [15]. In OCDMA system, the time and frequency management of all nodes is

6
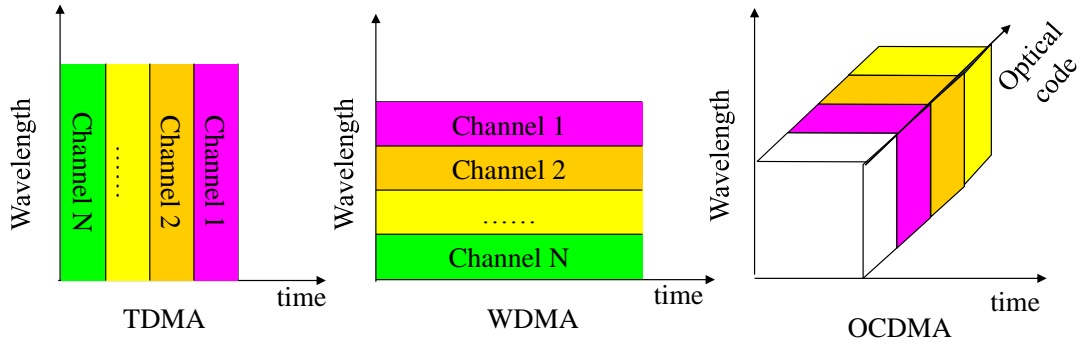
Figure 1.4 Comparison of three multiple access techniques: TDMA, WDMA and OCDMA.

relaxed, and it exhibits the advantages of asynchronous transmission, simplified network control, physical layer quality of service control, soft capacity on demand, low latency access and does not suffer from packet collisions, *etc* [15, 17-20]. It is also suited for symmetric access network operation with the OLT and ONU transmitting at multi-gigabit rates [13, 18]. Moreover, the OCDMA can even be hybrid with the WDMA or TDMA to significantly enhance the system capacity. A 111km field trial of 3WDM×10OCDMA×10.71Gb/s/user with 10 users per wavelength has been previously demonstrated [21]. Additionally, as prominent as the other advantages, the potential physical layer security provided by the optical code processing is also rather attractive for secure optical communication [15, 20], because the data signal is transformed into a noise-like signal by the OC. Therefore, the OCDMA is emerging as a promising solution for next-generation broadband access network and it may also become a potential candidate for secure optical communication.

## 1.4   Motivation and contributions of the thesis

In recent years, the OCDMA technique has attracted worldwide attention with the rapid development of optical en/decoder, which is the key component in OCDMA systems. In 2001, superstructured fiber Bragg gratings (SSFBG) based optical en/decoder with 63-chip, 160Gchip/s was fabricated and demonstrated in a two-user OCDMA system [22]. A record-long 511-chip, 640Gchip/s phase shifted SSFBG was also reported for optical code generation and recognition [23]. More recently, a high chip count of 1023-chip SSFBG based on reconstruction equivalent chirp technique has been realized [24]. Some other optical en/decoders including fiber optical delay line, spatial light phase modulator (SLPM), planar lightwave circuit (PLC), array waveguide grating (AWG) have also been extensively investigated [17].

To fulfill the demand of future flexible and dynamic reconfigurable OCDMA network, it is highly desirable to rapidly reconfigure and translate the optical code into other codes. By rapidly reconfiguring the optical code, it can also reduce the required code number in the network because the code can be reallocated and shared among the users. However, most of the previously proposed devices do not offer the reconfigurable capability. The earliest implementation of OCDMA is based on the discrete fiber delay lines [16, 25], in which the optical code can be reconfigured by changing the optical delay, but it is difficult to accurately control the length of individual fiber length [22]. The spatial light phase modulator based optical en/decoder is attractive because the amplitude/phase of the phase mask can be changed, but it is based on free-space diffractive bulk optics. Implementations in optical waveguide such as using planar lightwave circuit technology [26] and arrayed waveguide gratings for OCDMA have also been proposed [27]. These devices are suitable for large-scale integration and can exhibit certain tunability, but suffer from the disadvantages of high fabrication complexity and cost [22]. More recent studies for improving the code reconfigurability in a phase shifted SSFBG en/decoder based on thermal induced phase shift have also been reported [28-29]. Nevertheless, achieving fast optical code reconfigurability still remains a challenge.

On the other hand, providing information security in the optical network is of great concern for the research communities. By using all-optical code processing technologies, the OCDMA can potentially enhance the information security in the physical layer. Because intuitively, the optical signal is encoded into a noise-like signal after the encoder, an eavesdropper cannot recover the original signal and intercept the confidential data without the knowledge of the applied code. However, in an OCDMA network, there could be some single user's links. When a single user is isolated, the security of OCDMA system is questionable. Security vulnerability of coding induced dips in either the waveform or spectrum has been revealed [30-31]. An eavesdropper can easily extract the code information by analyzing the fine structure of the encoded spectrum or waveform, and then illegally perform the interception. It has also been found that the OCDMA security is related to the optical modulation formats. The OCDMA systems employing on-off-keying (OOK) and differential-phase-shift-keying (DPSK) modulation formats are vulnerable to an eavesdropper's attack using proper detection methods [32-33]. The eavesdropper does not need to know the exact code but he can still access to the target data.

The limitation of rapid reconfigurable capability of conventional optical en/decoders and the security vulnerabilities existing in OCDMA systems have motivated the research on developing advanced optical modulation and fast reconfigurable en/decoding techniques to improve the flexibility and security of OCDMA systems. The key contributions of the thesis are summarized as follows and can also be found in the publication list:

1. A novel reconfigurable, time domain spectral phase en/decoding scheme using only dispersive devices and phase modulator is proposed and demonstrated for coherent OCDMA application.

2. A novel advanced optical modulation technique that can simultaneously generate DPSK data modulation and time domain spectral phase encoding using a single phase modulator is proposed and demonstrated.

3. A novel bit-by-bit optical code scrambling technique based on symmetric time domain spectral phase encoding/decoding schemes for secure optical communication is firstly proposed and experimentally demonstrated.

4. An approach by combining optical encoding and steganography techniques to enhance the OCDMA system security is proposed. Secure transmission of time domain spectral phase encoded OCDMA signal with OOK and DPSK data modulation formats over public WDM networks is achieved.

5. A rapid reconfigurable, code-length variable, time domain bit-by-bit code shifting technique for high speed secure optical communication is proposed. Secure optical communication systems with a high data rate and ultra-long code length of up to 40-Gb/s and 1024-chip for both the OOK and DPSK data modulation formats are demonstrated.

6. A novel tunable two-dimensional (2-D) coherent optical en/decoder that can simultaneously perform wavelength hopping and spectral phase encoding based on coupled micro-ring resonator optical waveguide is proposed and theoretically investigated.

## 1.5   Organization of the thesis

The rest of this thesis is organized as follows:

Chapter 2 gives a overview of the OCDMA research background, including the system architecture and classifications of OCDMA, as well as the key enabling techniques such as optical en/decoding, data modulation formats, optical thresholding/time gating. A detailed introduction of the security issues in OCDMA systems is also included in this chapter.

Chapter 3 focuses on the proposed time domain spectral phase encoding scheme for rapid reconfigurable OCDMA application. The basic principle is described at first and then proof-of-principle experimental demonstrations for the proposed scheme using conventional array-waveguide-grating (AWG) and variable-bandwidth-spectrum-shaper (VBS) based spectral phase decoders are presented. Followed by that, an advanced optical modulation technique that uses a single phase modulator for simultaneous time domain spectral phase encoding and DPSK data modulation is proposed and demonstrated. Finally, a 2.5Gb/s, two-user OCDMA system is presented based on the proposed time domain spectral phase encoding scheme.

In Chapter 4, a symmetric reconfigurable time domain spectral phase encoding and decoding scheme using a similar setup for both the transmitter and receiver is investigated. Based on this scheme, simultaneous DPSK data modulation and optical en/decoding using a single phase modulator are demonstrated. At the end of this chapter, a novel bit-by-bit optical code scrambling technique for secure optical communication is proposed, and then an experimental demonstration of the security enhancement for 2.5Gb/s DPSK data encoded by scrambling five 20Gchip/s, 8-chip optical codes is presented.

In Chapter 5, the time domain spectral phase en/decoding technique is applied into optical steganography to enhance the security of OCDMA signal. Experimental demonstration of secure transmission of time domain spectral phase encoded OOK-OCDMA signal over public WDM system is presented. Then, a novel transparent time domain spectral phase encoded DPSK-OCDMA signal overlay DWDM network architecture enabled by spectral notch filtering is proposed and investigated. Transmission of a 2.5Gb/s, time domain SPE-OCDMA signal with DPSK modulation format over a 10Gb/s, two-channel DWDM network is demonstrated.

Chapter 6 describes a rapid programmable, code-length variable bit-by-bit code shifting technique based on the time domain spectral phase en/decoding scheme with symbol overlapping for high speed secure optical communication. By using this

technique, security enhancements for both the OOK and DPSK data in various OCDMA systems with high bit rates of 10-Gb/s or even 40-Gb/s, and code lengths of up to 1024 are investigated.

In Chapter 7, a novel tunable two-dimensional (2-D) coherent optical en/decoder based on coupled micro-ring resonator optical waveguide is proposed and theoretically studied. The design procedure of the coupling coefficient to achieve single peak reflection, the effect of fabrication error and loss on the reflection, and the resonant wavelength tuning are also discussed. Finally, the capability of simultaneous two-dimensional wavelength hopping and spectral phase encoding using the proposed device is investigated and verified by simulation.

A conclusion of the thesis is given in Chapter 8. The future work is also included in this chapter.

# CHAPTER 2

# Background of optical code division multiple access (OCDMA)

In this chapter, the background knowledge of the essential components and techniques in general OCDMA system is reviewed. A brief overview and classification of the OCDMA system are given in Section 2.1, based on which different techniques including the encoding and detection methods in incoherent OCDMA and with a special emphasis on coherent OCDMA systems are discussed in Section 2.2 and 2.3, respectively. Following that, the optical modulation formats including OOK, DPSK and CSK that are widely used in OCDMA system are reviewed in Section 2.4. Finally, in Section 2.5, the security issues in OCDMA system are presented, which is closely related to the research work of this thesis.

## 2.1　Overview of OCDMA system

Since the first proposal of bringing CDMA technique into optical domain in 1978 [34], various approaches and schemes have been proposed for implementing OCDMA as it provides another dimension: optical code for multiple access, such as the earliest implementations using fiber optical delay line [16] and spatial lightwave modulator [35]. Figure 2.1 illustrates the basic architecture of an OCDMA system [13, 36], in which the OLTs are located in the central office while a number of ONUs are installed in the user's terminals. The data transmitted from the OLT is transformed by optical encoding operation using an optical encoder with a unique optical code assigned to different users. The encoded signal is then combined with the other users' encoded signals by a star coupler and then broadcasted to the network. In the ONU side, each user has an optical decoder that performs the matched filtering, where an auto-correlation signal with high peak power is generated if the decoder has the same signature sequence as the encoder, while all the signals from the other users remain noise-like after the decoder acting as the multiple-access interference (MAI) noises because they corrupt the desired signal. The encoding and decoding operations alone constitute the optical coding. At the receiver, the original data can be recovered after a photo-detector and electrical data processing.
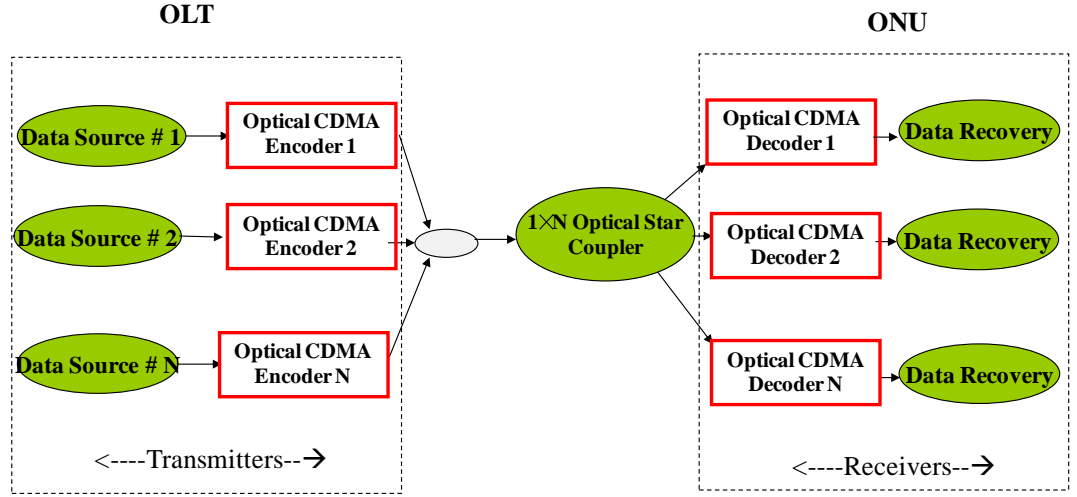
Figure 2.1 Basic OCDMA network architecture.

Although a number of OCDMA approaches have been previously investigated, the OCDMA system can be classified by two criteria, as illustrated in Figure 2.2 [17, 37]. According to the working principle or the superposition of optical signal, the OCDMA can be classified into two categories: incoherent OCDMA and coherent OCDMA [13, 38]. In incoherent OCDMA, the signal superposition is based on the light power and the signal is detected with the square-law devices at the receiving terminals. The most common incoherent OCDMA approaches include temporal (time) spreading [16], spectral-amplitude coding [39-40], and two-dimensional (2-D) wavelength-hopping time-spreading (WHTS) [41-44]. While coherent OCDMA differs in that it makes use of the coherent property of light and the signal superposition is based on the light amplitude rather than the power. The encoding is implemented using the phase of the optical signal and the phase manipulation can be done in the time domain (temporal-phase encoding) or in the frequency domain (spectral-phase encoding).

On the other hand, the OCDMA can also be identified according to the coding dimensions as one-dimensional (1-D) which can be either in time domain or spectral domain, and two-dimensional (2-D) (time, spectral), as shown in Fig.2.2 [17]. Up to now, only incoherent 2-D OCDMA system which is also known as wavelength hopping/time spreading (WHTS) has been proposed and demonstrated [41-44], and there is no coherent 2-D OCDMA system because of the lack of coherent 2-D optical en/decoder. In the following sections, I will briefly introduce different types of OCDMA schemes and their corresponding optical coding devices with a special focus on the coherent OCDMA system and related techniques, including the optical en/decoding, optical signal modulation and detection.
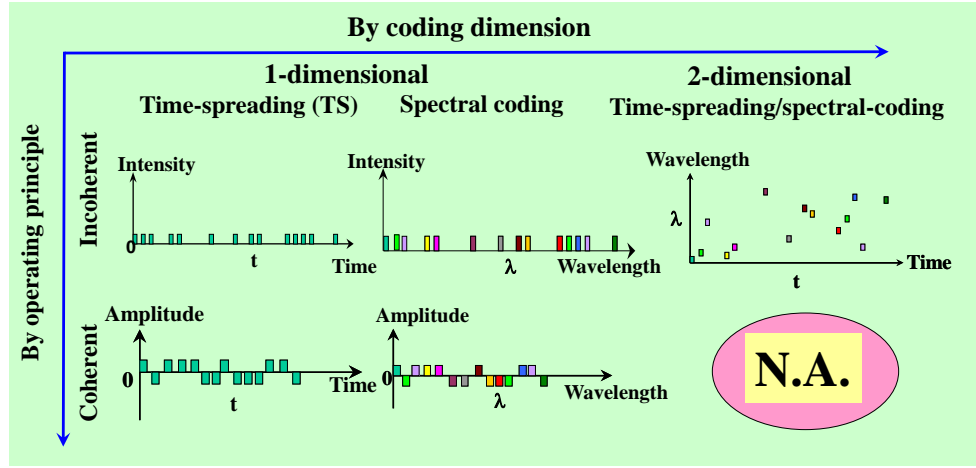
Figure 2.2 Classifications of OCDMA system.

## 2.2 Incoherent OCDMA

The incoherent OCDMA is the earliest and most well-known OCDMA scheme although it is not widely investigated today. In incoherent OCDMA, the optical en/decoding operation is performed based on the signal power and thus it usually works in a unipolar manner (1, 0), where "1" represents the presence of a signal, while "0" means no signal. As mentioned before, the incoherent time spreading, spectral amplitude coding and two-dimensional (2-D) wavelength hopping/time spreading are the main incoherent OCDMA schemes, which will be introduced as follows.

The incoherent time spreading OCDMA was historically the first OCDMA scheme implemented by *Prucnal*, *et al* [16]. Optical fiber delay line is the most simplest and mature optical en/decoder for the time spreading incoherent OCDMA, as shown in Figure 2.3 [36], which consists of a $1 \times W$ power splitter, fiber delay line and $W \times 1$ power combiner for coding. In this scheme, the bit interval $T_b$ is divided into a number of $W$ equal slots, which are called chips. When the data bit "1" is sent into the encoder, the input signal is firstly split into a series of optical pulses with identical energy by the power splitter. The number of the split pulses corresponds to the code weight. Then, these pulses are selectively delayed by different fiber optical delay lines. The positions of the pulses are predetermined by a unipolar spreading code sequence assigned to the delay line. The delayed pulses are finally combined by the power combiner to generate the encoded pulse burst. For the data bit "0", no any signal is transmitted. Prime code and optical orthogonal code (OOC) are generally employed for the time spreading incoherent OCDMA [45]. The structure of decoder is same as the encoder except that inverse time delay is applied to produce an auto-correlation signal that incoherently

14

Figure 2.3 Optical fiber delay line based en/decoder.

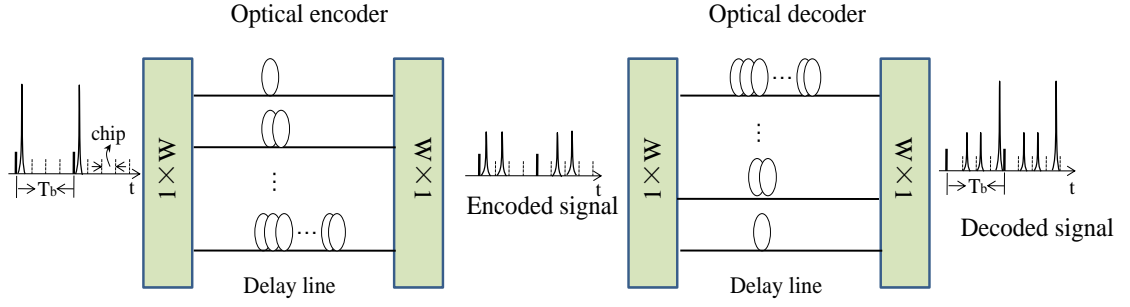sums the power of the desired pulse sequences. When the code applied in the decoder mismatches with that in the encoder, the output is a cross-correlation signal that remains spread in the bit interval. As the result of power splitting and combining based optical coding, the auto-correlation signal has the feature of large sidelobes. In order to achieve excellent decoding performance, the code sequences have to be very sparse to generate high peak auto-correlation and low cross-correlation signals. Though the fiber delay line based optical en/decoder is the first OCDMA encoding/decoding approach, it has the limitations of requiring short optical pulses, long code length for good correlation properties and large power loss [36].

Spectral amplitude encoding (SAE) is another widely explored incoherent OCDMA approach, whose basic scheme is shown in Figure 2.4 [39]. In the SAE-OCDMA system, the encoding is performed by spectrally decomposing a broadband light source such as light emitting diode (LED) or superluminance diode (SLD) using a diffractive grating followed by an optical element (spatial amplitude mask) $A(w)$ that can modulate the intensity of different spectral components according to a unipolar code before combining them again by another diffractive grating [39, 46]. The configuration is typically a 4f optical system performed in frequency domain. In the decoder, if the spectral filter matches with the encoder, maximum optical power will be output from filter $B(w)$ and the minimum optical power output from the complementary filter $\overline{B}(w)$. For an unmatched code, both filters will output the average optical power. Then, the balanced receiver is used to retrieve the original data, in which way the interferences from the cross-correlation signals can be mitigated. The main advantage of this scheme is that the laser source is very simple and of low cost. However, the en/decoder of this scheme requires very precise control and the performance is very sensitive to the shape of the broadband optical source and wavelength misalignment. In addition, the spectral resolution of the amplitude mask limits the available code length and thus the number of possible active users.
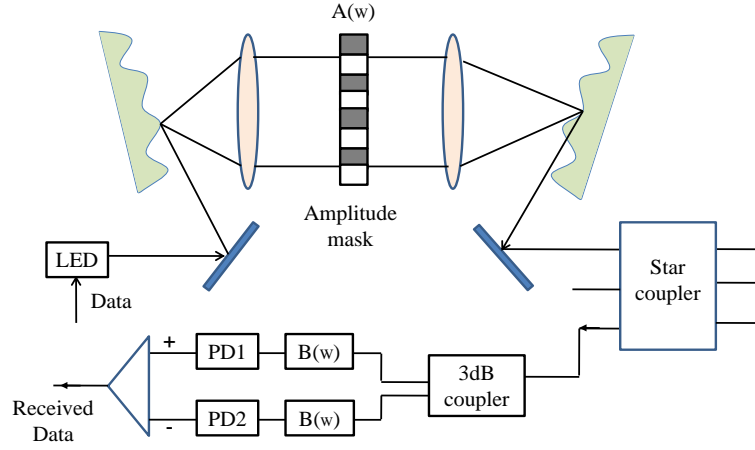
Figure 2.4 Spectral amplitude coding based on a *4f* optical system [39].

The 2-D wavelength-hopping/time-spreading (WH/TS) OCDMA that performs the coding in both the time and frequency domain has been proposed by *Tancevski, et al* in the early 1994 [42]. The WH/TS can be realized by combining fiber optical delay line and an AWG [31, 47] or a fiber Bragg grating (FBG) [41]. The use of FBG in the WH/TS scheme is more compact and convenient than the using the AWG. Figure 2.5 (a) and (b) show a FBG based 2-D WH/TS optical en/decoder [41]. The WH/TS differs from the temporal spreading OCDMA in that the pulse is spread in both the time and frequency domain, and different chips are of different wavelengths following a wavelength hopping pattern, as shown in Fig. 2.5 (c). In this scheme, the spread pulses are placed in different chips across the bit period with different time delays according to the positions of the FBGs, which corresponds to the time-spreading pattern of a signature code. The FBGs can be tuned to different wavelengths to reconfigure the wavelength hopping pattern. The WH/TS codes can thus be represented by code matrices with time and wavelength as the two axes. At the receiver, the WH/TS decoder has similar configuration as the encoder, but the FBGs are constructed in the reverse
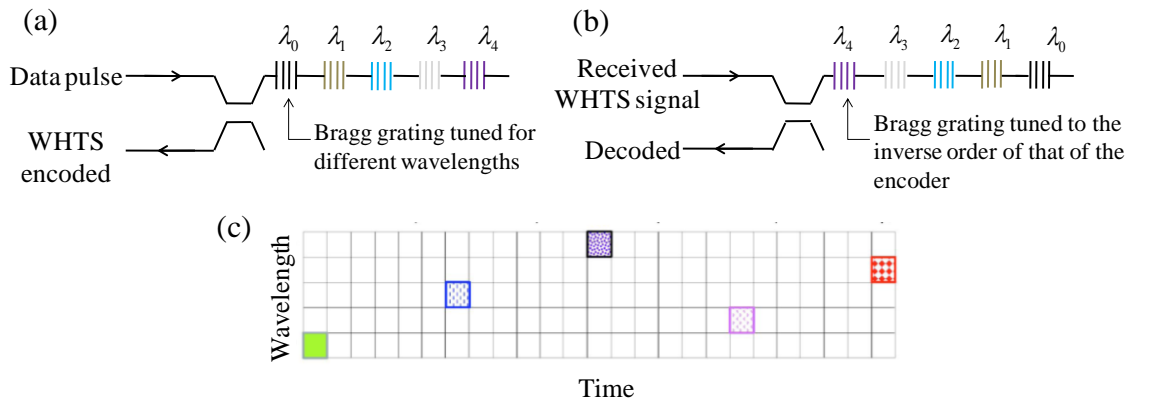


Figure 2.5 A 2-D WH/TS (a) encoder and (b) its decoder using FBGs, (c) is an example of the wavelength hopping pattern [41].

16

order. After passing through the decoder, different wavelength components from the targeted user will be matched and reconstructed by cancelling the relative time delay to generate an auto-correlation pulse, while if the wrong wavelength hopping pattern is applied in the decoder, only cross-correlation signals can be obtained. The main advantage of the WH/TS scheme is the improved code cardinality (the number of available codes) as coding is done in two dimensions. Although various en/decoding techniques have been studied for the incoherent OCDMA, these schemes are usually implemented at a relatively low bit rate and the coding is operated in a unipolar manner, which lead to the disadvantages of small code space and poor correlation performance [20]. The coherent OCDMA is more attractive because of the recent progress of coherent optical en/decoder and its overall superior performance than the incoherent OCDMA [20], and therefore, the research work undertaken in this thesis mainly focuses on the coherent OCDMA.

## 2.3   Coherent OCDMA

In coherent OCDMA system, the optical en/decoding are processed based on the optical field amplitude or the phase rather than the optical intensity. Generally, the coherent OCDMA includes time spreading coherent OCDMA (TS-OCDMA) and spectral phase encoding time spreading OCDMA (SPECTS-OCDMA). For the TS-OCDMA system, the input signal is directly spread in time domain. When data bit "1" is transmitted, a sequence of coherent pulses is generated by the encoder based on the optical code assigned to it. These pulses have some relative phase shifts according to the code sequence. The receiver performs time-reverse operation to make the encoded pulse sequences from the desired transmitter add up constructively and become in phase to generate an auto-correlation peak. The typical TS-OCDMA en/decoder is the superstructured fiber Bragg grating (SSFBG) [22-24, 48]. One drawback inherent to the TS-OCDMA is that the auto-correlation has not only a high level peak but also low level sidelobes [48-49]. On the other hand, in SPECTS-OCDMA system, the en/decoding is performed in spectral domain to the broadband spectrum of an ultra-short optical pulse, where different spectral component has a different phase shift pattern that also results in the pulse spreading in time domain. For the decoding, the phase conjugate pattern is applied to the decoder to recover the spectrum as well as the temporal shape of the original pulse. A typical optical en/decoder of this type is spatial light phase modulator proposed by *A. M. Weiner, et al* [35]. In SPECTS-OCDMA

system, the wavelength alignment between the en/decoding should be very precise and the spectral resolution should be high enough for the sake of the code length and spectral efficiency [49].

A simplified schematic diagram of the coherent OCDMA system is illustrated in Figure 2.6 [17], in which the coherent ultra-short optical pulse generated from the laser source is generally employed. After applying the payload data into the pulse stream by an electro-optic modulator (EOM) with various modulation formats, the original pulse is encoded into a noise-like signal by the encoder, and then the encoded signal is combined with the other user's signals which act as interferences by the star coupler for transmission.
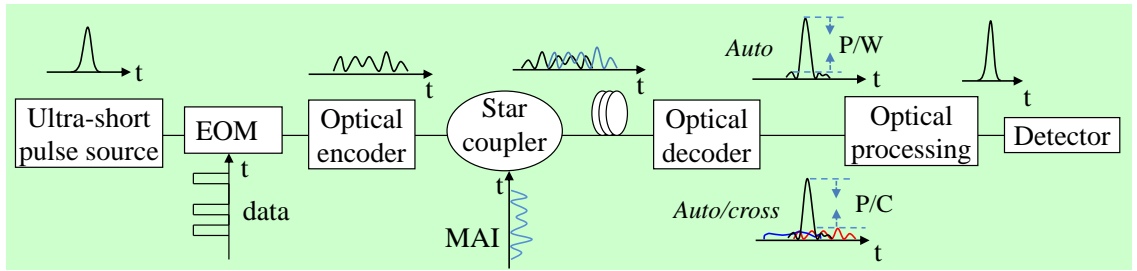


Figure 2.6 Simplified schematic diagram of a coherent OCDMA system.

At the receiver side, the decoder performs matched filtering to decode the received signals. For a target user, the decoder generates an auto-correlation signal, while for the improper users, the output will become cross-correlation pseudorandom noise. It is desirable for the auto-correlation signal to have high peak power but low sidelobes and the cross-correlation signal to have very low peak power. To quantitatively evaluate the auto-correlation and cross-correlation properties, two parameters are generally used [48]: P/W ratio which refers to the ratio of auto-correlation peak level over the maximum wing level for the measurement of the auto-correlation property, and the other one is the ratio of the auto-correlation peak level over the maximum cross-correlation level (P/C ratio) for measuring the cross-correlation property. The auto-/cross-correlation signals will both be directed into the receiver. To eliminate the MAI noise, optical processing such as optical thresholding or optical time gating technique is generally utilized after the decoding. Then, the decoded signal will be detected by proper square law photo-detector where the mixing of the target and interference optical signals will result in the beat noise. The receiver noises such as thermal, dark current and shot noise will arise at the receiver as well [17]. After electrical processing such as signal integration and electrical decision, the original data can be recovered.

In the following sections, the key components for a coherent OCDMA system including the optical sources, various coding devices, optical modulation formats as well as the nonlinear optical processing techniques (optical thresholding/time gating) will be introduced individually. Finally, the security issues in the OCDMA system will be discussed at the end of this chapter.

### 2.3.1  Optical source

The optical source is one of most important components in OCDMA systems. In general, different OCDMA schemes require different suited optical sources. For incoherent time spreading OCDMA scheme, the repetition rate of the optical source should be high enough and the light is incoherently superimposed [37]. Gain-switching distributed feedback laser diode (GS-DFB-LD) and Fabry-Perot laser diode (FP-LD) can be used for this purpose [37]. For incoherent spectral amplitude encoding (SAE) OCDMA scheme, the optical source should be incoherent (phase varies among the spectral components) and have a broadband spectrum with high spectral power density. Generally, light emitting diode (LED), superluminescent laser diode (SLD) and amplitude spontaneous emission (ASE) source can be used for the SAE-OCDMA [37]. For 2-D incoherent OCDMA, as it is operated in both the time and spectral domain, it requires the optical source to be high speed for time spreading and spectrally broadband for spectral coding. Furthermore, the optical source should have a relatively short coherence time compared with the pulse duration to achieve incoherent superposition of the decoded optical pulses [50]. Free-running gain-switched FP laser diode and ASE source with high speed modulator can be used for this scheme [50].

While in coherent OCDMA system, the en/decoding is based on the amplitude or phase so the optical source should generate transform-limited highly coherent optical pulses in the order of picoseconds [37]. In practice, mode locked laser diode (MLLD) is widely used for coherent OCDMA system which can provide ultra-short coherent optical pulses for time spreading and wideband discrete spectrum that is in phase for spectral phase encoding. As in this thesis, the mode locked laser is mainly used to perform the optical en/decoding, the basic principle of the mode-locking laser is briefly reviewed as follow. The laser usually has a ring cavity and a number of resonant frequencies called modes oscillate inside it. The frequency spacing $\omega_f$ between these modes is same and it is determined by the laser cavity length, which is given by [51] :

$$\omega_i - \omega_{i-1} = \frac{\pi c}{L} = \omega_f \ (i=1, 2\ldots) \tag{2.1}$$

The output electric field *E(t)* is the summation of all the oscillation modes in the time domain,

$$E(t) = \sum_n E_{nn} e^{j[(\omega_0 + n\omega_f)t + \phi_n]} \ (n = 1, 2\ldots) \tag{2.2}$$

where $E_n$ and $\Phi_n$ are the amplitude and phase of the $n_{th}$ mode. When the laser is operated at the free oscillating state, the $E_n$ and $\Phi_n$ can take any value and thus the superposition of all the modes with random amplitude and phase results in the energy distribution like a noise in the time domain. While if all the modes are in phase with each other and thus the summation of them becomes [51]:

$$E(t) = \frac{\sin(N\omega_f t / 2)}{\sin(\omega_f t / 2)} e^{j\omega_0 t} \tag{2.3}$$

which corresponds to a periodic pulse train with a period of $T=2\pi/\omega_f$. The peak power is *N* times of the single mode and the pulse width is *T/N* which shortens as *N* increases. In this thesis, the MLLD used in the experiments operates at standard telecommunication data rate 9.95328GHz (OC-192), with the spectrum tunable at around 1550nm.

### 2.3.2  Optical encoder/decoder

Despite the optical technology for fabricating the optical en/decoder is still in its infancy, great achievements have been made on developing various types of optical en/decoders for photonic networks applications such as the optical packet switching (OPS) [52-53] and OCDMA. In particular, in OCDMA system, the optical en/decoder is the key component that mainly determines the system performance. However, the optical en/decoding operated in coherent OCDMA system have not been discussed until now. The typical optical en/decoders demonstrated in coherent OCDMA system are concluded as follows:

**1.  Planar lightwave circuit (PLC)**

The planar lightwave circuit (PLC) base optical en/decoder is mainly used for temporal phase encoding coherent OCDMA, and was firstly reported by *Wada, et al* in 1997 [26, 54-55]. The temporal phase encoding OCDMA is to manipulate the phase of optical signal in the time domain by firstly splitting the short pulse into multiple optical pulses through the differently temporal-delays and then imprinting the different phase shifts to these optical pulses through using multiple different phase shifters [36]. The

20
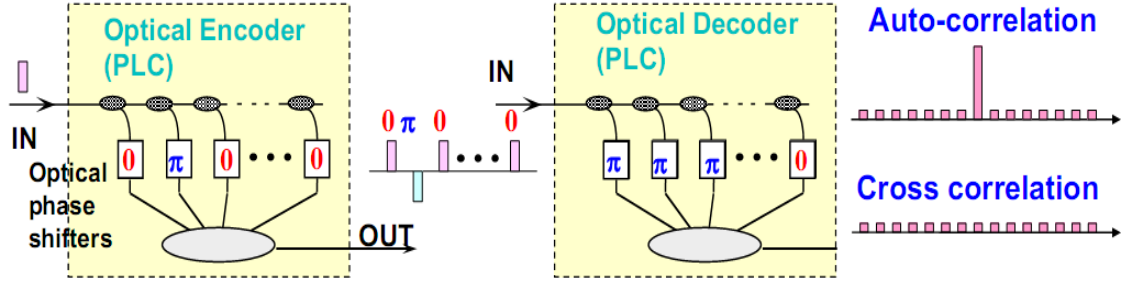
Figure 2.7 PLC based temporal phase optical en/decoder [26].

PLC based optical en/decoder comprises of tunable taps, optical phase shifters, delay lines, and a combiner, as shown in Figure 2.7 [26]. They are monolithically integrated on Si-substrate by PLC fabrication method and are installed in a temperature-controlled box. In the encoder, taps are connected via delay lines whose delay time corresponds to the time interval between chip pulses. The tunable tap is a Mach-Zehnder interferometer (MZI) which is composed of two 3-dB couplers and two optical phase shifters. The optical carrier phase can be varied by changing the refraction index of the waveguide that is altered by the variation of its temperature. Different chip pulse can thus have a phase shift of 0 or $\pi$. The decoder has the same structure with the encoder, so that the time-reversal operation to the encoded signals received can be done by it. Figure 2.8 (a) shows the reported encoded waveform of 8-chip bipolar optical code {0, $\pi$, 0, $\pi$, 0, $\pi$, 0, $\pi$} [26]. The time interval between each chip pulse is 5ps corresponding to the chip rate of 200Gchip/s. After correctly applying the matched code in the decoder, the measured intensity distribution of the auto-correlation signal is shown in Fig. 2.8 (b), which has a peak intensity of 64 volts. While the cross-correlation signal for an unmatched code {0, $\pi$, 0, $\pi$, $\pi$, 0, $\pi$, 0} has a maximum peak intensity of 16 volts, as shown in Fig. 2.8 (c).



Figure 2.8 (a) Encoded waveform of 8-chip code using PLC and its auto-correlation (b) and cross-correlation signals (c) [26].

21

The PLC based optical en/decoder with 8-chip was successfully demonstrated in a 10-Gb/s, time spreading coherent OCDMA system [26]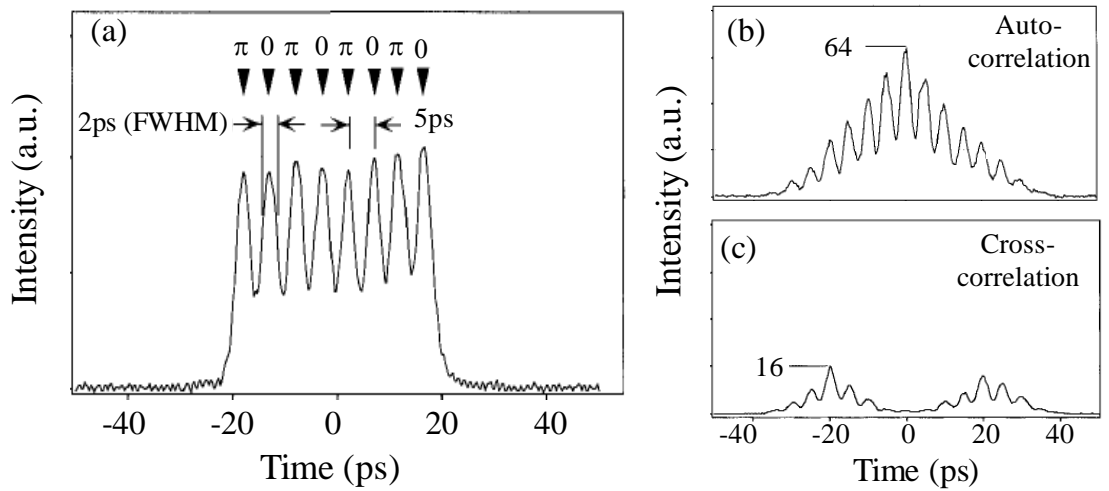. However, the main drawback of the PLC based device is the difficulty of generating ultra-long temporal phase code due to the physical constraint of the silica substrate and design complexity, and hence the code scalability as well as the performance are relatively poor [36, 48].

## 2. Phase shifted superstructured fiber Bragg grating (SSFBG)

To improve the drawback of the PLC based temporal phase optical en/decoder, another temporal phase en/decoder that can generate very long bipolar codes is proposed: phase shifted superstructured fiber Bragg grating (SSFBG) [22-23]. The SSFBG is a special type of fiber Bragg gratings, which is defined as a FBG with slowly varying modulation envelope imposed on the rapidly varying refractive index along the grating length [22-23, 56]. It can be employed to implement sophisticated functions such as pulse shaping [57], pulse repetition rate multiplication [58] as well as optical en/decoding. In the weak SSFBG grating limit (typically reflectivity less than 20%), the light can penetrate through the whole grating and each individual grating element can contribute more or less to the reflection, and the wave vector response $F(k)$ can be expressed as the Fourier transform of the spatial refractive index modulation profile $A(x)$ [22],

$$F(k) = \frac{1}{2\pi} \int_{-\infty}^{\infty} A(x) e^{jkx} dx \tag{2.4}$$

Here, the grating central wavelength is determined by the uniform rapid refractive index modulation. The impulse response $h(t)$ of the grating is given by the inverse Fourier transform of the grating frequency response $H(\omega)$,

$$h(t) = \int_{-\infty}^{\infty} H(\omega) e^{-j\omega t} d\omega \tag{2.5}$$

As the wave vector is proportional to the optical frequency $\omega$, the impulse response of the grating will have a temporal profile given by the complex form of the superstructured refractive index modulation profile. When a short optical pulse is injected into the SSFBG based encoder, its encoded temporal profile $y(t)$ will be given by the convolution of the input pulse $x(t)$ and the impulse response $h_e(t)$:

$$y(t) = x(t) \otimes h_e(t) \tag{2.6}$$

which is actually the product of the spectrum of the input pulse $X(\omega)$ and the frequency response of the SSFBG $H_e(\omega)$ in frequency domain. The decoding is essentially the matched filtering of the frequency response $H_d(\omega)$ with the encoded signal, and the

overall frequency response $R(\omega)$ of the encoder and decoder associated with an impulse response of $r(t)$ can be expressed as:

$$R(\omega) = H_e(\omega) \times H_d(\omega) \qquad (2.7)$$

From which it is clear that if the $H_d(\omega) = H^*_e(\omega)$, the $r(t)$ is the autocorrelation function of the superstructure profile in the encoder with the impulse response of the decoder, and $h_e(t) = h_d(-t)$. Physically, this requires the superstructure function of the decoder is the spatially reverse form used to write the encoder grating [22]. The final temporal profile $S(t)$ of the decoded signal for the input pulse $x(t)$ can be obtained by the inverse Fourier transform:

$$S(t) = \int_{-\infty}^{\infty} X(\omega)R(\omega)e^{-j\omega t}d\omega = x(t) \otimes r(t) \qquad (2.8)$$

By inserting multiple phase shifts between different grating segments, a phase shifted SSFBG can be formed and the temporal phase code pattern can be imprinted on the spatial structure of the grating [22, 48]. Figure 2.9 shows the en/decoding principle of a typical phase shifted SSFBG based optical en/decoder [48]. As a short optical pulse propagates through the SSFBG, it generates a reflected temporal response that consists of a series of coherent "chip" pulses with chip duration $T_{chip}$ given by the $2L_{chip}n/c$ ($L_{chip}$ is the length of each grating segment). The relative phase between the chip pulses is determined by the phase shift pattern or the refractive index modulation profile in the SSFBG. To decode the encoded signal, the time reversed phase shift pattern should be applied into the decoder to generate a high-level auto-correlation signal, otherwise only low-level cross-correlation signals will be output.
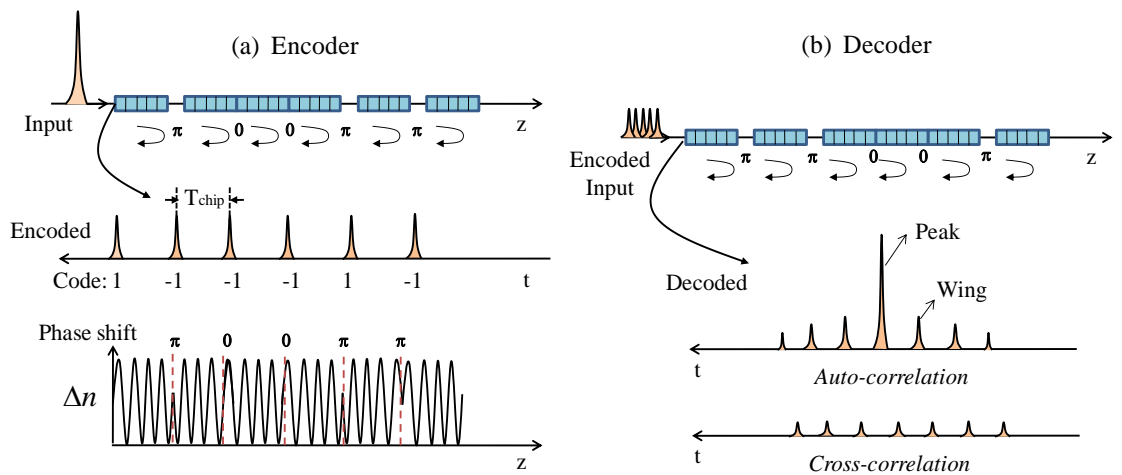


Figure 2.9 (a) SSFBG based optical encoder and its refractive index profile and (b) decoder.

Previously, researchers from University of Southampton have fabricated seven- and 63-chip phase shifted SSFBG based optical en/decoders, and investigated their coding performances in a two-user OCDMA system [22]. Figure 2.10 (a) shows the measured
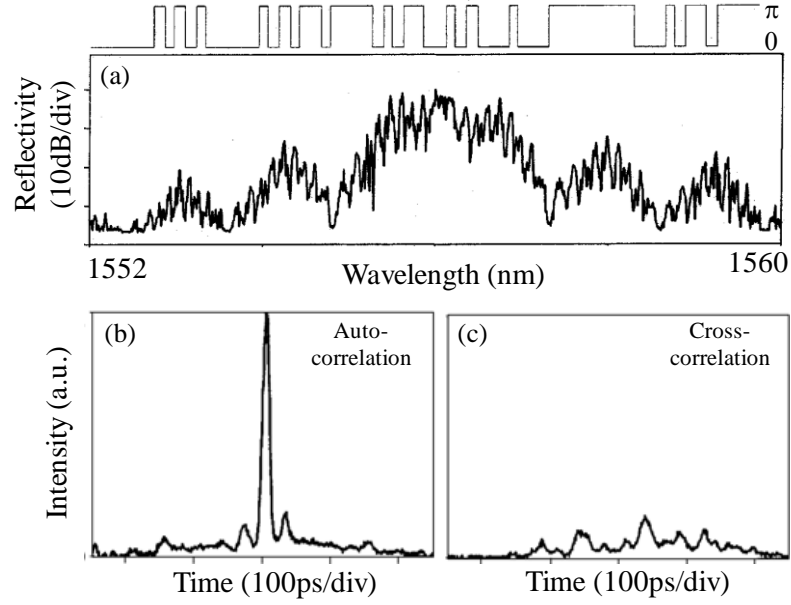
Figure 2.10 (a) Measured encoded spectrum of 63-chip SSFBG based optical encoder and its auto (b) and (c) cross-correlation signals [22].

spectral response of the fabricated SSFBG with 63-chip optical code [22]. Many peaked reflectivity profiles in the spectra are generated due to the numerous discrete phase transitions. The measured auto-/cross-correlations are also shown in Fig. 2.10 (b) and (c), respectively. Clear peak distinction of the auto-/cross-correlation signals was obtained. The phase shift in the SSFBG can even be upgraded to multi-level such as quarternary phase shifting to improve the code cardinality and coding performance [59]. A quaternary phase coding SSFBG with 255-chip and 320Gchip/s chip rate has been demonstrated in [59]. The key advantages of the SSFBG en/decoder are the capability of generating ultra-long optical code with ultra-high chip rate to achieve good correlation performance and the potential low cost. For example, in [23], a record 511-chip, and 640Gchip/s SSFBG based optical en/decoder has been reported. Figure 2.11 (a)~(f) shows the encoded waveforms and auto-/cross-correlation performances for two 511-chip optical codes OC-A and OC-B [23]. It can be seen that the encoded waveforms have decayed profiles because when the light is reflected from the SSFBG, the signal reflected from the far-end of the grating experiences more loss after penetrating through the whole grating than the near-end. High quality code recognition performance has been observed with well-defined auto-correlation peak and low-level cross-correlation. The peak to wing ratio and peak ratio of auto-/cross-correlations signals are roughly estimated to be 40 and 14 for OC-A, and 23 and 10 for OC-B, respectively. Based on this SSFBG with a high chip count, a 10-user truly asynchronous gigabit OCDMA transmission experiment has been successfully demonstrated [60].

24

Apodization technique can be employed to balance the intensity of the reflected chip pulses to make the encoded waveform more uniform to further improve the coding performance [48]. In addition, by using electrical heating method, the phase pattern in the SSFBG can even be reconfigured [28-29]. Currently, the SSFBG can achieve the highest code length, but the reflectivity is usually not very high and the long code length may hinder the individual user's data rate [61].
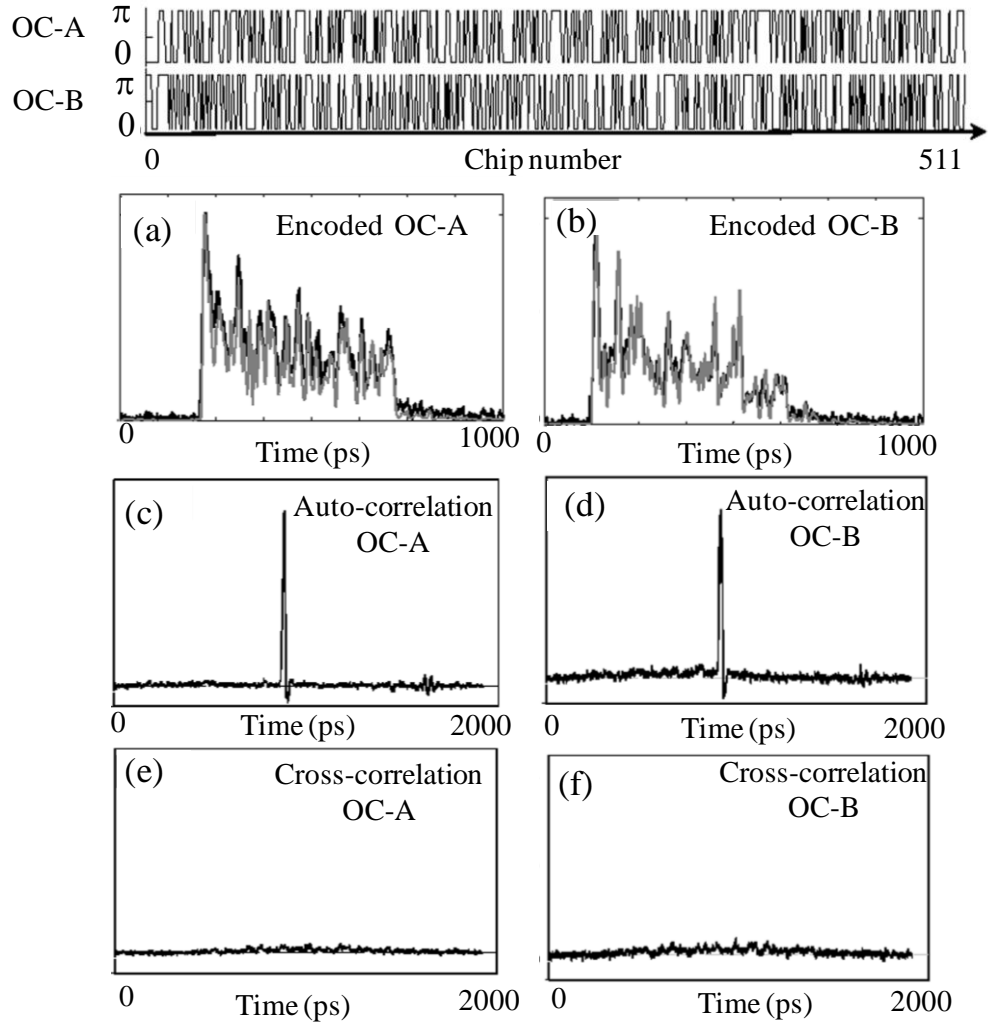


Figure 2.11 (a)~(f) are the measured encoded waveforms, auto-correlation and cross-correlation signals for OC-A and OC-B, respectively [23].

## 3. Spatial light phase modulator

The spatial light phase modulator (SLPM) based optical spectral phase en/decoder is similar to the SAE en/decoder, which is essentially a *4f* optical system using grating apparatus [61-63], but the amplitude mask is replaced by a phase mask and the laser source is an ultra-short optical pulse. One typical SLPM based optical en/decoder for SPECTS-OCDMA system was originally proposed by *A.Weiner, et al* [35]. Figure 2.12
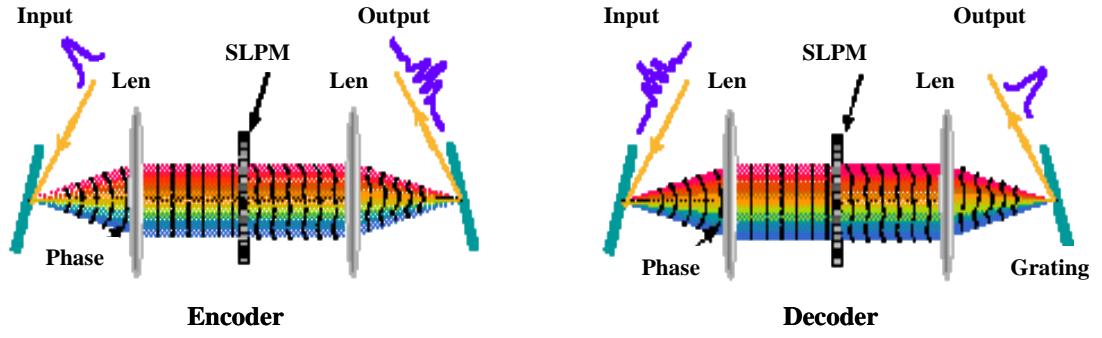
Figure 2.12 Spatial light phase modulator based optical en/decoder [61].

shows the basic structure of this kind of en/decoder, which consists of diffractive grating, lens and SLPM [61-63]. In the encoder, each frequency component of the input ultra-short pulse is diffracted onto the spatial domain by the grating. The focal lens is used to collimate the diffracted light into parallel light, and a phase mask placed at the center focal plane is used to apply spatial phase shifts to different frequency components. The code length of the phase mask is determined by the spectral resolution that is related to the beam diameter on the grating, the grating spectral dispersion, and the spot size of the SLPM. After the second grating, the phase encoded signal at the output is reconstructed, which exhibits a noise-like signal in the time domain. To reconstitute the original pulse, the phase conjugate mask is added into the decoder and simply compensates the phase offset introduced by the encoder. If the second mask does not match with the first, the spectral phases are rearranged and the waveform remains a spread, low-intensity, pseudonoise burst. The measured waveforms of the encoded and decoded signals for a 44-element pseudorandom binary sequence are shown in Figure 2.13 [35]. Dramatic reduction in the intensity of the encoded and incorrectly decoded signals has been achieved, and the contrast ratio can reach to 25. The SPLM can support programmability by addressing the phase mask, but it is based on bulk optics which introduces high loss and requires accurate spatial alignment of the diffraction gratings for the sake of en/decoding performance [36].



Figure 2.13 Measured autocorrelation trace of the (a) uncoded and coded pulse and (b) correctly decoded and incorrectly decoded pulses for a 44-element phase mask [35].

26

## 4. Array waveguide grating (AWG)

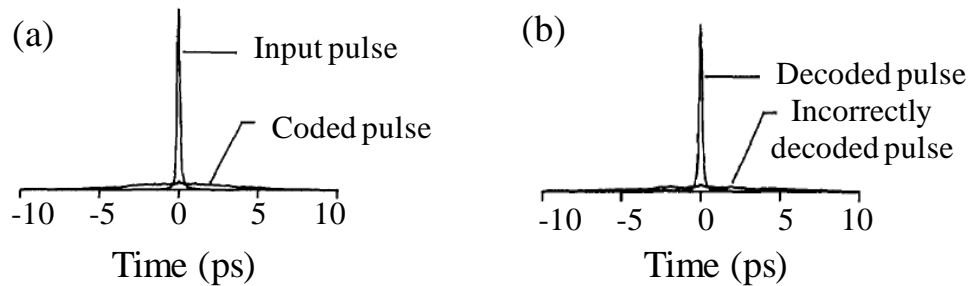The AWG based optical en/decoder is mainly used for spectral phase en/decoding. But unlike the SLPM that is based on the bulk optics which makes it has high loss and incompatible with the fiber optical system, the AWG has the potential advantage of integrated with other photonic components in a chip. Figure 2.14 shows the layout of an AWG based optical en/decoder designed by Prof. *S. J. Ben Yoo's* group in the University of California at Davis [27, 64]. In this device, the AWG pair performs spectral demultiplexing and multiplexing. For the optical encoder, the input coupler collimates the input pulse from the input waveguide to the array of waveguides which can provide a wavelength-dependent phase shift, and the output coupler focuses different wavelengths onto different output waveguides, so spectral demultiplexing can be achieved. Each output waveguide arm is fabricated with a waveguide electro-optic phase modulator that can apply a phase shift corresponding to the desired OCDMA code to each demultiplexed spectral channel. The second AWG recombines the spectral components with different phase shift and generates the encoded signal. The input and output waveguides of the device are chosen for wavelength match of the two AWGs. The decoder has similar configuration except that the phase shift is applied using the phase conjugate code pattern.
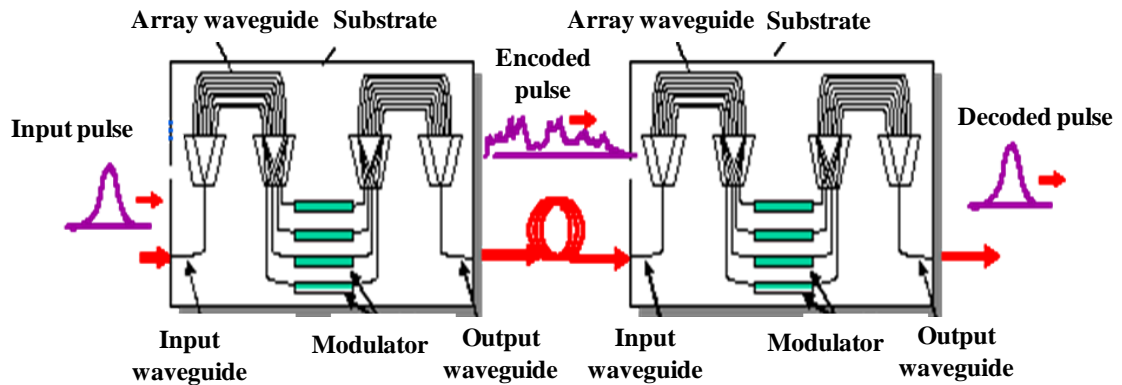


Figure 2.14 AWG based optical encoder/decoder fabricated in *UC Davis* [64].

Figure 2.15 (a) shows the reported optical transmission spectrum through the packaged InP OCDMA en/decoder, which consists of an identical pair of eight-channel AWGs with 180 GHz channel spacing and a free spectral range of 12-channel spacing [64]. The total wavelength span of 1.4 THz provided by the eight channels is sufficient for encoding subpicosecond ~0.5 ps pulses. The decoded auto-/cross-correlation signals for code 11110000 are shown in Fig. 2.15 (b)~(c), respectively. Clear contrast between

27

the correctly decoded versus the incorrectly decoded OCDMA waveforms can be observed. Based on the 8-chip AWG based optical en/decoder in InP, a three-user, two time slot (6 users totally) OCDMA demonstration has been achieved using time coordination and optical gating techniques [64].
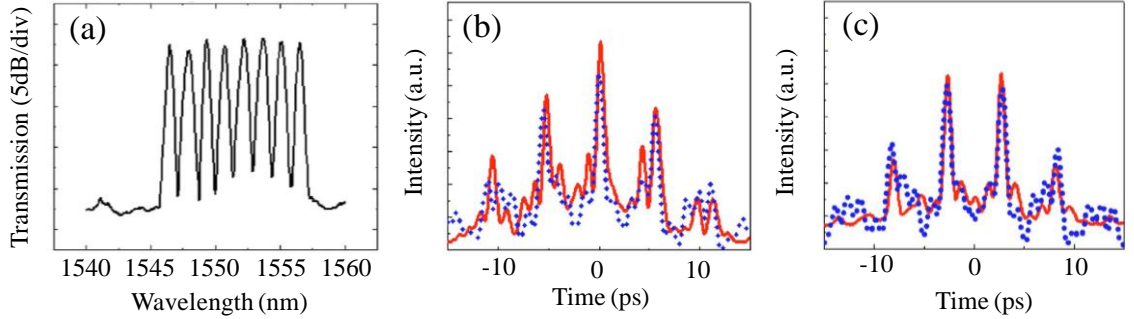


Figure 2.15 (a) Transmission spectrum of the AWG based OCDMA encoder; (b) and (c) are the correctly and incorrectly decoded output from the decoder for code 11110000. (The solid curves are experimental results and dotted lines are simulated results) [64].

## 5. Micro ring resonator

Micro-ring resonators are wavelength selective devices that have various applications in channel filtering, dispersion compensation, optical switching and so on [65-67]. With the maturity of fabrication technology, immense progress has been made in the micro-ring resonator. In 2005, *Anjali Agarwal, et al* [68-69] reported a micro-ring resonator based spectral phase en/decoder, as is shown in Figure 2.16 (a). The structure was fabricated by high refractive index glass in planar waveguide geometry. A common input bus and output bus waveguide are combined with stacks of micro-ring resonators that form a fourth-order resonator. The ring radii are 47 μm. The fourth order filter cell occupies a chip area of 100μm×400μm allowing for a large number of filter cells to physically reside on a chip. Each stack act as a bandpass filter which is defined as a frequency bin. A number of micro-ring resonator stacks are tuned to select individual axial modes of the mode-lock laser. The relative phase shift between two adjacent
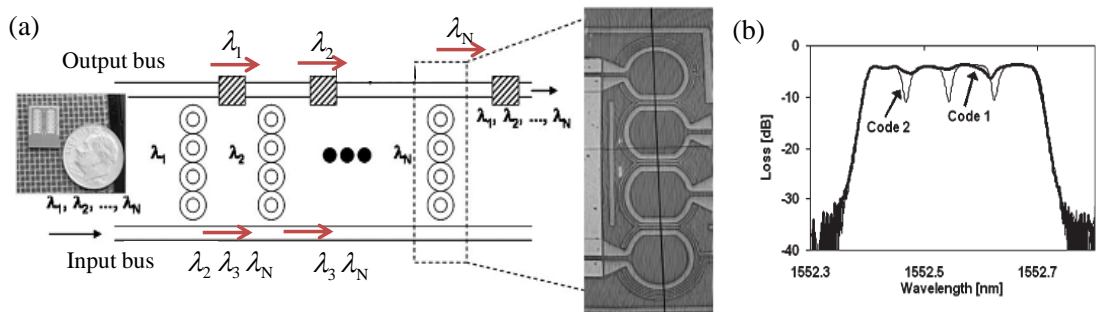


Figure 2.16 (a) Micro-ring based spectra phase encoder and (b) its encoded spectrum [69].

frequency bins is controlled by thermal-optic phase heaters along the bus waveguide. When a short pulse with broadband spectrum is injected, different spectral components can be adjusted to be resonant on different frequency bins and then experience a phase shift, so the original pulse is spectrally phase encoded. Figure 2.16 (b) shows the encoded spectrum for four bins with two different codes. The output has a flat topped sharp filter response and sharp dips are seen in the spectrum when the relative phase difference between adjacent frequency bins is $\pi$. The 3dB bandwidth is 8GHz with a spacing of 10GHz between the frequency bins. The decoding uses phase-conjugate decoder to realign the phase of the shifted frequency components to recover the original pulse [69]. Figure 2.17 shows the reported en/decoding performances for four optical codes [69]. The encoding after applying the phase pattern results in the temporal spreading of the pulse energy away from the central position of the original uncoded pulse. The decoded signal recovers the original pulse when the phase patterns in the encoder and decoder are matched, whereas for the other unmatched codes, the energy of the decoded signal remains distributed away from the central position of the correctly decoded pulse [69]. By using terahertz optical asymmetric demultiplexer (TOAD) based time gating technique, the auto-correlation signal can be discriminated and extracted in the central time slot from the cross-correlation signals [69]. The micro-ring resonator based optical en/decoder has good tunability and ultra-high resolution, which can potentially improve the reconfigurability and the spectral efficiency of the OCDMA system. The code length can be increased by adding more frequency bins, and a six-user OCDMA experiment at 5-Gb/s using the micro-ring resonator with 8 frequency bins has been reported in [70].



Figure 2.17 Temporal response after four-chip optical encoder and its corresponding decoded waveforms after the decoder with code 4 [69].

## 6. Multi-port optical en/decoder

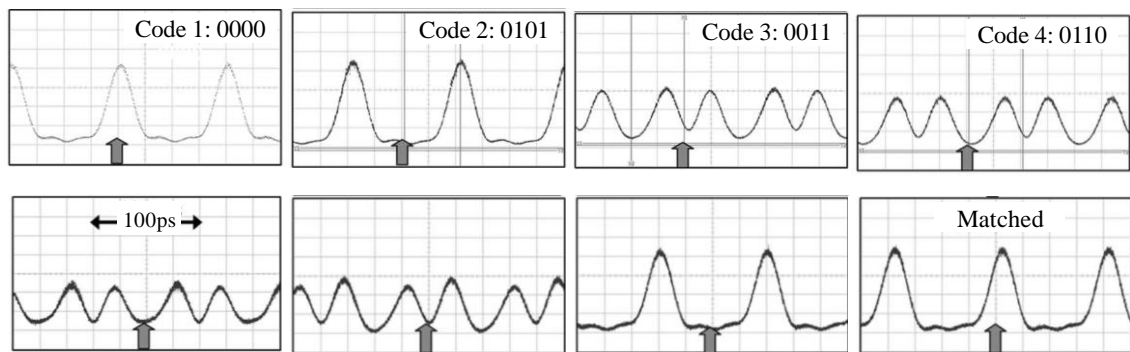For traditional optical en/decoder, each optical code is generated by one device and allocated for a single user, which makes the system rather complex and the total cost will be increased accordingly. An innovative passive planar multi-port en/decoder that is able to generate and process a set of code words simultaneously has been designed [71]. By using the multi-port encoder in the central office, and low cost decoder in the user's side, the number of coding device will be reduced and the whole OCDMA system would become more flexible and cost effective. As shown in Figure 2.18, the multi-port optical en/decoder is in arrayed waveguide grating (AWG) configuration [72]. When a short pulse is fed into one of the input ports, several copies of the pulses are generated by the slab coupler. These pulses travel different paths in the grating with different phases and the output slab coupler recombines these pulses to simultaneously generate multiple codes from the output ports (OC1, OC2 …). To process the decoding, the incoming OC is forwarded into the same input port, and the auto-correlation peak can be detected at the corresponding output port while all the other ports will produce cross-correlation signals [72]. The multi-port device has periodic spectral response and multiple optical codes are processed in multiple wavelength bands simultaneously, so it has a powerful code discrimination capability. A 16×16 multi-port optical en/decoder with a chip time interval of 5ps corresponding to 200Gchip/s has been firstly fabricated [71-72]. Researchers have also developed 50chip, 500Gchip/s multi-port en/decoder that is able to generate 50 different phase shift keying codes simultaneously by using this structure and successfully demonstrated a hybrid 5-WDM channels and 25-OCDMA users system with a total capacity of 1.24 Tbit/s [73].
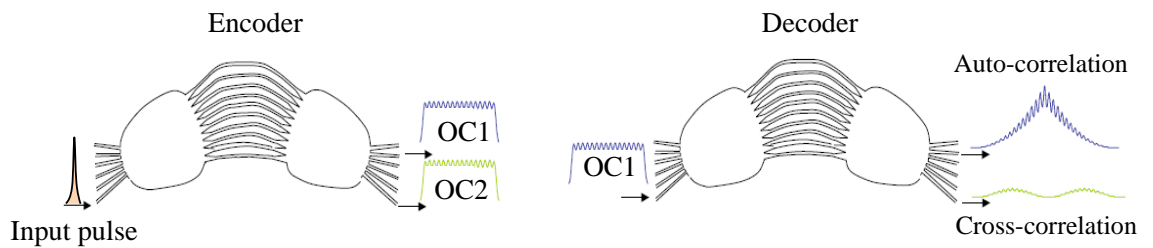


Figure 2.18 Multi-port optical encoder (a) and decoder (b) [72].

## 2.3.3 Nonlinear optical processing in OCDMA

In OCDMA system, after the encoded signal is decoded by the corresponding optical decoder, the signal must be identified and retrieved, which requires the decoded optical signal to be converted into an electronic signal in order to recover the target data with low-error probability using a photo-detector. In coherent OCDMA system, the properly

decoded signal is usually a short optical pulse which is in the order of chip time (several *ps*) compared with the bit duration (several hundred *ps*), and thus it requires chip rate detection (several hundred GHz) which is usually higher than the data rate (tens of GHz) by using an ideal photo-detector with a response time less than, or equal to the chip duration to effectively discriminate the auto-/cross-correlations [74]. However, no photo-detector up to date has a response time in this range and most of them are bandwidth-limited that cannot match with the chip-rate detection. Moreover, the ideal photo-detector with a high bandwidth will induce high cost of the system. In practice, it is desirable to employ the current commercial available photo-detector with relatively higher response time (low bandwidth) that performs "data-rate" instead of "chip-rate" detection to reduce the system cost. But in the case of data rate detection, the photo-detector cannot distinguish the correctly decoded auto-correlation signal and the incorrectly decoded cross-correlation signal as the two kinds of signals have the same integrated energy from the perspective of the detector. The cross-correlation signals that contribute to the MAI noise will eventually degrade the OCDMA system performance. Therefore, in a practical system with data-rate detection, ultrafast nonlinear optical signal processing techniques are proposed as a solution to discriminate the auto-/cross-correlation signals and reduce the MAI noise to improve the system performance in optical domain.

Optical time gating and optical thresholding (or hard limiting) are two widely used techniques to suppress the MAI noise in OCDMA system. Figure 2.19 (a) and (b) show the general principle of optical time gating and thresholding. The optical time gating technique usually requires additional pump source to perform nonlinear interaction with the decoded auto-/cross-correlation signals, and only the signal synchronized to the pump signal in time domain can participate in this nonlinear process, so the MAI noise out of this timing window can be eliminated and the desired signal can be extracted. Many optical time gating techniques have been explored in OCDMA systems including the four-wave mixing (FWM) in semiconductor optical amplifier (SOA) [76] or highly nonlinear fiber [77], ultrafast nonlinear interferometer [63], and nonlinear optical loop mirror (NOLM) [63] and so on. The NOLM is the most frequently used technique in many demonstrations, such as in the spatial light phase modulator [63] and micro-ring resonator [70] based optical en/decoding experiments. Figure 2.20 (a) shows the basic configuration of a NOLM based optical time gating [63]. The NOLM is essentially a Sagnac interferometer, which consists of an optical loop formed by a 2×2 coupler and a nonlinear element placed in the loop. The input signal will be divided into two optical
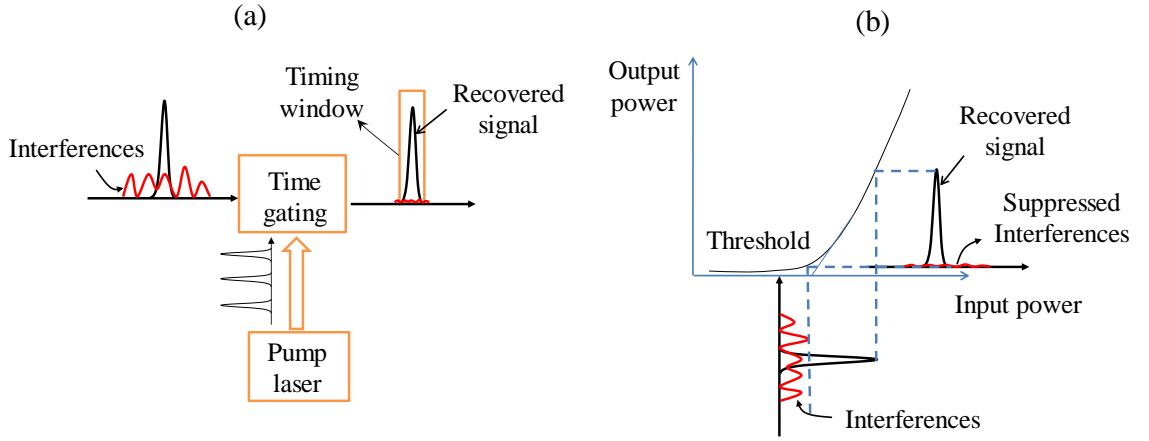
Figure 2.19 Schematic diagram of (a) time gating and (b) optical thresholding.

signals by the coupler: one circulates in the clockwise direction (CW) and the other one circulates in the counter-clockwise direction (CCW). In the absence of the control pulse, the CW and CCW optical pulses meet and interfere at the coupler after circulating through the loop and then the interfered signal will be reflected back to the input port, which is thus called "loop mirror". However, if the control pulse with a wavelength other than the signal is injected and synchronized with the CW pulse, nonlinear interaction occurs (cross-phase modulation) in the nonlinear element because of the high intensity of the control pulse and thus the CW pulse will experience a phase shift while the CCW pulse has no such phase shift. If the accumulated phase difference inside the loop for the CW and CCW pulses reaches to $\pi$, destructive interference happens when the two pulses meet at the coupler, and then the interfered signal will be gated out from the other port. Additional bandpass filter can be used to block the control pulse and extract the gated signal. Figure 2.20 (b) and (c) show the reported demonstration of an eight-user OCDMA system using the NOLM based optical time
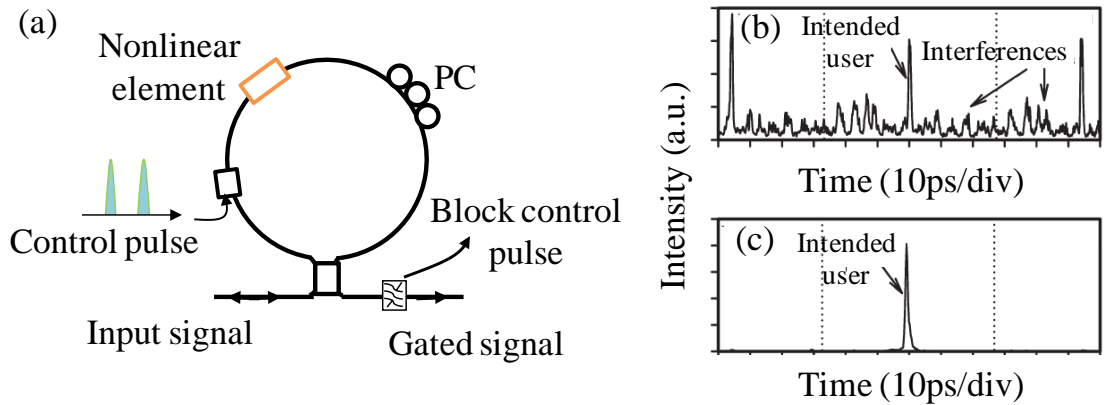


Figure 2.20 Schematic diagram of (a) nonlinear optical loop mirror based time gating; (b) and (c) are the measured cross-correlation input and output signals of the NOLM with eight users [63].

gating [63]. The intended user's signal is this case has a pulse width ~900fs and the cross-correlation signals from the other users are visible in the adjacent time slots. After the NOLM gating, the intended user's signal has been extracted and nearly all the energy of the interference signals has been suppressed. Although the optical time gating can efficiently reduce the noise as have been demonstrated [76-77], it requires chip-level synchronization between the control pulse and the target signal, and as a result it will diminish the asynchronous access without any time coordination for OCDMA, which is one of the advantages over TDMA and WDMA [13]. And also, after optical time gating, there still exists interference noise within the time-gating window, so the other approach optical thresholding seems more attractive for OCDMA system.

Fig. 2.19 (b) illustrates the basic principle of optical thresholding. Unlike the optical time gating that performs the chip-rate detection to reduce the MAI noise by eliminating the noises outside the time window, the optical thresholding employs peak power of the signal rather than the average power to discriminate the auto-/cross-correlation signal, and it does not require any synchronization. As the peak power of the incorrectly decoded signal is generally smaller than the auto-correlation signal, it can be significantly suppressed after passing the optical thresholder with a sharp transfer function whose transmittance dramatically increases when the input signal power is larger than the thresholding power. By amplifying the auto-correlation signal to a magnitude that its peak power is larger than the threshold, the auto-correlation signal can be transmitted without influence while the MAI noise will be suppressed due to the relatively small peak power induced low transmittance, which can be clearly seen in Fig. 2.19 (b). The main challenge for optical thresholding technique is to minimum the thresholding power whilst keeping its MAI suppression performance and to achieve very steep response of the transfer function.

Various optical thresholding approaches have been previously demonstrated, which includes second-harmonic generation in periodically poled lithium niobate (PPLN) [75], super-continuum generation (SC) based on dispersion flattened fiber (DFF) and holey fiber [74, 78], two-photon absorption [79-80] and nonlinear optical loop mirror (NOLM) [81-82]. Compared with the other techniques, the super-continuum generation (SC) based optical thresholder has the advantages of easy to operate using low cost devices, polarization-independency and has very steep transfer function [74], and thus it has been used in most of the experiments in this thesis. The operation principle of the SC generation based optical thresholder in a DFF fiber is explained in Figure 2.21 (a)

[74]. It is composed of an EDFA, a DFF, and a bandpass filter (BPF). For the correctly decoded auto-correlation signal, the EDFA boosts it to a proper power level to enable the super-continuum generation in the DFF, which is based on the third-order nonlinear effect self-phase modulation (SPM). As the short-pulse with high peak power propagates through the nonlinear optical fiber, the nonlinear refractive index and thus the phase of the pulse changes with its own intensity, causing the spectral broadening effect as frequency is the derivative of phase over time [3]. Then the BPF only allows the newly generated SC signal passing through and rejects the original signal. While the incorrectly decoded signals (MAI noise) spreading over a large time span with very low peak power is unable to generate the SC. Therefore, after BPF, the incorrectly decoded signal can be suppressed and only the correctly decoded signal passes through the thresholder [74]. Figure 2.21 (b) shows the measured transfer function of the SC based optical thresholder in DFF [74]. It can be seen that a rather steep transfer function can be achieved and the operation power is also as low as ~ 1dBm. Unfortunately, current optical thresholding techniques can only be applied for on-off-keying (OOK) data based on the signal intensity because the signal phase cannot be preserved after the thresholder. Saturable absorber may be a possible solution for implementing the optical thresholding for phase modulated signal [83].



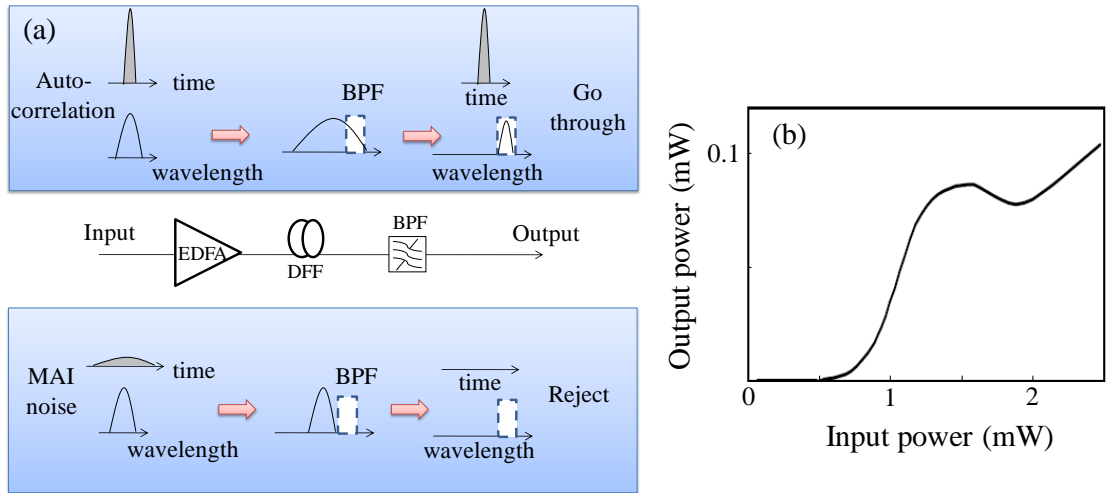Figure 2.21 Schematic diagram of (a) SC based optical thresholder and (b) its transfer function [74].

## 2.4 Optical modulation formats in OCDMA

In fiber optical communication system, it is necessary to modulate the information into the carrier light signal for transmission. Generally, there are two ways for the data modulation in fiber-optic system: direct modulation and external modulation [84, 85].

For direct modulation, the data is directly injected into the laser diode, so the output optical signal is modulated by the injection current. This approach is very simple, compact and has low cost. However, as the injected data rate is increased to gigabit per second, the generated laser has serious frequency chirp [84, 85], which deteriorates the signal and limits the system performance. External modulators that can solve the problem of direct modulation are developed, which enable signal transmission at high data rate of gigabit per second with small frequency chirp. In today's optical communication, two types of external modulators are used: electro-absorption modulator (EAM) and Lithium Niobate (LiNbO$_3$) modulator [84, 85]. The EAM modulator uses semiconductor material that has a band gap higher than the photon energy of the incident light, so it allows the light propagates through in the normal state [86]. When applying an electric field to the EAM, the band gap of the semiconductor will shrink due to the stark effect causing the incident photos to be absorbed by the material and thus modulation can be achieved [86]. The response time is sufficiently fast to enable up to gigabit modulation. The EAM can also be combined with a continuum laser (CW) to generate periodic pulse train [86]. The LiNbO$_3$ modulator is based on the electro-optical effect that the refractive index of the optical waveguide in the modulators is changed by the applied electrical data, leading to the modulation of the intensity, phase and even polarization state of the incident light, according to which a variety of modulation formats have been developed, such as on-off-keying (OOK), differential-phase-shift-keying (DPSK), differential quadrature-phase-shift-keying (DQPSK) [84-85], and so on. A phase modulator can be easily realized by using a straight LiNbO$_3$ waveguide. By making LiNbO$_3$ waveguide into different structures, various modulation formats can also be achieved. A typical structure is a LiNbO$_3$ Mach-Zehnder modulator also known as interferometer modulator [86], which will be widely used as an intensity modulator in this thesis.

Figure 2.22 shows the configuration of a single drive LiNbO$_3$ Mach-Zehnder modulator, which could also be dual-drive [86]. The input optical signal is split equally and sent into two different optical straight waveguides. The two split signals recombine at the output port of the waveguide and interference happens. The optical field amplitude of the output signal can be given by:

$$E_{out} = \frac{1}{\sqrt{2}}(e^{j\phi_1} + e^{j\phi_2})E_{in} \qquad (2.9)$$

where $\Phi_1$ and $\Phi_2$ are the phase changes through the two optical paths. By driving the straight waveguide using the electrical signal, the refractive index and thus the phase

difference $\Delta\Phi$ can be changed, which becomes:

$$\Delta\phi = \phi_1 - \phi_2 + \phi_{bias} \propto \Delta n \frac{2\pi}{\lambda} L + \phi_{bias} \qquad (2.10)$$

where $\Delta n$ is the refractive index change relating to the applied voltage, $\Phi_{bias}$ is the DC bias voltage induced phase shift. The phase change will induce the constructive and destructive interference of the output signal. A measured transmission curve of the Mach-Zehnder modulator is shown in Fig. 2.22 (b). The required voltage to make transmittance change from maximum and minimum is ~4.5V, which is known as the $V_\pi$. By adjusting the bias voltage to the linear region, the intensity modulation can be achieved. More complicated waveguide configurations using the Mach-Zehnder interferometer as the basic structures can be constructed for advanced optical modulations.
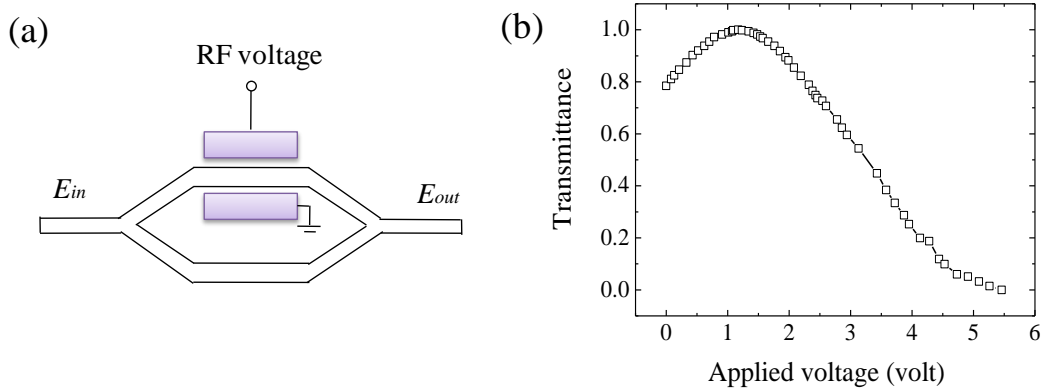


Figure 2.22 (a) A Mach-Zehnder modulator configuration and (b) its transfer function.

So far, the most widely used modulation formats in OCDMA system are OOK and DPSK, as illustrated in Figure 2.23 (a) and (b), respectively. The OOK is the simplest modulation format that employs the intensity of the light to transmit information (on for "1", off for "0"), and therefore, the Mach-Zehnder intensity modulator and a single photo-detector can be used for the modulation and detection. In a multi-user OCDMA system, as the number of user increases, dynamic threshold level setting is required to get a wide margin at the receiver because the noise probability distributions for marks "1" and "0" are asymmetric in OOK-OCDMA [87]. By employing advanced modulation formats (DPSK, CSK, etc), the system tolerance to the noise and the spectral efficiency can be improved [87-88]. Instead of optical intensity, the DPSK modulation format based on the optical phase transition between adjacent bits in differential format is another attractive technique because of the ~3dB receiver sensitivity improvement compared with the OOK which can be seen from the separation

between the two symbols, and larger fiber nonlinearity tolerance [89]. It usually employs a phase modulator at the transmitter and is demodulated by a DPSK interferometer with one bit delay followed by a balanced detector that performs subtraction instead of a single photo-detector. By using the DPSK demodulator, the phase information can be converted into the intensity and then detected by the photo-detector. When the successive bits are in phase, the interference signal between them will be output from the constructive port, while if they have a phase difference of π, the interference signal will appear in the destructive port. The logical bit "1" and "0" can thus be distinguished after balanced detection. If only one output port of the interferometer is used, the 3dB receiver sensitivity advantage will disappear, so the balance detection is quite essential for DPSK modulation.
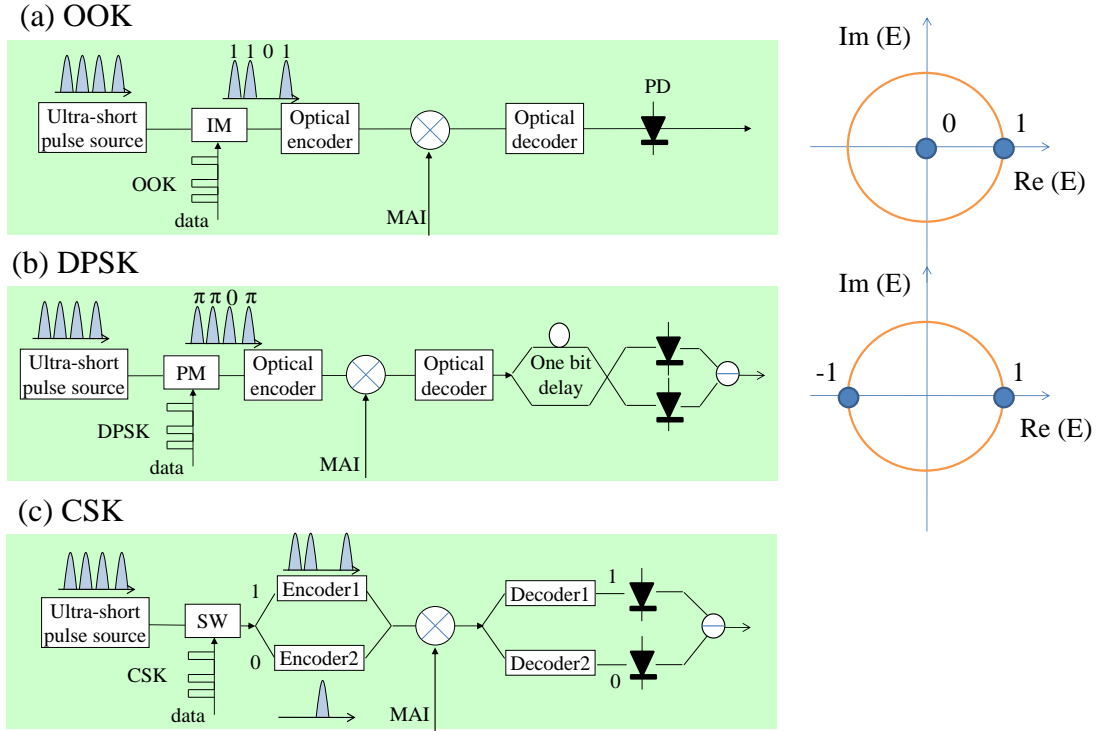


Figure 2.23 Various modulation and detection schemes for OCDMA system: (a) OOK, (b) DPSK and (c) CSK. *Re (E)* and *Im (E)* are the real and imaginary parts of the optical field.

Recently, a novel code-shift-keying (CSK) modulation format has been proposed for OCDMA application [33, 90], as shown in Figure 2.23 (c). In the CSK-OCDMA system, an optical switch is used for splitting the pulse into two parts according to the data, so different bits of "1" and "0" go to different arms, which are encoded by two optical encoders independently and finally combined for multiplexing. At the receiver, both single photo-detector [33] and balanced detector [90] can be used for data recovery. However, in the case of single photo-detector, only one decoder is used for

recovering the target data from the encoded signals by two encoders, and thus it is equivalent to an OOK data modulation with an interference user. While for the balanced detection, two optical decoders are used for decoding the received signal "1" and "0", and the decoded signals are detected by a balanced detector to perform the subtraction. Because the optical pulses for bit "1" and "0" are encoded by either optical code OC1 or OC2, the receiver sensitivity can also be improved after balanced detection comparing with the OOK and single photo-detector cases. It is also possible to hybrid these modulation formats to improve the OCDMA system capacity. An optical orthogonal modulation based on DPSK and CSK has been recently demonstrated [91]. In addition, the security improvement is also one of the most important advantages of using DPSK, CSK, *etc* advanced modulation formats than the OOK [87, 88], as will be discussed in the next section.

## 2.5   Security issues in OCDMA

With the explosive growth of massive internet resources, it is vital to securely exchange certain critical information such as military confidential data and personal privacy message in the fiber-optic communication system, and therefore, the information security is receiving more and more attention, and may become a challenge in the deployment of next generation optical network. The term "security" in this thesis means the confidential information cannot be accessed by a malicious eavesdropper without authorization (or without a key) at any point along its transmission path.

Generally, the information security in an optical fiber network includes two aspects from the perspective of information theory: the information source and transmission channel, which are complementary with each other. In current deployed optical fiber communication systems, most of the researches on security are mainly limited to the information source. Software encryption based on mathematical algorithms is widely used for providing the information security and privacy [92]. For instance, data can be protected from unauthorized observation using an encryption algorithm such as the Advanced Encryption Standard (AES), where the transmitter and receiver share a secret key. However, the development of superpower computers threatens the viability of this technique. And moreover, encryption methods employed today for the data source cannot provide sufficient privacy from a motivated eavesdropper, because the signals are broadcasted to all the customers. A potential eavesdropper can still receive the signal, record it and finally analyze or even extract the secure information after a long

time. Development of new and innovative ways to provide secure communication is highly desirable. In future broadband optical network, it is particularly attractive to provide data security during its transmission in the optical layer which has been paid considerable research attention in recent years [93-94], because of the hardware based attacking complexity and the ultrafast optical signal processing based low electromagnetic radiation. The optical layer security is fully compatible with the conventional software encryption techniques.

Previously, various approaches for achieving secure optical communications in the optical layer have been reported [95-99]. Quantum techniques especially quantum key distribution (QKD) is being heavily promoted, which can offer the potential for ultra-secure communications because a measurement of an unknown quantum system changes its state [95-96]. However, quantum cryptographic systems suffer from low bit rate operation, limited transmission distance, and complex implementation. Secure fiber optical communication using optical chaos as a carrier has also been studied [97-98]. In such a system, a small analog or digital signal is imposed on both the transmitter and receiver. The encryption is achieved by encoding the chaotic carriers at the physical layer which requires that the broadband chaotic emission of two spatially separated lasers synchronized to each other. The decoding is based upon the non-linear phenomenon of chaos synchronization between the transmitter and receiver. Therefore, the chaos based security approach is very sensitive to the synchronization process for effective decoding and thus induces the complexity of the carrier [99]. Moreover, the chaotic system usually has a few controllable parameters and suffers from small modulation depth, low signal to noise ratio and eventually relatively poor bit-error-rate performance [98].

Recently, optical code division multiple access (OCDMA) is another frequently cited technique that has the potential for enhancing the information security [15, 17-20], since it allows the implementation of information security in the optical layer based on the optical code processing, which provides a secure and high-speed optical approach for enhancing the data confidentiality. As shown in Figure 2.24, in OCDMA network, the optical pulse is encoded as a noise-like signal by the optical encoder, making an eavesdropper rather hard to intercept the data without knowledge of the applied code. When a few users are sending information data with different codes, the difficulty for an eavesdropper to intercept the target information data without knowing the code being used is further increased, and thus OCDMA technique indeed can provide security
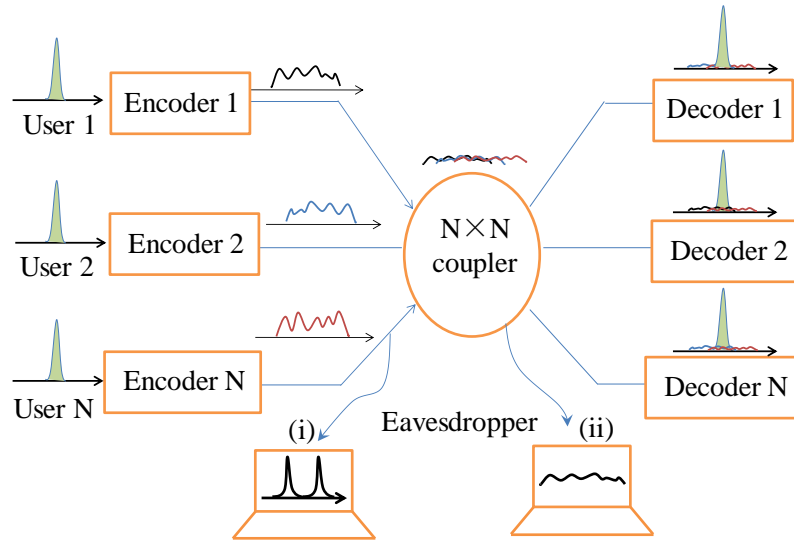
Figure 2.24 Security of OCDMA system eavesdropped (i) before and (ii) after multiplexing.

against the eavesdropping in a multi-user's environment, as can be seen clearly in the inset (ii) of Fig. 2.24, where a noise-like signal is obtained after multiplexing many users' encoded signals. However, even in an OCDMA network with many active users, there could be a single user's link before multiplexing, so the security of OCDMA system needs to be carefully considered. It has been pointed out by *Shake* that when a single user is isolated, the OCDMA network cannot guarantee the physical layer security any more [100-101].

The security vulnerabilities in OCDMA system arise from two aspects: coding induced dips and optical modulation formats. The eavesdropper can extract the code by analyzing the fine structure of coding induced spectral dips in the spectral phase encoded spectra [30, 61] or encoded waveform in time spreading OCDMA scheme [31]. Figure 2.25 (a) and (b) illustrate this kind of vulnerability [61], from which it can be seen that when a phase shift of $\pi$ is applied, a dip will be generated in either the encoded spectrum or the waveform, according to which the eavesdropper can extract the code. In the given example, the code can be extracted as either $\{\pi, 0, 0, \pi, \pi, \pi, 0\}$ or $\{0, \pi, \pi, 0, 0, 0, \pi\}$ assuming the preliminary phase state of 0 or $\pi$. An approach by applying $\pi/2$



Figure 2.25 Coding induced dips in (a) encoded spectrum and (b) encoded waveform [61].

phase shift code pattern in the SSFBG has thus been proposed to improve the vulnerability arising from coding induced dips [102], in which the encoded waveform has uniform dips when the injected pulse into the SSFBG is not longer than the chip duration and thus the eav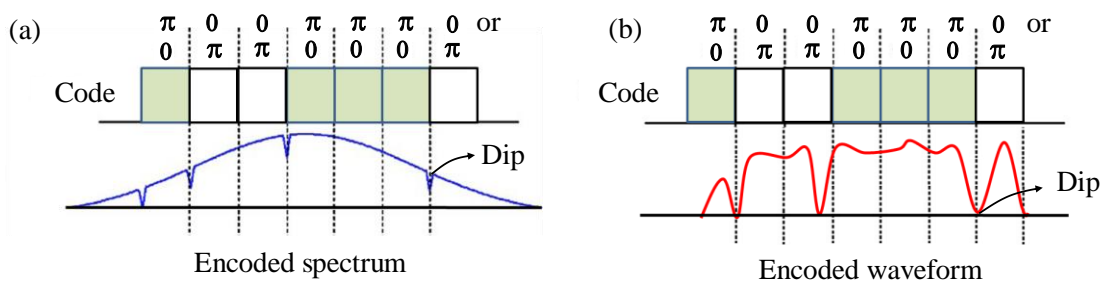esdropper cannot extract the code. However, it has been shown that even if the user's signal is not correctly decoded and the eavesdropper does not know the applied code, he can still intercept the data information easily by using a band-limited photo-detector [100], as illustrated in the inset (i) in Fig. 2.24. *Jiang*, *et al* has also experimentally demonstrated the security vulnerability in a spectrally phase encoded OCDMA system employing OOK data modulation [30, 33]. Figure 2.26 shows the measured waveforms and eye diagrams for properly decoded (a) and encoded signal (b), respectively [33]. A clear eye diagram was obtained although the encoded signal exhibits as a noise, which verified the argument of security vulnerability in OOK-OCDMA system. This is mainly due to the fact of data-rate detection by the standard energy detector to perform the integration of the whole energy in one bit period, so a clear eye-diagram can still be obtained for the cross-correlation signals [30, 33].
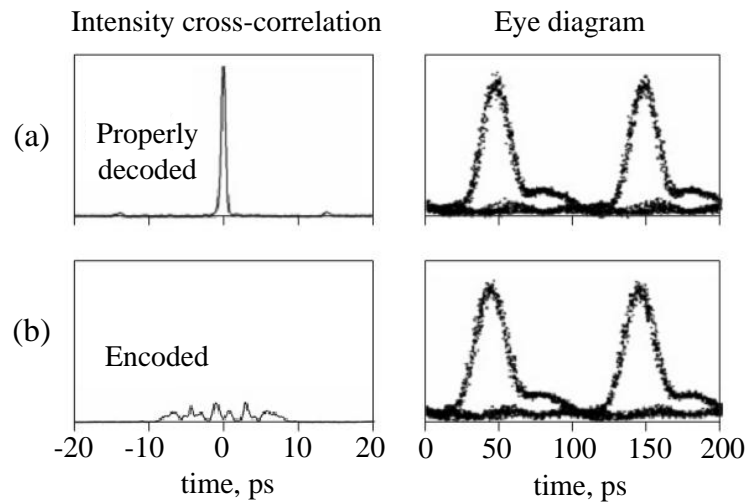


Figure 2.26 Security vulnerability of OCDMA system employing OOK data modulation [33].

To overcome the security vulnerability in OCDMA system using OOK data modulation, a number of approaches has been proposed [33, 87, 90]. Among them, advanced optical modulation formats have been adopted to address this issue. In [87], the differential-phase-shift-keying (DPSK) data modulation format and balanced detection have been proposed to combat the noise as well as enhancing the security. As different bit "1" and "0" have the equal energy for DPSK data, so the DPSK modulation format can eliminate the vulnerability of simple power detection attack. However, it has also been demonstrated that the eavesdropper can still decipher the data using a

common DPSK demodulator without any information of the code in the DPSK-OCDMA system [30]. A code switching data modulation format for enhancing the security was also investigated in [33]. In this scheme, bit '1' and '0' are encoded into two noise-like waveforms with equal energy according to two different codes, so it is also robust to the power detector attack. However, as demonstrated by *Jiang, et al* that the two-code code shifting keying (CSK) modulation format in a spectral phase encoding time spreading (SPECTS) OCDMA system is still vulnerable to the DPSK demodulation attack [30], because the interference of the adjacent bit with identical coded waveform generates high level output while the interference is nearly zero if the adjacent bits are from different codes. It has been suggested that the data confidentiality could be significantly improved in the OCDMA system by rapidly reconfiguring and scrambling the optical codes [100-101], but this concept has not been demonstrated yet, because the conventional optical encoding devices cannot offer the fast reconfigurable capability. Therefore, it is imperative to develop new optical en/decoding techniques to rapidly generate and recognize the optical code, and advanced optical modulation formats to improve the security of OCDMA system.

## 2.6   Summary

In this chapter, the basic architecture and classifications of OCDMA system are introduced at first. The background of incoherent OCDMA and coherent OCDMA including their optical sources, related optical en/decoders, and nonlinear optical processing techniques such as optical thresholding/time gating are individually discussed. Then, the optical modulation formats which include the OOK, DPSK, CSK and their detection methods in OCDMA systems are subsequently reviewed. Finally, a comprehensive review on the security issues in OCDMA systems arising from the optical encoding induced dips in the spectrum and waveform, as well as the data modulation related vulnerabilities to power detection and DPSK demodulation attack is also provided. In the following chapters, advanced optical modulation and fast reconfigurable en/decoding techniques to improve the flexibility and security of OCDMA system will be introduced and investigated.

# CHAPTER 3

# Time domain spectral phase encoding scheme for coherent OCDMA application

## 3.1    Introduction

In coherent OCDMA system, coherent time spreading TS-OCDMA and spectral phase encoding time spreading SPECTS-OCDMA are two major coding techniques: which are realized either in time or spectral domain based on the phase and amplitude of optical field. As has been discussed in Chapter 2, in TS-OCDMA, the encoding is performed in time domain by directly spreading the short optical pulses with the phase shift pattern, and the decoding is to perform convolution with the encoded pulse using an optical decoder with the time-reversed phase shift pattern to generate high level auto-correlation. The main drawback of this coding technique is that the auto-correlation has not only a high level peak but also many low level sidelobes, which prevents it from fully recovering the original pulse [49]. However, in SPECTS-OCDMA, as the coding is generally realized in spectral domain where different spectral components of optical are encoded by different phase shifts that also results in the pulse spreading in time domain, the proper decoder can fully recover the spectrum as well as the temporal waveform of the original pulse by giving the inverted phase shift pattern, so ideally, there are no sidelobes for the auto-correlation signal in SEPCTS-OCDMA system [49], which is quite attractive to get relatively good system performance. Generally, in SPECTS-OCDMA system, the en/decoders are based on free-space bulk optics with high loss, and the spectral resolution of them needs to be high enough to get long code length. Moreover, the wavelength stability requirement of the laser source and the en/decoder is very stringent to guarantee the decoding performance, which appears to be a severe problem.

In this chapter, a novel time domain spectral phase encoding (SPE) scheme using two dispersive elements with opposite dispersion for stretching and compressing the ultra-short optical pulse, and a high speed phase modulator placed between them is proposed for coherent OCDMA application. This approach is very robust to the wavelength drift of the laser source. Comparing with the traditional SPECTS schemes, it is also very flexible in reconfiguring the optical codes and compatible with the fiber-optic systems.

## 3.2  Chromatic dispersion

As the optical dispersive device based on chromatic dispersion is used throughout this thesis, knowing the basic of chromatic dispersion is essential for understanding the rest of the thesis. The chromatic dispersion is the term given the phenomenon that different spectral components travel at different velocities and arrive at the different times at the receiver. It originates from the electromagnetic wave interaction with the electron in a dielectric medium that has its refractive index $n(\omega)$ dependent on the optical frequency $\omega$, so when the short optical pulse propagates through such a medium, different spectral components associated with the pulse will travel at different speeds given by $c/n(\omega)$ [3]. One of the main effects induced by the chromatic dispersion is the pulse broadening, as illustrated in Figure 3.1. Different spectral components (different colours) will locate in different time scale after transmitting for the same distance with chromatic dispersion and thus the pulse shape can be no longer preserved.
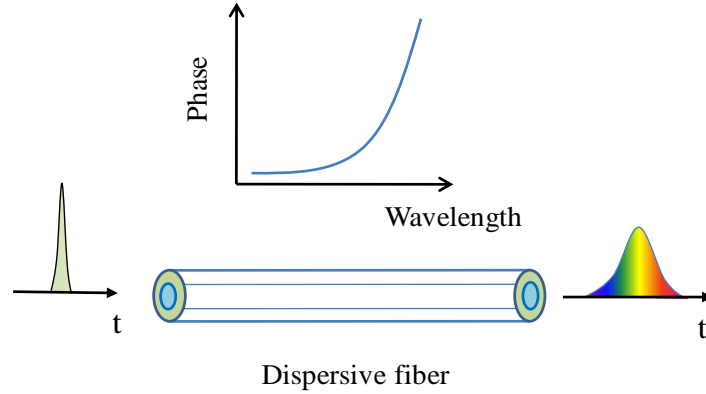


Figure 3.1 Schematic of proposed time domain spectral phase encoding scheme.

Mathematically, the effect of fiber chromatic dispersion is related to the propagation constant $\beta(\omega)$, which can be expanded into Taylor series about the center frequency $\omega_0$ [3],

$$\beta(\omega) = n(\omega)\frac{\omega}{c} = \beta_0 + \beta_1(\omega - \omega_0) + \frac{1}{2}\beta_2(\omega - \omega_0)^2 + ... \qquad (3.1)$$

where

$$\beta(\omega) = \frac{d^m\beta}{d\omega^m} \quad (m=0, 1,2) \qquad (3.2)$$

The parameters $\beta_1$ and $\beta_2$ are related to the refractive index $n(\omega)$. The $1/\beta_1$ is the group velocity that describes the envelope of an optical pulse moves at the medium while the $\beta_2$ represents group velocity dispersion parameter. When transmitting over a distance $L$,

the dispersion parameter will apply a phase term to each spectrum component as follows that is responsible for the pulse broadening:

$$\phi(\omega) = \frac{1}{2}\beta_2(\omega - \omega_0)^2 L \tag{3.3}$$

Generally, the chromatic dispersion parameter $D$ is more widely used in the fiber optical communication, and is related to the $\beta_2$ by the relation:

$$D = \frac{d\beta_1}{d\lambda} = -\frac{2\pi c}{\lambda^2}\beta_2 \approx \frac{\lambda}{c}\frac{d^2 n}{d\lambda^2} \tag{3.4}$$

In the absence of chromatic dispersion, the $\beta_2=0$. If the $\beta_2>0$ and $D<0$, the high-frequency components of an optical pulse travel slower than low-frequency components of the same pulse, and is called normal dispersion. While if the $\beta_2<0$ and $D>0$, it's called to be anomalous dispersion. Standard single mode fiber can provide anomalous dispersion at the telecommunication wavelength of 1550nm.

## 3.3 Time domain spectral phase encoding

### 3.3.1 Proposed time domain spectral phase encoding scheme

Figure 3.2 shows the schematic diagram of the proposed reconfigurable time domain SPE scheme. In this scheme, the pulse generator generates ultra-short optical pulses, which have a broadband spectrum. The SPE section is composed of a pair of dispersive devices with opposite dispersion values (–D and +D) and a high speed phase modulator (PM). The first dispersive device with dispersion value of –D is to stretch the pulse in time domain, so that different spectral components of the signal spread at different
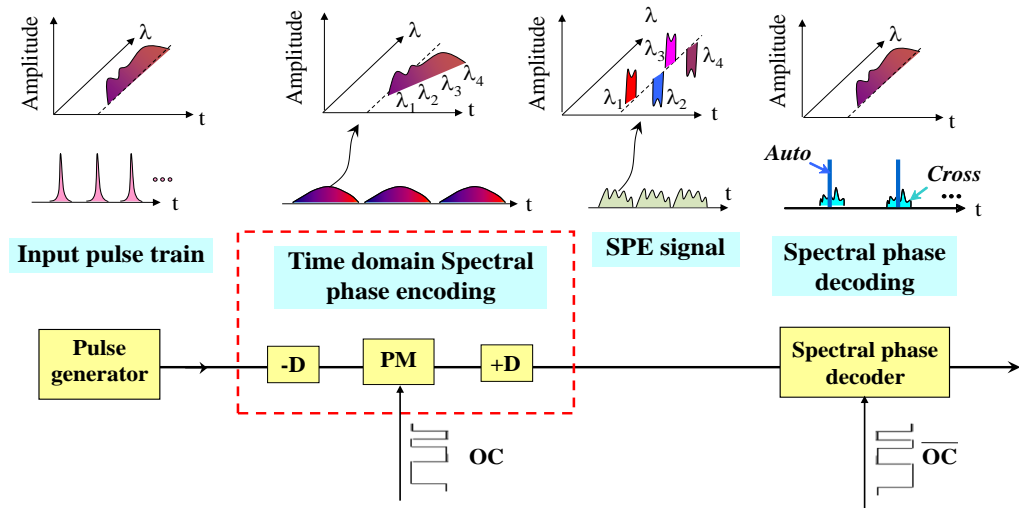


Figure 3.2 Proposed time domain spectral phase encoding scheme.

positions in one bit duration. The PM is driven by OC patterns to modulate the phases of different spectral components. The second dispersive component with dispersion value of +D (opposite to the first one) is used to compress the stretched pulse and generate SPE encoded signal. Because different spectral component is given a different phase shift according to the OC pattern, this encoding procedure is essentially a spectral phase encoding process realized in time domain. The potential advantages of the proposed SPE scheme includes simple configuration, rapid reconfigurability, good compatibility with fiber-optic system, and relaxed wavelength stability requirement which can easily compensate the wavelength misalignment for the laser and optical en/decoder in time domain by using either a tunable optical or electrical delay line. The SPE signal generated in this way can be decoded by conventional spectral phase decoders that generate auto-/cross-correlations for proper or improper OCs.

### 3.3.2 Demonstration of the time domain SPE scheme

To demonstrate the proposed time domain SPE scheme, a proof-of-principle encoding/decoding experiment has been carried out, whose setup is shown in Figure 3.3. In the experiment, the optical pulse source is a mode-locked-laser-diode (MLLD) producing nearly transform-limited ~4ps (FWHM) Gaussian-like pulses with a repetition rate of 10GHz, spectrally centered at 1550.28nm. A Mach-Zehnder intensity modulator (IM) driven by a pulse pattern generator (PPG) is used to down convert the source repetition rate to 2.5GHz. Then, the optical pulse is stretched in time domain
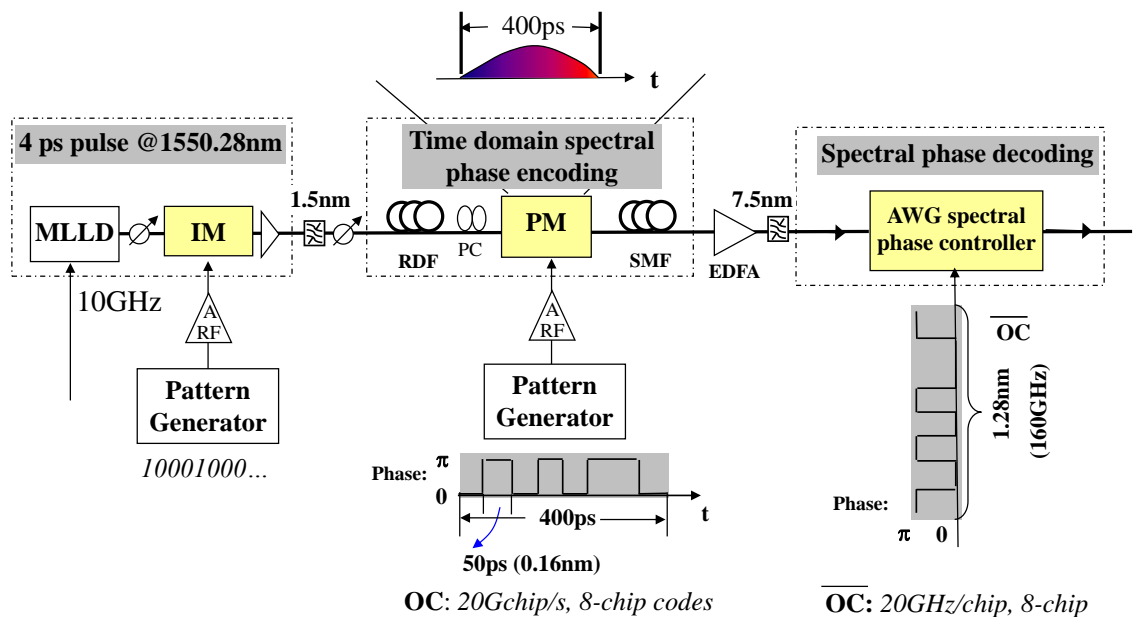


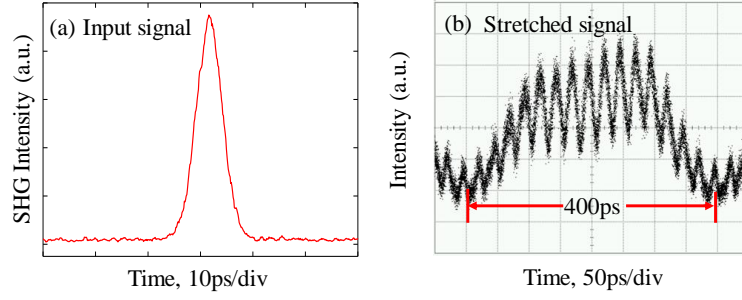Figure 3.3 Experimental setup of the proposed time domain SPE scheme.

Figure 3.4 (a) Autocorrelation trace of the input optical signal and (b) stretched signal after the RDF.

by a piece of reverse dispersion fiber (RDF) for spectral phase encoding. Figure 3.4 (a) and (b) show the autocorrelation trace of the input optical pulse before the RDF and the waveform of the stretched pulse after the RDF, from which one can see the original ultra-short optical pulse has been stretched in time domain due to the chromatic dispersion of the RDF. Each longitude mode of the optical spectrum has been temporally dispersed into different time position. The total dispersion of the RDF is -312.5ps/nm, so one bit duration of 400 ps covers 1.28nm (160 GHz) spectral range, and thus a cascaded optical bandpass filters with 2nm bandwidth has been used before the RDF to reduce the bandwidth of the input optical pulse into ~1.5nm which slightly causes the pulse broadening to ~8ps. The stretched pulse is then directed into a phase modulator driven by 20Gchip/s, 8-chip binary phase shift keying (BPSK) code patterns (corresponding to 20GHz/chip, 8-chip spectral phase patterns) with a repetition rate of 2.5GHz for spectral phase encoding, so each spectral component can experience a different phase shift according to the phase pattern. Each chip occupies 50ps time duration and corresponds to 0.16nm spectral range. To accurately synchronize the optical code pattern and stretched pulse, a tunable optical delay line is employed before the phase modulator, so the optical code pattern can precisely modulate the phase of corresponding spectral component. After the phase modulation, a span of 34 km single mode fiber (SMF) is used to compress the stretched optical pulse and generate the SPE signal. The SMF functions as the transmission fiber as well. The dispersion of the whole transmission system is managed globally by utilizing another piece of dispersion compensation fiber (DCF) to compensate the dispersion mismatch. The total dispersion of the SMF and DCF is approximately +312.5ps/nm.

Seven different BPSK optical code patterns OC1~OC7: 10101010, 1110100, 11100100, 00100010, 11110000, 11001100 and 10101100 have been tried in the encoding experiment. Figure 3.5 shows the measured encoded spectra and waveforms
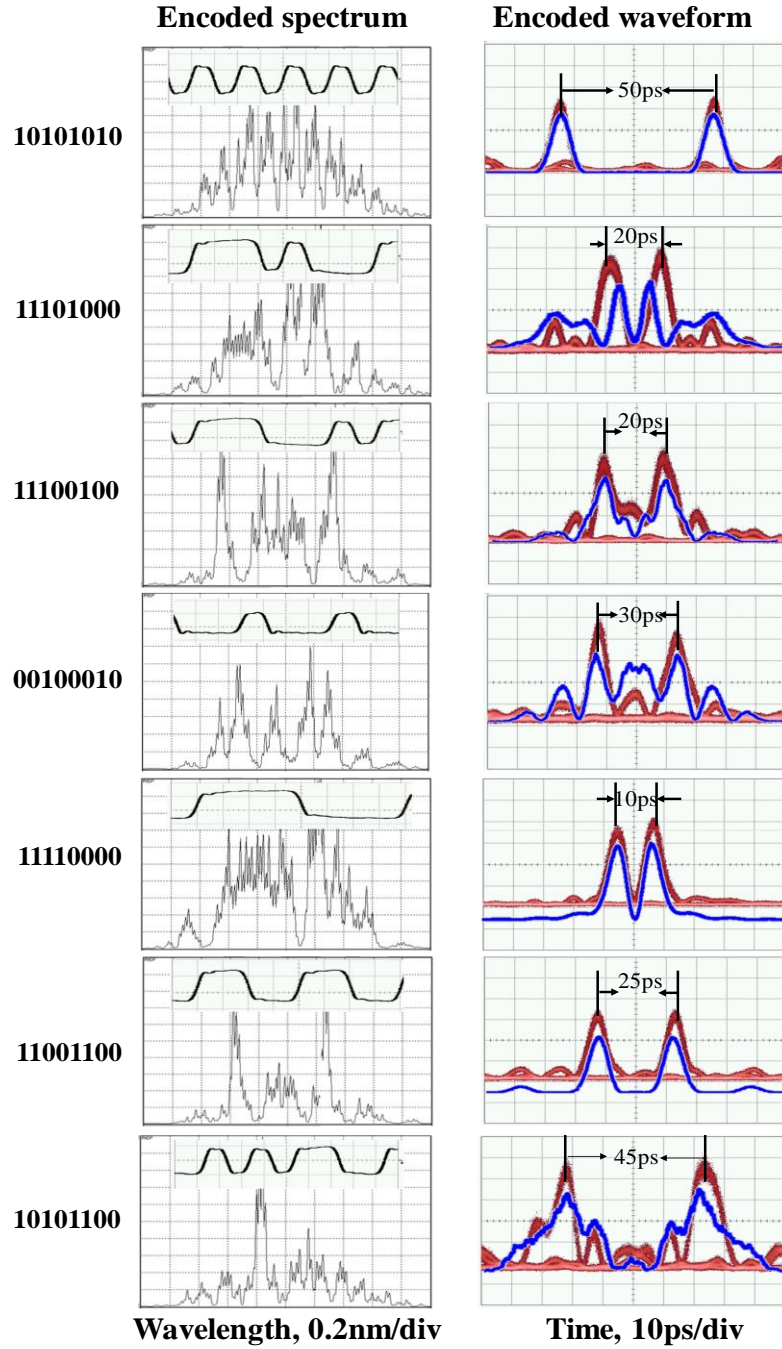
Figure 3.5 Measured encoded spectra (left column) and encoded waveforms (right column). The blue lines in the right column are the simulated encoded waveforms.

using an optical sampling oscilloscope (solid red lines), and simulated results (solid blue lines) using Matlab programming, from which one can see that there are some spectral dips in the encoded spectrum because of the introduction of the phase shift pattern. The profiles of the encoded waveforms agree well with the theoretical prediction, showing the excellent encoding performance of the time domain SPE scheme. The agreement of the measured and simulated encoded waveforms indicates that the time domain SPE encoding technique can be potentially used for fast programmable pulse shaping

applications such as the generation of rectangular, triangular arbitrary waveforms by properly choosing the optical code since it is equivalent to spectral line-by-line manipulation that has been demonstrated before in spectral domain [103]. To recover the original pulse, the generated SPE signal is directly spectrally phase decoded in spectral domain by utilizing a conventional AWG based spectral phase decoder with phase conjugate code pattern. The channel spacing of the AWG is 10GHz (0.08nm), so two spectral lines of the spectral phase decoder correspond to one chip for the 8-chip, 20GHz/chip spectral phase pattern. Figure 3.6 shows the spectral response of the AWG based decoder. The center wavelength is ~1550nm and it has 21 channels, so the free spectral range is about 210GHz. It can be seen that the spectral response is not very smooth as the amplitude fluctuation has been applied into the spectrum which may affect the decoding performance. Each channel of the AWG can be adjusted independently for decoding. As two spectral lines of the AWG correspond to one chip for the 20GHz/chip phase pattern, so the phase shifts can be adjusted identically for two adjacent spectral lines. A 40Gchip/s, 16-chip optical code pattern with each chip occupies 25ps time duration could also be applied in the time domain SPE section, in which case each spectral line in the AWG has to be independently controlled.
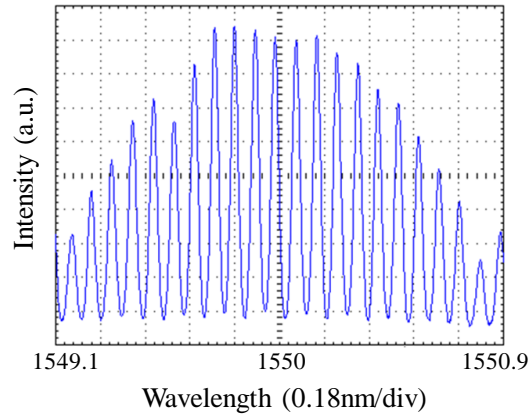


Figure 3.6 Spectral response of AWG based spectral phase decoder.

In the experiment, the dispersion of the RDF is one of the key factors to determine the decoding performance. Figure 3.7 (a)~(c) show the simulated decoded waveforms for the RDF with dispersion of -270.5ps/nm, -300.5ps/nm and -340.5ps/nm, respectively. The deviation of the fiber dispersion from the ideal value (-312.5ps/nm) will result in lower peak intensity and relatively higher sidelobes due to the mismatch of the corresponding time domain SPE code pattern with that in the spectral phase decoder. Figure 3.7 (d) shows the calculated peak to wing ratio (P/W) of the correctly decoded waveform for different dispersion values, from which one can see the P/W can reach up
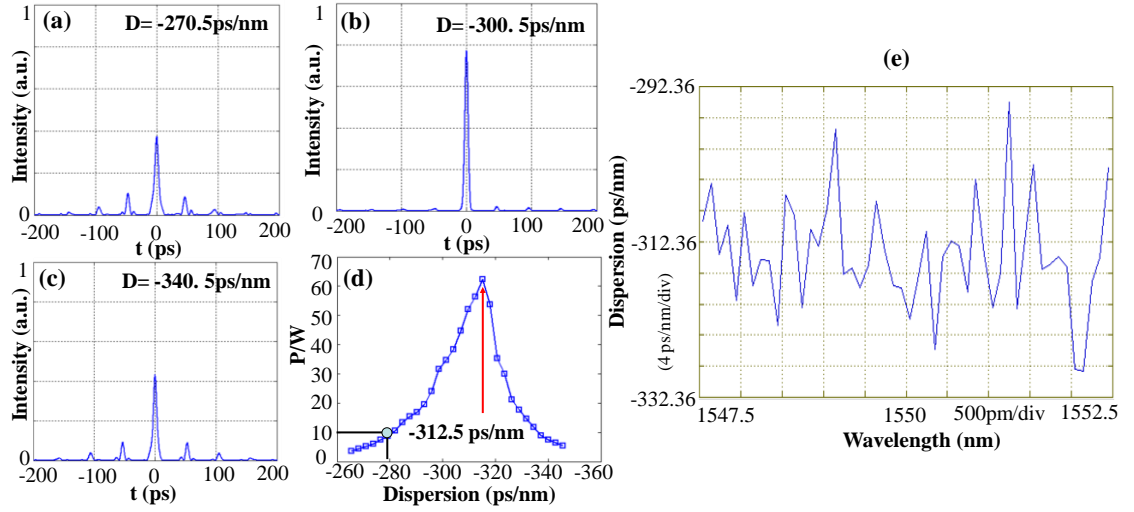
Figure 3.7 (a) Decoded waveform for dispersion of (a) -270.5ps/nm, (b) -300.5ps/nm and (c) -340.5ps/nm; (d) Peak to wing ratio versus RDF dispersion and (e) measured dispersion of the RDF used in the experiment.

to ~63 for the dispersion of -312.5ps/nm but it will be degraded as the dispersion deviation increases. For the dispersion of -312.5ps/nm, the 8-chip, 20Gchip/s (50ps/chip) optical code pattern corresponds to exactly 8-chip, 20GHz/chip spectral code pattern, so the spectral phase decoder with channel spacing of 10GHz can be used to effectively decode the encoded SPE signal, while for the other dispersion values, the spectral code pattern deviate from the 20GHz/chip chip rate leading to higher sidelobes in the decoded waveform. The requirement of the dispersion deviation is not very strict, for P/W=10, the deviation tolerance is about ±32.5ps/nm, which can be easily maintained in the system. Figure 3.7 (e) shows the measured chromatic dispersion of the RDF used in the experiment. The average dispersion value of the RDF is approximately -312.5ps/nm in the wavelength range of 1547.5nm and 1552.5nm, which can guarantee the feasibility of decoding using the spectral phase decoder with 10GHz channel spacing.

In the setup, as the RDF has a dispersion of -312.5ps/nm, 1.28nm (~160GHz) spectral range will spread within the one bit duration of 400ps, and thus the original optical pulses with 4ps pulse width covering a 10-dB bandwidth of ~4nm will generate significant overlap between two adjacent stretched pulses, which may degrade the decoding performance. Figure 3.8 shows the peak to wing ratio (P/W) and peak intensity of the decoded pulse versus the light pulse width for code 10101010 using the spectral phase decoder with eight-chip spectral phase pattern. It can be seen that as the light pulse width decreases from 6ps, the decoding performance gradually degrades with lower P/W and peak intensity. The inset (i) in Figure 3.8 shows the decoded waveform for light pulse width of 3ps, from which one find that the decoded waveform
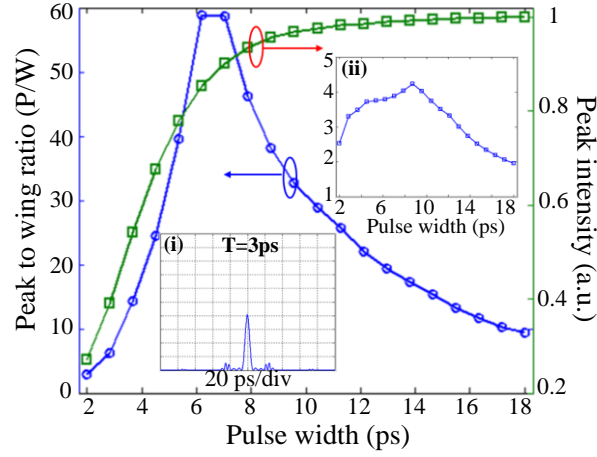
50

Figure 3.8. P/W and peak intensity versus light pulse width. The inset (i) is the decoded waveform for pulse width of 3ps. The inset (ii) shows the P/C versus the pulse width.

has relatively high sidelobes and low peak intensity. This is mainly caused by the significant pulse overlap between two adjacent stretched pulses in time domain (which exceeds one bit period of 400ps). The overlapped spectral components will be phase modulated by other code patterns that cannot be correctly decoded by the spectral phase decoder and thus generate large sidelobes in the decoded waveform, which directly lower the P/W and peak intensity. On the other hand, when the pulse width increases from 8ps, the stretched pulse can no longer cover the whole bit period, so the effective code length will gradually decrease resulting in the degradation of the P/W. The average peak power ratio (P/C) between the auto-/cross-correlations versus the light pulse width is also shown in the inset (ii) in Fig.3.8, from which one can see that the P/C exhibit the similar trend as the P/W. Too narrow or wide laser pulse will degrade both the P/W and P/C. To address this issue, a suitable optical bandpass filter can be used in the proposed scheme to cut-off the wing spectrum of the ultra-short optical pulse to improve the decoding performance. In the experiment, two cascaded optical band-pass filters with 3dB bandwidth of 2nm but different center wavelengths are employed before the RDF to cut off the residual input spectrum to reduce the signal overlap between two adjacent stretched pulses to improve the decoding performance.

In addition, as the spectral phase encoding is realized in time domain in this scheme, the timing error defined as the time delay between the stretched optical pulse and the desired spectral phase pattern will have significant effect on the decoding performance. The P/W versus the timing error ($T_d$) is depicted in Figure 3.9, from which one find that the P/W gradually decreases from 63 to 0 as the timing error increases from 0 to 20ps. The two insets in Fig.3.9 are the decoded waveforms for timing error of 2ps and 10ps,
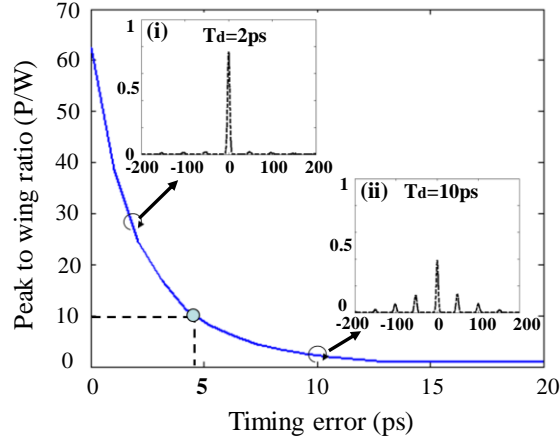
51

Figure 3.9. P/W versus the timing error. The insets of (i) and (ii) are the decoded waveforms for a timing error of 2ps and 10ps, respectively.

respectively. For the inset (i), the decoded waveform still has high peak intensity while for the inset (ii), large sidelobes appear in the decoded waveform. The timing error corresponds to wavelength mismatch in the experiment. When the timing error increases, the code pattern will modulate the phase of different spectral components resulting in phase error in the spectral phase decoder, and thus the decoding performance will be significantly degraded. For a P/W of 10, the tolerance to the timing error is ~4.5 ps. A commercial available tunable optical delay line with a tuning range of ~ 400ps (one bit period) and resolution of 0.2ps is used to accurately control the timing error in the experiment.

The decoding of the spectral phase encoded signal with various OCs is directly performed in spectral domain using the 10GHz channel spacing AWG based spectral phase decoder with phase conjugate patterns. Figure 3.10 (a) and (b) show the auto-/cross correlation performances for codes OC1~OC4: 10101010, 11101000, 11100100 and 00100010 respectively. All these codes have been successfully decoded with high auto-correlation peaks in the experiment, which verifies the feasibility of using a traditional spectral phase decoder (e.g. AWG) to decode the time domain spectral phase encoded signal. The relatively high sidelobes in the auto-correlation signals are mainly caused by the non-smooth Gaussian-shaped spectral response of the AWG device and the errors in controlling the amplitude and phase. The cross-correlation signals for OC1 with the other codes are shown in Figure 3.10 (b), from which one can see that the cross-correlation signals behavior like a noise with low peak power. The peak power ratio between the auto-/cross-correlation signals is about 2 which can be further improved by reducing the phase control error in the AWG.

Although the AWG can be used for decoding the time domain SPE signal as has been
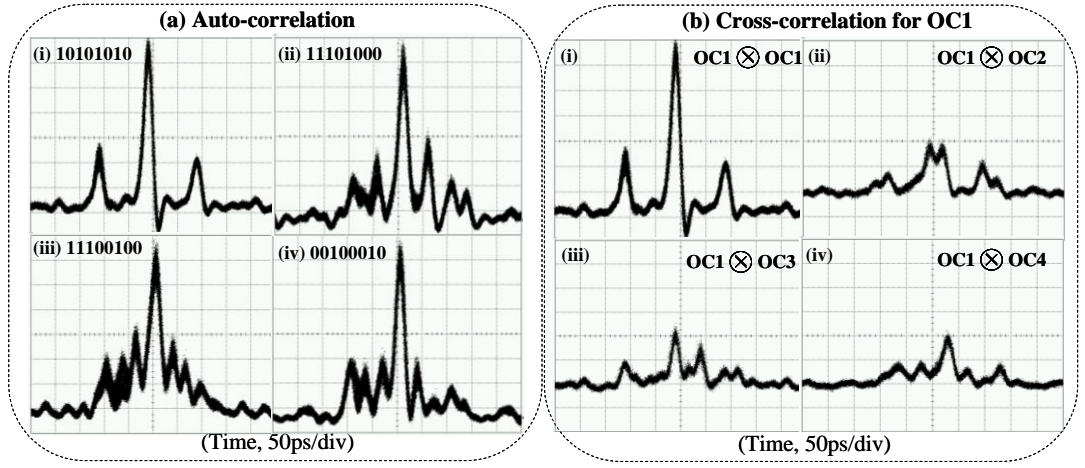
52

Figure 3.10 (a) Auto-correlation signals for OC1-OC4; (b) Cross-correlation signals for OC1 with the other codes.

demonstrated, the decoding performance is not very well, which is mainly due to the difficulty of accurate phase control in the AWG device. The phase pattern applied in the AWG device depends on the relative phase shift of two adjacent spectral channels, so the phase error in the initial channels will be accumulated in the latter channels resulting in significant phase errors and then induces the degradation of the decoded waveform. Moreover, because the AWG device is polarization dependent, the amplitude and phase of each channel is very sensitive to the polarization change of the input optical signal.

To effectively improve the decoding performance, a Variable-Bandwidth-Spectrum-Shaper (VBS), which is composed of grating, lens, spatial light modulator (SLM) and reflector, is proposed to be used as the spectral phase decoder. This device is developed by the photonic network group in the National Institute of Information and Communications Technology (NICT). The VBS can synthesize arbitrary optical spectrum and waveform with the advantages of polarization independent, high-precision amplitude and phase control, compact and low-insertion loss [104-105]. It can control the amplitude and phase with high resolution in the wavelength region covering the entire C band. The amplitude and phase control in VBS is very straightforward, which only need to adjust the absolute value instead of the relative value in the AWG. The amplitude control range is 30dB with a fluctuation of 0.1dB, and the phase control range is $2\pi$ with a resolution of $0.04\pi$ [105]. The VBS has 340 control channels with channel spacing of 10GHz. The spectral phase decoding can also be directly performed in spectral domain by utilizing the VBS. To verify it, the en/decoding have also been tried for the optical code patterns OC1~OC7. Figure 3.11 (a) shows the measured decoded waveforms using a 10GHz optical sampling oscilloscope. Compared with the AWG decoding results, the VBS exhibits relatively better decoding performance though there are still a few

**(a)  Auto-correlation**



Time, 10ps/div

**(b) Cross-correlation for OC3**



Time, 10ps/div
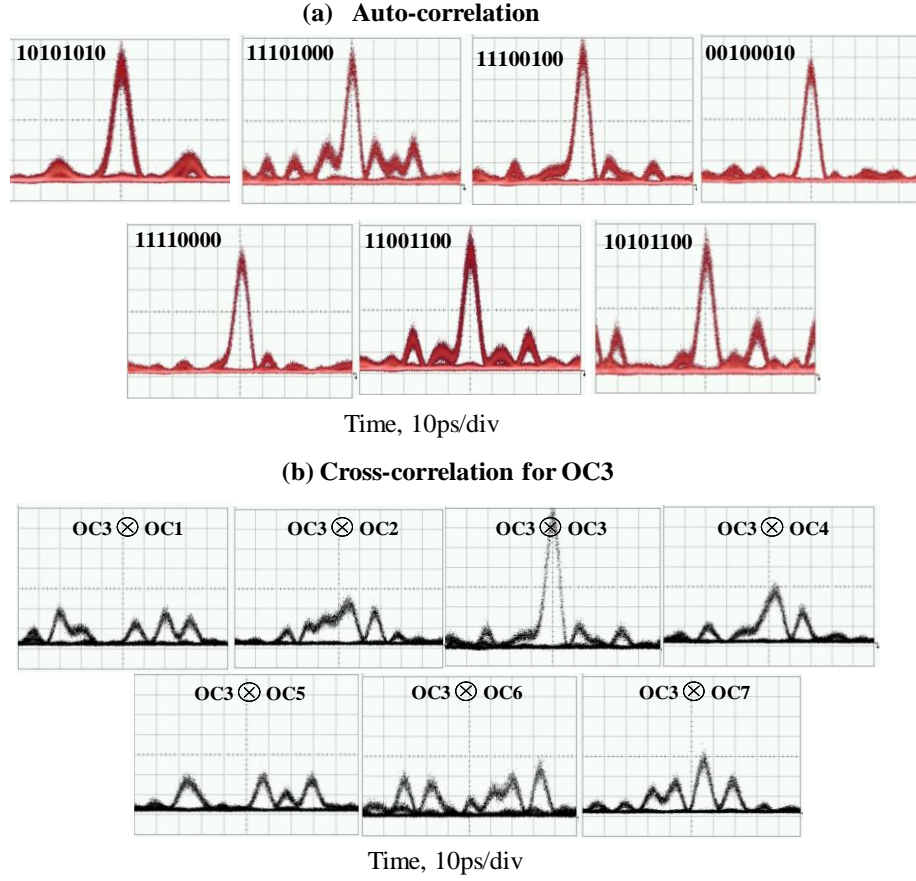
Figure 3.11 (a) Measured decoded waveforms for codes OC1~OC7 using VBS; (b) Cross-correlation signals for OC3.

sidelobes around the auto-correlation peak which can be partially ascribed to the non-ideal phase control and channel crosstalk. Figure 3.11 (b) shows the waveforms of the cross-correlation signal for OC3, from which it can be seen that the P/C is ~2 due to the limited code length. By increasing the code length and chip rate, the P/C could be further improved. The discrimination of different codes can be realized by proper optical thresholding. The en/decoding experiment verifies that the proposed time domain SPE scheme is compatible with conventional spectral phase decoder and has the capability of fast reconfiguring the optical code patterns by programming the PPG.

## 3.4    Time domain SPE/DPSK data modulation using single phase modulator

### 3.4.1  Principle of time domain SPE/DPSK data modulation

Based on the time domain SPE scheme, a novel advanced optical modulation technique that can simultaneously realize time domain spectral phase encoding and

DPSK data modulation using only a single phase modulator is proposed [106-107]. Figure 3.12 (a) shows the principle of the proposed SPE and DPSK data modulation scheme. The SPE section is still composed of a pair of dispersive devices with opposite dispersion sign (–D and +D) and a high speed phase modulator (PM). When the ultra-short optical pulse train with a broadband spectrum (λ1, λ2, λ3, λ4…) is directed into the SPE section, the short pulse is stretched in time domain by the first dispersive device with dispersion value of –D. Different spectral components of the input pulse will spread at different time positions within one bit duration. Unlike the previous SPE
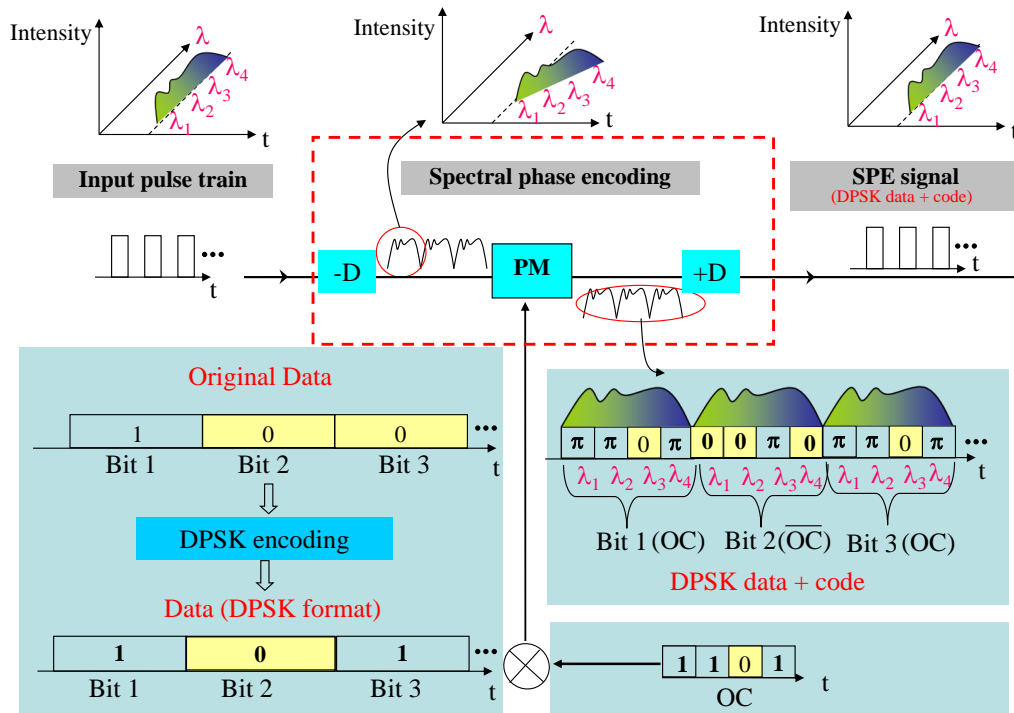


**(a) Optical code generation and DPSK data modulation using single PM**
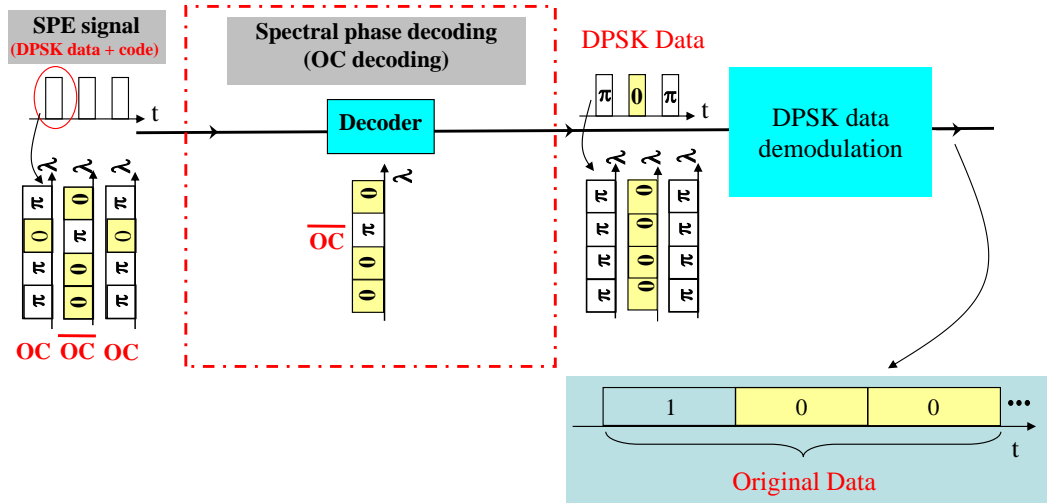


**(b) Optical code recognition and DPSK data demodulation**

Figure 3.12. Principle of the proposed scheme (a) time domain SPE and DPSK data modulation; (b) Decoding using spectral phase decoder and DPSK data demodulation.

scheme in Section 3.3, in which the PM is driven only by the OC, the PM here is driven by combining the DPSK data and OC patterns to generate the data modulation and time domain spectral phase encoding. A fixed data pattern (100…) and 4-chip OC (1101) are used as an example to show this coding process. The DPSK data is generated by precoding the original data (100…) into DPSK data format (101…) and then combined with the OC pattern in the following way to modulate the phase of the stretched optical signal: when the DPSK data is symbol "1", the PM is driven by OC (1101…), while if the symbol is "0", the PM is driven by $\overline{OC}$ (0010…). Thus, the three bits are phase modulated by code patterns: OC (1101), $\overline{OC}$ (0010) and OC (1101), respectively. After that, the second dispersive device with opposite dispersion value of +D is used to compress the stretched pulse in time domain and generate the DPSK data modulated SPE signal.

The decoding of the generated SPE signal is same as conventional SPECTS, as shown in Figure 3.12 (b). The decoder with spectral phase pattern of $\overline{OC}$ is used to decode the DPSK data modulated SPE signal. The spectral components of each encoded pulse are in phase after the decoder. For symbol "1", the total phase is "OC+$\overline{OC}$=π", while for symbol "0", the total phase is "$\overline{OC}$+$\overline{OC}$ =0". Therefore, the total phase of the three bits becomes (π, 0, π…) after the decoding, and the DPSK data is extracted from the SPE signal as (101…). A DPSK demodulator with a one-bit delay interferometer followed by a balanced detector can then be used to demodulate the DPSK data and recover the original data as (100…).

In this scheme, only a single phase modulator is used to realize the optical code generation and DPSK data modulation simultaneously, which provides an attractive approach to simplify the architecture of the whole OCDMA system and reduce the cost. This scheme is also compatible with the SPECTS-OCDMA system, as conventional spectral phase decoder can be used to perform the optical code recognition. It is capable of rapidly reconfiguring the optical code pattern and DPSK data to improve the data confidentiality, which is a unique feature than conventional OCDMA schemes. Moreover, the proposed scheme exhibits the potential to be applied for secure optical communication application.

## 3.4.2 Demonstration of time domain SPE/DPSK data modulation using single PM and 2.5Gb/s transmission experiment

An experimental demonstration of the proposed scheme for simultaneous optical encoding and DPSK data modulation using only a single phase modulator has been carried out, as shown in Figure 3.13. The experimental setup is similar to that of the en/decoding experiment. In this setup, a mode-locked-laser-diode (MLLD) producing nearly transform-limited ~4ps (FWHM) Gaussian-like pulses with a repetition rate of 10GHz, spectrally centered at 1550.28nm is used. The source repetition rate is converted to 2.5GHz by a Mach-Zehnder intensity modulator (IM). The insets (i) and (ii) in Figure 3.13 show the spectrum of the original 10GHz and generated 2.5GHz optical pulse trains, respectively. In the time domain SPE and DPSK data modulation section, a reverse dispersion fiber (RDF) is used to provide a negative dispersion (-312.5ps/nm) and stretch the input optical pulse. Different spectral components will spread at different positions in time domain. A phase modulator driven by combining 8-chip, 20Gchip/s optical code patterns (corresponding to 8-chip 20GHz/chip spectral phase patterns) and 2.5Gbps DPSK data then phase modulate the stretched optical pulse. After the phase modulation, a span of 34 km single mode fiber (SMF) and dispersion compensation fiber (DCF) with total dispersion of approximately 312.5ps/nm is used to compress the stretched optical pulse and generate the DPSK data modulated SPE signal.
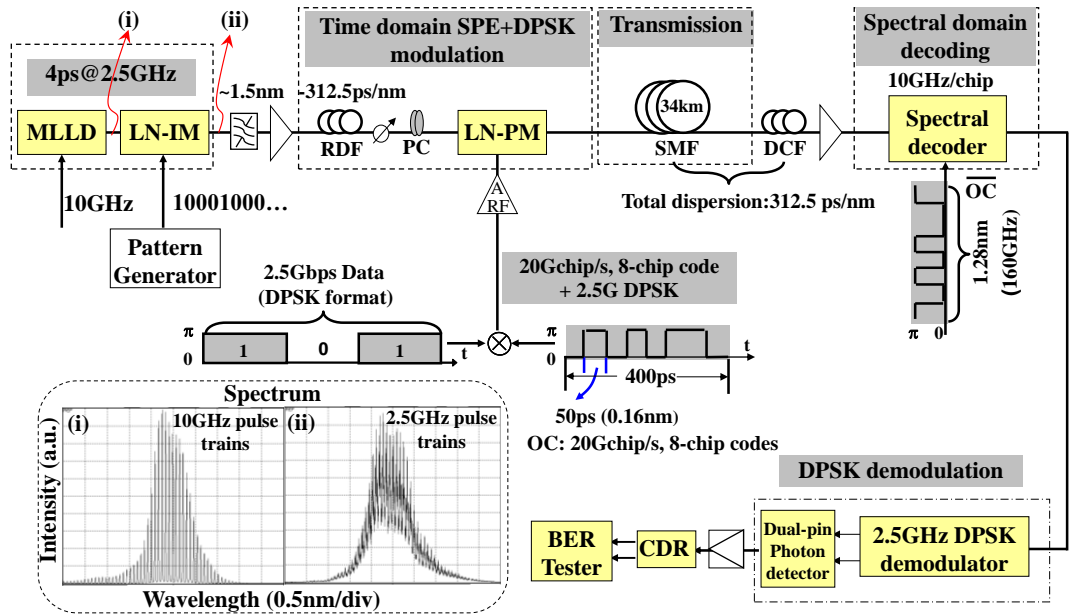


Figure 3.13. Experimental setup for the time domain SPE and DPSK data modulation scheme.

As the RDF has a dispersion of -312.5ps/nm, the original short pulses covering ~4nm spectral range will be significantly overlapped after stretching in time domain that will degrade the decoding performance, and thus cascaded optical bandpass filters (BPF) are

used to cut-off the wing spectrum. Figure 3.14 (a) and (b) show the spectrum after the cascaded BPFs and the waveform of stretched pulses, respectively. As shown in Fig.3.14 (a), the original spectrum has been cut by the BPFs into ~1.5nm spectral range corresponding to a light pulse width of ~8ps. The adjacent stretched pulses have little temporal overlap due to the relatively lower intensity of the wing spectrum as can be seen from Fig.3.14 (b), which ensures the decoding performance for each DPSK data of "1" and "0" by using the spectral phase decoder.
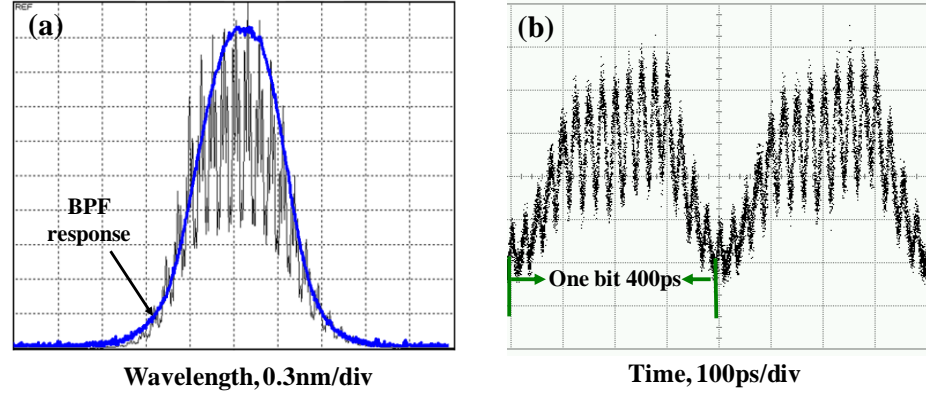


Figure 3.14. (a) Input spectrum before the RDF (the solid blue line is the spectral response of the cascaded BPFs) and (b) waveform of two adjacent stretched optical pulses.

To recover the original data, the DPSK data modulated time domain SPE signal has to be spectrally phase decoded and then DPSK demodulated. As the VBS based device has a relatively good performance, the spectral phase decoding is directly performed in spectral domain by using the VBS with the phase conjugate code pattern. The channel spacing of the VBS is 10GHz, so two spectral lines of the spectral phase decoder correspond to one chip for the 8-chip, 20GHz/chip spectral code pattern. After the spectral phase decoding, the auto-correlation signal is directed into a 2.5GHz DPSK demodulator followed by a balanced detector to recover the original data. A 2.65GHz low pass filter is used after the balanced detector to perform data-rate detection. The bit-error-rate (BER) performance is finally measured by an error detector.

A DPSK transmission experiment using VBS based spectral phase decoder for simultaneous generation of the time domain SPE and 2.5Gbps DPSK data modulation with 8-chip, 20Gchip/s optical code patterns is then carried out. A fixed data pattern with $2^7$-1 pseudo-random binary sequence (PRBS) is used in this experiment. As shown in Figure 3.15, the original data 111111001111010111000011... is precoded into DPSK data format as 0000001000001100000101000 and then mixed with the optical code pattern to drive the phase modulator. The decoded DPSK signal using the VBS for OC3

is shown in Figure 3.15 (a), from which one can see that the decoded pulses have similar waveform but different phases according to the DPSK data. In this case, the phases are $000000\pi00000\pi\pi0000\pi0\pi000\ldots$, respectively. After the 2.5GHz DPSK demodulator and balanced detector followed by a 2.65GHz low pass filter to perform data-rate detection, the original data pattern has been recovered as 111111001 111010111000011…whose waveform is shown in Fig.3.15 (b). The corresponding eye diagram with clear eye opening is also shown in Fig.3.15 (c). The DPSK demodulation has no obvious degradation because of introduction of the spectral phase decoding. Fig. 3.15 (d) shows the measured BER performance together with the eye diagram after 34km transmission using the 2.5Gb/s $2^7$-1 PRBS data for all the codes. BER<$10^{-9}$ and clear eye opening have been successfully achieved for all the codes. The difference of the power penalty indicates the different decoding performance of each OC. The successful 2.5 Gb/s DPSK data transmission verifies the feasibility of the proposed advanced modulation scheme that can generate time domain spectral phase encoding and DPSK data modulation simultaneously using a single phase modulator, and decoding using a VBS based spectral phase decoder in spectral domain. In the proposed SPE/DPSK scheme, the optical code pattern and DPSK data can be generated and rapidly reconfigured by programming the pulse pattern generator, therefore, the flexibility of the proposed time domain SPE-OCDMA system can be significantly improved, exhibiting the potential to enhance the data security.
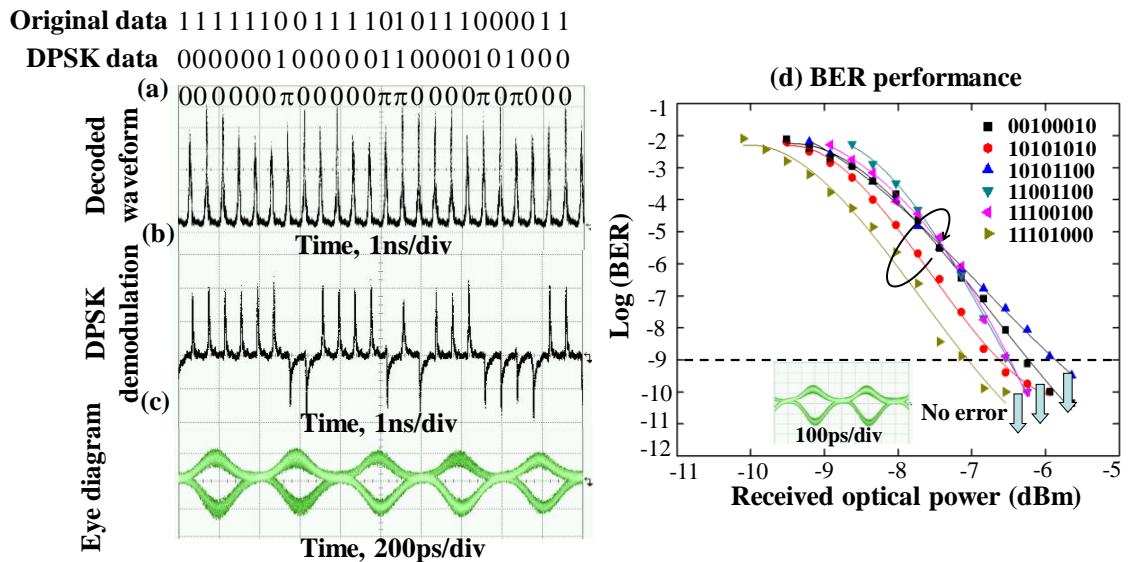


Figure 3.15 (a) Decoded waveform; (b) Demodulated DPSK data; (c) Eye diagram and (d) BER performances for $2^7$-1 PRBS data with different codes.

## 3.5 2.5Gb/s, two-user time domain SPE-OCDMA system demonstration

In the previous sections, based on the time domain SPE scheme, an advanced optical encoding and DPSK data modulation technique has been proposed and demonstrated, but the capability of supporting the multi-user transmission using this scheme has not been studied yet. In this section, a two-user 2.5-Gb/s time domain spectral phase encoding OCDMA system with OOK data format using the VBS based spectral phase decoder is demonstrated [108].

Figure 3.16 illustrates the two-user time domain SPE-OCDMA system. In the experimental setup, the short optical pulse is produced by a MLLD with pulse width of ~4ps and repetition rate of 10GHz, spectrally centered at 1550.28nm. The pulse train is gated down at four-to-one ratio by a Mach-Zehnder intensity modulator (IM) driven by $2^{11}$-1 PRBS output from a programmable pulse pattern generator (PPG) to generate the 2.5-Gb/s OOK data. Then a piece of RDF fiber with dispersion of ~ -312.5ps/nm is used to stretch the optical pulse, so different spectral components will spread into different positions in time domain. As one bit duration of 400ps corresponds to 1.28nm (~160GHz) spectral range, cascaded optical band-pass filters has also been used before the RDF to cut the input spectrum into ~1.5nm. The stretched pulses have very little overlap with other, so the decoding performance by the spectral phase decoder can be guaranteed.
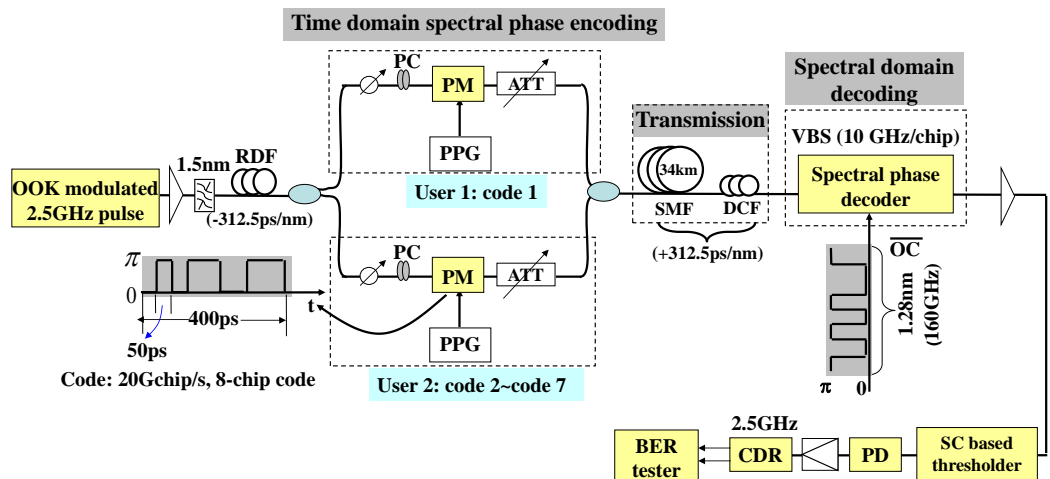


Figure 3.16 Experimental setup of the two-user time domain SPE-OCDMA system.

After the temporal stretching, the optical pulse is amplified and split into two paths by a 3-dB coupler to emulate a two-user OCDMA system. Two phase modulators

driven by 8-chip, 50ps/chip optical codes (corresponding to exactly 8-chip, 20GHz/chip spectral code pattern) are used for the time domain spectral phase encoding. To accurately synchronize the optical code pattern and stretched pulse, a tunable optical delay line is employed before the phase modulator, so the optical code patterns can precisely modulate the phase of the corresponding spectral component. A span of 15m optical fiber is used in one arm to decorrelate the two encoded signals. Tunable optical attenuator is used to balance the power in the two arms. After that, the encoded signals are recombined, amplified and launched into a span of SMF and DCF with total dispersion of ~ 312.5ps/nm to compress the stretched pulse and generate the SPE signal. The SMF and DCF also function as the transmission fiber in this experiment.

In the decoding part, the spectral phase decoding is directly performed in spectral domain by utilizing a VBS with the complementary spectral code ($\overline{\text{OC}}$) pattern. The VBS can control the amplitude and phase with high resolution independently. If the spectral code pattern matches with that in the encoding part, an autocorrelation peak pulse will be generated while a cross-correlation signal with low peak power acting as a multiple-access interference noise will be produced for the unmatched code pattern. After the spectral phase decoding, the decoded signal is directed into a super-continuum (SC) based optical thresholder which is composed of a preamplifier EDFA and a piece of 2000m dispersion-flattened-fiber (DFF) followed by a 5nm BPF to suppress the MAI noise. Finally, the decoded signal is data-rate detected by a photo-diode followed by a 2.65GHz low-pass filter (LPF), and measured by a BER tester.

Three Walsh codes and four other quasi-orthogonal codes are used in this experiment, which are OC1~OC7: 00100010, 10101010, 10101100, 11001100, 11100100, 11101000 and 11110000, respectively. Figure 3.17 (a)~(b) and (c)~(d) show the encoded and decoded waveforms by using the VBS based spectral phase decoder for OC1 and OC2, respectively. As can be seen, the profiles of the encoded waveforms agree well with the simulated results. By adjusting the amplitude and phase of each spectral channel individually in the VBS, the SPE signal has been successfully decoded with very low sidelobes. Fig.3.17 (e)~(h) show the measured waveforms of the cross-correlation signals for OC1 with four other codes, respectively. The profiles of these waveforms agree well with the simulated results as well, indicating the accurate phase control in the VBS and excellent decoding performance. The average P/C is about 2 due to the limited code length of eight and non-ideal decoding, but it is enough to distinguish the two users by employing a proper optical thresholder to suppress
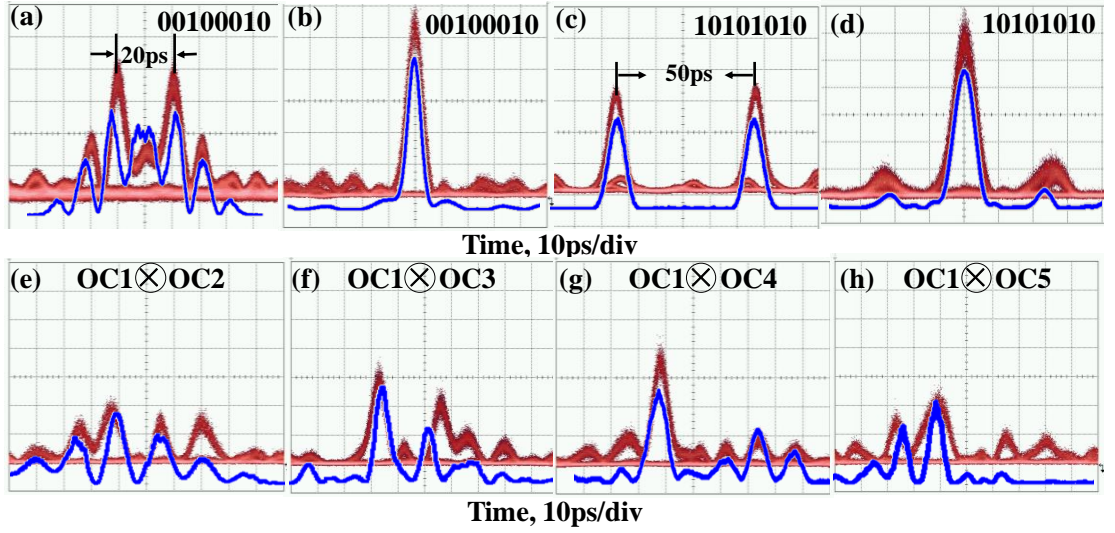
Figure 3.17 (a)~(b) and (c)~(d) are measured and simulated waveforms (red and blue lines) of encoded and decoded signals for OC1 and OC2, respectively; (e)~(h) are the waveforms of cross-correlation signals for OC1.

the interference noise which becomes more prominent as the number of user increases [74-75].

After the decoding, the correctly decoded signals are directed into the SC based optical thresholder to suppress the interference. Figure 3.18 shows the spectra of the decoded signals after the DFF and OBPF for the two-user's transmission. The auto-correlation pulse, which has a well-defined pulse shape and high peak power, is able to generate the broadband SC spectrum in the DFF, as can be seen in Fig.3.18. In contrast, the interference user's signal with low peak power is unable to generate SC and thus its spectrum still remains in the vicinity of 1550.28nm. After the OBPF, the generated SC
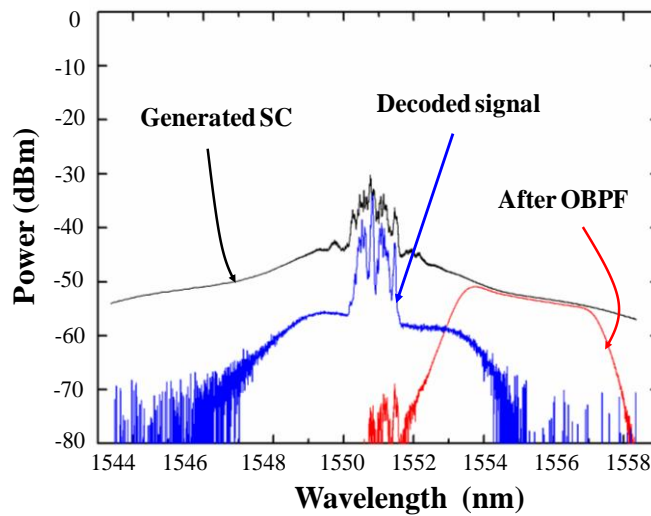


Figure 3.18 Measured spectra of the decoded signal, generated SC and the signal after OBPF.
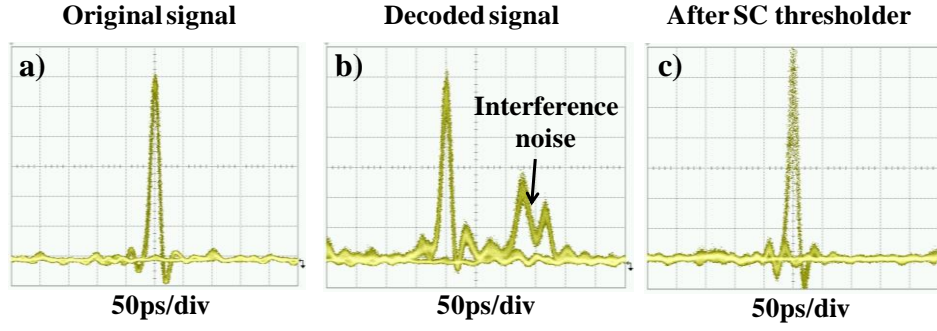
Figure 3.19 (a) ~ (c) are the waveforms of original signal, decoded signal and the signal after SC based optical thresholder for two-user's transmission (Measured by a 50GHz oscilloscope).

spectrum by the auto-correlation signal will remain while the rest of the whole spectrum including the multi-user's interference noise can be eliminated. Figure 3.19 (a)~(c) show the waveforms of the original single user's signal, decoded two-users' signals and the extracted signal after the thresholder, respectively. It can be seen that after correct decoding by the VBS, the encoded signal for the target user has been recovered as a short optical pulse with high peak power, while the other user's signal cannot be decoded and thus exhibits as an interference noise. To correctly recover the data for the target user, the interference noise should be suppressed. It can be seen from Fig. 3.19 (c), after applying the SC based optical thresholder, the interference has been suppressed and the target optical signal has been extracted from the cross-correlation signal. The noise exists in the extracted signal is mainly caused by the signal and interference beat noise as well as the non-ideal optimization of the input signal power before the optical thresholder that may introduce amplitude fluctuation. By using time coordination technique and further optimizing the input optical power, the extracted signal could be significantly improved.

Finally, a photo-diode followed by a 2.65GHz low-pass filter is used for power detection. The bit-error-rate of user 1 (OC1) with different user 2 after the transmission
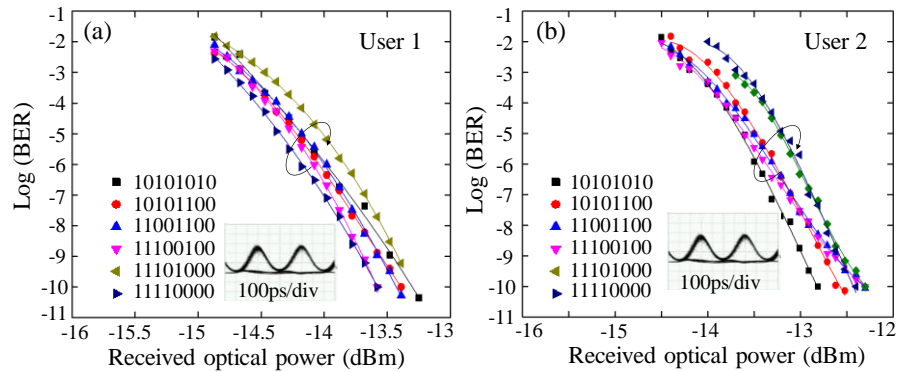


Figure 3.20 BER performances for (a) user 1 (OC1) and (b) user 2 (OC2~OC7).

is measured, as shown in Figure 3.20 (a). Error free has been achieved for the user 1 in all cases. The BER performance of user 2 for the rest six different codes is also shown in Fig.3.20 (b), from which one can see that the average power penalty is about 1dB compared to the user 1 due to the non-ideal decoding for these codes. Clear eye opening and error free transmission are also achieved for user 2. Due to the limited chip rate and code length, the peak power ratio between auto-/cross-correlation signals is not very high, which may limit the active user's number at this stage. One promising approach is to increase the chip rate or decrease the data rate to have long code length to improve the P/C, and another approach is to employ similar time domain decoding scheme as the SPE counterpart to further improve the decoding performance.

## 3.6    Summary

In this chapter, a novel time domain spectral phase encoding scheme which is compatible with conventional spectral phase decoder is proposed and experimentally demonstrated. The proposed scheme has simple configuration, and exhibits the capability of rapidly reconfiguring the optical code by simply programming the pulse pattern generator, which provides an attractive approach for future flexible and dynamic reconfigurable OCDMA system. It may also find its applications in high-repetition rate optical pulse generation and pulse shaping. An advanced modulation scheme that can simultaneously generate time domain spectral phase encoding and DPSK data modulation using only single phase modulator is proposed and experimentally demonstrated. A 2.5Gb/s DPSK data transmission experiment has also been conducted. 2.5Gb/s DPSK data with 8-chip, 20GHz/chip optical code patterns have been successfully generated using a single phase modulator simultaneously, decoded using a VBS based spectral phase decoder and transmitted over 34km fiber with error free. As the DPSK data can be combined with the optical code for encoding, it has the potential to improve the data confidentiality. Finally, the time domain SPE scheme in a two-user's OCDMA system is investigated. A 2.5Gb/s, two-user OOK-OCDMA system with time domain spectral phase encoded OOK data and VBS based decoder has been demonstrated, which shows its potential application for multiple access and the capability of enhancing the network security. The proposed reconfigurable time domain spectral phase encoding technique also has the potential to be used for optical label generation and recognition in optical packet switching networks.

# CHAPTER 4

# Rapid reconfigurable time domain spectral phase encoding and decoding scheme for security enhancement in OCDMA system

## 4.1 Introduction

In chapter 3, a novel time domain spectral phase encoding scheme using a pair of dispersive fibers with opposite dispersions and a high speed phase modulator has been proposed and experimentally demonstrated. This scheme can offer fast reconfigurable capability and is compatible with the conventional spectral phase decoder. It can also simultaneously generate DPSK data modulation and time domain spectral phase en/decoding using a single phase modulator, which can potentially improve the data security. However, this capability has not been demonstrated yet. Moreover, the accurate control of both the amplitude and phase in the spectral phase decoder is rather difficult which will greatly limit the code length and decoding performance. In addition, due to the relatively stringent requirement of dispersive value to adapt to the channel spacing of the spectral phase decoder, high insertion loss, non-ideal dispersion compensation and poor compactness, the dispersive fiber in the scheme is not an ideal element. Linearly chirped fiber Bragg grating (LCFBG) can also be used in the time domain SPE scheme and has the advantages of good compactness, low insertion loss, serving as dispersive component and an optical filter simultaneously, as well as ideal dispersion compensation.

In this chapter, a symmetric time domain spectral phase encoding and decoding (SPE/SPD) scheme based on the LCFBG and high speed phase modulator is proposed for improving the decoding performance and enhancing the data security in OCDMA system. In the proposed scheme, the time-domain SPD has similar configuration as the SPE part but with another PM synchronously driven by the complementary code pattern for OC recognition. The proposed scheme has several potential advantages, with respect to the previous time-domain SPE system that utilized a spectral phase decoder for spectral domain decoding: potentially simplified network architecture by using similar setup for the transmitter and receiver, improved en/decoding performance and relaxed

controlling accuracy of the amplitude/phase in the spectral phase decoder, more flexible to rapidly reconfigure the OC and data with the potential to enhance the network security, all of which combine make this scheme more attractive for OCDMA application and secure optical communication. This chapter is organized as follows: In Section 4.2, the proposed symmetric time domain SPE/SPD scheme is introduced with a 2.5Gb/s OOK data transmission experiment; Then in Section 4.3, the experimental demonstration of an advanced modulation technique using time domain SPE scheme for simultaneous generating the time domain spectral phase encoding and DPSK data modulation, and decoding using similar SPD scheme is presented; Followed by that, in section 4.4, a two-dimensional (2-D) time domain SPE/SPD scheme is proposed and demonstrated; In Section 4.5, a novel bit-by-bit optical code scrambling technique for enhancing DPSK data security based on the time domain SPE/SPD scheme is proposed. A proof-of-principle experiment for 2.5Gb/s DPSK data scrambled by code hopping sequences is presented; Finally, the summary of this chapter is given.

## 4.2 Time domain SPE/SPD scheme and 2.5Gb/s OOK experiment

Figure 4.1 shows the proposed time domain SPE/SPD scheme and the experimental setup of a 2.5Gb/s OOK data demonstration. A MLLD at repetition rate of 10GHz is used to generate a series of 1.9ps optical pulse trains with center wavelength of 1550.28nm. To generate the 2.5Gb/s OOK data, an intensity modulator driven by a programmable $2^7-1$ PRBS is used to modulate the output pulses of the MLLD into
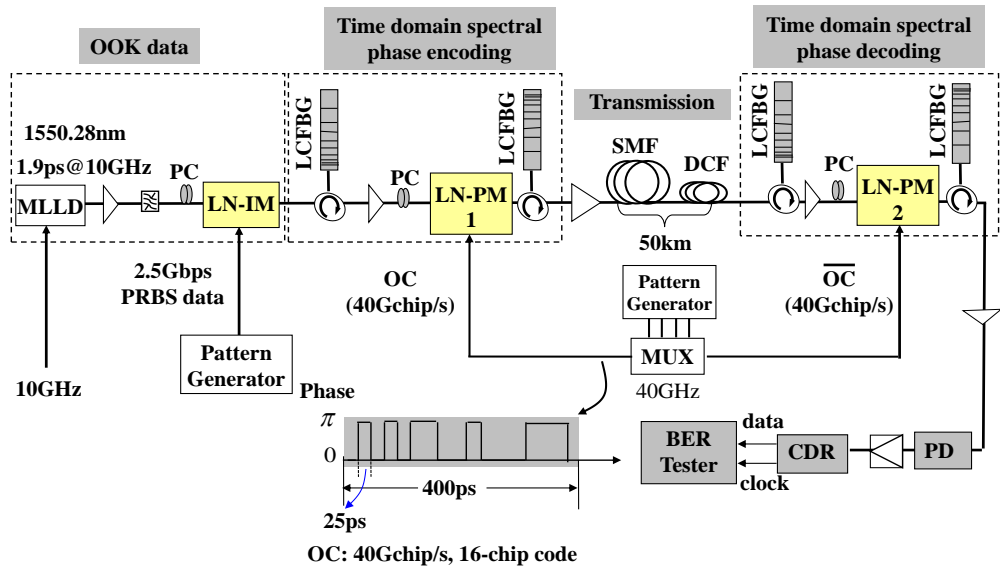


Figure 4.1 Experimental setup of the proposed time domain SPE/SPD scheme.
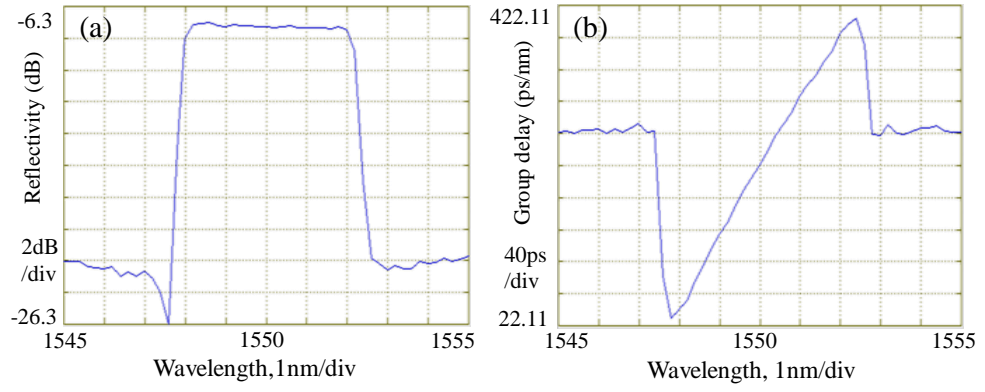
Figure 4.2 (a) Reflection and (b) group delay of the LCFBG.

2.5GHz OOK data pulse trains. Then, a LCFBG is used as the dispersive element to stretch the optical pulse train. Figure 4.2 (a) and (b) shows the measured reflective profile and group delay of the LCFBG, respectively. It can be seen that the LCFBG has a center wavelength of 1550nm, and the 10-dB bandwidth and dispersion slope are ~4.7nm and -80ps/nm, respectively. After the chromatic dispersion by the LCFBG, different spectral component will be spread into different position in time domain.

Figure 4.3(a) shows the spectrum of the stretched pulse output from the LCFBG, from which one can see that the tail of the signal spectrum has been slightly cut due to the use of LCFBG. The corresponding waveform of the stretched pulse exhibits similar profile as the spectrum, as is shown in Fig.4.3 (b). The stretched pulse covers ~376ps time duration which is within one bit period of 400ps. A phase modulator driven by 16 chips, 40Gchip/s (25ps/chip) optical code patterns corresponding to 16chips, 40GHz/chip spectral code patterns from an electrical multiplexer (MUX) is used to phase modulate the stretched optical pulse. By adjusting the optical delay line, the optical code pattern can precisely modulate the desired spectral component of the stretched pulse. After that, another LCFBG with opposite dispersion is used to compress the stretched pulse and generate the SPE signal. A span of SMF and DCF fiber with
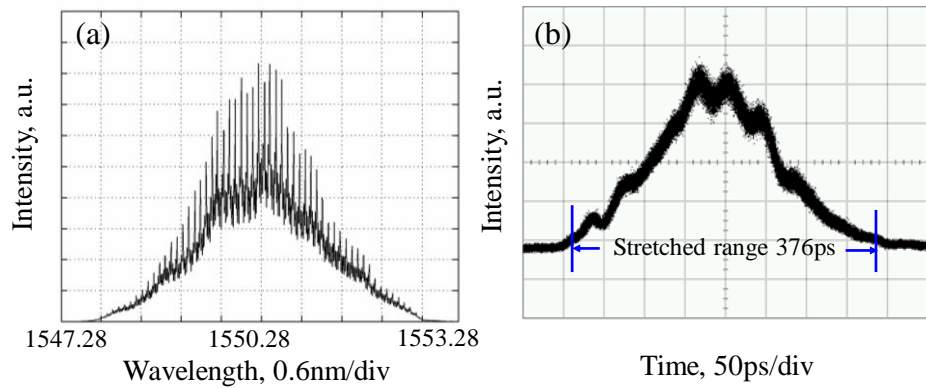


Figure 4.3 (a) Spectrum and (b) waveform of the stretched pulse after the LCFBG.

67

total length of about 50km is used as the transmission fiber. In the decoding side, time domain spectral phase decoding scheme with similar configuration as the encoding part is used, which also includes a pair of LCFBG and a phase modulator but is synchronously driven by the complementary code pattern $\overline{OC}$ from the other output port of the electrical multiplexer. In this setup, a global optical clock is used synchronization between the transmitter and receiver.

Five 16-chip optical codes OC1~OC5: 1110001001101010, 1010101010101010, 1111000011110000, 1111111100000000 and 1110101100100010 have been used for the encoding/decoding experiment. Figure 4.4 shows the encoded spectrum (upper trace), waveform (middle trace) and decoded waveform (lower trace) measured by an auto-correlator with 60ps scanning range for the five codes. All the five codes have been successfully decoded, with a pulse width of about 2.49ps, 2.32ps, 2.57ps, 2.57ps and 2.26ps, respectively. The red line in each figure of the lower trace represents the original input pulse of 1.9ps. It can be seen that the decoded pulse is similar to the original pulse and its broadening is negligible which verifies the excellent decoding performance using the time domain spectral phase decoding scheme in the experiment. Based on the decoding results, a 2.5Gb/s OOK data transmission experiment is then carried out. The correctly decoded signal is directly detected by a photo-detector. The measured BER performances for the back-to-back (B-to-B) and transmission are shown
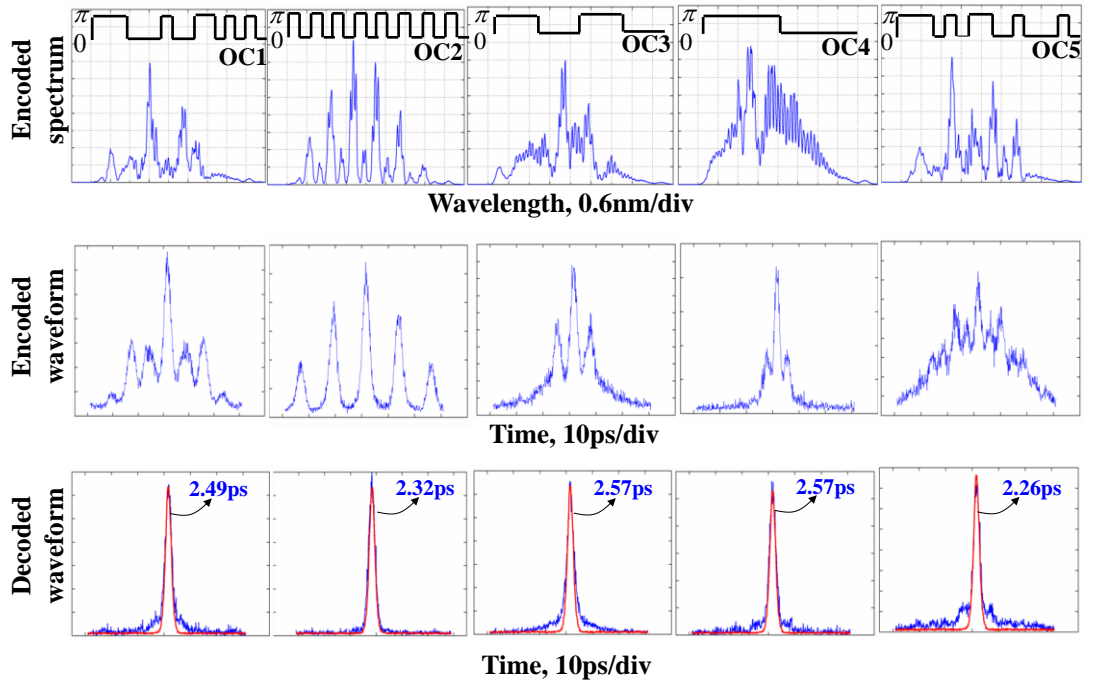


Figure 4.4 Encoded spectrum (upper row), waveform (middle row) and decoded waveform (lower row) for the five codes.
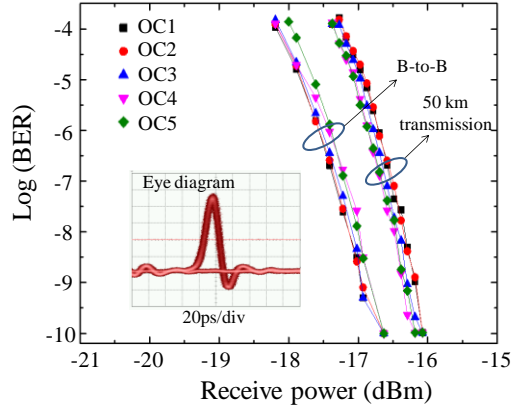
Figure 4.5 BER performances for different optical codes after transmission.

in Figure 4.5, from which one can see the BER performances for all the codes are identical and the power penalty due to the transmission is ~0.6dBm. Error free transmission (BER<$10^{-9}$) has been achieved for all the codes that demonstrates the feasibility of the proposed time domain spectral phase encoding and decoding scheme using LCFBGs for OCDMA application.

## 4.3 Simultaneous time domain SPE/SPD and DPSK data modulation using single PM

As demonstrated in Section 4.2, the symmetric time domain SPE/SPD scheme has superior decoding performance than using a spectral phase decoder in Chapter 3. Based on this scheme, in this section, the time domain SPD scheme is applied in the advanced modulation scheme that uses a single phase modulator for simultaneous generation of time-domain SPE and DSPK data to improve the decoding performance and reconfigurability. The symmetric configuration that employs a similar setup for both the transmitter and receiver can potentially simplify the whole system architecture, enable duplex transmission, and improve the system flexibility and data confidentiality.

### 4.3.1 Principle of time domain SPE/SPD and DPSK data modulation

Figure 4.6 illustrates the operation principle of the SPE/SPD-DPSK OCDMA scheme. As shown in Fig.4.6 (a), the time domain SPE part is same as that in Chapter 3, which is also composed of a pair of dispersive devices with opposite dispersion values (–D and +D) and a high speed PM. The first dispersive device with dispersion value of –D is used to stretch the pulse in time domain. Different spectral components of the

69

input pulse spread at different positions in one bit duration. The PM is driven by combining the DPSK data (101…) and OC patterns as follows to modulate the phase of the stretched optical signal: when the DPSK data is symbol "1", the PM is driven by OC (1101…), while if the symbol is "0", the PM is driven by $\overline{OC}$ (0010…). Therefore, the SPE and DPSK data modulation can be achieved by using only a single PM (i.e. 1101, 0010, 1101…). After that, the second dispersive device with opposite dispersion value of +D is used to compress the stretched pulse in time domain and generate the DPSK data modulated SPE signal.

**(a) Time domain spectral phase encoding and DPSK data modulation using single PM**
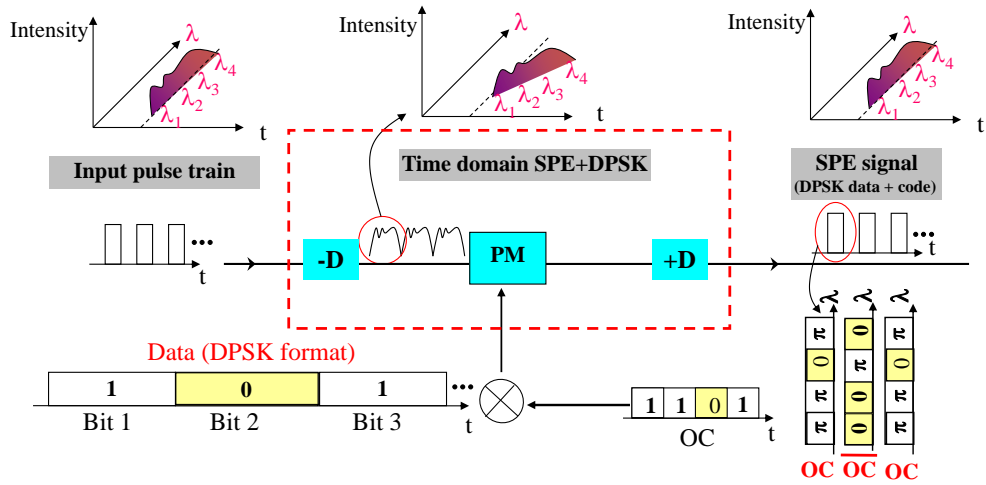


**(b) Time domain spectral phase decoding and DPSK data demodulation**
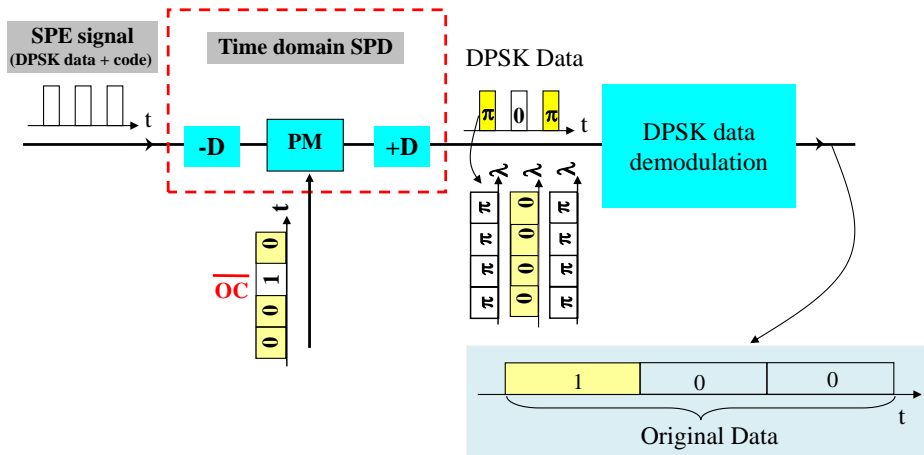


Figure 4.6 Proposed scheme for: (a) time domain SPE and DPSK data modulation using a single PM and (b) time domain SPD and DPSK data demodulation.

To recover the original data, the generated DPSK data modulated SPE signal has to be recognized by proper OC and then DPSK demodulated, as shown in Fig.4.6 (b). Time domain SPD scheme, which has the similar configuration as the SPE that is composed of another pair of dispersive device and PM driven only by the complementary code pattern $\overline{OC}$ is used to perform the OC recognition. The spectral

70

components of each bit are in phase after the decoding. For symbol "1", the total phase is "OC+$\overline{\text{OC}}$=π", while for symbol "0", the total phase is "$\overline{\text{OC}}$+$\overline{\text{OC}}$ =0". Therefore, the DPSK data are extracted from the SPE signal as (101…). The correctly decoded DPSK data can then be demodulated by a DPSK demodulator followed by a balanced detector to recover the original data (100…). In the proposed scheme, the OC generation and DPSK data modulation are simultaneously generated by using single phase modulator, while the OC recognition and DPSK data demodulation are achieved separately, therefore, the configuration of this system can be greatly simplified, and meanwhile, the data security can be potentially improved.

### 4.3.2 Experimental demonstration and results

Figure 4.7 shows the experimental setup for simultaneous generation of SPE/SPD and DPSK data modulation. At the transmitter, the MLLD produces ~4ps Gaussian-like pulses with a repetition rate of 10 GHz and spectrally centered at 1550.28nm. A Mach-Zehnder intensity modulator driven by a pulse pattern generator is used to convert the source repetition rate into 2.5 GHz. For the generation of time domain SPE and DPSK data modulation, a LCFBG with 10-dB bandwidth of ~4.7 nm and dispersion slope of ~ -80 ps/nm is used to stretch the input optical pulse. To effectively stretch the input short optical pulse within one bit duration of 400ps after the LCFBG, super continuum (SC) generation based on the MLLD, an EDFA, and a piece of 2km dispersion-flattened-fiber (DFF) is employed in the light source to broaden the bandwidth of the original signal. Figure 4.8 (a) and (b) show the spectrum and waveform of the stretched pulse after the
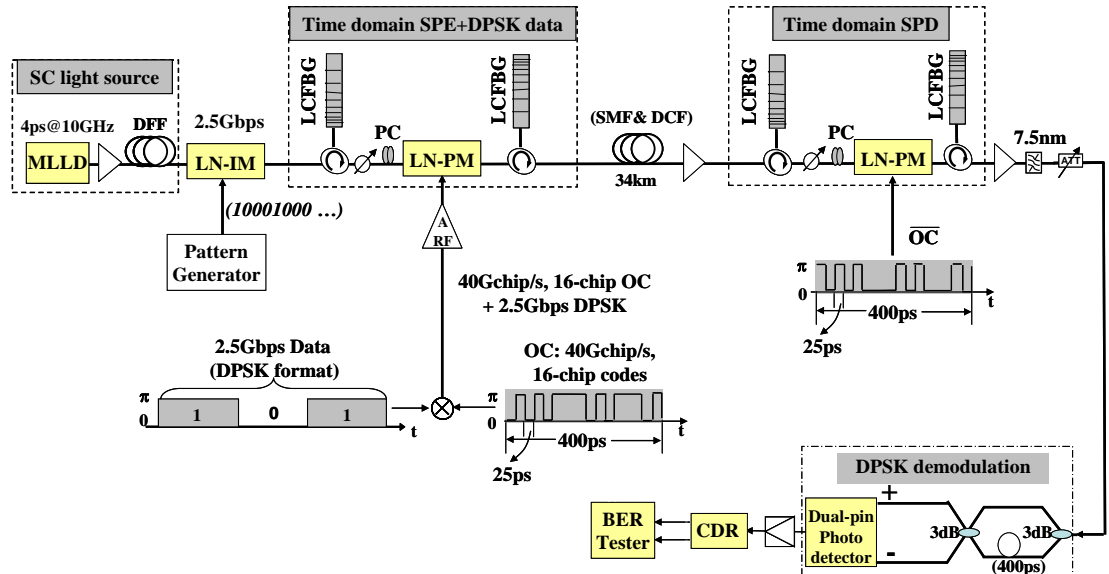


Figure 4.7 Experimental setup of the time domain SPE/SPD DPSK-OCDMA system.

71

LCFBG, respectively. Different spectral components spread into different positions in time domain because of the chromatic dispersion. It can be seen from Fig.4.8 (a) that the tail of the input spectrum has been slightly cut into ~4.7nm due to the sharp spectral response of the LCFBG, which functions as a dispersive device as well as an optical bandpass filter. As shown in Fig.4.8 (b), the stretched pulses exhibit similar profile as the input spectrum, covering about 376 ps within one bit period of 400 ps, and hence there is no obvious overlap between adjacent stretched pulses in the experiment. Fig.4.8 (c) shows the waveform of the stretched pulse without SC generation, in which case the stretched pulse occupies only ~200ps in time domain that will directly reduce the effective code length (~8 chips) and degrade the peak power ratio between the auto-/cross-correlation signals. A PM driven by combining 16-chip, 40-Gchip/s OC pattern (corresponding to 16-chip, 39GHz/chip spectral code pattern) and 2.5-Gb/s DPSK data then phase modulate the stretched optical pulse.
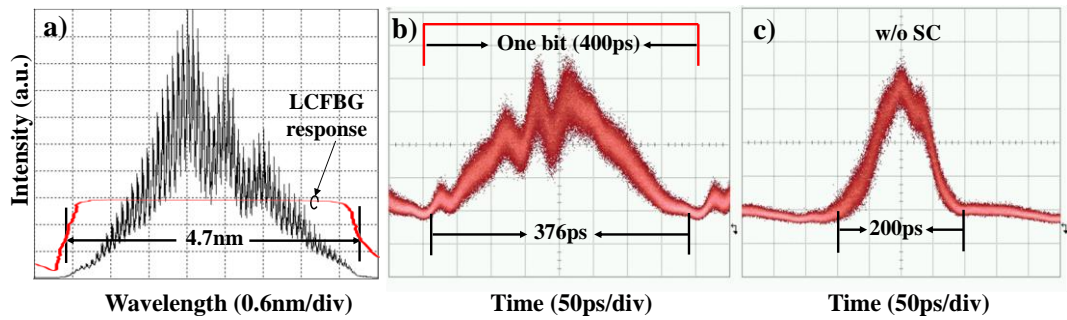


Figure 4.8 (a) Spectrum after LCFBG; (b) Waveform of stretched pulse with SC generation; (c) Waveform of stretched pulse without SC generation.

The data rate mainly depends on the chip rate and code length in this system. For a chip rate of 40-Gchip/s and code length of no less than 16, the achievable maximum data rate is 2.5-Gb/s. To scale the data rate, one can either increase the chip rate, which is mainly limited by the electronic processing technology or decrease the code length and thus sacrifice the en/decoding performance. The DPSK data are mixed with the OC to drive the PM in the same way: when the DPSK data is symbol "1", the PM is driven by OC, while if symbol is "0", the PM is driven by $\overline{OC}$. A tunable optical delay line is employed before the PM to accurately synchronize the OC pattern and stretched pulse, so the OC patterns can precisely modulate the phase of the corresponding spectral component. After that, another LCFBG with opposite dispersion of +80 ps/nm is used to compress the stretched pulse and generate the SPE signal. A span of 34 km SMF is used as the transmission fiber in the experiment. A dispersion compensation fiber (DCF) module is employed to compensate the dispersion mismatch. Although the dispersion

can be managed globally, because the dispersion before the encoding PM and after the decoding PM has been cancelled with each other, here, to show its flexibility of dispersion management, the dispersion is managed individually for each subsystem.

To recover the original DPSK data, the generated SPE signal is firstly spectral phase decoded and then DPSK demodulated. The decoding part has the similar configuration as that of the encoding but the PM is driven only by the $\overline{OC}$. Note that careful temporal alignment between the encoding and decoding side by properly adjusting the tunable optical delay line before the PM is essential for decoding the SPE signal and improving the security, because it is quite difficult for an eavesdropper to recover the target data without proper synchronization even if he knows the applied OC. The correctly decoded signal is then directed into a 2.5-GHz DPSK demodulator followed by a balanced detector to recover the DPSK data. A 2.65-GHz low-pass filter is used after the balanced detector to perform data-rate detection.

The encoding/decoding using five different 16-chips, 40-Gchip/s OC patterns: two of them are from M-sequence, one is randomly selected and the other two are from Gold codes has been investigated firstly. The patterns used in the experiment are: OC1 (111000100110101) and OC2 (1110101100100010) are 15-chip M-sequence plus a zero, OC3 is (1010101010101010), OC4 (101000010110100) and OC5 (11010001 0100100) are 15-chip Gold codes plus a zero. Figure 4.9 shows the encoded waveform (upper trace), encoded spectrum (middle trace) and autocorrelation (lower trace) measured by a 10 GHz optical sampling oscilloscope for the five codes after
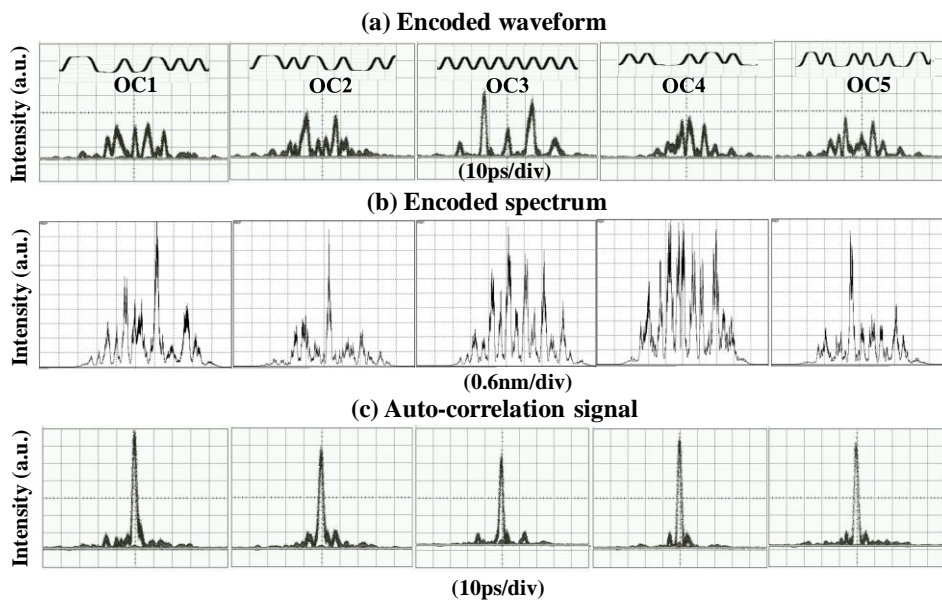


Figure 4.9 (a) Encoded waveform (upper row), (b) encoded spectrum (middle row) and (c) auto-correlation signal for the five OCs.

73
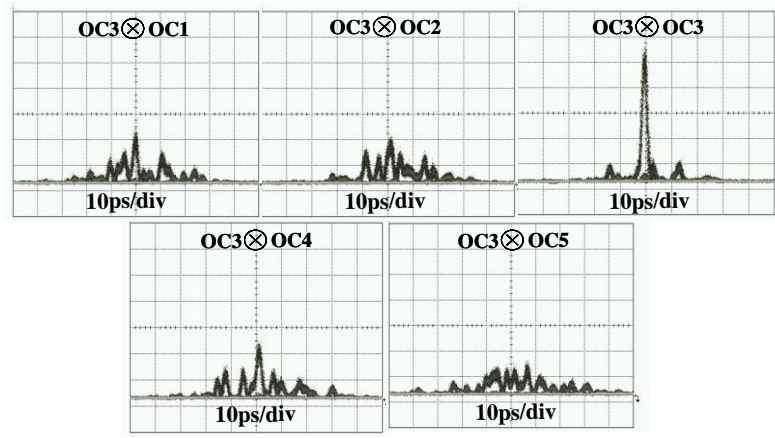
Figure 4.10 Waveforms of the cross-correlation signals for OC3 with the other codes.

transmission. All the five codes have been successfully decoded in the experiment. The cross-correlation signals for OC3 are also shown in Figure 4.10, from which one can see that the P/C between the auto-/cross correlations has been improved to ~3 (compared to that of no SC generation with a maximum of P/C~2 because of the relatively short effective code length of ~8). To further improve the P/C, the peak intensity of the autocorrelation signal has to be increased. It is worth noting from the lower trace in Fig.4.9 that there are some low sidelobes in the decoded waveforms, which can be partially ascribed to the non-ideal synchronization between the encoding and decoding side as well as the modulation index difference between the two PMs that introduces phase shift difference. In addition, there are several other factors that need to be taken into account: code transition of the electrical signal from the PPG, dispersion mismatch of the LCFBGs between the encoding and decoding side, and the residual dispersion of the transmission fiber SMF & DCF.

Figure 4.11 depicts the effect of code transition on the en/decoding performance for OC3. The code transition $\eta$ is defined as $\eta=a/b$, where $a$ is the rise or fall time, and $b$ is the time duration of one chip, as shown in the inset of Fig.4.11 (b). It can be seen from Fig.4.11 (a), the code transition will induce more pedestal pulses in the encoded waveform compared to the simulated encoded waveform in Fig.4.11 (b) that without code transition. The dashed blue line in Fig.4.11 (a) is the simulated encoded waveform with a code transition of 45% which agrees well with the experimental result (solid line). In the experiment, as the SPD configuration is similar to the encoding part, the relative code transition between the two PPGs in the encoding and decoding side will significantly affect the decoding performance. Fig.4.11 (c) shows the simulated decoded waveform (dashed line) with identical code transition between the encoding and decoding, from which one can see the decoded signal still exhibit as a well-defined

74
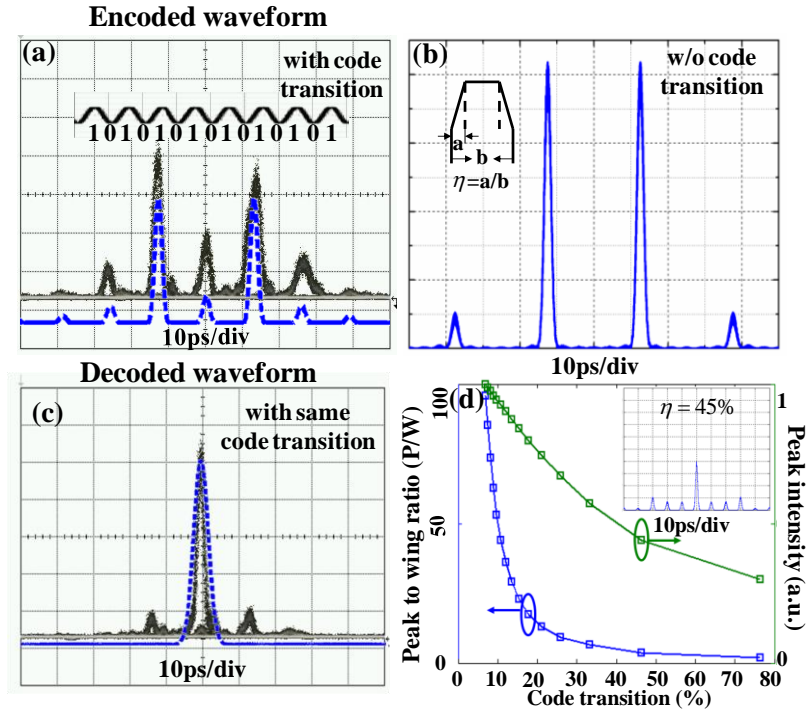
Figure 4.11 (a) Encoded waveform (solid line) and simulated waveform (dashed line) with code transition; (b) Encoded waveform without code transition; (c) Decoded waveform (solid line) and simulated waveform (dashed line) with identical code transition in the encoding and decoding side; (d) P/W and peak intensity versus relative code transition; Inset is the decoded waveform for η=45%.

auto-correlation pulse. While if the code transitions for the encoding and decoding sides are slightly different, a few sidelobes will appear in the auto-correlation signal, as can be seen from the decoded waveform in Fig. 4.11 (c) and the inset in Fig. 4.11 (d). The peak to wing ratio (P/W) and peak intensity versus the relative code transition are also shown in Fig.4.11 (d), respectively. As the relative transition increases, both the P/W and peak intensity gradually decrease that may degrade the transmission performance. For a relative code transition of ~25%, the P/W and peak intensity is around 10 and 0.7, respectively. There is no obvious degradation of the decoding performance, showing the relative code transition is very small in the experiment.

Besides the code transition, the dispersion mismatch in the encoding and decoding side is another key factor for the decoding performance. Assuming that the dispersion has been fully compensated in both the encoding (-D1, D1) and decoding side (-D2, D2), but there is dispersion mismatch between them (D1≠D2). Figure 4.12 (a) and (b) show the P/W and peak intensity of the decoded waveform versus the dispersion mismatch for OC3, respectively. As the dispersion mismatch increases, the peak intensity gradually decreases and the sidelobes are generated in the decoded waveform,

and hence the P/W dramatically decreases. The tolerance to dispersion mismatch is calculated to be ~ ±20 ps/nm for a minimum P/W and peak of 10 and 0.53, which can be easily maintained. In the experiment, two pairs of LCFBGs with identical dispersion in the encoding and decoding sides are used, so the effect of dispersion mismatch can be easily eliminated.
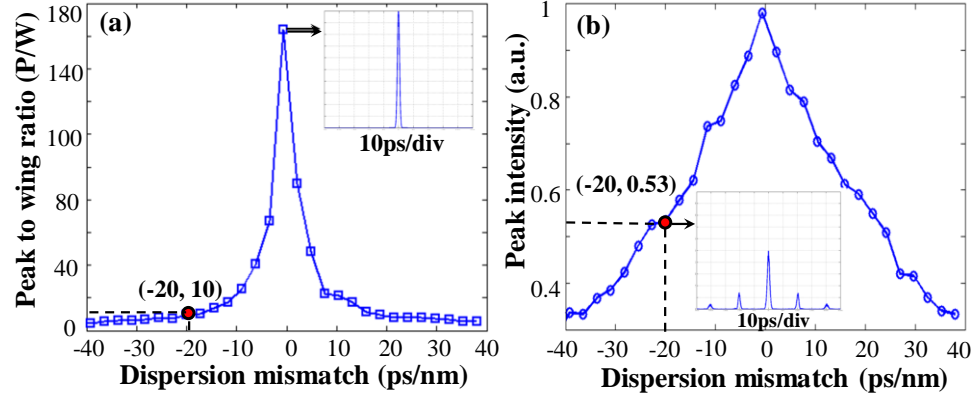


Figure 4.12 (a) Peak to wing ratio (P/W) and (b) peak intensity of the decoded waveform versus the dispersion mismatch. The insets are the simulated decoded waveforms.

In addition, since the proposed SPE/SPD scheme is performed in time domain, the residual dispersion of the SMF and DCF cannot be neglected. Figure 4.13 (a) shows the measured and simulated decoded waveform considering the residual dispersion of 20ps/nm in the transmission fiber for OC1, from which one can see that the asymmetric sidelobes of the simulated decoded waveform agree well with the experimental result, which verifies the decoding performance degradation due to the residual dispersion in the SMF & DCF. The P/W versus the residual dispersion is depicted in Fig.4.13 (b), from which one can see that the P/W will dramatically decrease with the increase
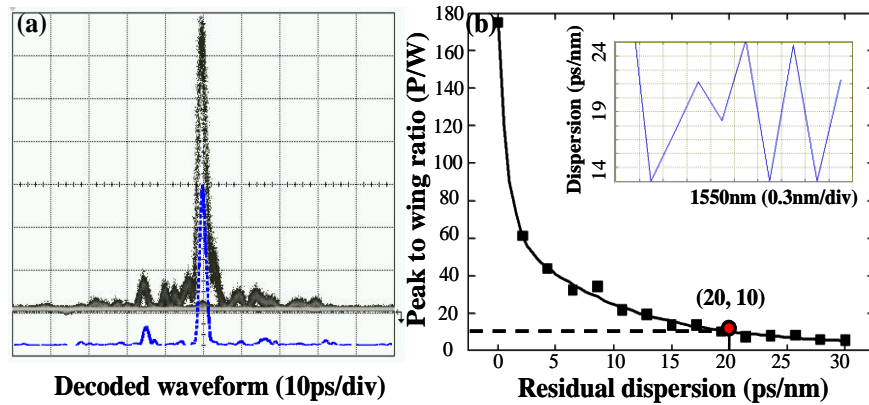


Figure 4.13 (a) Measured (solid grey line) and simulated (dashed blue line) decoded waveform with residual dispersion of ~20ps/nm for OC1; (b) Peak to wing ratio versus residual dispersion of transmission fiber; the inset is the dispersion of the transmission fiber.

of residual dispersion. The inset in Fig.4.13 (b) is the measured total dispersion of the transmission fiber in the experiment. Although the dispersion compensation is not ideal in the experiment with a residual dispersion of around 20ps/nm corresponding to a P/W of ~10, it is enough for the time domain SPE/SPD-OCDMA system.

Finally, a proof-of-principle experiment with the setup for simultaneous generation of SPE and DPSK data modulation using a single PM, and a 2.5-Gb/s DPSK data transmission experiment with the 16-chip, 25-ps/chip OC patterns has been carried out. A trial of fixed data pattern 010100111001 for OC1 has been done at first, as shown in Figure 4.14. The original data (a) is firstly precoded into DPSK data format (b) 011000101110, and then mixed with the OC1 to drive the phase modulator in the encoding part, whose electrical waveform is shown in Fig. 4.14 (c). The combined DPSK data and OC1 looks like a pseudo random bit sequence that is not easy to directly extract the DPSK data. Fig.4.14 (d) shows the waveform of the encoded SPE signal. At the receiver side, the complementary code pattern $\overline{OC1}$ is used to drive the second PM to generate the decoded signal as shown in Fig.4.14 (e), from which one can see the decoded signals for symbol "0" and "1" have similar waveforms but totally different phases according to the DPSK data ($0\pi\pi000\pi0\pi\pi\pi0$ …). Fig.4.14 (f) shows the recovered data pattern after the DPSK demodulator and balanced detector which is exactly the original data pattern: 010100111001, indicating the feasibility of using the
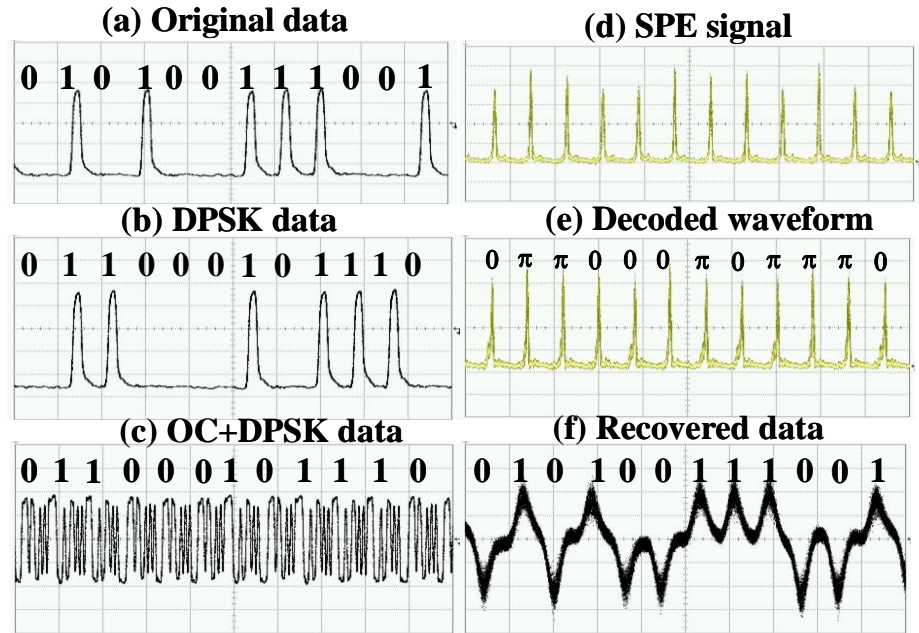


Figure 4.14 Fixed data pattern trial: (a) Original data pattern: 010100111001; (b) Precoded DPSK data: 011000101110; (c) Combined OC1 and DPSK data; (d) Waveform of generated SPE signal; (e) Waveform of decoded signal and (f) recovered data pattern: 010100111001.

proposed time domain SPE/SPD scheme for DPSK-OCDMA application.

In addition, the 2.5-Gb/s DPSK data transmission experiment has also been carried out using $2^7$-1 PRBS for all the five codes. The measured BER performances for back-to-back and transmission with the five codes are shown in Figure 4.15 (a) and (b), respectively. Error-free (BER<$10^{-9}$) has been achieved in both cases for all the codes though the received optical power is a little high due to the lack of a 2.5 GHz clock and data recovery circuit at the time of this experiment. The power penalty for the transmission is less than 1dB. Clear eye opening have been achieved for all the five codes which demonstrate the proposed SPE/SPD scheme using a single PM for simultaneous OC generation and DPSK data modulation, and decoding using time-domain SPD scheme. Based on this modulation technique, the OC can even be rapidly reconfigured bit-by-bit and scrambled with the DPSK data to significantly enhance the data confidentiality for secure optical communication.
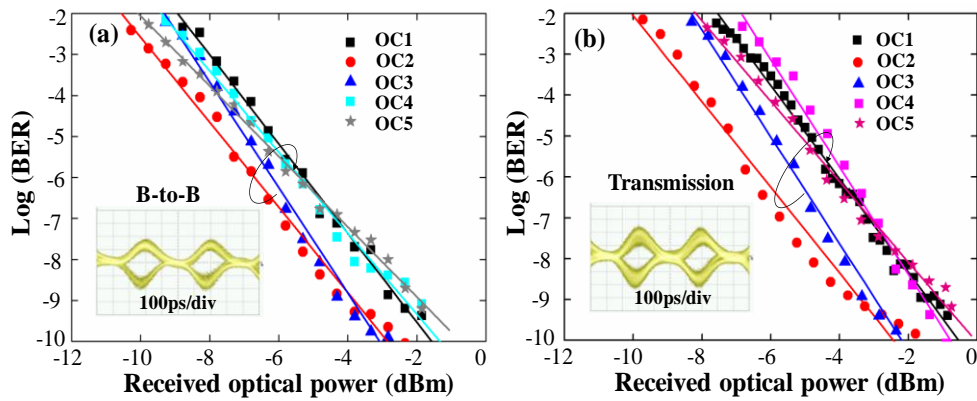


Figure 4.15 BER performances for (a) back-to-back and (b) transmission over 34km fiber.

## 4.4  2-D Time domain SPE/SPD-OCDMA scheme

In the time domain SPE/SPD scheme, the spectral phase pattern could be rapidly applied onto the continuous spectral components in time domain. However, due to the limitation of chip rate, the code length and thus the code space is not very high. In this section, a 2-D (temporal, spectral) encoding scheme which is composed by an array of discrete FBGs with different reflection wavelengths is proposed to perform wavelength hopping, as shown in Figure 4.16 (a). By using the FBG array, different spectral components can be hopped into different time positions according to the FBGs structure rather than continuously spread in time domain, so it provides another dimensional degree of coding and thus the available code could be increased. After the wavelength
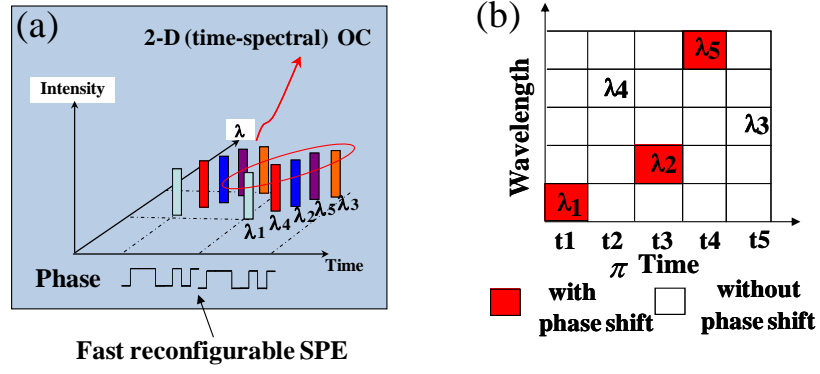
Figure 4.16 (a) Schematic diagram of the 2-D coding scheme and (b) code look up map.

hopping, the fast reconfigurable spectral phase pattern can then be applied onto different spectral components for spectral phase encoding according to the coding map, as shown in Fig.4.16 (b) with wavelength hopping code of {1, 4, 2, 5, 3} and spectral phase pattern of {1, 0, 1, 1, 0} as an example. Therefore, both wavelength hopping and spectral phase encoding can be simultaneously achieved to enhance the code cardinality and system security.

Figure 4.17 illustrates the experimental setup to investigate the proposed 2-D SPE/SPD scheme. At the transmitter, a super-continuum (SC) light source is employed, which is generated by a MLLD with ~4ps optical pulses, spectrally centered at 1546.1nm. The source repetition rate is gated down to 2.5-GHz by using an intensity modulator IM. For the generation of 2-D optical encoding, a Fiber-Bragg-Gratings array based optical encoder is used as a nonlinear discrete dispersive component to temporally spread the input optical pulse into a multi-color pulse train with the wavelength hopping pattern (WHP) (e.g. $\lambda 1$, $\lambda 4$, $\lambda 2$, $\lambda 5$, $\lambda 3$), as shown in Fig.4.16 (b). Different spectral bands will be hopped into different time positions, and then spectrally
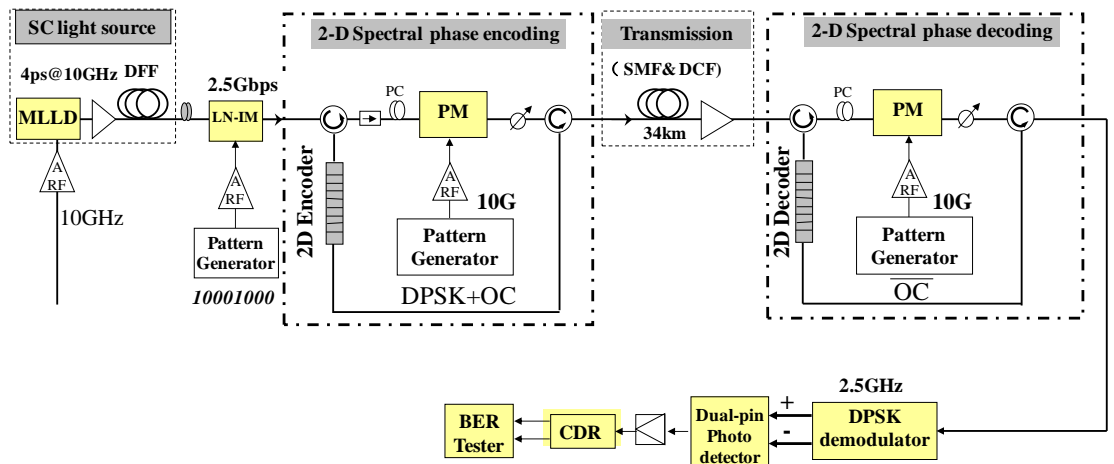


Figure 4.17 Experimental setup of the 2-D time domain SPE/SPD DPSK-OCDMA system.

phase modulated by the phase modulator driven by combining DPSK data and 4-chip, 10-GHz/chip spectral phase pattern (SPP). The spectral phase encoded pulse train is then temporally compressed via an optical circulator through the transmission port of the same FBG array to generate the 2D DPSK data modulated SPE signal. To recover the original data, the generated 2D SPE signal has to be firstly wavelength hopping/spectral phase decoded and then DPSK demodulated. The 2D spectral phase decoding part has the similar configuration as the encoding part, where a 2D FBG array based optical decoder is used for decoding the WHP and another PM driven only by the complementary code is used for decoding the SPP. The DPSK data can be extracted and then demodulated by the 2.5G DPSK demodulator followed by a balanced detector for recovering the original data.

Figure 4.18 (a)~(c) show the reflection and group delay of three pairs of 2-D FBGs array encoder used in this experiment, respectively. The spacing between adjacent wavelengths is 0.8 nm and chip-rate is 10 GHz/chip. The different group delay indicates that different colors (spectral bands) will be hopped into different time positions. The three 2-D code patterns showing are {1, 2, 3, 4, 5}, {1, 4, 2, 5, 3} and {1, 3, 5, 2, 4}, which are denoted as ABCDE, ADBEC and ACEBD. For the spectral phase encoding,
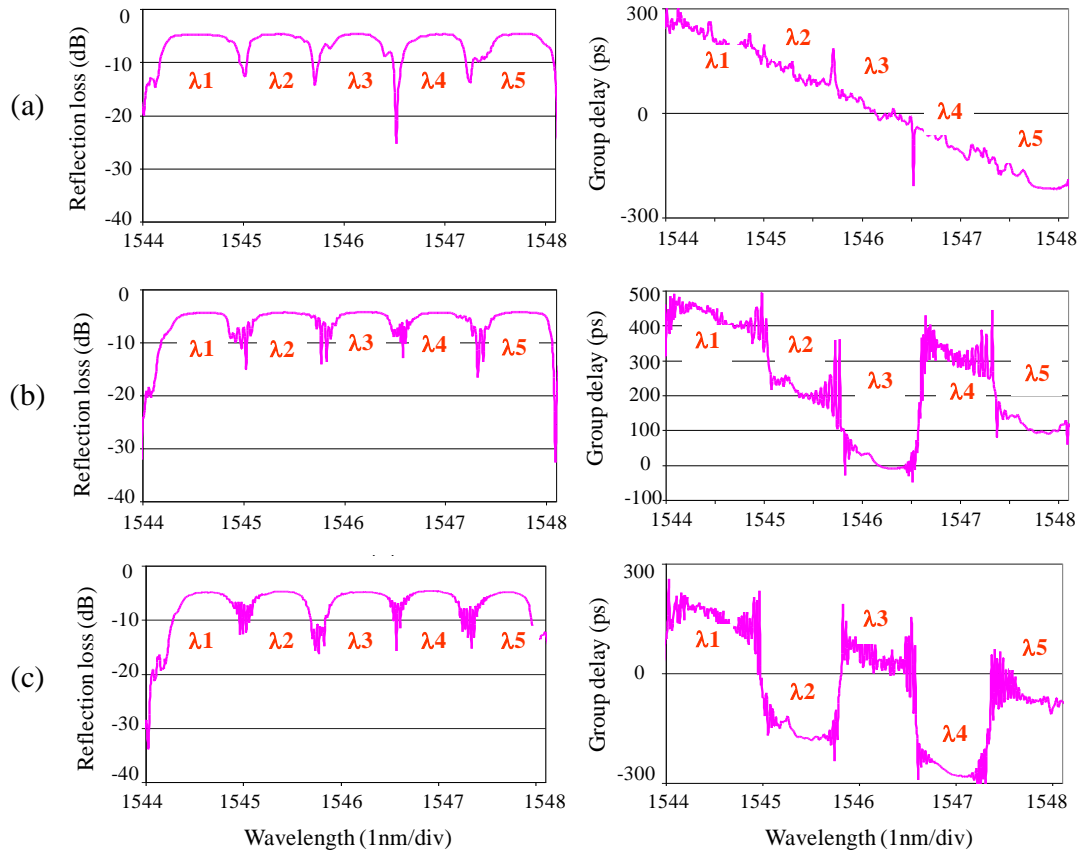


Figure 4.18 Measured refection loss and group delay for different FBGs arrays.

80
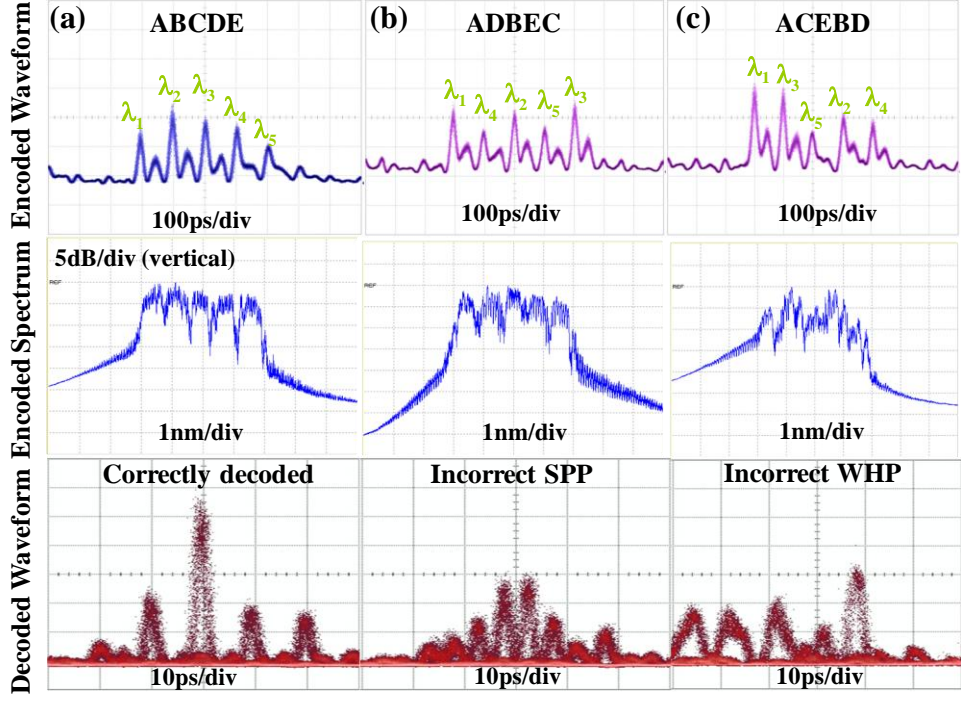
Figure 4.19 (a)~(c) Encoded waveform, spectrum and decoded waveforms for the three FBGs array en/decoders.

three spectral phase patterns (SPP) OC1~OC3 (1001, 1010, 1100) are used for ABCDE, while the OC2 are used for both ADBEC and ACEBD. Figure 4.19 (a) ~ (c) show the waveforms of the spread 2-D pulses for the three FBGs encoders, from which one can see the WHP can be generated by the encoders with a chip rate of 10GHz/chip. The middle row in Fig.4.19 shows the encoded spectrum with spectra phase pattern OC2 for the three FBGs. The decoding performance for FBGs ABCDE is shown in the lower row in Fig.4.19, from which we can see the correctly decoded waveform has a high peak intensity pulse with some sidelobes mainly due the mismatch of the FBG arrays, while for either incorrect SPP or WHP, only a cross-correlation signal with many low peak intensity pulses spread in time domain can be obtained. Finally, the transmission experiment with $2^7$-1 PRBS DPSK data has been carried out, and the BER performance for ABCDE with three SPPs is shown in Figure 4.20 (a). The power penalty after transmission is around 1dB. The BER performance for FBGs ADBEC and ACEBD with SPP-OC2 is shown in Fig.4.20 (b). Error-free transmission has been achieved in all the different cases.

Although simultaneous wavelength hopping and fast reconfigurable spectral phase encoding can be achieved by employing the 2-D en/decoder and phase modulator in the time domain SPE/SPD scheme, the wavelength hopping pattern is actually fixed by the FBG array, which limits its flexibility and the number of available codes. Also

81

practically, it is very difficult to fabricate long FBG array consisting of FBGs with different central wavelengths in a high precision, and thus the coding performance is relatively poor with very high sidelobes in the auto-correlation signal and the peak power ratio of the auto-/cross correlation signal is also very low. This prompts us to develop innovative reconfigurable 2-D optical en/decoder that can simultaneously generate wavelength hopping and spectral phase encoding, as will be discussed in chapter 7 of this thesis.
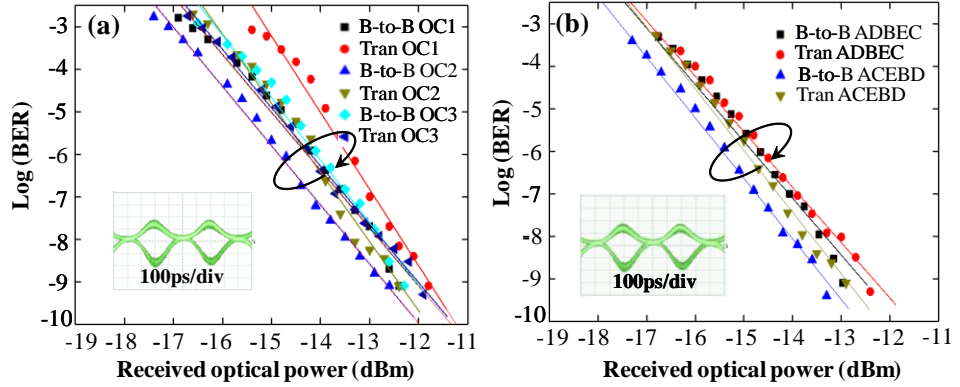


Figure 4.20 (a) BER performances for FBGs ADBEC and (b) ACEBD with OC2.

## 4.5 Time domain bit-by-bit optical code scrambling and DPSK data modulation for security enhancement

As providing information security is considered as an inherent advantage of OCDMA technique based on the optical code processing, a large amount of research activity of OCDMA technique has been focused on its security lately [15, 30-31, 61]. However, as presented in Chapter 2, security vulnerability of the optical code arising from coding induced dips in either the spectrum or waveform has been pointed out [30-31]. An eavesdropper may even do not need to know the applied code but can easily intercept the confidential data by using a proper energy detector for OOK data modulation or a DPSK demodulator for DPSK and CSK modulation. In the proposed time domain SPE/SPD scheme, the DPSK data can be simultaneously generated with the optical code as has been demonstrated in Section 4.3, which exhibits the capability of improving the data security, but this concept has not been demonstrated up to now.

In this section, for the first time, to the best of the author's knowledge, a novel bit-by-bit code scrambling technique based on the proposed time domain SPE/SPD scheme for secure optical communication has been demonstrated [109]. 2.5-Gb/s DPSK data

modulation and five 8-chip, 20-Gchip/s optical Gold codes have been simultaneously generated, and scrambled by prime-hop patterns bit-by-bit using a single phase modulator in the experiment. The rapid reconfigurable capability of the combined DPSK data and code hopping sequence makes the system immune to simple data rate energy detection and DPSK demodulation attack, and therefore, it can significantly improve the information security and exhibit the potential to realize even "one time pad" that is absolutely secure in theory.

## 4.5.1 Principle of bit-by-bit optical code scrambling

Figure 4.21 (a) shows the principle of the simultaneous bit-by-bit code scrambling and DPSK data modulation using a single phase modulator. The time domain SPE scheme is employed, which consists of a pair of dispersive devices with opposite



Figure 4.21 Principle of the proposed scheme (a) transmitter for bit-by-bit code scrambling/DPSK data modulation; (b) receiver for bit-by-bit SPD/DPSK data demodulation.

dispersion values (–D and +D) and a high speed phase modulator for bit-by-bit spectral phase encoding. Frequency to time mapping can be realized ($\lambda_1$, $\lambda_2$, $\lambda_3$, $\lambda_4$…spread in different time positions) by the first dispersive device (–D). The PM is then driven by bit-by-bit combining the OC patterns and DPSK data which is generated by precoding the original data (101000…) into DPSK data format (100101…) and then combined with the corresponding OC in the following way to modulate the phase of the stretched optical signal: when the DPSK data is symbol "1", the PM is driven by OC, while if symbol is "0", the PM is driven by $\overline{OC}$. The optical codes can thus be scrambled in this scheme, for example, in the case of Fig.4.21 (a), the PM can be driven by the combined DPSK data and code sequence as OC5, $\overline{OC2}$, $\overline{OC4}$, OC6, $\overline{OC1}$, OC3. Therefore, the DPSK data can be spectrally phase encoded bit-by-bit by using only one PM. After that, the second dispersive device with opposite dispersion of +D is used for compressing the pulse and generating the DPSK data modulated SPE signal. The spectral phase of each encoded bit is different from the others representing different optical codes (i.e. the phase of the third data OC4 is $00\pi0\pi00$…, while the fourth data is OC6:$\pi0\pi\pi\pi0\pi\pi$…, respectively).

At the receiver side, the generated DPSK data modulated SPE signal has to be spectrally phase decoded and then DPSK demodulated to recover the original data. The setup for the SPD is similar to that of the transmitter, as shown in Fig. 4.21(b) which is also composed of a pair of dispersive devices and a high speed PM. However, the PM is driven only by the complementary scrambled optical code sequences $\overline{OC5}$, $\overline{OC2}$, $\overline{OC4}$, $\overline{OC6}$, $\overline{OC1}$, $\overline{OC3}$, so the spectral components of each encoded pulse are in phase after the decoder (i.e. For the third data, if the symbol "1", the total phase is "OC4+$\overline{OC4}$=$\pi$", while for symbol "0", the total phase is "$\overline{OC4}$+$\overline{OC4}$=0"). Therefore, the total phase of each decoded pulse becomes ($\pi00\pi0\pi$…) and the DPSK data is extracted from the SPE signal as (100101…). Finally, a DPSK demodulator with one-bit delay interferometer followed by a balanced detector is used to demodulate the DPSK data and recover the original data as (101000…).

In this scheme, the SPE and SPD utilize similar configurations to perform the optical code generation and recognition, and only a single phase modulator is used to realize the simultaneous DPSK data modulation and time domain spectral phase encoding, which enables the capability of rapid bit-by-bit optical code scrambling with the DPSK data to significantly enhance the DPSK data confidentiality.

## 4.5.2 Experimental demonstration of bit-by-bit code scrambling

Figure 4.22 illustrates the experimental setup of the proposed bit-by-bit code scrambling and DPSK data modulation scheme. At the transmitter, a super-continuum (SC) light source is employed. The source repetition rate is converted to 2.5GHz by using a Mach-Zehnder intensity modulator and pulse pattern generator. The following setup includes two main sections: bit-by-bit spectral phase encoding using the mixed DPSK data and scrambled code sequence, and bit-by-bit code recognition using only the complementary code hopping sequence.
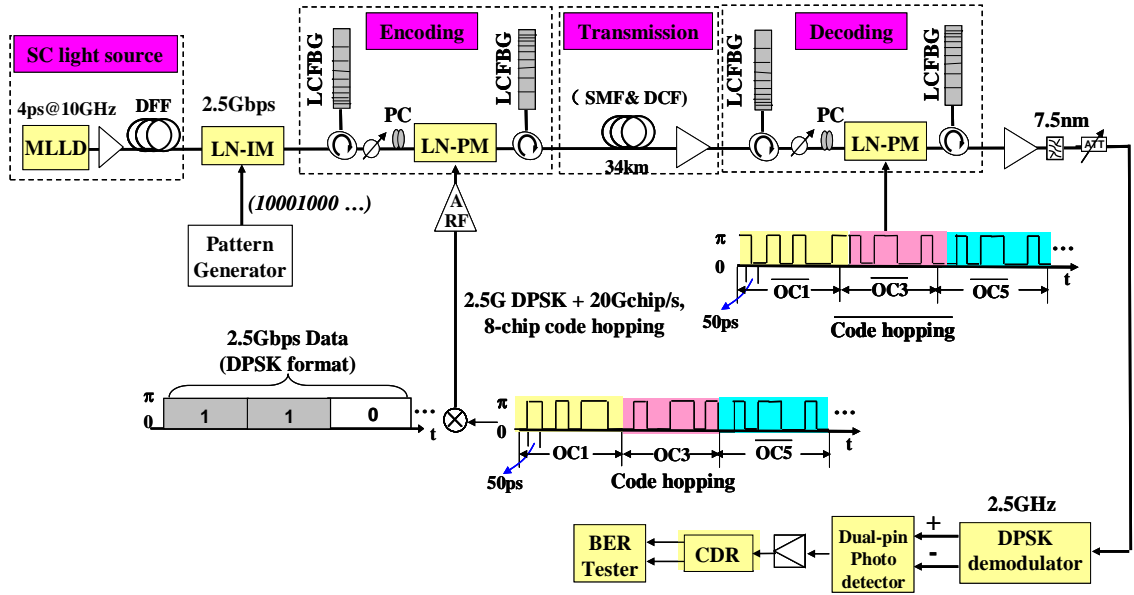


Figure 4.22 Experimental setup of bit-by-bit OC scrambling time domain SPE/SPD scheme.

In the encoding section, a LCFBG with bandwidth of ~4.7nm and dispersion slope of about -80ps/nm is used to stretch the 2.5GHz optical pulse into 376ps time duration. Different spectral components spread into different positions in time domain as a result of the chromatic dispersion. The dispersed pulse is then temporally phase modulated by a PM driven by the combination of 2.5-Gb/s DPSK data and scrambled code hopping sequence, which contains five 8-chip, 20-Gchip/s (corresponding to 8-chip, 78-GHz/chip spectral code pattern) Gold codes with 7 chips plus a zero. The five Gold codes are: OC1: 10010110, OC2:11100010, OC3:10101010, OC4:10101100 and OC5:00001010, respectively. The correlation properties of the Gold codes are of vital importance to guarantee the security of the proposed code scrambling scheme, because the eavesdropper can still decipher the DPSK data using a wrong code hopping sequence if the peak power ratio (P/C) between the auto-/cross-correlations is very low. Figure 4.23 (a)~(c) shows the measured encoded waveform (upper row), encoded

spectrum (middle row) for the five Gold codes and the auto/cross-correlation signals (lower row) for OC2, respectively. All five codes have been successfully decoded in the experiment and the decoded pulses have well-defined auto-correlation peaks. An identical phase modulator in the encoding and decoding sides, and less than 20ps/nm residual dispersion of the SMF & DCF are essential to reduce the sidelobes and improve the decoding performance of the auto-correlation signal. As shown in Fig.4.23 (c), the average P/C for the 8-chip, 20-Gchip/s codes can reach to ~2, which is sufficient to discriminate different codes and perform the DPSK code hopping experiment. By increasing the chip rate and chip number of the optical code, the P/C can be further improved to enhance the security.
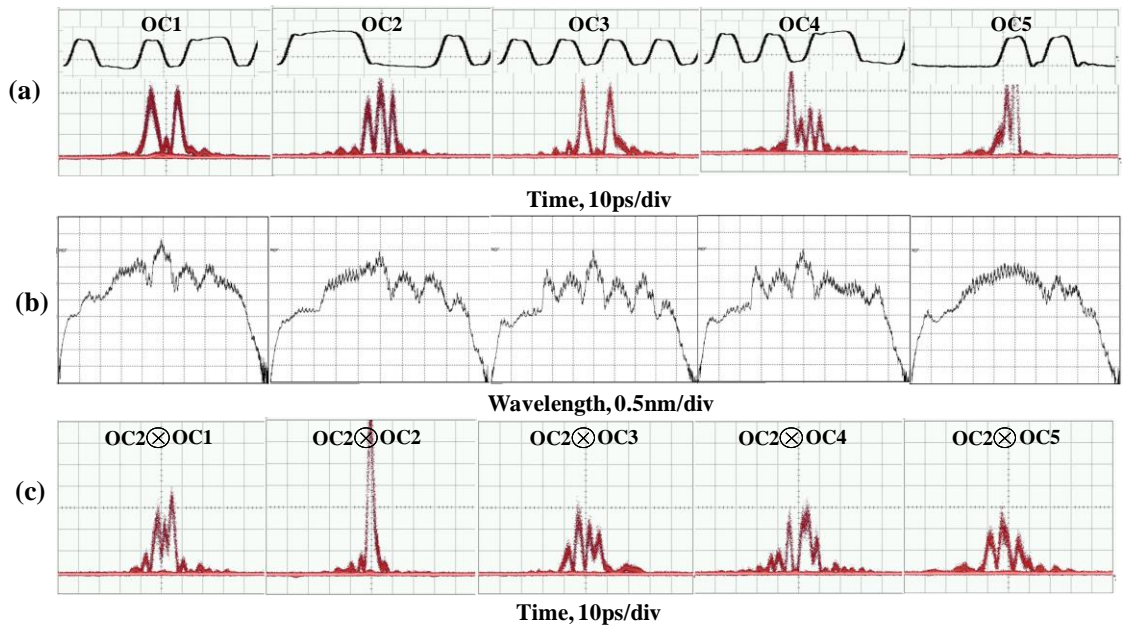


Figure 4.23 (a) Encoded waveform (upper row) and (b) encoded spectrum (middle row) for the five codes; (c) Auto-/cross- correlation signals for OC2 (lower row).

Figure 4.24 shows the procedure to combine the DPSK data with the code hopping sequence bit-by-bit. Firstly, the DPSK data stream is segmented every five bits into a group and mapped onto an existing prime-hop code pattern H1~H4. i.e. the first five bits (11001…) are mapped onto H2 (OC1, OC3, OC5, OC2, OC4). Each Gold code (OC) in the prime-hop code pattern corresponds to one bit in the DPSK data stream. Then, each DPSK data is mixed with its corresponding OC to drive the PM: when the DPSK data is symbol "1", the PM is driven by OC, while if symbol is "0", the PM is driven by $\overline{OC}$, therefore, the first five bits are encoded by OC1, OC3, $\overline{OC5}$, $\overline{OC2}$, OC4 as shown in Fig.4.24 (a). Similarly, the following grouped DPSK data is also encoded by the corresponding prime-hop code pattern (see Fig.4.24 (b)) that is very flexible to

reconfigure according to a look-up table (i.e. H2, H4, H3, H1, H4, H3, H1, H2…) shown in Fig. 4.24 (c). To accurately synchronize the phase pattern and the stretched pulse, an optical delay line is employed before the phase modulator so the code hopping patterns can precisely modulate the phase of the corresponding spectral component for each stretched pulse. After that, another LCFBG with opposite dispersion is used to compress the stretched and phase modulated pulse trains to generate the time domain code hopping sequence encoded SPE signal. A span of single mode fiber and dispersion compensation fiber with total length of 34km and residual dispersion of ~20ps/nm are used for transmission.
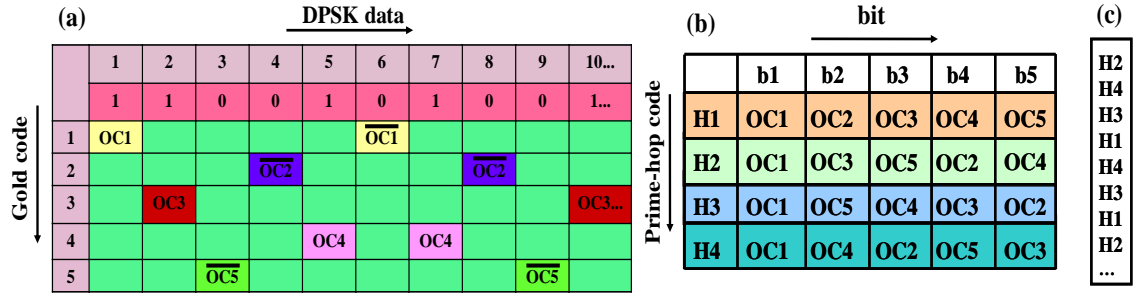


Figure 4.24 (a) DPSK data and corresponding Gold code; (b) Prime-hop code patterns and (c) Look-up table of prime-hop code pattern.

In the decoding section, the identical configuration as the encoding part is used but the PM is driven by the complementary code hopping sequence with all the Gold codes become $\overline{OC}$ (i.e. $\overline{OC1}$, $\overline{OC3}$, $\overline{OC5}$, $\overline{OC2}$, $\overline{OC4}$…). The correctly decoded signal is launched into a 2.5GHz DPSK demodulator followed by a balanced detector to extract the original DPSK data. It is worthy to note that the synchronization requirement between the encoding and decoding stages is rather strict in this experiment, making it very difficult for an eavesdropper to correctly decode and recover the DPSK data without accurate chip-level time coordination even if he knows all the code hopping sequences. The security of our system relies on both the optical codes (physical layer security) and the prime-hop pattern look-up table (electrical layer security). An eavesdropper that is able to sift the code hopping sequence encoded signal firstly has to know the number of Gold codes taken from the code space, then he needs to know the correspondence of the Gold codes with the prime-hop code pattern (i.e.H2: OC1, OC3, OC5, OC2, OC4) as well as the scrambling prime-hop code look-up table (i.e. H2, H4, H3, H1, H4, H3…), and eventually he should correctly decode the code hopping sequence by proper time coordination. Thus, the proposed bit-by-bit code scrambling

scheme can provide higher degree of security and has the potential to realize even one time pad.

A proof-of-principle experiment using four different code hopping sequences CH1~CH4 by combining the optical code patterns with a $2^7$-1 pseudo-random-bit-sequence (PRBS) DPSK data has been carried out. The electrical waveforms of the four code hopping sequences CH1~CH4 are shown in Figure 4.25, from which one can see that the code pattern stream has been scrambled with DPSK data inside it. An auto-correlation pulse stream with high peak power will be generated if the code hopping sequence for decoding matches with that in the encoding, and the two code hopping sequences are accurately synchronized by adjusting the optical delay line before the PM, otherwise a cross-correlation signal with low peak power will be produced.

**CH1**          **CH2**



**CH3**          **CH4**



**Time (500ps/div)**          **Time (500ps/div)**
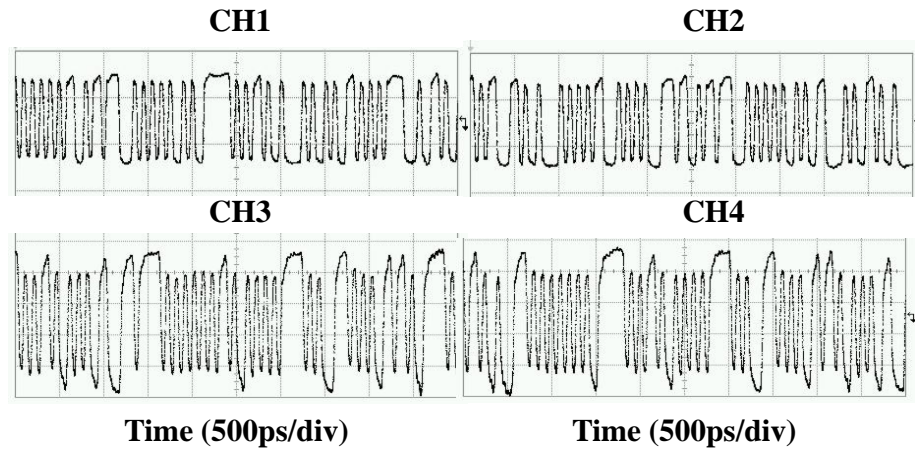
Figure 4.25 Electrical patterns of the four code hopping sequences.

Fig.4.26 (a) shows the correctly decoded optical waveform for CH4 (H3 H4 H1 H2 H2 H4 H1 H3 H2 H3 H1 H4 H4 H3 H2 H1…) measured by a 10GHz optical sampling oscilloscope which exhibits clear eye opening. The electrical pattern and corresponding eye diagram are shown in Fig.4.26 (b) and (c), respectively. Correct pattern (1111110111111001111010111…) and clear eye opening of the DPSK data are obtained as expected. The dense sidelobes in the decoded optical waveform can be attributed to the different decoding performances of the five Gold codes. For comparison, the decoded optical waveform, electrical pattern and eye diagram of the cross-correlation signal are illustrated in Fig.4.26 (d) ~ (f). In contrast, the incorrectly decoded optical waveform behaviors like a noise representing the cross-correlations among all the Gold codes. The electrical pattern is evidently wrong and its corresponding eye diagram is closed, which clearly shows that an eavesdropper cannot break the security of this system without knowledge of the code hopping sequence. The

aperiodic eye diagram for the incorrect decoding is mainly caused by the non-ideal triggering in the measurement. Even though the eavesdropper may get an obscure eye diagram due to the limited code length in the experiment as is shown in Fig 4.26 (f), he still cannot recover the correct data pattern. Fig.4.26 (g) shows the auto-/cross-correlation trace measured by an auto-correlator with a maximum scan range of 60ps, from which one can see that the peak intensity of the correctly decoded signal is slightly lower than that of no encoding/decoding due to the discrepancy of the code transition generated from the two PPGs and non-ideal transmission dispersion compensation, but it is twice higher than that of the incorrectly decoded signals. The measured BER performance after transmission for the correctly decoded signal is shown in Fig. 4.26 (h). Error-free transmission has been achieved for all the four code hopping sequences. Note that in the absence of optical en/decoding, an eavesdropper could easily break the DPSK data security by simply using a 2.5GHz DPSK demodulator and the measured



Figure 4.26 (a) Correctly decoded optical waveform, (b) correct electrical pattern and (c) correct eye diagram. The decoded waveform, electrical pattern and eye diagram of the cross-correlation signal are shown in (d) ~ (f), respectively. (g) Auto-/cross-correlation signals measured by an auto-correlator for CH4; (h) BER performances.

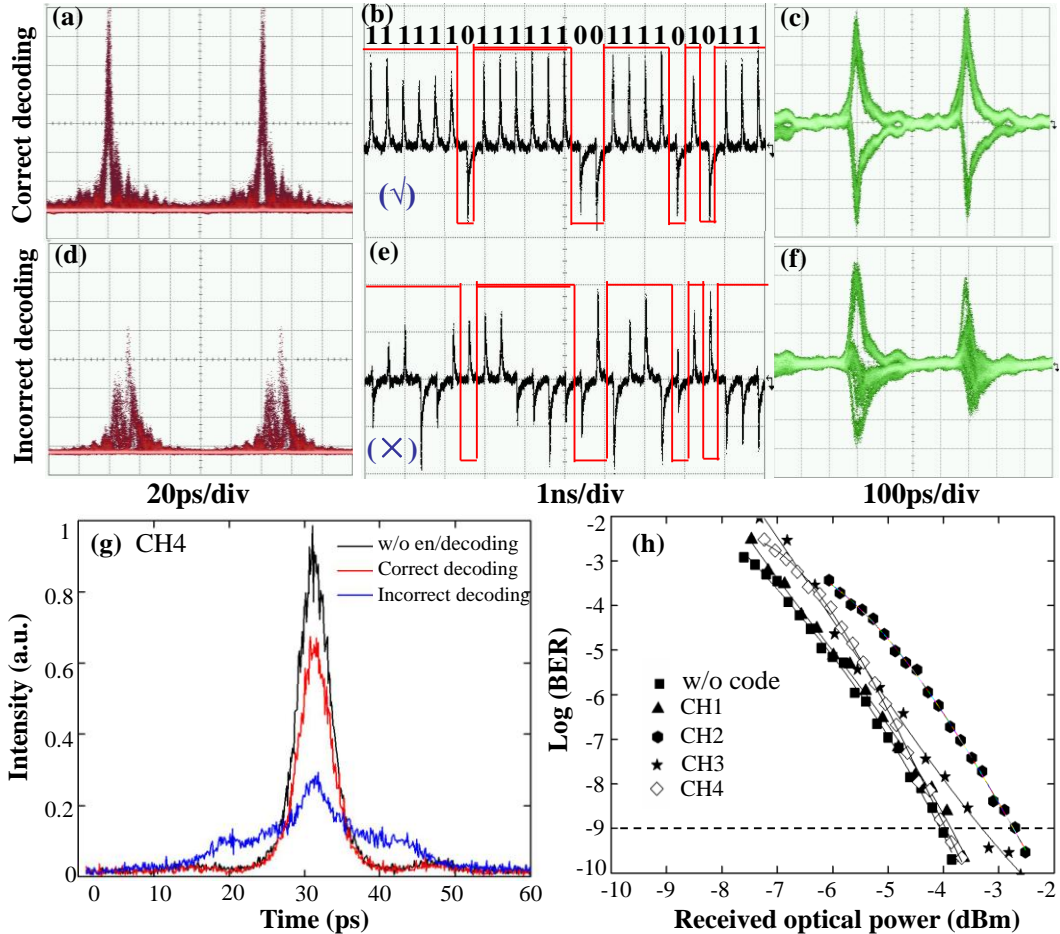BER is also shown in Fig.4.26 (h). Compared to the case of without en/decoding, the average power penalty for the four code hopping sequences is ~0.6dB due to the non-ideal decoding. As for the cross-correlation signals, no BER can be measured, indicating significant security enhancement using the bit-by-bit optical code scrambling technique based on the time domain SPE/SPD scheme.

### 4.5.3 Security analysis and application for CSK modulation

In this section, the data confidentiality of the proposed bit-by-bit code scrambling/ DPSK data modulation scheme is analyzed. The security analysis in this part is also contributed by another student Xuhua Wang in the same group. Let's define Key Length ($L$) as the length of the hopping pattern and Code Number ($n$) as the number of optical codes used in the code hopping pattern, respectively. In the example shown in Figure 4.27, $L$=12, $n$=6. Assuming that a sophisticated eavesdropper knows the $n$ in the system, thus the confidentiality of user data is mainly guaranteed by the $L$. The cardinality of the hopping patterns is given by $C$:

$$A = P_L^n \bullet n^{L-n}/C_{L-1}^{n-1} \quad (L \geq n) \tag{6.1}$$

| User Data | 1 | 0 | 1 | 0 | 1 | 1 | 0 | 0 | 1 | 0 | 1 | 1 | 1 | 0 | 1 | …… |
|---|---|---|---|---|---|---|---|---|---|---|---|---|---|---|---|---|
| Hopping Pattern | OC1 | $\overline{OC3}$ | OC4 | $\overline{OC1}$ | OC6 | OC5 | $\overline{OC2}$ | OC4 | OC6 | $\overline{OC5}$ | OC3 | OC2 | OC1 | $\overline{OC3}$ | OC4 | …… |

Key Length: 12          Code Number: 6

Figure 4.27 An example for definition of Key Length and Code Number.

Here $P_L^n = L!/(L-n)!$ denotes the permutation of $L$ with $n$ elements, $C_{L-1}^{n-1}$ is the combination of $L$-1 with $n$-1 elements. The average number of trials to break the hopping pattern by brute-force attack is $A/2$.

To compare with the traditional software symmetric encryption system [110], the term effective key length ($L_{eff}$) is adopted, which is defined as $L_{eff}=\log_2 A$ [111]. The effective key length of the proposed scheme is given by

$$L_{eff} = Log_2(P_L^n \bullet n^{L-n}/C_{L-1}^{n-1}) \quad (L \geq n) \tag{6.2}$$

In practice, a system encrypted by 128-bit symmetric key is nearly unbreakable by brute-force attack, which is considered from time, cost and thermodynamic limitations [110]. Currently, both Advanced Encryption Standard (AES) and Route Coloniale 4 (RC4), which are widely used in Secure Sockets Layer (SSL) and Wired Equivalent Privacy (WEP), adopted 128-bit key as a standard [110]. So here the 128-bit symmetric key is taken as a reference to compare the level of computational security of the
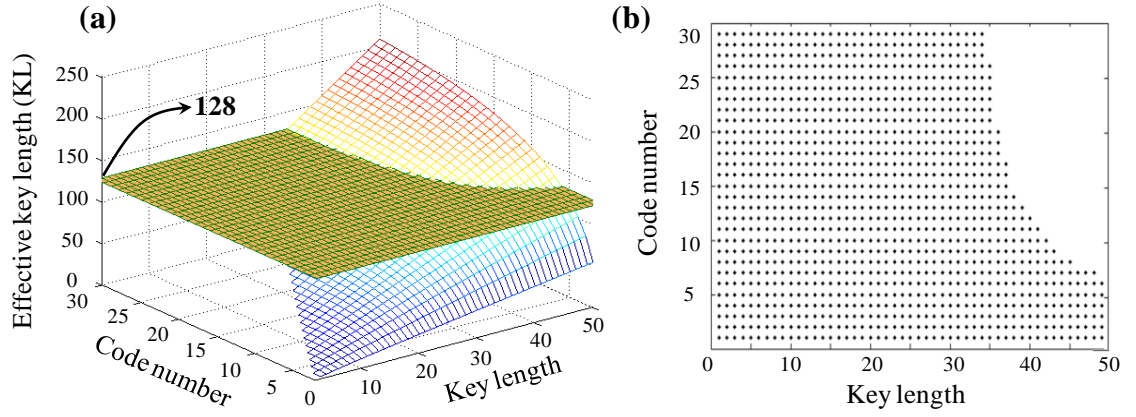
Figure 4.28 (a) The increasing trend of effective key length ($L_{eff}$) versus code number ($n$) and the key length ($L$); (b) Region of the $n$ and $L$ for higher security level than 128-bit symmetric key.

proposed scheme. Figure 4.28 (a) shows the dependence of $L_{eff}$ with the code number $n$ and the key length $L$. The plane of $L_{eff}$ =128 is shown here as a reference level. By increasing the key length $L$ or the code number $n$, $L_{eff}$ can be greater than the reference level, showing significant security improvement based on the proposed scheme. Figure 4.28 (b) shows the conditions when $L_{eff}$ =128 (which means that the security level equals to 128-bit symmetric key system). In the marked area, the $L_{eff}$ is lower than 128, while in the blank area, the security level is higher than 128. The shortest key length $L$ is around 35 to achieve the reference security level.

Compared with the traditional symmetric-key encryption, the proposed scheme is in the physical (optical) layer and is totally transparent to upper-layer protocol/contents in the communication system. The ultrafast, real-time all-optical signal processing techniques are also huge barriers for the eavesdropper to apply any traditional cryptanalysis method to break the security of the proposed scheme. The eavesdropper must take much more time than doing the same process in electrical domain even when performing the simplest brute-force attack. With the great flexibility provided by the proposed scheme, the code can be rapidly reconfigured to enlarge $L$ to a magnitude as same as the data length. If the $L$ equals the data length, the so-called "perfect secrecy" (the same security level as "one time pad") can be achieved. Therefore, the proposed bit-by-bit code scrambling/DPSK data modulation technique can provide a high security level, and exhibits the potential to provide unconditional transmission security and realize even the perfect secrecy.

It should be noted that the proposed scheme could also be used for improving the security of CSK data modulation. As mentioned in Section 3.5 and 3.6, in conventional CSK data modulation scheme, the data pulses are split into two paths and encoded by

two separate optical encoders with fixed code patterns. Although it is robust to energy detector attack because every bit has similar energy, an eavesdropper can easily intercept the data by either performing DPSK demodulation [33] or differential detection attack [112]. Figure 4.29 shows the application of the bit-by-bit code scrambling technique in a CSK data modulation system for improving the security. As can be seen, after the optical switch, the stretched data pulses (100101) are split into two paths according to the data pattern "1" or "0", then a phase modulator driven by code hopping (CH) patterns ("OC1 OC3 OC5…" for "1" or "OC2 OC4 OC6" for "0") individually is used to perform time domain spectral phase encoding. After compressing by the opposite dispersive device, the scrambled code will be applied into the encoded signal as "OC1 OC2 OC4 OC3 OC6 OC5". At the receiver side, the complementary scrambled code should be applied for decoding and the CSK data can be recovered after balanced detection. However, it is impossible for an eavesdropper to extract the CSK data from the encoded signal by only using a DPSK demodulator, in which case only noise-like signal will be obtained, showing potential significant security improvement for even CSK data. Compared with the bit-by-bit code scrambling scheme with DSPK data modulation, the main disadvantage of this CSK modulation scheme is that it requires additional optical components, such as optical switch, phase modulator, dispersive element, *etc*, but it does provide an attractive approach for improving the security of CSK data modulation.
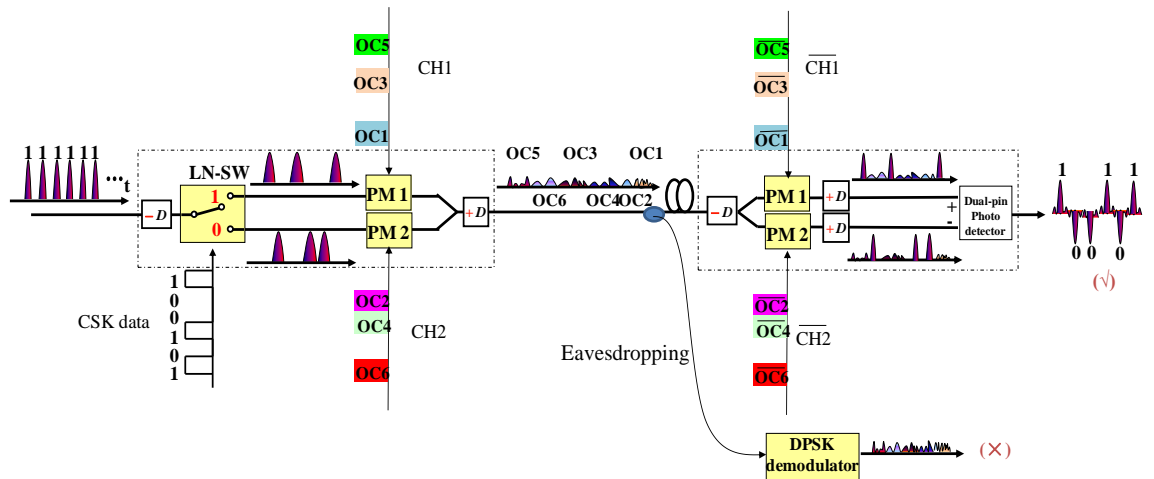


Figure 4.29 Application of proposed bit-by-bit code scrambling scheme for CSK modulation.

## 4.6   Summary

In this chapter, a symmetric time domain spectral phase encoding and decoding scheme with similar configurations which include a pair of dispersive devices and phase

modulator is proposed and demonstrated for simplifying the OCDMA system architecture and improving the coding performance. Based on this scheme, an advanced modulation scheme for simultaneous time domain spectral phase encoding and DPSK data modulation using a single phase modulator is demonstrated. The effect of code transition, dispersion mismatch on the coding performance is also investigated and verified by the experiment. A 2-D coherent OCDMA system that can generate wavelength hopping and spectral phase encoding pattern with improved code cardinality using the time domain SPE/SPD scheme is also presented. Finally, for the first time, a novel bit-by-bit optical code scrambling technique that can perform bit-by-bit optical code generation and DPSK data modulation for enhancing the data security has been proposed and demonstrated. 2.5Gb/s DPSK data has been encoded by five 20-Gb/s, 8-chip optical code patterns which are scrambled by prime-hopping pattern in the experiment, and then decoded and successfully transmitted over 34km with error free. The proposed technique could significantly improve the security of the time domain spectral phase encoded OCDMA signal, exhibiting the potential to realize even "one time pad" with perfect secrecy. It is even possible to apply the bit-by-bit encoding technique in a CSK data modulation scheme to enhance the security of CSK data. In the symmetric time domain SPE/SPD scheme, although individual dispersive elements and phase modulator have been used for the demonstrations which may seem bulky, it is potentially possible to integrate these devices in an optical waveguide to reduce the size of the whole setup and to enable reconfigurable optical en/decoding.

# CHAPTER 5

# Secure transmission of time domain spectral phase encoded OCDMA signal over public WDM network

## 5.1 Optical steganography

With the rapid development of today's communication networks, providing information security based on ultrafast optical signal processing becomes increasingly important and many approaches have been proposed [92-99]. As one of the attractive approaches, optical encryption that allows the signal to be encrypted with low latency has been previously widely studied [113-116]. In optical encryption, it is very difficult for the eavesdropper to decrypt the signal without the encryption key. The OCDMA technique can be considered as a kind of the optical encryption technologies to provide intrinsic data security. Recently, another kind of secure approach "optical steganography" that can provide an additional layer of privacy by hiding the very existence of data transmission underneath the public channel has been proposed and studied [117-120]. While the goal of optical encryption is to conceal the content of the information, the goal of information hiding or optical steganography is to conceal their existence, and therefore, optical steganography can be complementary to the optical encryption for improving information security [120].

The optical steganography technique has been previously implemented in optical communication for data hiding based on group velocity dispersion (GVD), a phenomenon that the velocity of light depends on its frequency [117-120]. Figure 5.1 shows the basic principle of optical steganography [119-120]. When an optical pulse passes through a highly dispersive medium, the differences of the transmission speed of various frequency components of the pulse result in a temporal spreading of the pulse. By using chromatic dispersion (-D) to stretch the stealth signal such that its peak amplitude is reduced to a very low level comparable to the system noise, the stealth signal can be concealed underneath an existing public WDM channel with a high amplitude to make the eavesdropper unaware of its existence, as shown in Fig.5.1 (a). For the restoration of the stealth signal, the combined stealth signal and public signal is firstly temporally compressed by another dispersive element with an equal but opposite

(a) Signal hiding

Temporal spreading

-D

Stealth signal

Public signal

Stealth signal hidden into public channel

+

(b) Signal restoration

Temporal compressing

+D

PD

Optical thresholder

Public signal detection

Extracted stealth signal
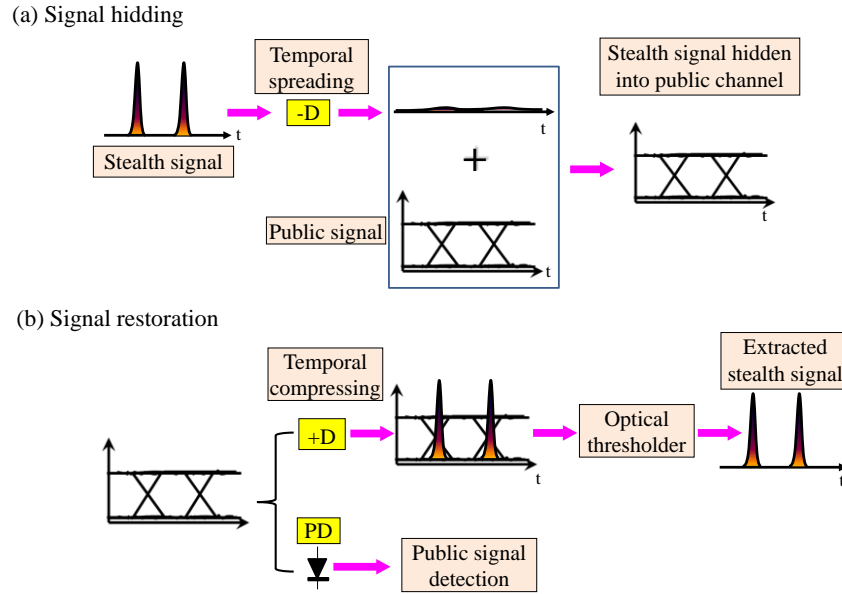
Figure 5.1 Schematic illustration of (a) optical signal hiding and (b) restoration in steganography based on group velcocity dispersion.

amount of dispersion (+D), such that the stealth signal appears above the public signal. As the peak amplitude of the stealth signal is higher than the public channel due to its short-pulse nature, the stealth signal can be retrieved from the public channel through a proper optical thresholder, which can be seen from Fig.5.1 (b). While for the detection of the public signal, a photo-diode can be directly used for power detection as the stretched low amplitude stealth signal has no obvious influence on the public signal. Since the optical steganography can hide the stealth signal underneath a public signal, making it imperceptible in the public channel, it could provide additional physical layer security in the optical network. It is not easy for an eavesdropper to restore the stealth signal from the public channel without the knowledge of the spreading function. Transmission of 622-Mb/s RZ-OOK stealth signal over a 10-Gb/s public WDM channel by using a large amount of group velocity dispersion provided by optical dispersive fiber has been demonstrated [119].

However, the GVD based approach is still vulnerable to a sophisticated eavesdropper's attack because he can try to use a tunable dispersion compensation module to compress the stretched pulse and then extract the confidential data. In Chapter 4, a symmetric time domain SPE/SPD scheme using dispersive components and phase modulator for enhancing the reconfigurability and security of an OCDMA system has been proposed and demonstrated. In such a system, an OC is applied to the phase modulator to perform time domain spectral phase encoding. If the OC in the decoder is unmatched with that in the encoder, only a cross-correlation signal with low-

level peak amplitude is generated and the original data cannot be fully recovered. By combining the time domain spectral phase en/decoding technique and the GVD based optical steganography, the difficulty for an eavesdropper to attack the system by simply using a dispersion compensation module would be increased, and thus the OCDMA system security can be significantly enhanced, as will be discussed in this chapter.

## 5.2 Time domain SPE encoded OOK-OCDMA signal transmission over public WDM system

In this section, an experimental demonstration of the security enhancement for an OCDMA signal by combining the time domain SPE/SPD technique and optical steganography is presented. Figure 5.2 shows the experimental setup of the proposed scheme. In the experiment, the public WDM signal is generated by a continuous-wave (CW) laser at 1550.24nm followed by an intensity modulator driven by $2^7$-1 PRBS-OOK data operating at 10Gb/s. In the stealth channel, a mode-locked laser diode with center wavelength of 1550.28nm is used to generate a series of nearly ~4ps optical pulse trains with a repetition rate of 10GHz. An IM driven by $2^7$-1 PRBS is used to down convert the optical pulse repetition rate and generate the 1.25-Gb/s OOK data. The modulated pulse trains are then temporally broadened in the whole bit period of 800ps through GVD by using a LCFBG with dispersion of -160ps/nm and bandwidth of ~4.7nm for stealth channel hiding and optical encoding. Figure 5.3 (a) and (b) shows the spectrum and waveform of the broadened pulse after the LCFBG. Different spectral components spread into different positions in time domain, thus the broadened waveform has same temporal profile as its spectrum. The broadened pulse is then



Figure 5.2 Experimental setup of the stealth time domain encoded OOK-OCDMA signal transmission over a public WDM system.
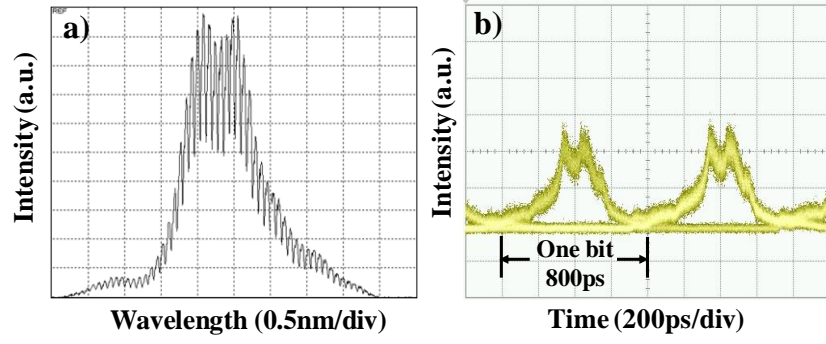
Figure 5.3 (a) Spectrum and (b) waveform of the broadened stealth OCDMA signal.

directed into a phase modulator driven by 32-chip, 40-Gchip/s optical code patterns to generate the time domain spectral phase encoded stealth OCDMA signal. An optical delay line is used to guarantee the optical code patterns precisely modulate the phase of the desired spectral component of the broadened pulse. Four different Gold codes with 31chips plus a zero are used in the experiment: OC1: 10001100001111001111010101001110, OC2: 1110101100110 0011011110111111000, OC3: 0010010100101011 0010110010010000 and OC4: 10111001000111100000111001000110, respectively. Figure 5.4 shows the measured encoded waveforms, encoded spectra and the corresponding decoded auto-/cross correlation signals for OC1-OC4, respectively. It can be seen that the encoded waveforms have been spread in the time domain exhibiting as a noise with very low peak power by the encoding. The encoded spectra also have different profiles according to the OCs. After applying the correct OCs in the decoding
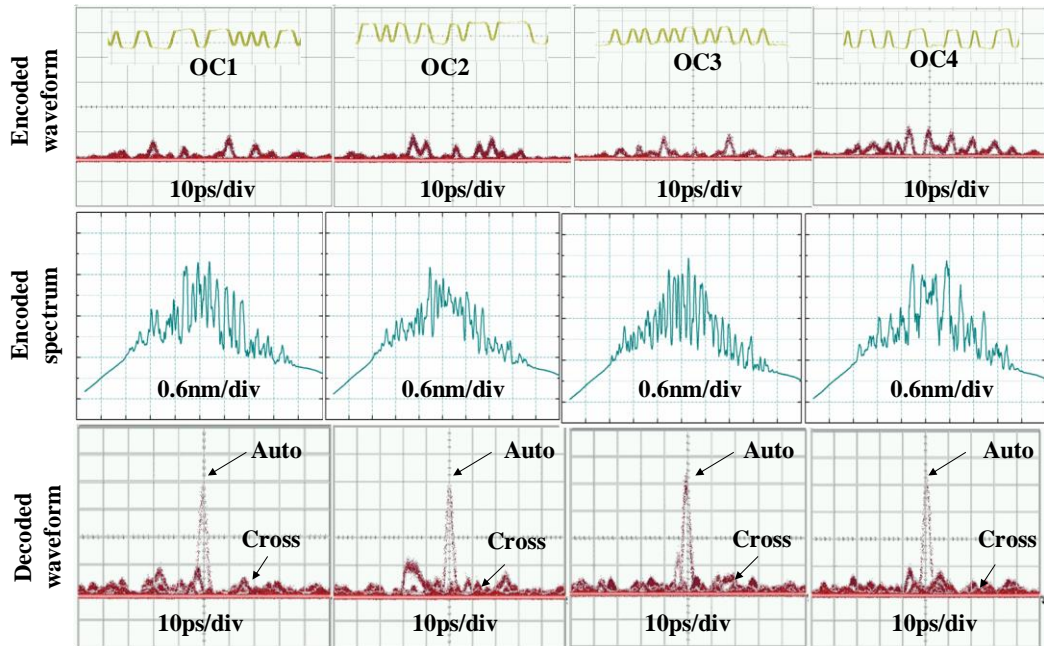


Figure 5.4 Encoded waveform (upper row), encoded spectrum (middle row) and auto-/cross-correlation performance (lower row) for four different OCs.

side, auto-correlation signals with high peak power can be generated while for the incorrect OC, only cross-correlation signals with lower peak power are generated, as can be seen from the lower trace in Fig.5.4. The P/C can reach up to ~5 due to the relatively long code length of 32. After the spectral phase encoding, the generated stealth signal is combined with the WDM signal by a 3-dB coupler and directed into a span of 34-km SMF and DCF for transmission. Amplified spontaneous emission (ASE) noise from a separate erbium doped fiber amplifier (EDFA) has been launched into the system to emulate the system noise in a real all-optical network.

At the receiver side, a 3-dB optical coupler is used to split the public and stealth signal into two portions. For the public channel detection, an optical BPF with 3-dB BW of 1nm followed by a conventional energy detector is used. While for the stealth channel detection, the received signal is launched into the second phase modulator driven by the complementary code $\overline{OC}$. Synchronization between the encoding and decoding is highly required in order to correctly decode the stealth signal. Even if the stealth signal is revealed, it is still very difficult for an eavesdropper to correctly recover the stealth OCDMA signal without knowledge of the code used in the stealth channel and accurate time coordination. After that, another LCFBG with opposite dispersion is used to compress the correctly decoded signal, such that the stealth channel appears above the public channel. Finally, a super-continuum (SC)-generation-based optical thresholder [74] composed of a preamplifier EDFA and dispersion-flattened-fiber (DFF) followed by a 5-nm BPF is used to extract the stealth OCDMA signal from the public WDM network.

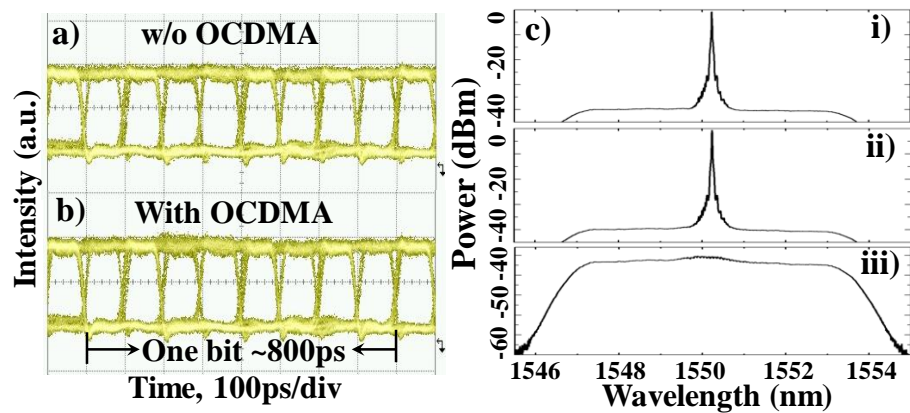In the experiment, the stealth OCDMA signal can be temporally hidden underneath



Figure 5.5 Eye diagram of public WDM channel without (a) and with (b) stealth OCDMA signal; (c) spectrum of public WDM channel without (i) and with (ii) OCDMA signal and (iii) spectrum of stealth channel with ASE noise.

the WDM channel by properly adjusting the optical attenuator. The average power ratio ($P_r$) of the public channel and stealth channel is about 13dB. The eye diagrams of the public WDM channel without and with the stealth OCDMA signal are shown in Figure 5.5 (a) and (b), respectively. The resemblance of the two eye diagrams indicates that the stealth channel has been hidden into the public channel. The spectra of the public WDM channel without and with OCDMA signal are shown in Fig. 5.5 (c) (i) and (ii), respectively. The two spectra are indistinguishable as well. The spectrum of the stealth channel is shown in Fig.5.5 (c) (iii). The peak power of the spectrum for the stealth channel is approximately 40dB lower than that of the public channel.

In the stealth channel detection, the public WDM channel will also be phase-modulated and then temporally broadened by the LCFBG, and as a result, the public signal appears like a noise in the time domain. Figure 5.6 (a) shows the correctly decoded signal for OC2 with WDM signal. The stealth OCDMA signal has been recovered above the public WDM signal. The extracted OCDMA signal after the SC based optical thresholder for the correctly decoded signal (a) is shown in Fig.5.6 (b). The public WDM signal has been significantly suppressed by the optical thresholding. Fig.5.6(c) shows the waveform of the incorrectly decoded signal with public WDM signal. In contrast, the incorrectly decoded signal has a low signal-to-background ratio and cannot be extracted from the public channel. The decoding performance is related to the bandwidth (BW) of the input spectrum before the LCFBG and residual dispersion (RD) during transmission. Fig.5.6 (d) shows the simulated result of the RD and BW effect on the peak-to-wing ratio and peak intensity of the decoded waveform for
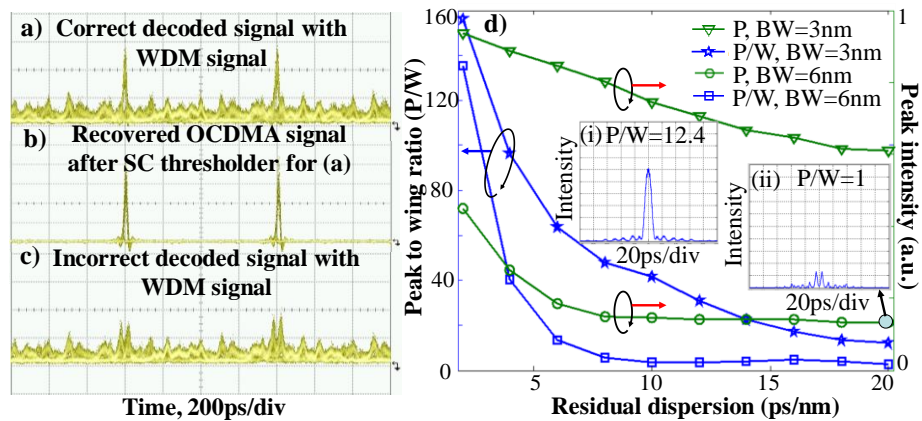


Figure 5.6 (a) Correct decoded signal with WDM channel; (b) recovered stealth signal after thresholder; (c) incorrect decoded signal with WDM channel; and (d) peak-to-wing ratio (left) and peak intensity (right) of decoded waveform versus RD for different BW. Insets (i) and (ii) are the decoded waveforms for BW=3nm and BW=6nm with RD=20ps/nm.

OC2. As the RD increases, the high bandwidth case (BW=6nm) will significantly degrade the decoding performance with lower P/W and P compared to that of low bandwidth (BW=3nm). The insets (i) and (ii) show the decoded waveform for BW=3nm and 6nm with RD=20ps/nm, from which one can see the decoding is rather poor for BW=6nm, while for the BW=3nm, P/W and P can still reach up to 12.4 and 0.6 for RD=20ps/nm, respectively. High residual dispersion can be tolerated in the case of low bandwidth. In the experiment, the LCFBG functions as a dispersive device as well as a bandpass filter to cut the input spectrum into ~4.7nm to enable the decoding for an RD of ~20ps/nm that exists in the system.

The measured bit-error-rate of the stealth OCDMA signal is shown in Figure 5.7 (a). Error-free transmission has been achieved for the stealth channel with four different codes. In the absence of optical en/decoding, there is only ~1-dB power penalty when the WDM signal is introduced. The optical en/decoding induces ~2-dB power penalty due to the non-ideal decoding. The discrepancy of BER performance for different OCs can be ascribed to the difference of decoding performance that will be affected by the code transition, residual dispersion and so on. The measured BER for the public WDM channel with different power ratio ($P_r$) is shown in Figure 5.7 (b). The effect of OCDMA signal on the public channel is very small, and less than 1-dB power penalty is obtained when varying $Pr$ between 10dB to 15dB. To investigate the influence of the
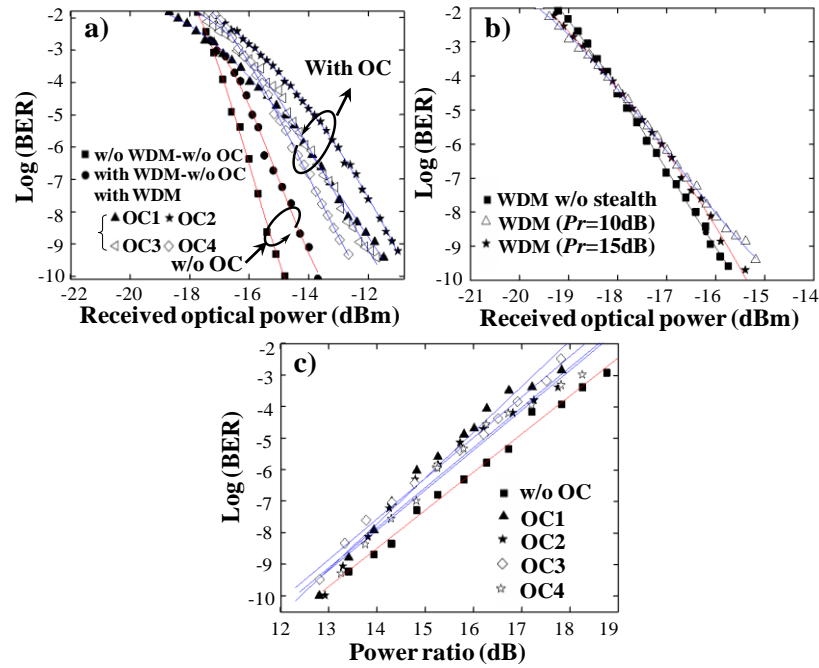


Figure 5.7 (a) BER for stealth OCDMA channel with and without OC; (b) BER for public WDM channel; and (c) BER versus power ratio for stealth channel.

public channel on the stealth channel, the BER performance of stealth channel for different $Pr$ is also measured with a received optical power of around -12dBm at BER of $10^{-9}$, as shown in Fig.5.7 (c). As $Pr$ increases from 13dB to 19dB, the BER of the stealth channel gradually degrade from $10^{-9}$ to $10^{-2}$. By further compensating the RD and utilizing identical phase modulators in both the encoding and decoding sides to improve the decoding performance, higher power ratio can be supported. The proposed technique provides an effective and attractive approach for improving the security of time domain spectral phase encoded OOK-OCDMA signal by optical encoding and overlaying it onto an existing public WDM network.

## 5.3 Transparent transmission of time domain SPE encoded DPSK-OCDMA signal over DWDM network

### 5.3.1 Transparent OCDMA overlay DWDM network architecture

Besides providing network security, to meet the explosive growing capacity demand of the fiber-optic network, efficient utilization of the limited bandwidth is also particularly important. Dense WDM (DWDM) can efficiently exploit the bandwidth and has been widely deployed in current fiber-optic infrastructure. In the DWDM network, the data is transmitted over multiple carrier wavelengths, which are kept far apart to avoid the crosstalk between different channels. The method of overlaying the OCDMA channel on an existing public DWDM network may be a prospective solution to improve both the system security and bandwidth efficiency. In the OCDMA overlay DWDM system, the usable channels can be significantly expanded in two dimensions: wavelength and code. It is possible to make full use of the broadband spectrum between the DWDM grids through spectrally overlaying the OCDMA channel on the public DWDM network, and simultaneously process the OCDMA and DWDM signals during the transmission by using the same EDFA to increase the bandwidth efficiency, system flexibility as well as energy efficiency. Efforts have already been made to demonstrate this capability by overlaying the OCDMA channel on a public DWDM channel [121-124]. Meanwhile, the OCDMA overlay DWDM system can also provide additional level of security that can supplement the optical encoding.

In the last section, it has been demonstrated that one can spectrally overlay a broadband, low power density OCDMA signal on a public WDM channel to avoid the attention of the OCDMA channel and improve the data confidentiality by combining the

chromatic dispersion based approach and the time domain spectral phase encoding technique. Because the spectrum of the OCDMA and WDM signal occupies the same spectral band, the main issue in the network is to correctly recover the secure OCDMA data from the hybrid signals. Optical thresholding [119] and time gating techniques [121] have been employed to suppress the interference of the WDM signal in the hybrid system. To simplify the OCDMA detection, a spectral notch filter has been proposed to directly reject the public channel interference in a temporal phase encoding time spreading (TS) OCDMA system [125]. Transmission of a stealth amplitude modulated signal over a public DPSK data link has also been demonstrated by using a spectral notch filter [126]. However, up to now, only OOK data modulation format for the stealth channel has been reported in the OCDMA overlay public WDM system, which may not satisfy the indispensible requirement of network transparency for future all-optical network. A transparent all-optical network should be able to support versatile advanced optical modulation formats, bit-rate and protocols [127]. While the network transparency can enable a low cost, power efficient, highly flexible and scalable all-optical network, the implementation of the OCDMA channel over the public DWDM network should also be compatible with this transparent environment by supporting various modulation formats, optical en/decoding schemes, and detecting the OCDMA signal without inducing any additional architecture requirement and impairment of the existing public channel.

In this section, a transparent OCDMA overlay public DWDM optical network architecture is proposed and demonstrated by transmission of a secure 2.5-Gb/s time domain spectral phase encoded OCDMA signal with DPSK modulation format over a two-channel 10-Gb/s DWDM system without any complicated optical thresholding/time gating techniques. The OCDMA channel has been secured by both the time domain spectral phase encoding and the public DWDM channels. A fiber Bragg grating based spectral notch filter is employed to enable the network transparency. Error-free transmission of the 2.5-Gb/s DPSK-OCDMA signal and the two-channel 10-Gb/s DWDM signal over 49km fiber has been successfully achieved.

Figure 5.8 shows the schematic diagram of the proposed OCDMA overlay public DWDM network. In this architecture, the multi-channel DWDM signals are generated individually by different laser diodes and multiplexed by the optical multiplexer. Whereas the secure OCDMA signal, encoded by different optical encoder for each channel and combined by a power combiner, is injected into the public network together
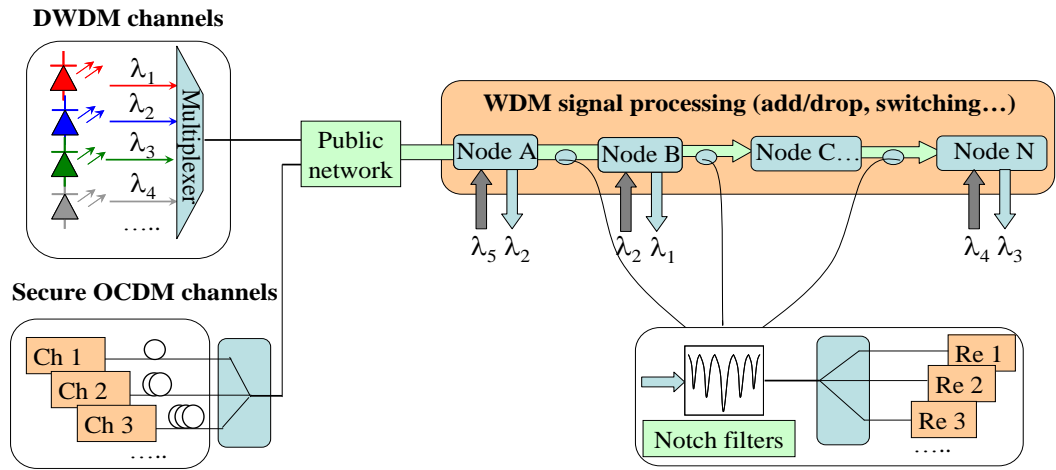
Figure 5.8 Proposed transparent OCDMA overlay public DWDM network architecture.

with the DWDM signals. As the OCDMA signal manifests itself as a noise-like signal after encoding, security enhancement can be achieved via spectrally overlaying the OCDMA channel onto the public multi-channel DWDM network. With the introduction of the high power public DWDM channels, the difficulty for an eavesdropper to aware and intercept the secure OCDMA channel will be increased.

Compared with the previous architectures, which need complicated optical thresholding or time gating [124, 126] to suppress the interferences arising from the public channel and recover the OCDMA signal before any DWDM signal processing (such as add-drop, wavelength conversion, optical switching as well as regeneration), the proposed scheme enables extraction of the OCDMA signal from the spectrally overlapped hybrid OCDMA/DWDM signals by using a low cost, passive spectral notch filter. After inserting the passive spectral notch filer with high notch depth into the public network, all the DWDM channels can be rejected and directly transmit through the notch filters with negligible deterioration, while the encoded OCDMA signal will be dropped down for the following decoding and detection. Thanks to the adoption of spectral notch filtering, this architecture not only excludes the utilization of optical thresholding/time gating techniques, but also can support versatile advanced modulation formats OOK, DPSK and differential-quadrature-phase-shift-keying (DQPSK), etc. It can also enable various optical encoding schemes and detection of the OCDMA signal at any point (before or after each network node) during its transmission throughout the whole network. Because the spectral notch filter can directly reject the DWDM interference, a high power ratio between the DWDM and OCDMA signal can be anticipated while keeping excellent system performance. The existence and architecture of the public DWDM channel is completely independent of the secure OCDMA

channel, and thus, the proposed OCDMA overlay DWDM network with various modulation formats can be fully transparent and enable secure OCDMA transmission.

## 5.3.2 Experimental demonstration and results

Figure 5.9 illustrates the experimental setup to demonstrate the proposed hybrid network, in which the top left is the WDM transmitter consists of two-channel non return-to-zero (NRZ)-OOK signals which are generated by two independent CW lasers spectrally centered at 1550.52nm and 1551.32nm, and then modulated by an intensity modulator driven by 10-Gb/s, PRBS of length $2^{31}$-1. To generate the 2.5-Gb/s OCDMA signal, an active mode-locked laser (MLL) producing nearly transform-limited 2.8ps pulses at repetition rate of 10-GHz and spectrally centered at 1549.9nm is used as the laser source. The pulse train generated from the MLL is directed into an EDFA and a piece of 2km dispersion-flattened-fiber for super-continuum generation in order to broaden the spectrum. The source repetition rate is then converted to 2.5GHz by another intensity modulator. After that, a LCFBG centered at 1550nm is used to stretch the input pulse for spectral phase encoding. The 10-dB bandwidth and chromatic dispersion of the LCFBG are around 4.7nm and -80ps/nm, respectively. Each bit of the original pulse will be stretched into ~376ps time duration after the LCFBG. A single high speed phase modulator driven by a pulse pattern generator is employed to simultaneous generate the 2.5-Gb/s DPSK data mixed with 8-chip, 20-Gb/s optical code. An optical delay line is used before the phase modulator to temporally align the spectral phase code and the corresponding spectral component for each stretched pulse. After that, the OCDMA signal is combined with the DWDM signal via a 3-dB coupler and then launched into a span of 49km dispersion compensated transmission fiber.
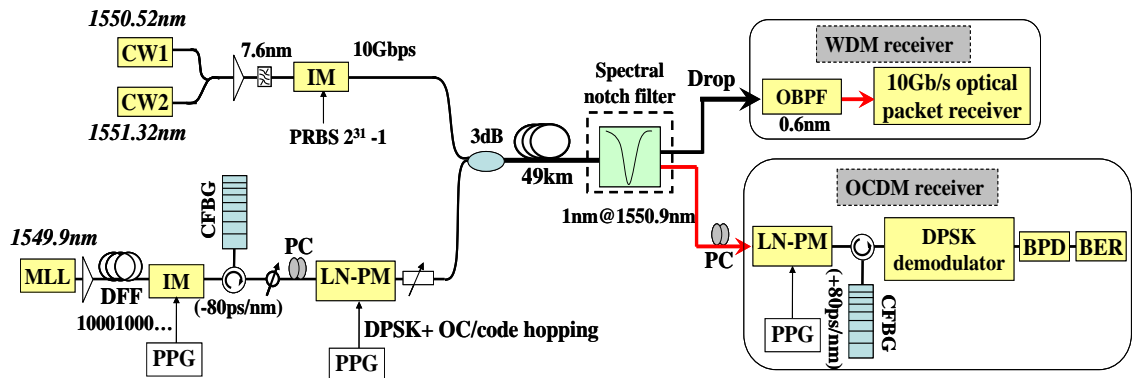


Figure 5.9 Experimental setup of the proposed time domain SPE/SPD OCDMA system spectrally overlaid on a two-channel DWDM network.

At the receiver side, a fiber Bragg grating (FBG) based spectral notch filter is used to emulate the transparent optical network. The reflection response of the notch filter is shown in Figure 5.10, from which it can be seen that the center wavelength and 10-dB bandwidth are 1550.9nm and 1nm, respectively. The two DWDM signals can be simultaneously dropped from the reflection port of the notch filter, distinguished by a 0.6nm optical bandpass filter and finally detected by a 10-Gb/s optical packet receiver which is composed of a photo-detector, an electrical amplifier and a 10-Gb/s clock and data recovery circuit. After the drop operation of the DWDM signals, the OCDMA signal output from the transmission port of the notch filter still remains, and can be decoded using the similar configuration as the encoding part but with another PM driven by only the complementary code pattern sequence. Another LCFBG with opposite dispersion of +80ps/nm is used to compress the spectrally phase decoded pulse to recover the original data. The decoded signal is then directed into a 2.5-Gb/s DPSK demodulator followed by a balanced photo-detector (BPD) and a BER tester to measure the bit-error-rate.
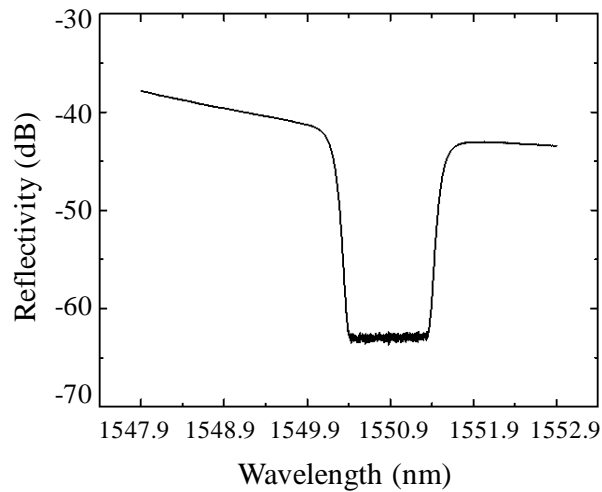


Figure 5.10 Reflection spectrum of the FBG based spectral notch filter.

To investigate the signal distortion after decoding and resultant performance degradation due to the introduction of the spectral notch filter in the encoded OCDMA signal, the effect of notch filtering on the spectrum and recovered waveform has been simulated using a commercial available software package optisystem 7.0. Figure 5.11 (a)~(d) show the encoded spectra after four different notch filters with rectangular profile: (i) without filter; (ii) one filter with center wavelength of 1550.9nm and bandwidth of 1nm (used in this experiment); (iii) five 0.2nm bandwidth (BW) filters in accordance with the DWDM ITU-T grid with channel spacing (CS) of 0.8nm, and (iv) fifteen 0.2nm BW filters for more dense WDM with the CS of 0.3nm. The
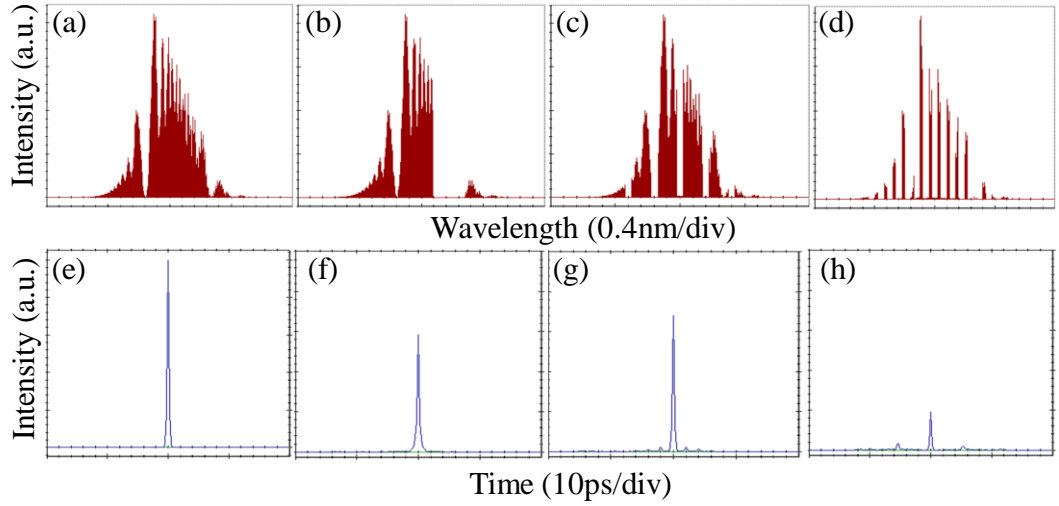
Figure 5.11 (a) ~ (d) and (e) ~ (h) are the encoded spectrums and corresponding decoded waveforms with four different kinds of notch filters.

corresponding waveforms after decoding are shown in Fig. 5.11 (e)~(h), from which one can see that compared to the case of without filter, the 1nm bandwidth filter has cut nearly one third of the spectrum and the peak intensity of the recovered pulse has been degraded to ~60% (see fig. 5.11 (f)). For the case (iii) with seven filters and channel spacing of 100GHz, the peak intensity of the decoded pulse can reach up to the similar level as case (ii), indicating that the notch filter used in this experiment actually emulate seven DWDM channels. While for multiple filters in case (iv), the maximum intensity of the decoded pulse is ~20% of the ideal one. It is worth to note from Fig.5.11 (f) ~ (h) that the auto-correlation signal after notch filtering still exhibit as an optical pulse but it has some small sidelobes, inducing the phase noise in the DPSK signal and the degradation of the BER performance. Figure 5.12 depicts the effect of filter bandwidth (centered at 1550.9nm) on the decoding and BER performance for three different code
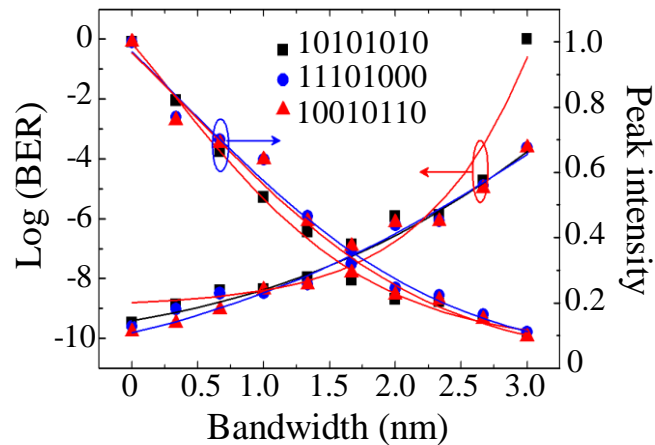


Figure 5.12 BER performances and peak intensity of the decoded pulse versus the bandwidth of notch filter for different codes.

patterns, from which one find that as the bandwidth of the notch filter increases to 3nm, the normalized peak intensity of the decoded pulse decays gradually from 1 to 0.1 and the corresponding BER degrades from $10^{-9}$ to $10^{-4}$ for code 11101000 and 10010110. The received optical power is assumed as -15.5dBm at BER of $10^{-9}$ in the calculation and all the following simulations. The other code 10101010 exhibits similar trends but the peak intensity and corresponding BER degrade more rapidly than the others especially when the bandwidth is large, which can be ascribed to the decoding performance discrepancy produced by the code transition of the pattern generator. In the experiment, the spectral notch filter with a bandwidth of 1nm is used to reject the two CW channels simultaneously, which can keep the peak amplitude and BER at an appropriate level. The dependence of the center wavelength of the notch filter with the BER and Q factor has also been simulated for code 11101000, as shown in Figure 5.13 (a) and (b), respectively. It can be seen that notch filtering at the left spectra edge (1549.1nm) causes the BER performance and Q factor degrade to $10^{-4}$ and 4.5 for 3nm filtering bandwidth, while for the notch filtering at the spectral center (1550nm) and right edge (1550.9nm), the log(BER) and Q factor both degrade to 0. The notch filtering at the spectra center that with most of the energy suffers from more severe degradation than the others, which is more obvious at larger filtering bandwidth. Due to the asymmetry of the encoded spectrum for code 11101000, notch filtering at the left and right spectra edge exhibits different performance. To alleviate the degradation, a notch filter with center wavelength of 1550.9nm is thus employed in the experiment.
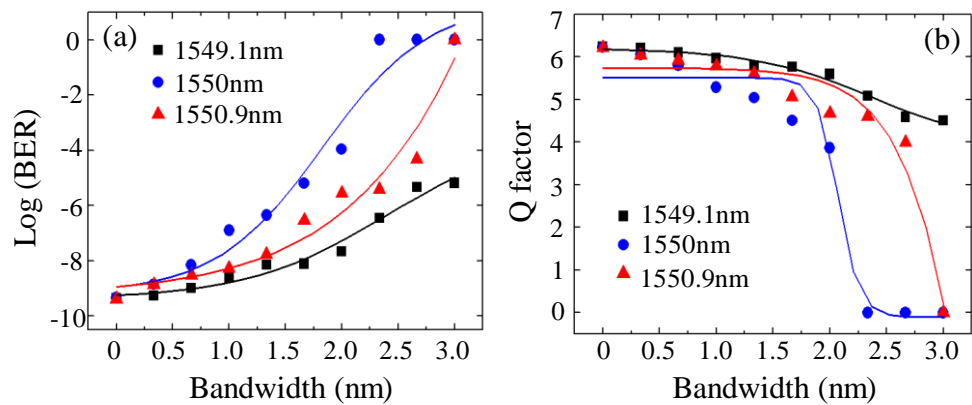


Figure 5.13 (a) BER performance and (b) Q factor versus the notch filtering bandwidth at different center wavelengths.

Figure 5.14 (a) and (b) show the spectrum and waveform of the stretched OCDMA signal after the first LCFBG, from which one can see that the input broadband SC spectrum has been cut off by the LCFBG, resulting in a stretched pulse of time duration

within one bit period of 400ps corresponding to an effective code length of 8-chip for a chip rate of 20-Gchip/s. By adjusting the optical attenuator after the PM, the DPSK data modulated SPE-OCDMA signal can be combined with the two-channel DWDM signal with a power ratio of ~19dB for transmission. It can be seen from Fig. 5.14 (c) that the secure OCDMA channel occupies the same spectral bandwidth as the DWDM signal, thus the OCDMA/DWDM signals can be simultaneously processed during the transmission to improve the bandwidth efficiency. The peak power of the OCDMA spectrum is approaching the system noise level, which is ~35dB lower than that of the DWDM channels. By injecting ASE noise into the system, the broadband OCDMA spectrum could be further masked without jeopardizing the public channel. The eye diagrams of the DWDM signals without and with OCDMA signal are shown in Fig. 5.14 (d) and (e), from which one can see a clear 10-Gb/s NRZ-OOK eye diagram. There is no obvious difference of the NRZ-OOK eye diagrams before and after introducing the OCDMA signal that can make the eavesdropper unaware of the OCDMA channel.
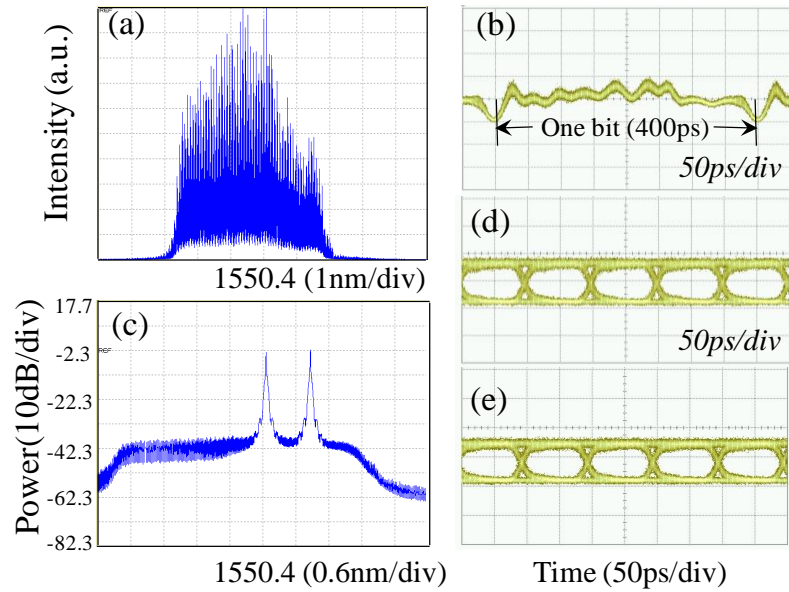


Figure 5.14 (a) and (b) are the spectrum and waveform of the OCDMA signal after the LCFBG; (c) is the spectrum of the combined DWDM and OCDMA signals; (d) and (e) are the eye diagrams for the DWDM signal without and with OCDMA signal.

After the spectral notch filter with a notch depth of ~30dB, most of the DWDM signal has been rejected from the broadband OCDMA signal and directly detected for both the two different wavelengths, while the OCDMA signal survives from the transmission port. To investigate the decoding performance of the OCDMA signal after the notch filter, four optical codes OC1~OC4: 11101000, 10010110, 11011100 and 10101010 have been used in this experiment. By properly applying the correct optical
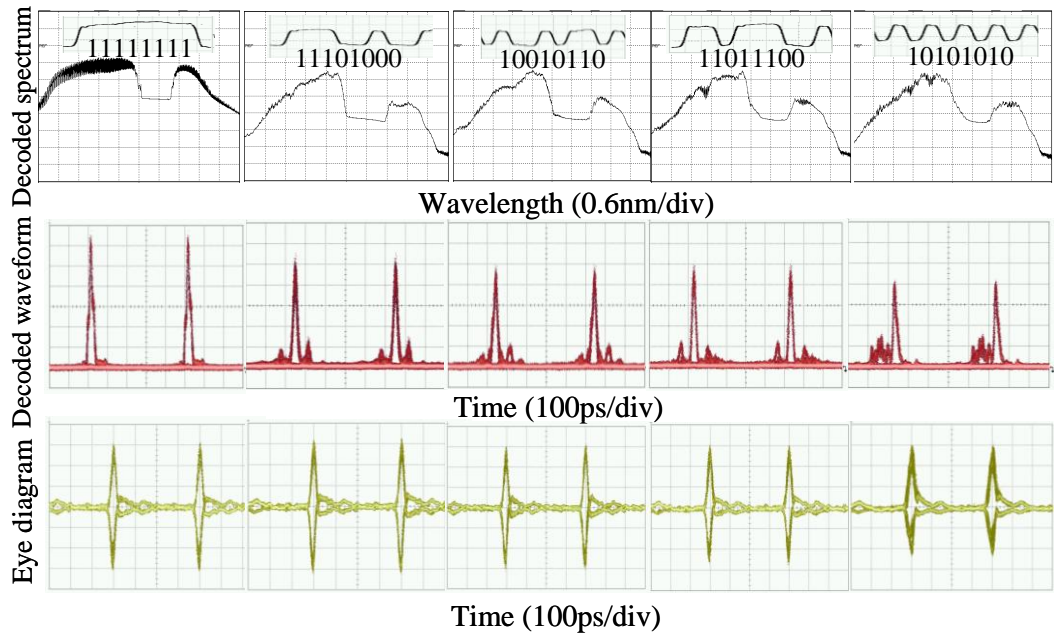
Figure 5.15 Decoded spectra after the notch filter (upper row), decoded waveform (middle row) and corresponding eye diagram (lower row) for different code patterns.

code sequence, the encoded SPE-OCDMA signal can be spectrally phase decoded and compressed by the LCFBG to recover the original-like pulse with different phase. Figure 5.15 shows the correctly decoded spectrum (upper row) and recovered waveform (middle row), from which one can see that compared to the case of using code (11111111), the correctly decoded waveforms for the other codes has been slightly degraded because of the notch filtering. The corresponding eye diagram of the 2.5-Gb/s DPSK-OCDMA signal after the DPSK demodulator and balanced photo-detector is also shown in the lower row of Fig. 5.15, where clear DPSK eye diagrams have been obtained, indicating that the phase information has been successfully preserved.

To further improve the security of the OCDMA signal, a prime hopping code pattern comprised by OC1~OC3 is used to modulate the phase of the stretched optical signal: for a series of data stream, each bit of the optical pulse can be encoded bit-by-bit by scrambling the code patterns. For instance, the PM can be driven by the code sequence of OC3, OC1, OC2, OC1, OC3… for encoding. To combine DPSK data (e.g. 10010) with the code pattern, the PM is driven by OC when the DPSK data is symbol "1", while if the symbol is "0", the PM is driven by $\overline{OC}$, so the data stream can be encoded by OC3, $\overline{OC1}$, $\overline{OC2}$, OC1, $\overline{OC3}$ for enhancing the security. To decode the SPE-OCDMA signal, the PM in the SPD section should be driven only by the complementary scrambled code patterns $\overline{OC3}$, $\overline{OC1}$, $\overline{OC2}$, $\overline{OC1}$, $\overline{OC3}$…to generate an auto-correlation pulse stream with high peak intensity, otherwise a cross-correlation signal with low peak power will be produced. Figure 5.16 (a) and (b) show the correctly
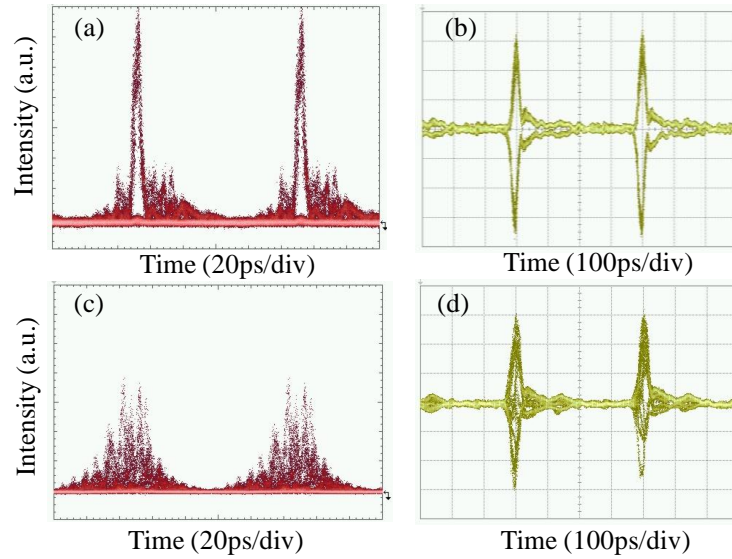
Figure 5.16 (a) and (b) are the waveform and corresponding eye diagram for the correctly decoded scrambled OCDMA signal; (c) and (d) are the waveform and eye diagram for an incorrectly decoded signal.

decoded optical signal measured by an optical sampling oscilloscope and its corresponding electrical eye diagram, both of which exhibit clear eye opening. However, an eavesdropper can only get an obscure eye diagram and it is not easy to break the security of this system without the knowledge of the scrambled code pattern, as can be seen from the decoded optical waveform and eye diagram of the cross-correlation signals in Fig. 5.16 (c) ~ (d). By further increasing the code length, the security of the OCDMA signal can be significantly enhanced. Finally, the BER after 49km transmission for the correctly decoded OCDMA signal is measured, as shown in Figure 5.17 (a). Error-free transmission has been achieved for all the three codes, and the power penalty is ~ 1.5dB compared to that of no WDM/notch filter. As shown in Fig. 5.17 (a), by using a correct code hopping sequence to drive the PM, the scrambled OCDMA signal can also be decoded and error-free transmitted with low penalty. Fig.5.17 (b) and (c) show the measured BER for the two DWDM channels in presence of the OCDMA signal with different codes, respectively. Error-free transmission has been obtained for both the WDM channels and no power penalty has been observed for different codes.

In the experiment, the power ratio of the two-channel WDM and OCDMA signals is ~19dB, which can be further increased as long as the notch depth of the filter is large enough. It is also possible to get error-free detection of the OCDMA and DWDM signals in the hybrid system with multiple channels to improve the bandwidth efficiency and security. Figure 5.18 (a) shows the simulated BER performance and peak intensity
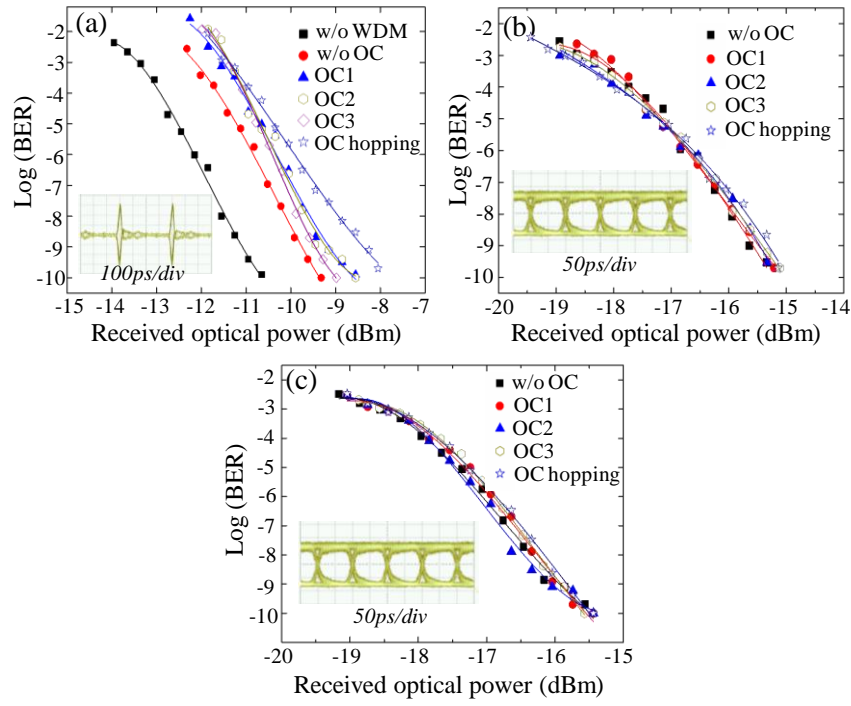
Figure 5.17 BER performances for the OCDMA signal with different codes; (b) and (c) are the BER performances of the WDM channels 1 and 2, respectively.

for two kinds of notch filters with bandwidth of 0.2nm and different channel spacing (CS): one is ITU-T DWDM grid 0.8nm, and the other one is 0.3nm. For the CS of 0.8nm, as the channel number increases to 5, the peak intensity gradually decreases from 1 to 0.6, and the corresponding BER has been degraded from $10^{-9}$ to $10^{-8}$. For channel number of more than 5, the peak intensity and BER will keep stable because the residual channels are out of the OCDMA bandwidth. While for denser channels of 0.3nm spacing, the peak intensity and BER degrade rapidly with the channel numbers. The required additional power to compensate the peak intensity reduction is shown in
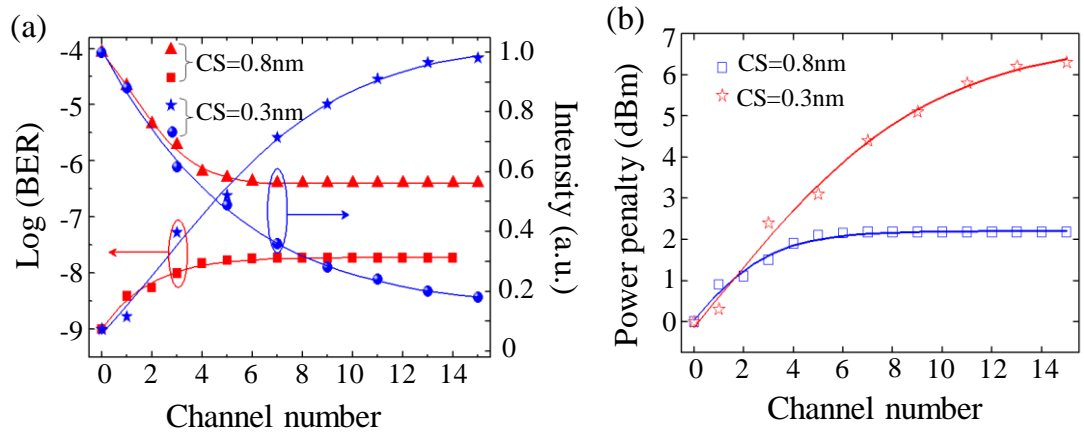


Figure 5.18 (a) BER and normalized intensity versus the channel number for CS of 0.8nm and 0.3nm, respectively; (b) Power penalty versus the channel number.

Fig.5.18 (b), from which one can see that the maximum power penalty due to the notch filtering is about 2dB and 6dB for the CS of 0.8nm and 0.3nm, which indicates the feasibility of error-free detecting the OCDMA and DWDM signal with low power penalty in the OCDMA overlay DWDM network.

## 5.4    Summary

In this chapter, a novel approach by combining the optical encoding and group velocity dispersion based optical steganography technique is proposed for enhancing the security of the time domain spectral phase encoded OCDMA signal. The OCDMA signal can be hidden into the public WDM network by temporal spreading, making the eavesdropper unaware of its existence and thus improving the data security. Secure transmission of 1.25Gb/s time domain SPE-OCDMA signal with OOK data modulation format over a 10Gb/s public WDM channel has been achieved. To simplify the extraction of the OCDMA signal and improve the bandwidth efficiency, a transparent optical network architecture is further proposed, in which the OCDMA signal with various modulation formats can be spectrally overlaid onto the public DWDM network and detected by a spectral notch filter. Time domain spectral phase encoding/decoding scheme that can simultaneously generate bit-by-bit DPSK data modulation and optical code scrambling has also been applied into the transparent optical network to improve the security of the OCDMA channel. Transparent transmission and detection of a secure 2.5-Gb/s time domain spectral phase encoded DPSK-OCDMA signal overlaid on a two-channel 10-Gb/s DWDM network has been demonstrated, which was enabled by a fiber Bragg grating based spectral notch filter. The impairment of the notch filtering on the OCDMA channel has been investigated, which shows that it is possible to apply the proposed technique to multiple OCDMA and DWDM channels with low power penalty to achieve higher system security and capacity.

# CHAPTER 6

# High speed time domain SPE-OCDMA system with security improvement based on bit-by-bit code shifting

## 6.1   Introduction

In modern optical communication, with the increasing usage of the network resources, there is a growing demand of high speed optical signal transmission and secure data exchange, which are two most important concerns for the OCDMA research community. Because of the inherent advantage of providing information security by optical code processing, the OCDMA is emerging as a promising technique to achieve physical layer security that can supplementary to mathematical algorithm for computational security in the high level of protocol [15, 111, 120]. However, as previously discussed in Chapter 2, the security vulnerabilities associated with the coding induced dips [30-31] and the data modulation formats in OCDMA systems have been discovered and demonstrated [61, 100-101]. Careful analysis reveals that the conventional approaches by assigning a fixed OC using one en/decoder for all the bits is not resistant to eavesdropping with an appropriate detector such as energy detector and DPSK demodulator whatever en/decoding and modulation formats are used. By assigning a different OC for each bit, the information security could be dramatically enhanced. A rapid reconfigurable time domain spectral phase encoding/decoding OCDMA scheme has thus been proposed in Chapter 4 to improve the data security by dynamically generate bit-by-bit optical coding and DPSK data modulation. This technique has also been applied into optical steganography to securely transmit the OCDMA signal over public WDM network in Chapter 5, but due to the limitation of electronic signal processing, only a low data rate of 2.5Gb/s with relatively short code length has been achieved in these demonstrations. What's more, in most of the previous demonstrated OCDMA systems using various optical en/decoders, the data rate was mainly restricted within 10-Gb/s [128]. The application of OCDMA technique to future optical network desires high speed modulation and the ability to operate at a higher data rate, which is a great challenge for general OCDMA systems.

In this chapter, a novel programmable and code-length variable bit-by-bit code

shifting technique is proposed to improve the information security and enable high speed operation of the time domain SPE-OCDMA system. In the proposed scheme, the optical code with ultra-long code length can be rapidly reconfigured and each bit can be assigned a different effective OC, so significant security improvement could be achieved. Moreover, as the optical coding is independent of data rate, high speed data processing could also be supported. Based on this scheme, experimental demonstrations of the security enhancement for both OOK and DPSK data with high data rate and code length of up to 40Gb/s and 1024-chip are presented. The rest of this chapter is organized as follows: In section 6.2, the basic principle of the bit-by-bit code shifting technique is introduced followed by an experimental demonstration of security improvement for a 10-Gb/s time domain spectral phase encoded DPSK-OCDMA signal; Then in section 6.3, a two-user OOK time domain SPE-OCDMA system operated at 10-Gb/s is presented; In section 6.4, a novel approach based on symbol overlapping of the time domain spectral phase encoded and decoded signals for enhancing the security of 40-Gb/s OOK data is proposed and demonstrated; After that, in section 6.5 and 6.6, the applications of the bit-by-bit code shifting technique in a 40-Gb/s DPSK-OCDMA system will be investigated.

## 6.2   10-Gb/s, security enhancement of DPSK-OCDMA system using bit-by-bit code shifting

### 6.2.1  Principle of bit-by-bit code shifting

Figure 6.1 illustrates the basic principle of the proposed bit-by-bit code shifting technique. Phase-shift-keying modulation format is employed in this scheme, as shown in Fig.6.1 (a) with DPSK data format. The ultra-short data pulse is stretched by a highly dispersive element in time domain and each bit of the stretched pulse occupies $T_s$ time duration as a result of the chromatic dispersion. If $T_s$ is greater than the data pulse period $T_b$, the adjacent pulses will be temporally overlapped with each other. After the pulse stretching, a rapid reconfigurable, ultra-long code length variable OC with chip duration of $T_c$ is applied onto the overlapped pulses to perform time domain spectral phase encoding, as shown in Fig.6.1 (b). By using a long pseudo random OC, each stretched pulse can experience different OC section with an effective code length of $T_s$ /$T_c$ and these sections are shifted by $T_b/T_c$ chips bit-by-bit, which can be referred to bit-by-bit code shifting. In this scheme, the OC could have an unprecedented code length
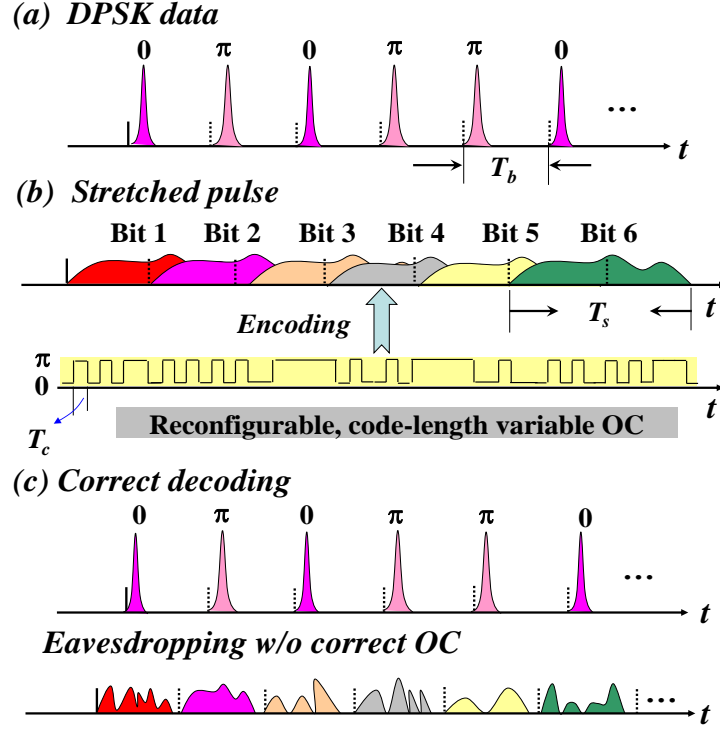
Figure 6.1 Principle of the proposed bit-by-bit code shifting scheme. (a) Original DPSK data, (b) bit-by-bit code shifting after pulse stretching; (c) correctly decoded signal and eavesdropper intercepted signal without correct OC.

and thus a large code space. Notice that the encoding process is completely data rate independent and there is no specific requirement of the dispersion value as long as the $T_s > T_b$ is satisfied. For achieving long effective code length, high dispersion is desirable. To decode the overlapped spectral phase encoded signal, the inverse process with complementary OC and opposite dispersion should be conducted to reconstruct an autocorrelation signal with high peak power, as shown in Fig.6.1 (c). An eavesdropper that is able to intercept the DPSK data should be able to know both the chromatic dispersion and the applied ultra-long OC. Even if he knows the dispersion value for pulse compression, it is still impossible for him to extract the DPSK data without the correct OC, because only a noise-like cross-correlation signal with random phase for each bit is obtained in this case and the phase shift between different bits is no longer 0, $\pi$ or any constant value.

## 6.2.2  Experimental setup and results

A proof-of-concept experimental demonstration of the bit-by-bit code shifting technique has been carried out. Figure 6.2 shows the schematic diagram of the experimental setup. A 10 GHz MLLD producing ~2.8 ps pulses at 1550.75nm is
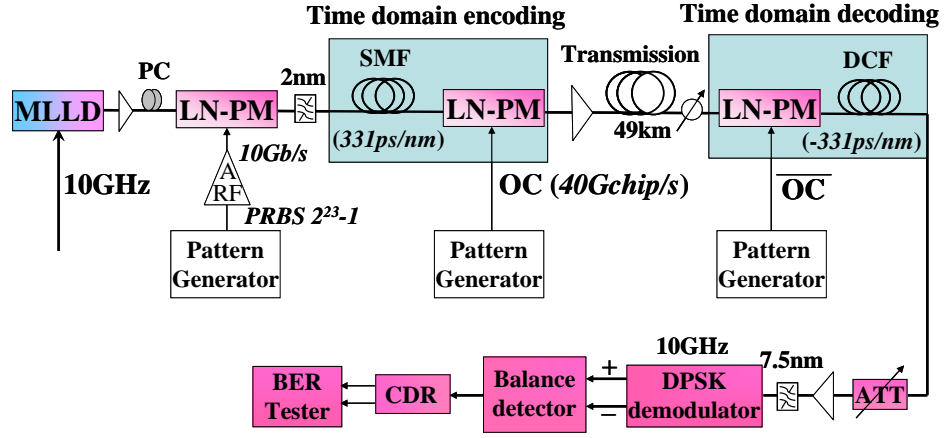
Figure 6.2 Experimental setup of the proposed time domain bit-by-bit code shifting scheme.

modulated at 10-Gb/s by a phase modulator driven by $2^{23}$-1 PRBS data. A span of SMF with dispersion of ~331 ps/nm is used to significantly broaden the pulse train. To reduce the dispersion mismatch caused by the non-ideal dispersion compensation at the receiver, an optical band-pass filter with 3-dB bandwidth of ~ 2nm is employed before the SMF. Because of the high chromatic dispersion, each bit of the original pulse is stretched into ~662 ps time duration and thus the adjacent consecutive pulses are significantly overlapped with each other.

After the temporal stretching, a 40-GHz LN-phase modulator driven by the reconfigurable 40-Gchip/s, code length variable OC is used to perform the time domain spectral phase encoding. Different stretched pulse will thus experience an effective ~26 chips spectral phase pattern according to the $T_s/T_c$. Four different kinds of OCs (each has two Gold codes with code length of 64-chip, 128-chip, 512-chip and 1024-chip) are used in the demonstration. A piece of ~49 km dispersion-compensated-fiber is used for the transmission. For the time domain spectral phase decoding, similar configuration as the encoding is utilized but the PM is driven by the complementary OC, and a span of dispersion compensation fiber (DCF) with opposite dispersion of ~ -331 ps/nm is used to compress the spectral phase decoded signal in order to retrieve the original pulse. The correctly decoded pulses are finally directed into a DPSK demodulator with a one-bit delay (~100ps) interferometer followed by a balanced detector to recover the DPSK data for bit-error-rate measurement.

Figures 6.3 (a) and 6.3(b) show spectrum and waveform of the stretched 10-Gb/s DPSK pulse train after the dispersive SMF. It can be seen that the data pulse has been significantly stretched in time domain and the adjacent pulses overlap with each other, so the waveform exhibits as a system noise. Fig.6.3 (c) shows the spectrum of the

116

correctly decoded signal, from which one find that it has similar profile as the original DPSK data modulated spectrum, which indicates the phase has been successfully retrieved after the decoding. Whereas for the incorrectly decoded signal, as shown in Fig.6.3 (d), the spectrum is quite different from Fig.6.3(a) and 6.3(c), showing that the phase information is lost. There are no coding induced dips in the encoded spectra or waveform that exists in conventional encoding approaches, so it can eliminate the possibility of attacking the system by analyzing the dips.
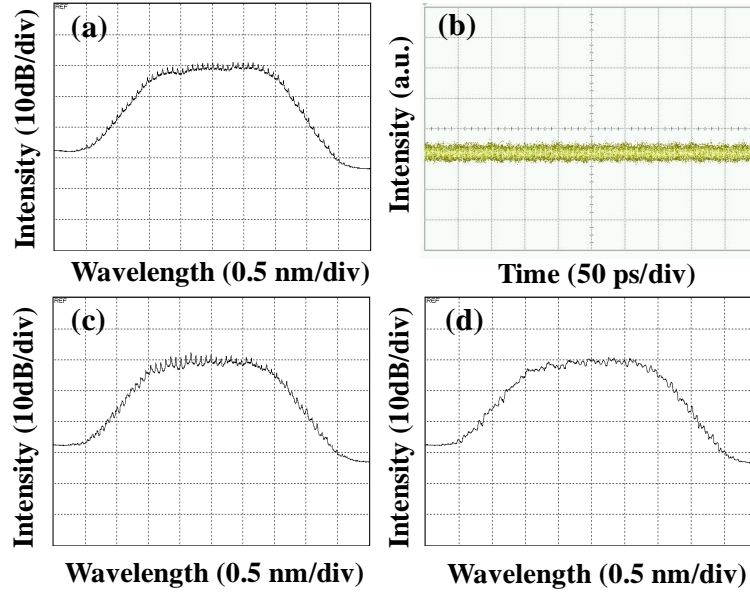


Figure 6.3 Spectrum (a) and waveform (b) of the stretched pulse after the dispersive SMF; (c) and (d) are the spectrum of the correct and incorrect decoded signal, respectively.

Figure 6.4 (a) and 6.4(d) show the correctly decoded waveform and the corresponding eye diagram after applying the correct OC, both of which have clear eye opening. In contrast, it is impossible for an eavesdropper to sift the DPSK data by using a simple power detector or DPSK demodulator without proper chromatic dispersion compensation and OC. As shown in Fig. 6.4(b) and 6.4(e) without proper dispersion, the eavesdropper can only get a noise-like signal. As for Fig.6.4(c) without proper OC, although the stretched pulses have been compressed, the phase relationship has not been preserved and only noise-like eye diagrams have been achieved, as shown in Fig.6.4 (f). By using dispersive elements with higher dispersion, the compressed pulses in Fig.6.4 (c) can also be overlapped with each other, indicating potential security enhancement based on the proposed time domain bit-by-bit code shifting technique.

In this experiment, synchronization between the optical encoding and decoding side is quite essential to recover the original data pulses and improve the security. The
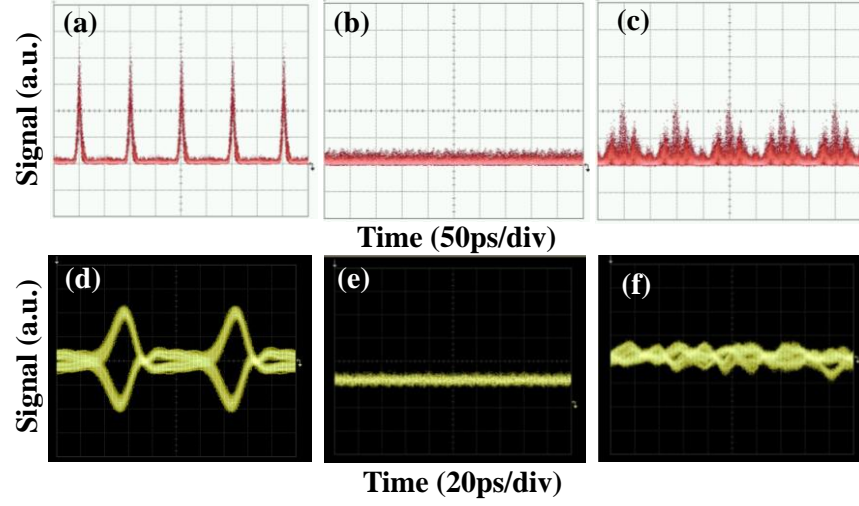
Figure 6.4 Waveforms of decoded signals for (a) with proper dispersion and OC, (b) without proper dispersion and (c) without proper OC. (d)-(f) are the corresponding eye diagrams after DPSK demodulator for (a)-(c).

measured peak intensity reduction of the decoded pulses versus the timing error between the en/decoding sides for different OCs is shown in Figure 6.5. It can be seen that as the timing error increases to ~ ±10 ps, the normalized peak intensity is degraded from 1 to 0.4, which is shown in the insets of Fig.6.5 (i) and (ii), in which case the decoded pulses gradually submerge in the noise-like background and no BER can be measured. A tunable optical delay line with a resolution of 0.2 ps is employed before the phase modulator in the decoding side to temporally align the complementary spectral phase pattern with the encoding OC to guarantee the decoding performance. The synchronization is much easier to be achieved than the previous proposed bit-by-bit optical code scrambling scheme in Chapter 4.

The measured BER for the four types of OCs with different code lengths are shown in Figure 6.6. Compared with the back-to-back case, the transmission and optical
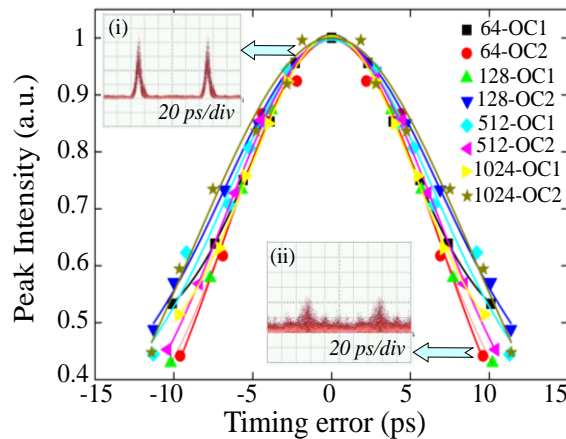


Figure 6.5. Peak intensity of the decoded pulse versus timing error for different kinds of OCs.

encoding/decoding induce a power penalty within ~2 dB (evaluated at BER=$10^{-9}$), partially due to the non perfect dispersion compensation and decoding. Error-free transmission over 49km has been achieved for all the OCs. By using the time domain bit-by-bit code shifting scheme that allows rapidly programming the code length variable ultra-long optical code from a large code space, the security enhancement in the DPSK-OCDMA system has been achieved. This scheme requires only conventional dispersive elements and phase modulators, exhibiting the potential to operate at higher data rate and realize even one time pad by increasing the code length for secure optical communication.
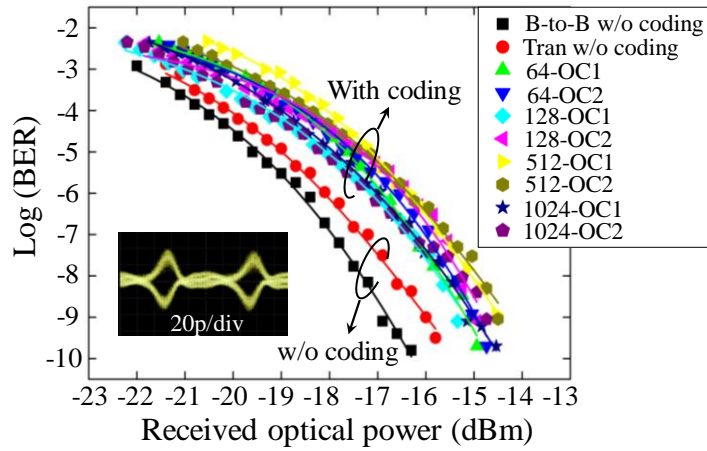


Figure 6.6 BER curves of the 10-Gb/s DPSK data with various OCs.

## 6.3    10-Gb/s, two-user time domain SPE OOK-OCDMA system

In OCDMA system, the multiple access is based on the concept that each user of the network is allocated a unique optical code, by which the authorized user can distinguish the target data from the interferences generated by other users. In Chapter 3, a novel time domain spectral phase encoding scheme using only dispersive element and phase modulator has been proposed for OCDMA application. However, only a two-user time domain SPE-OCDMA system with a data rate of 2.5-Gb/s by using a VBS based spectral phase decoder has been demonstrated. In the last section, a time domain bit-by-bit code shifting technique for security enhancement of DPSK data has been proposed, but the feasibility of this technique for a multi-user OCDMA system has not been investigated yet. In this section, the experimental demonstration of the bit-by-bit code shifting technique operating in the pulse overlapping regime for high speed time domain SPE-OCDMA application in a 10-Gb/s, two-user OCDMA environment with OC length of up to 1024 will be presented.

## 6.3.1 Multiple access based on bit-by-bit code shifting

To show the principle of multiple access based on the time domain bit-by-bit code shifting technique with pulse overlapping, we compare it with the non-overlapped case, both of which are composed of dispersive element (-D or +D) and phase modulator. Figure 6.7 (a) and (b) show the en/decoding schemes for different bit rates (e.g. 10-Gb/s and 2.5-Gb/s) operating in the non-overlap regime. For both cases, the data pulse is stretched by the dispersive element within one bit duration and as a result, different spectral components spread into different positions in time domain. By applying an OC into the phase modulator, different spectral components can have a different phase shift and thus be spectrally phase encoded. One can also apply a different OC for each bit to perform code hopping and increase the code space. As the spread pulse duration is lower than the bit period, there is a tradeoff between the bit rate and chip number. For a high bit rate of 10-Gb/s as shown in Fig.6.7 (a), assuming a 40-GHz chip rate which is limited by the electronic technology, the maximum chip number can only reach up to 4, resulting in rather poor auto-/cross-correlation performance that can be improved by increasing the chip number, but the bit rate has to be reduced as shown in Fig.6.7 (b).
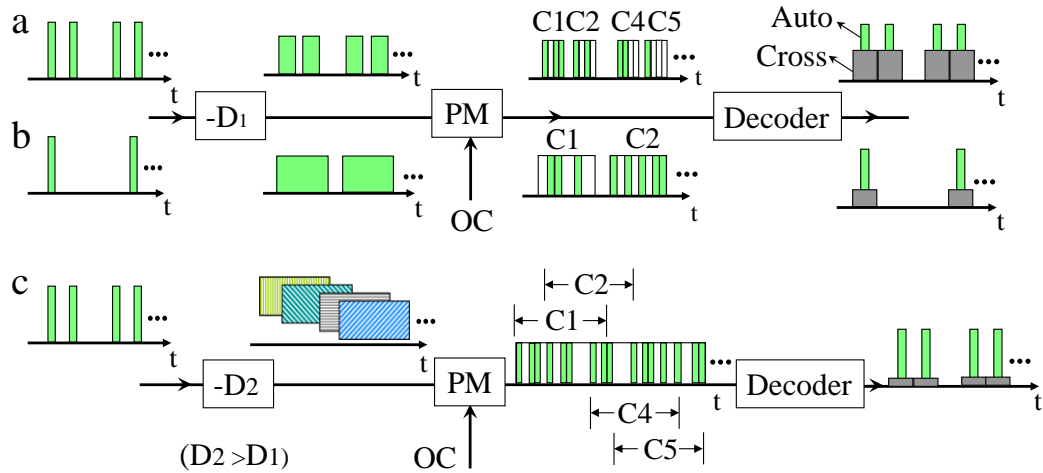


Figure 6.7 Principle of the time domain spectral phase en/decoding scheme operated in different regimes. (a) High bit rate without overlap, (b) low bit rate without overlap and (c) high bit rate with pulse overlap.

On the contrary, by employing the proposed bit-by-bit code shifting technique with pulse overlapping, one can achieve high bit rate and chip number simultaneously, which is shown in Fig.6.7 (c). In this case, the stretched pulse occupies more than one bit period and the adjacent pulses overlap with each other, therefore, it is possible to apply an ultra-long OC to the stretched pulses with a high bit rate, such that each bit can

experience a portion of the OC determined by the ratio of stretched pulse and chip duration, and thus different bit can have a different effective code. If the chromatic dispersion is large enough, the effective chip number of each bit can far exceed than that achievable by the non-overlapped cases and the decoding performance will thus be improved whilst ensuring a high bit rate operation. By assigning a rapid reconfigurable, code length variable ultra-long OC that has a large code space for each user, high speed time domain SPE based multiple access can be achieved.

## 6.3.2  Experimental demonstration

The experimental setup of the bit-by-bit code shifting technique for multiple access in a two-user OCDMA system at 10-Gb/s is shown in Figure 6.8. The 10 GHz optical pulse train with ~2.8ps Gaussian-like pulses is generated by the MLLD. A Mach-Zehnder intensity modulator driven by $2^{23}$-1 PRBS is used to generate the 10-Gb/s OOK data and then directed into a series of cascaded four identical chirped fiber Bragg gratings (CFBGs) with a 10-dB bandwidth and negative dispersion of ~ 4.7 nm and -80 ps/nm for temporally spreading the pulses. The pulse train is thus spread within ~1504 ps time duration and significantly overlapped with each other. The dispersed pulse train is amplified and split into two paths by a 3-dB coupler. Each path is then phase modulated by a different 40-Gchip/s OC from a Gold code with variable lengths of 128-chip, 512-chip, and 1024-chip for realizing the time domain spectral phase encoding with bit-by-bit code shifting. Each bit of the stretched pulse has an effective code length of ~60 which is high enough to distinguish different users. A span of 10 m optical fiber is used in one arm to decorrelate the two encoded signals and a tunable optical



Figure 6.8 Experimental setup of the 10-Gb/s, two-user OOK-OCDMA system.

attenuator is used to balance the power in the two arms. The two encoded signals are then combined and launched into a piece of 49 km SMF and DCF fiber for transmission.

At the receiver side, similar components as the encoding part are used, where the spectral phase decoding is directly performed by using another phase modulator driven by the complementary OC and then temporally compressed by CFBGs with equal but positive dispersion. The decoded pulses are injected into super-continuum based optical thresholder which consists of a preamplifier EDFA and a piece of 2000m dispersion flattened fiber followed by a 5nm bandpass filter to suppress the interference. Finally, the recovered signal is data-rate detected by a 10-Gb/s optical receiver.

Figure 6.9 (a) shows the measured auto-correlation signal by applying a matched OC in the decoding part for 128-chip. A needle-like pulse train with high peak power can be obtained after properly aligning the optical delay line before the phase modulator. The dense sidelobes are mainly attributed to the non-ideal decoding and dispersion compensation. Fig. 6.9 (b) shows the waveform of a cross-correlation signal for an unmatched OC, from which one can see a noise-like signal with low peak power. The adjacent pulses for the cross-correlations are slightly overlapped with each other such that the signal to background noise ratio is very low when a simple power detector is used for data-rate detection, which can improve the security against eavesdropping. Comparing Fig.6.9 (a) and (b), the peak to wing ratio and the peak power ratio between
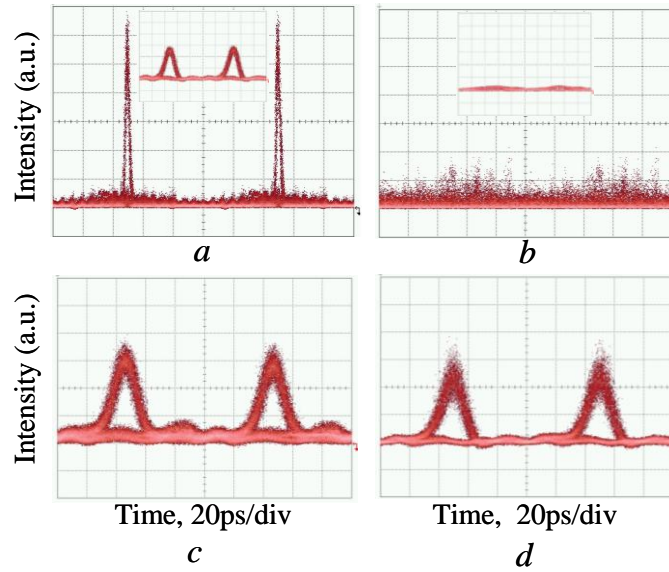


Figure 6.9 Decoding performance of the two-user OCDMA system. (a) Auto-correlation, (b) Cross-correlation, (c) Eye diagram of the decoded two users' signal and (d) Eye diagram after the optical thresholder.

the auto-/cross correlations are around 12 and 4.5, respectively. The eye diagram of the decoded signals in presence of both users is deteriorated a little because of the introduction of the multi-user interference, as shown in Fig.6.9 (c), which could be combated through optical thresholding or time gating technique. Fig. 6.9 (d) shows the recovered eye diagram after applying a SC based optical thresholder with clear eye opening.

To study the performance of the two-user system, bit-error-rate measurements for three kinds of OCs with code lengths of 128, 512 and 1024 are illustrated in Figure 6.10. Compared with the single-user system, a power penalty of around 1.5 dB is observed for the two-user system, which can be ascribed to the multiple access interference. Error-free (BER<$10^{-9}$) have been achieved for both the single-user and two-user OOK systems with various codes, which demonstrates the feasibility of supporting multi-user's optical access with high bit rates based on the bit-by-bit code shifting technique. The proposed technique exhibits the potential to accommodate more active users and improve the security of OOK-OCDMA system.
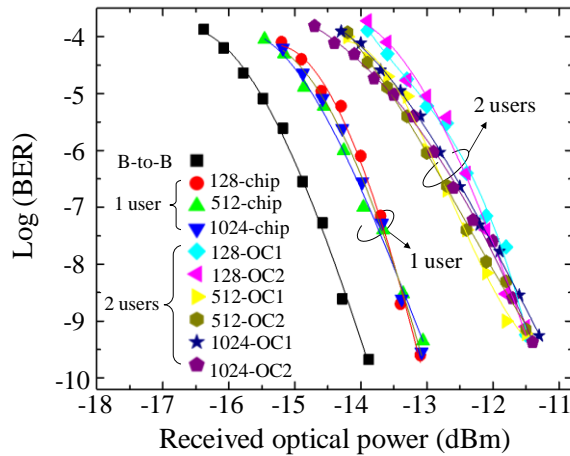


Figure 6.10 BER performances of the 10-Gb/s time domain SPE-OCDMA system.

## 6.4    40-Gb/s, secure OOK-OCDMA system based on time domain spectral phase encoded signal overlapping

As has been discussed in Chapter 2, the security of OCDMA system is related to the data modulation formats. In an OCDMA system employing OOK data modulation, an eavesdropper can tap the individual user's signal and recover the data by using a simple power detector to perform data-rate detection without the need of knowing the exact OC, and thus it is generally considered that there is no any security in such an OOK

optical system. In this section, we challenge the concept of OOK system security and propose a novel approach for enhancing the security of high speed OOK data based on the time domain SPE/SPD scheme deploying highly dispersive elements and a high speed phase modulator to introduce significant symbol overlapping for both the encoded and incorrectly decoded noise-like signals whose temporal durations are greater than twice the bit period. Security enhancement for 40Gb/s OOK data using fast reconfigurable 40Gchip/s optical code with code lengths of up to 1024 has been demonstrated and compared with a 10Gb/s system. The proposed scheme is very robust to malicious eavesdropping using power detection, and thus it can significantly improve the OOK data security.

## 6.4.1 Experimental setup

Figure 6.11 illustrates the experimental setup of the proposed time domain spectral phase en/decoding scheme with symbol overlapping for improving the security. The laser source is an actively MLLD producing 2.8ps pulses at repetition rate of 10 GHz and spectrally centered at 1549.8 nm. To investigate the security improvement for different data rates, both 10-Gb/s and 40-Gb/s data are used in the experiment, respectively. The 40GHz pulse train is generated by multiplexing the 10GHz pulses using a four-stage PLC-based optical time division multiplexer (OTDM). To generate the 10-Gb/s and 40-Gb/s OOK data, the pulse train is intensity modulated by a lithium-niobate intensity modulator driven by 10-Gb/s or 40-Gb/s pseudo random bit sequence (PRBS) of length $2^{11}$-1.

For the generation of time domain spectral phase encoding, three identical cascaded chirped fiber Bragg gratings (each has a 10-dB bandwidth of ~4.7 nm and dispersion slope of ~80ps/nm) are used to significantly broaden the pulse train. By using the LCFBGs as the dispersive elements, the dispersion is easier to be compensated and this system is compact, stable and has lower latency. Different spectral components spread into different time positions are thus the temporal of each stretched pulse is similar to the input spectrum. Due to the high chromatic dispersion, each bit of the original pulse with bit period of $T_b$ is broadened within the time duration $T_s$ of ~1128ps and hence the adjacent consecutive stretched pulses are significantly overlapped with each other. After the temporal stretching, a 40-GHz LN-phase modulator driven by the 40-Gchip/s, fast reconfigurable and code-length variable OC with with chip duration of $T_c$ is used to perform the time domain spectral phase encoding. Different stretched pulse will
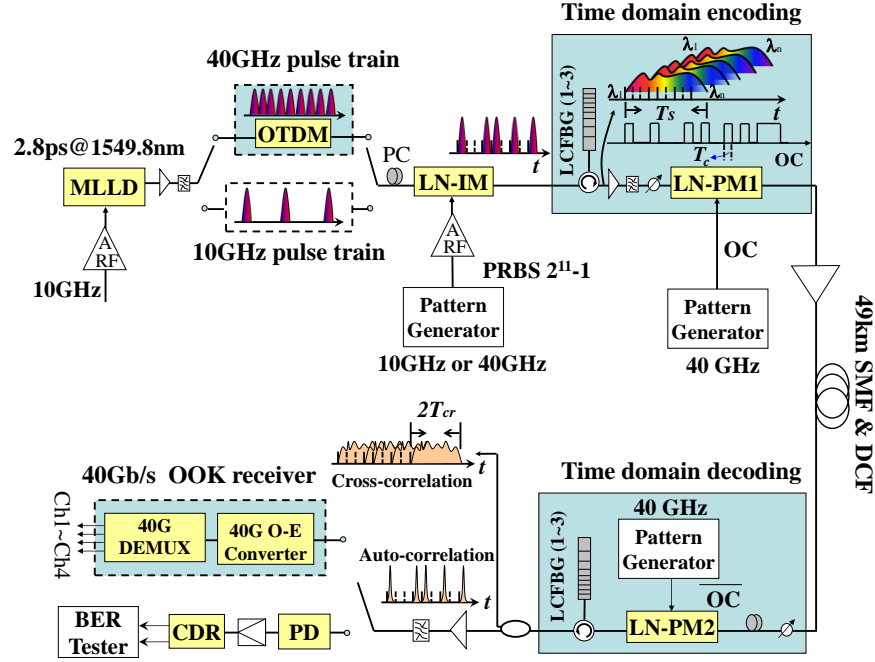
Figure 6.11 Experimental setup of the 40-Gb/s, OOK-OCDMA system.

relatively experience different sections of the OC and has a 45-chip spectral phase pattern according to $T_s/T_c$. A span of single mode fiber and dispersion compensation fiber with total length of 49km is used for transmission.

At the receiver side, similar configuration as the encoding part is utilized but the PM is driven by the complementary code patterns for spectral phase decoding. The synchronization between the optical encoding and decoding sides is essential for decoding the stretched pulse train. A global clock is used throughout the system and a tunable optical delay line is also employed before the phase modulator to temporally align the complementary spectral phase pattern and the applied OC in the encoding side. After that, another series of LCFBGs with opposite dispersion are used to compress the stretched and spectral phase decoded signal to recover the original pulse. The correctly decoded signal is finally launched into a 10-Gb/s or 40-Gb/s packet receiver for O-E conversion. The 10-Gb/s signal can be directly detected while for the detection of 40-Gb/s OOK data, a 40-GHz electrical de-multiplexer is used to de-multiplex the 40-Gb/s data into 4-channel 10-Gb/s OOK for measuring the bit-error-rate. The security of the proposed scheme arises from two aspects: a) physical layer security. If the eavesdropper does not know the chromatic dispersion used in the experiment, it is impossible for him to recover the temporally stretched pulse; b) rapid reconfigurable OC. One may assume that the sophisticated eavesdropper has plenty of resources and knows everything except the code. Even if he knows the dispersion and fabricates identical LCFBGs for decoding, he can only get a spectrally phase encoded and temporally significant overlapped cross-

correlation signal. The bit "0" is filled with the encoded signals from the other bits of "1", so it is difficult for the eavesdropper to discriminate the bit symbol by using a simple power detector.

## 6.4.2 Results and discussion

Figure 6.12 (a) and (b) show the spectrum and temporal profile of the stretched 40-Gb/s OOK optical pulses by the LCFBGs. Because of the significant overlapping of ~45 pulses after the stretching, the temporal profile of the overall signal in Fig.6.12 (b) is completely different from the spectrum and it looks like a noise. Unlike traditional OOK systems [31, 103], the eavesdropper cannot directly regenerate the original OOK data by simply detecting the power from the noise-like signal after time domain spectral phase encoding for both the 10-Gb/s and 40-Gb/s data rates. As mentioned before, the eavesdropper may be sophisticated enough and know the chromatic dispersion, so he can easily compress the stretched pulses and try to intercept the data. In this case, since the eavesdropper does not know the applied OC, only an incorrectly decoded cross-
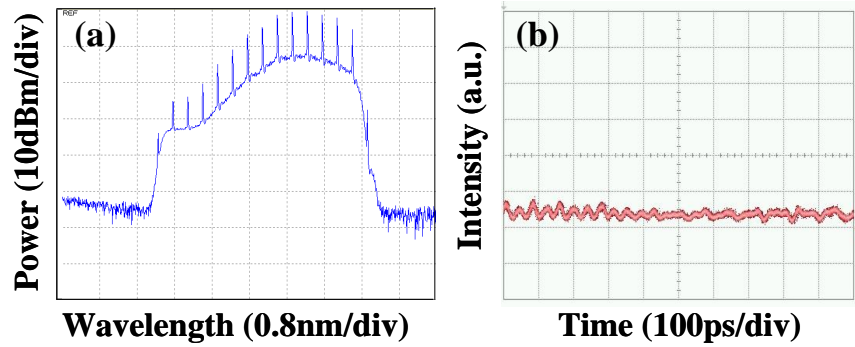


Figure 6.12 (a) Spectrum and (b) waveform of the stretched 40-Gb/s OOK pulse train.

correlation signal can be obtained. If the time duration of the incorrectly decoded signal for each bit is larger than twice the bit period after temporal compressing, the cross-correlation signal may still spread across the time scale with significant symbol overlapping, so the eavesdropper cannot intercept the data as well. The time duration of the incorrectly decoded signal in this scheme is mainly determined by the spectral resolution of each chip, which depends on the chromatic dispersion $D$ (ps/nm) and the chip rate $R_C$ (Gchip/s). Assuming that the input pulse is a transform-limited Gaussian pulse with a time-bandwidth product of 0.441, as each chip occupies $1000/(R_C \cdot D)$nm spectral range, the corresponding full-width at half maximum of the incorrectly decoded signal $T_{cr}$ (ps) can be approximately given by:

$$T_{cr} = \frac{0.8 \cdot 0.441 \cdot R_C \cdot D}{100} \tag{6.1}$$

Figure 6.13 (a) depicts the dependence of the $T_{cr}$ with the $D$ and $R_C$. The two planes are shown as the reference levels of the minimum required $T_{cr}$ to achieve security for 10-Gb/s and 40-Gb/s. By increasing the total dispersion $D$ and chip rate $R_C$, the $T_{cr}$ can be greater than the reference level, showing the feasibility of security improvement. Fig. 6.13 (b) shows the relationship of the minimum $D$ and $R_C$ when the $T_{cr}$ is on the reference planes, from which one can see that the minimum required $D$ for 10Gb/s is higher than that of the 40Gb/s, and the higher the chip rate, the lower the minimum $D$. Due to the limitation of current electronic technology, the highest chip rate achievable is ~ 40Gchip/s, which corresponds to a minimum $D$ of ~712 ps/nm and ~178 ps/nm for 10-Gb/s and 40Gb/s, respectively. In the experiment, the total dispersion of the LCFBGs is ~240ps/nm, which is higher than the minimum $D$ for 40Gb/s but lower than that of the 10-Gb/s, so security improvement for 40Gb/s can be expected.
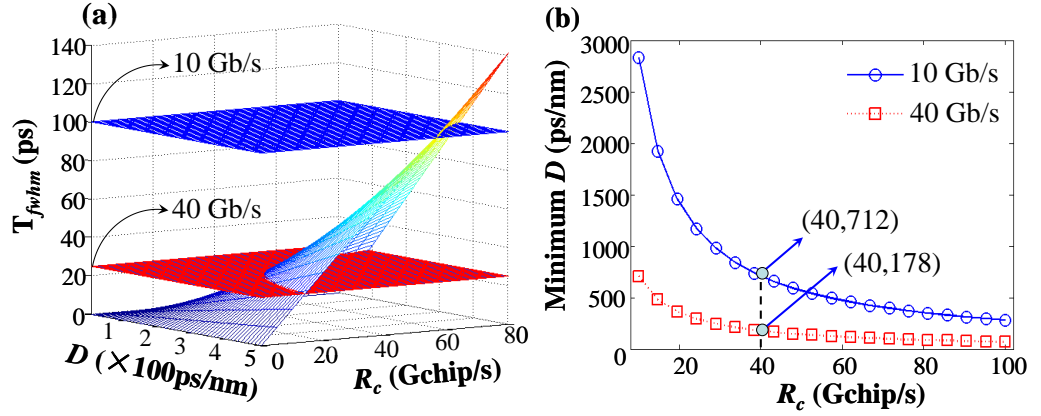


Figure 6.13 (a) Time duration of compressed incorrectly decoded signal versus $D$ and $R_C$; (b) Minimum required $D$ versus $R_C$ to achieve security for 40Gchip/s.

Three different codes with code lengths of 128, 512 and 1024 are used in the en/decoding experiment. These codes are randomly selected from Gold codes with different chips plus a zero. Figure 6.14 (a)~(b) shows the correctly decoded waveform and corresponding eye diagram for the 40Gb/s OOK data with 1024-chip OC. Autocorrelation short pulses with high peak power and clear eye opening have been obtained after the correctly decoding. However, as shown in Fig. 6.14 (c)~(d) with the correct opposite dispersive LCFBGs but incorrect OC, the decoded waveform exhibits as a noise-like signal and no eye opening can be observed in the corresponding eye diagram. It is unable to distinguish the symbol "1" and "0" from the waveform, showing that the eavesdropper cannot easily intercept the data by using simple power detection if he does not have any knowledge of the applied ultra-long OC. Fig.6.14 (e) ~ (f) show the incorrectly decoded waveform and corresponding eye diagram for chip rate of

10Gchip/s. In this case, the symbol "1" and "0" is distinguishable and the eye diagram has opening. This is due to the fact that the time duration $T_{cr}$ for each bit after LCFBGs compressing corresponds to ~34ps for 40Gchip/s chip rate, and thus the adjacent incorrectly decoded pulses have significant overlap for the 40Gb/s optical pulse train. While for 10Gchip/s corresponding to $T_{cr}$ of ~8.5ps, there is no significant symbol overlapping. Similarly, for the 10Gb/s data rate and 40-Gchip/s chip rate, because the $T_{cr}$ is smaller than one bit period, it is still possible for the eavesdropper to intercept the data by power detection even without the knowledge of OC, which can be seen from the waveform and clear eye diagram shown in Fig. 6.14 (g)~(h), but he can only get a relatively poor result when measuring the bit-error-rate. By further increasing the dispersion $D$ and chip rate $R_C$, security improvement for the data rate of 10Gb/s can also be anticipated.
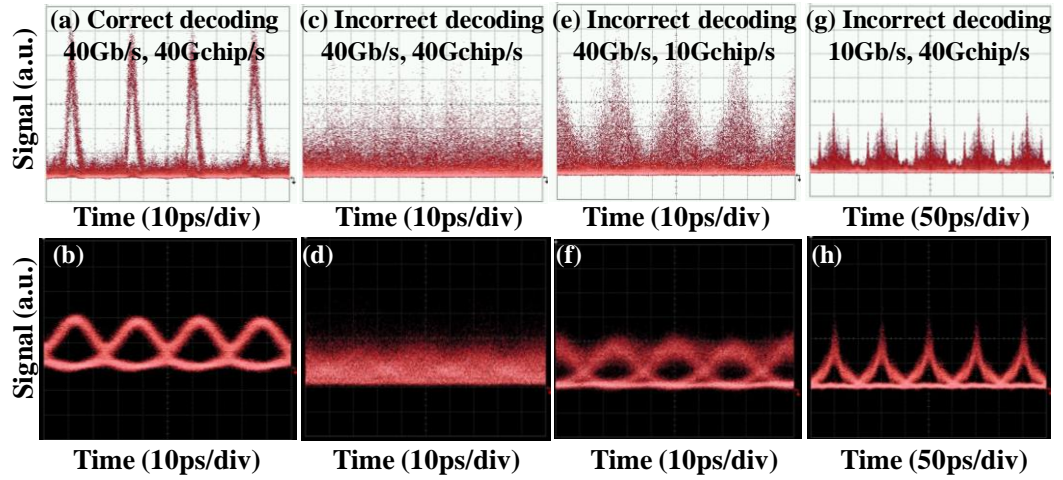


Figure 6.14 Waveforms and eye diagrams for correct (a)~(b) and incorrect (c)~(d) decoding for 40Gb/s, 40Gchip/s, and incorrect decoding (e)~(f) for 40Gb/s, 10Gchip/s, respectively; (g)~(h) are the incorrectly decoded waveform and eye diagram for 10Gb/s, 40Gchip/s.

Figure 6.15 (a) shows the measured spectrum for the correctly decoded signals which has similar profile as the original uncoded spectrum in Fig. 6.12 (a), whereas for the incorrectly decoded spectrum in Fig.6.15 (b), the spectrum profile has not been recovered. The behaviour of a 40Gb/s data pattern stream 101010101111111010110 has also been observed, as shown in Fig. 6.15 (c)~(e). It can be seen that for the low chip rate of 10Gchip/s in Fig. 6.15 (d), the data pattern can still be extracted from the encoded waveform, while for the high chip rate of 40Gchip/s in Fig.6.15 (e), the data pulsea have been spread in the time domain and distorted, so it's hard to extract the correct pattern by using a simple power detector. The measured BER performances for the correctly decoded and de-multiplexed four channel 10-Gb/s RZ-OOK tributaries are
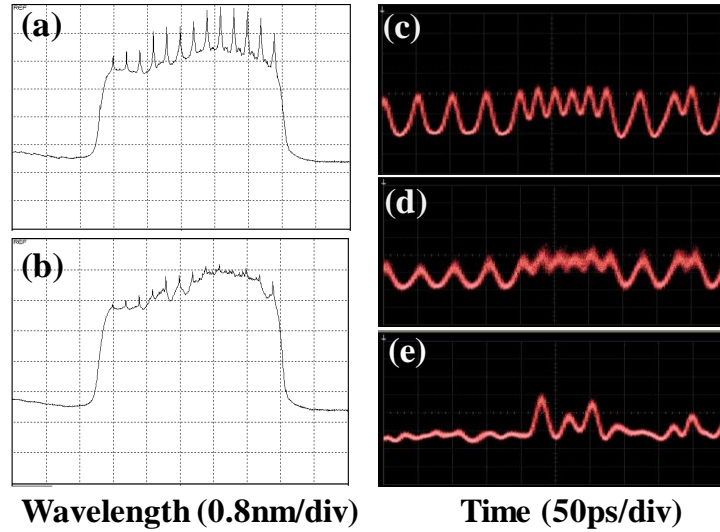
Figure 6.15 (a)-(b) are correctly and incorrectly decoded spectrum; (c)-(e) are waveforms of 40Gb/s original data pattern, encoded patterns with chip rate of 10Gchip/s and 40Gchip/s, respectively.

shown in Fig.6.16. Bit-error-rate lower than $10^{-9}$ has been achieved for all the tributaries with the three codes. Compared with the case of no en/decoding, the average power penalty for the three codes is ~ 1 dB due to the non-ideal decoding for every bit. As for the cross-correlation signals, no BER can be measured, indicating significant security improvement of the 40-Gb/s OOK data. Therefore, in this section, a 40-Gb/s, fast reconfigurable time domain spectral phase en/decoding OOK-OCDMA system secured by the symbol overlapping of both encoded and incorrectly decoded signals, and 40Gchip/s, code-length variable ultra-long OCs of up to 1024 chips is demonstrated. The proposed approach can significantly enhance the OOK data security against eavesdropping using conventional power detection method, which depends on the data rate, chip rate and dispersion. By introducing high dispersion and chip rate, security improvement for various data rates could be expected.



Figure 6.16 BER performances of the four 10-Gb/s tributaries with different code lengths.

## 6.5 40-Gb/s, 40-Gchip/s, secure DPSK-OCDMA system based on bit-by-bit code shifting

In Section 6.2, the security improvement for a 10-Gb/s DPSK data based on the time domain rapid programmable bit-by-bit code shifting technique with highly dispersive eleme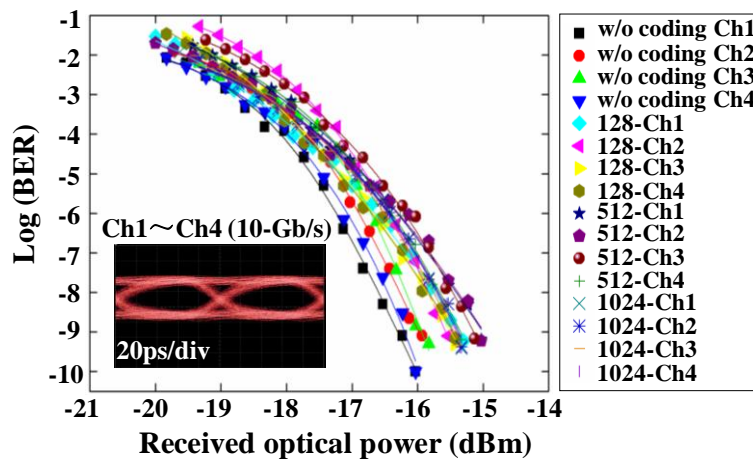nt and phase modulator has been demonstrated. However, to meet the increasing demand of high speed optical communication, the application of this technique desires it to be operated at a data rate beyond 10-Gb/s. In this section, by using the bit-by-bit code shifting technique, the security improvement for a high speed 40-Gb/s phase modulated data against DPSK demodulation attack will be investigated, which shows that this technique can be potentially used for high speed secure optical communication.

Figure 6.17 shows the experimental setup of the 40-Gb/s DPSK-OCDMA system using the time domain bit-by-bit code shifting technique. A 10-GHz MLLD producing 2.8ps optical pulses and spectrally centered at 1550.75 nm is used as the laser source. The 10 GHz pulse train is multiplexed into 40 GHz by a four-stage planar lightwave circuit (PLC) based optical time division multiplexer (OTDM), and then phase modulated at 40 Gb/s by a lithium-niobate phase modulator driven by $2^9$-1 PRBS to generate the 40-Gb/s DPSK data, whose spectrum and corresponding waveform are shown in Figure 6.18 (a) and (b), respectively. To realize the time domain bit-by-bit code shifting, a spool of reverse dispersion fiber with chromatic dispersion of ~ -331ps/nm is used to significantly stretch the input pulse train. As an optical bandpass



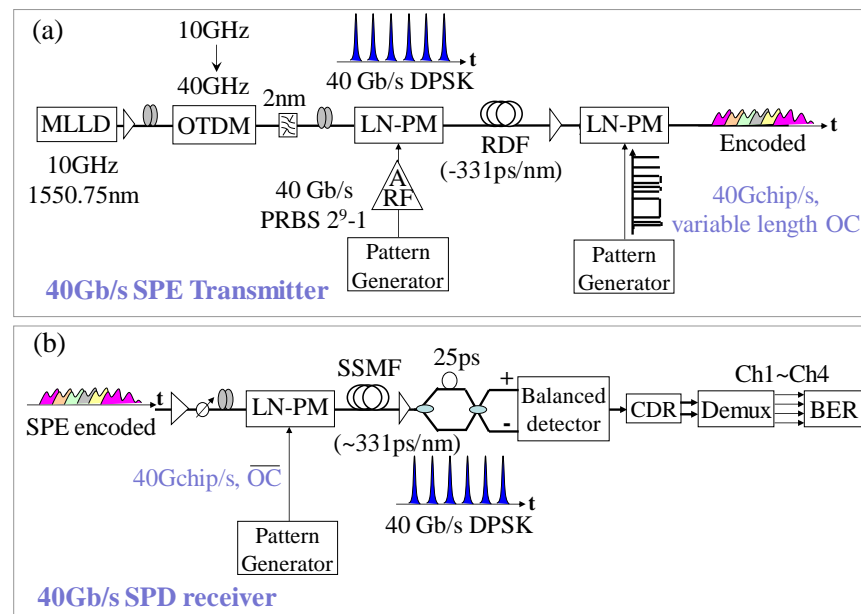Figure 6.17 Transmitter (a) and receiver (b) of the 40-Gb/s DPSK-OCDMA system.

filter with 3dB bandwidth of ~2nm has been used before the phase modulator to alleviate the dispersion mismatch in the system, each bit of the stretched pulse occupies ~662 ps time duration and thus the adjacent consecutive pulses are overlapped with each other after the temporal stretching. Fig. 6.18 (c) shows the waveform of the stretched pulses, which exhibits as a noise-like signal that can make an eavesdropper unaware of its existence. After that, an ultra-long code length variable OC pattern with a chip rate of 40-Gchip/s that can be rapidly programmed by the pulse pattern generator is used to drive another LN-phase modulator to perform time domain phase modulation. Because different spectral components spread into different time position, the phase modulation in time domain is equivalent to spectral phase encoding. Since each bit of the stretched pulse covers more than one bit period, different stretched data pulse will experience different part of the ultra-long OC and bit-by-bit shifted with each other with an effective chip number of ~26.
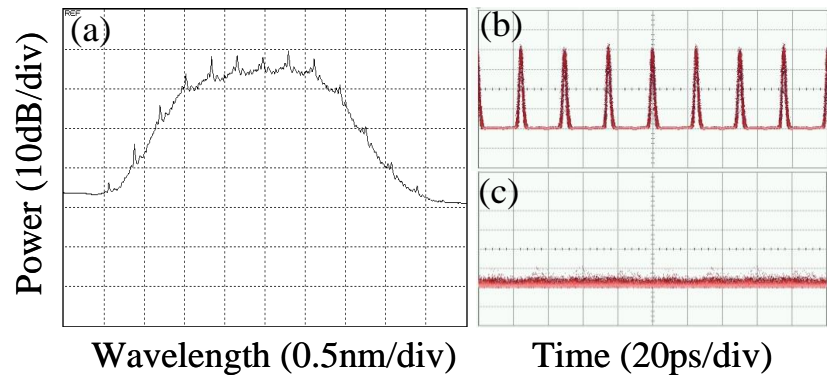


Figure 6.18 (a) Spectrum and (b) waveform of the 40-Gb/s DPSK pulse train; (c) is the waveform of the stretched pulse.

To recover the original data pulse, the SPE signal firstly has to be spectral phase decoded and then temporally compressed using a matched dispersion compensation fiber. Therefore, the security of this system can be guaranteed by both the rapid programmable ultra-long OC and appropriate dispersion. The 40-Gb/s receiver has similar configuration as the SPE section but the phase modulator is driven by the complementary OC patterns for spectral phase decoding, as shown in Fig.6.17 (b). A tunable optical delay line placed before the phase modulator is essential to temporally align the timing error between the encoding and decoding side. Then, a piece of standard single mode fiber (SSMF) with dispersion of approximately ~ +331ps/nm is used to compress the spectral phase decoded signal and regenerate the 40-Gb/s pulse train. A delay line interferometer with one bit delay of 25ps followed by a balanced

photo-detector (BPD) is used for DPSK demodulation and detection. The extracted DPSK data is directed into a 40-Gb/s clock and data recovery circuit and then demultiplexed into four-channel 10-Gb/s tributaries for bit-error-rate measurement.

In order to investigate the security of the 40-Gb/s DPSK-OCDMA system, three types of OC from Gold code plus a zero with different code lengths of 128, 512 and 1024 that are shorter, equal or longer than the data pattern sequence are used for emulating the eavesdropping. In this setup, it is evident that the eavesdropper cannot access to the confidential data if he does not know both the OC and dispersion value simultaneously. However, an eavesdropper may be sophisticated enough and knows the dispersion. Figure 6.19 (a) shows the decoded cross-correlation signal's spectrum for the eavesdropper with matched dispersion compensation but an incorrect OC of 512-chip, which is obviously distinct from the original 40-Gb/s DPSK data modulated spectrum in Fig. 6.18 (a), indicating that the phase relationship between different bits has been broken. The corresponding waveform and eye diagram are shown in Fig.6.19 (b) ~ (c), from which it can be seen that the compressed pulses are still overlapped with each other and the eye diagram exhibits as a noise, which clearly shows extremely high security against eavesdropping.
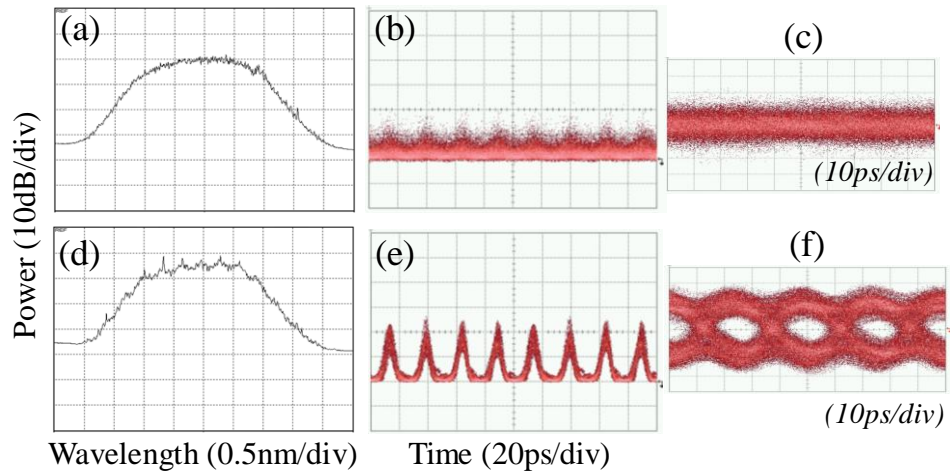


Figure 6.19 (a) Spectrum, (b) waveform and (c) eye diagram of the incorrectly decoded signal with matched dispersion compensation; (d)~(f) are the spectrum, waveform and eye diagram of the correctly decoded signal.

On the contrary, by using a matched dispersion compensation fiber and applying a correct complementary OC, the SPE signal can be decoded and the original data can be retrieved as well. Fig. 6.19 (d) shows the correctly decoded spectrum for the 512-chip OC, from which one can see the similar spectrum profile with some ripples as the original uncoded spectrum in Fig.6.18 (a). The waveform of correctly decoded signal

with high peak power auto-correlation pulse is shown in Fig. 6.19 (e). As each bit experiences a different effective spectral phase pattern, the decoding performance is slightly different for each bit and thus the decoded pulses are no longer uniform. Fig.6.19 (f) shows the corresponding eye diagram with clearly eye opening, which demonstrates that the original DPSK phase information has been successfully preserved after the decoding. One may notice that the waveform of the correctly decoded signal in Fig.6.19 (e) is broader than the original pulse train, which can be attributed to the slight dispersion mismatch of the SSMF in the decoding side. Figure 6.20 shows the auto-correlation traces of the original 40-GHz pulse train after the OBPF, the correctly and incorrectly decoded signals by using an auto-correlator with 60ps scanning range. It can be seen that the optical pulse has been broadened from ~4ps to ~8.7ps due to the non-
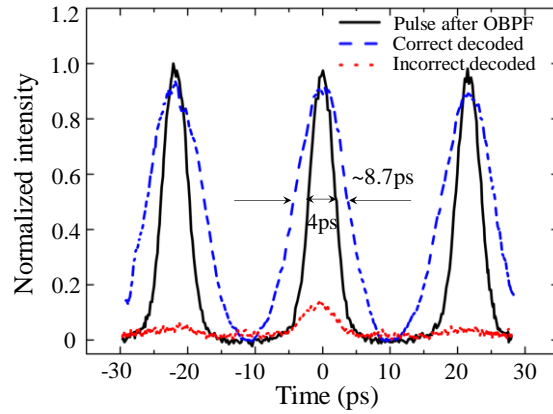


Figure 6.20 Auto-correlation trace of the original pulse after OBPF (solid black line), correctly decoded (blue dash) and the incorrectly decoded signal (red dot line).

ideal dispersion compensation, which corresponds to ~350m SSMF length mismatch with a dispersion slope of ~16.75 ps/nm/km. A tunable optical bandpass filter is thus used to reduce the dispersion mismatch in the experiment. The slight dispersion mismatch can actually emulate the residual dispersion in a practical environment. An auto-correlation signal with high peak power for the correct decoding can still be obtained despite of the mismatch, as shown in Fig.6.19 (e). In contrast, only a cross-correlation signal with low peak power is obtained for the incorrect decoding. By using a pair of chirped fiber Bragg gratings with ideal dispersion compensation, significant improvement of the decoding performance could be expected.

Figure 6.21 depicts the simulated peak intensity reduction and BER degradation due to the SSMF length mismatch using the software optisystem 7.0. The received optical power is assumed as -13.6dBm at BER of $10^{-9}$. It can be seen that the peak intensity and BER gradually deteriorate with the increase of the mismatch, and thus introducing
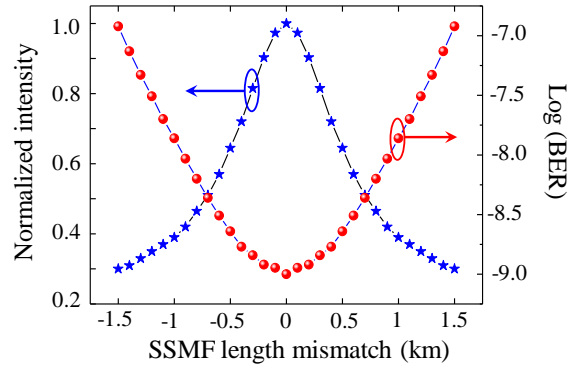
Figure 6.21 Peak intensity and BER degradation versus the SSMF length mismatch.

power penalty at the receiver. The tolerance to the SSMF length mismatch is ~1.5 km for a peak intensity and BER degradation from 1 to 0.3 and $10^{-9}$ to $10^{-7}$, respectively. As shown in Figure 6.22, the BER performances of the 40-Gb/s DPSK signals are evaluated after being demultiplexed into 10-Gb/s data using an electrical demultiplexer for the three OCs. The eye diagram of the demultiplexed four-channel 10-Gb/s tributaries is also shown in the inset with clear eye opening. Comparing with the back-to-back case, the power penalty is around 2.5dB after the decoding which is mainly caused by the SSMF length mismatch and non-ideal decoding. BER lower than $10^{-9}$ has been achieved for all the OCs, which demonstrates the time domain bit-by-bit code shifting approach for high data rate secure optical communication.
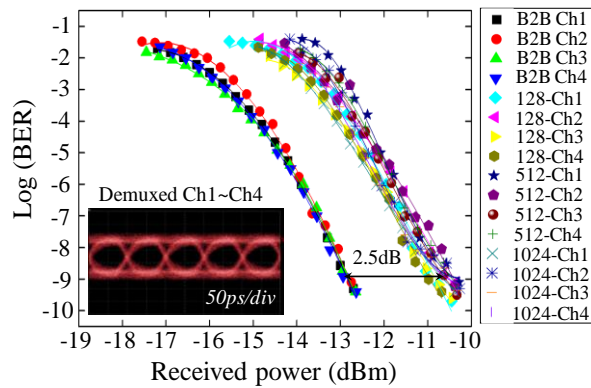


Figure 6.22 BER curves of the four demultiplexed 10-Gb/s DPSK data tributaries.

## 6.6 Investigation of security improvement for 40-Gb/s, DQPSK-OCDMA system using bit-by-bit code shifting

In optical communication system, it is always desirable to improve the transmission capacity by efficiently utilizing the limited spectral bandwidth. In addition to improve

the data rate from 2.5Gb/s to 40Gb/s, advanced optical modulation formats are one of the most appreciable solutions to improve the spectral efficiency [84]. As has been employed in the experimental demonstrations, DPSK data modulation is a primary example which can provide a 3dB receiver sensitivity improvement compared to the OOK as well as its high tolerance to nonlinear impairment [84-85]. However, there is a research trend towards multi-level modulation format as they are more spectrally efficient [129-130]. A typical format is differential-quadrature-phase-shift-keying (DQPSK), which can provide a spectral efficiency of 2 bit/symbol. And also for the same data rate, the symbol rate is reduced by a factor of two, and consequently, the spectral occupancy is reduced, and the requirement for the transmitter and receiver bandwidth is relaxed [130]. In this section, the application of the time domain bit-by-bit code shifting technique for the DQPSK data modulation format is investigated.

## 6.6.1  Differential quadrature phase shift keying

DQPSK data modulation usually has four phase levels $(0, \pi/2, \pi, 3\pi/2)$, as shown in Figure 6.23. Each symbol can carry two bits information, for example, the phase level "0" represent for bit "00", "$\pi/2$" for "01", "$\pi$" for "10" and "$3\pi/2$" for "11". Therefore, in DQPSK system, the symbol rate is only half of the bit rate that leads to the reduction of cost and complexity [84-85]. Conventionally, the DQPSK transmitter can be implemented by parallelly cascaded two Mach-Zehnder (MZ) modulator [84-853, 129-130], as shown in Figure 6.24 (a). In this structure, two sub MZ modulators are embedded in both arms of a main MZ modulator, and they are driven independently by the in-phase component (I) and quadrature component (Q) that are synchronously aligned with each other. Each sub MZ modulator is biased at its null point and driven by a data voltage of $2V_\pi$. A phase difference of $\pi/2$ is introduced in one of the arms in the main MZ modulator to form a quadrature phase combination. The DQPSK can also be
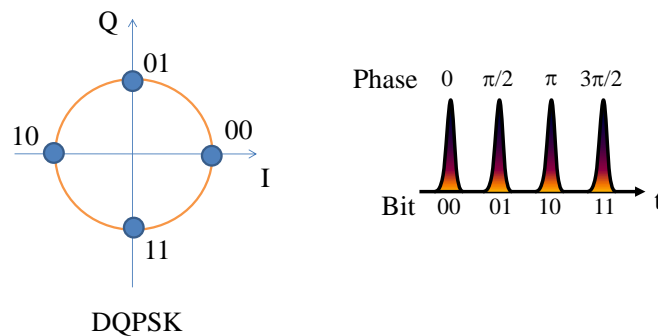


Figure 6.23 Symbol diagram and example waveform of DQPSK modulation format.

realized by serial cascading an MZ modulator for I-channel encoding followed by a phase modulator for the Q-channel encoding [129-130]. The optical phase between the I and Q channels is set to π/2 by adjusting the applied bias to the PM. In both structures, the MZ modulators can be replaced by a phase modulator with appropriate phase modulation depth. The parallel configuration is practically easy to integrate and has improved stabilization in phase shift between the two arms [129].

To recover the I and Q channel data, a DQPSK demodulator should be used, as illustrated in Fig. 6.24(b) [84-85]. An optical delay interferometer with a delay of the symbol period (twice the bit period) is employed for both the I and the Q channels, while the phase shift between the two arms in both interferometers is set as π/4 and -π/4, respectively. The output instructive and destructive signals of the interferometer are detected by a balanced detector, and the data signal can be eventually recovered after electrical signal processing.
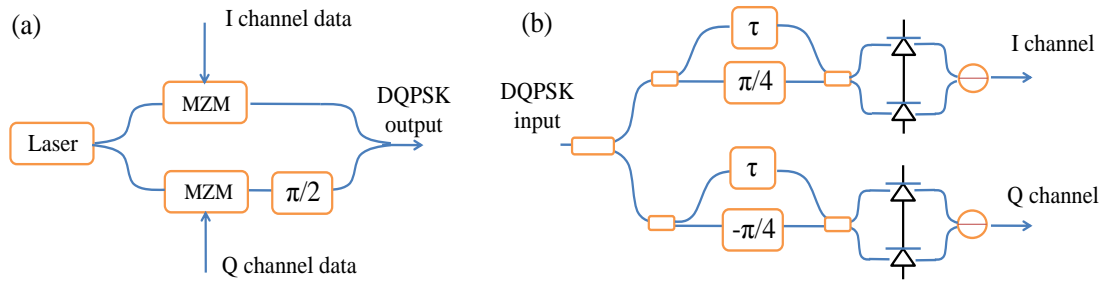


Figure 6.24 (a) DQPSK transmitter using parallel cascaded MZ modulators and (b) receiver.

## 6.6.2  40-Gb/s, DQPSK-OCDMA system simulator and results

To investigate the capability of supporting advanced DQPSK modulation format based on the time domain bit-by-bit code shifting scheme, a system simulation has been carried out by using the commercial available software package optisystem 7.0. Figure 6.25 shows the simulation setup, which employs a parallel cascaded MZM for the DQPSK transmitter. The pseudorandom 40-Gb/s data is precoded by an encoder into DQPSK modulation format and split into two 20-Gb/s pattern streams: the I and Q channel, which drive the sub MZMs independently. The generated 40-Gb/s DQPSK signal is shown in Figure 6.26, from which one can see that the output 40-GHz DQPSK pulse train has a pulse width of ~3 ps and the spectrum occupies ~ 4nm bandwidth. To verify the four phase levels in pulse stream, the DQPSK data modulated pulse is firstly directly injected into the I and Q demodulator in the back-to-back case, whose symbol
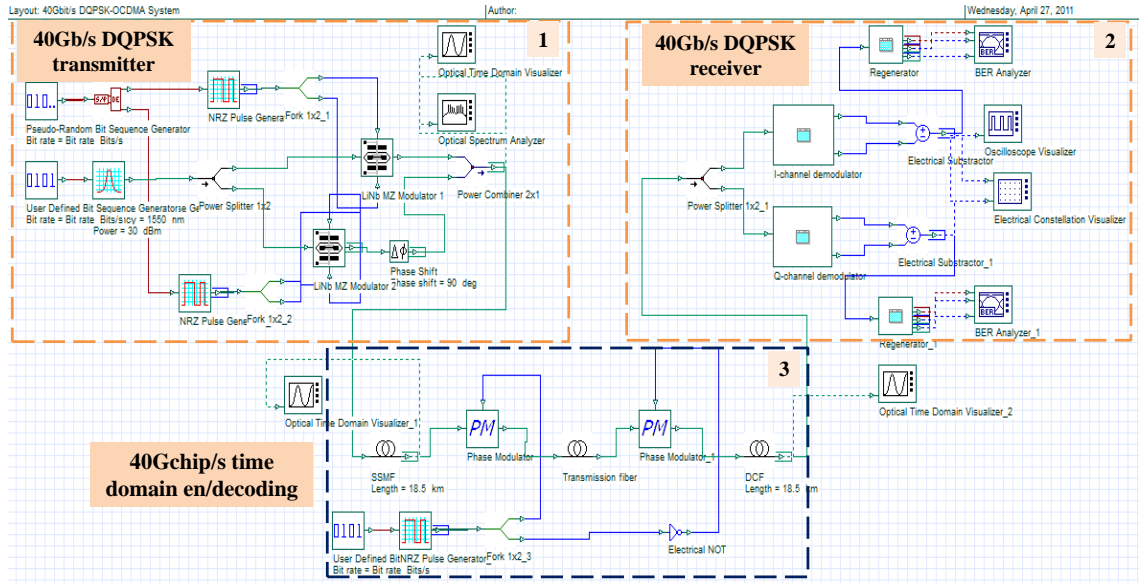
Figure 6.25 Simulation setup of the 40-Gb/s, time domain DQPSK-OCDMA system.

constellation diagram and demodulated eye diagrams for the I and Q channels are shown in Figure 6.27 (a) ~ (c), respectively. As can be seen, there are four phase levels in the symbol constellation diagram corresponding to the symbol {00, 01, 10, 11} and clear eye diagrams have been achieved for both the I and Q channels. After that, the time domain bit-by-bit code shifting block which consists of a piece of 18.5km SSMF for pulse stretching and a high speed 40-Gchip/s phase modulator driven by 32-chip OC: 01001010010100010101010111001011, is introduced after the DQPSK transmitter for optical encoding. The non-return-to-zero (NRZ) OC generator is assumed to have a rise and fall time of 0.1 bit in the simulation. The time domain spectral phase encoded signal is then decoded using a similar setup with another phase modulator driven by phase conjugate code pattern and a fiber with opposite dispersion for temporal compression, and finally demodulated for DQPSK data recovery. Figure 6.28 (a)~(c) show the detected symbol constellation diagram and corresponding I and Q eye diagrams after correct decoding, from which one can clearly see that the four phase
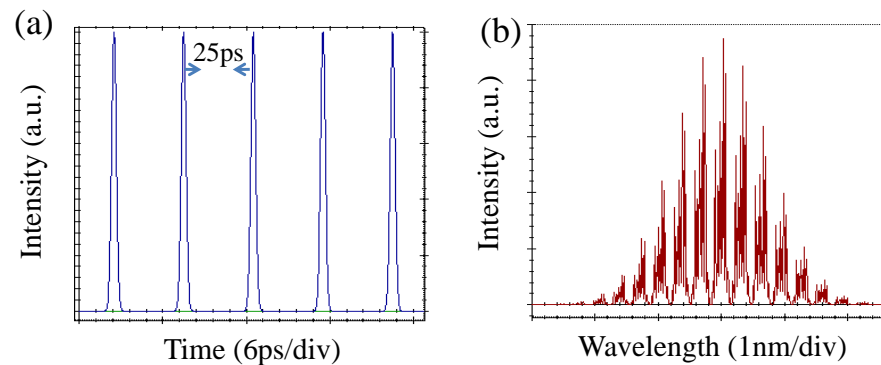


Figure 6.26 Waveform (a) and spectrum (b) of the 40-Gb/s DQPSK pulse train.
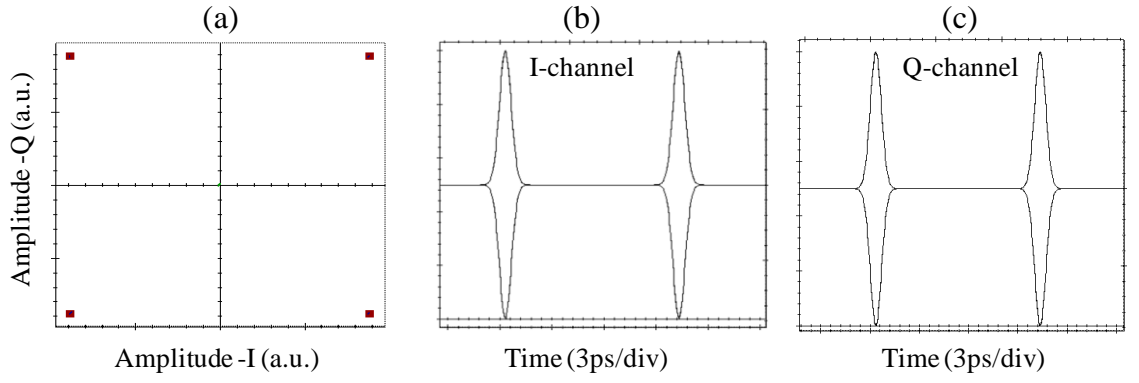
Figure 6.27 (a) Back-to-back symbol constellation diagram and demodulated eye diagram for (b) I and (c) Q channels.

levels can be extracted and the eye diagrams are opening. Compared with that of the back-to-back, the constellation diagram has some phase drifts resulting in the phase noise in the eye diagrams, which is primarily caused by the rise and fall code transition of the pattern generator assumed in the simulation. Conversely, for the incorrect decoding, a pseudorandom phase shift has been applied into the decoded signal, so only a constellation diagram with random phase levels can be obtained, and the resultant eye diagrams for the I and Q channels exhibiting as a noise and have no opening as can be seen from Fig.6.28 (d)~(f), which verifies security enhancement against eavesdropping
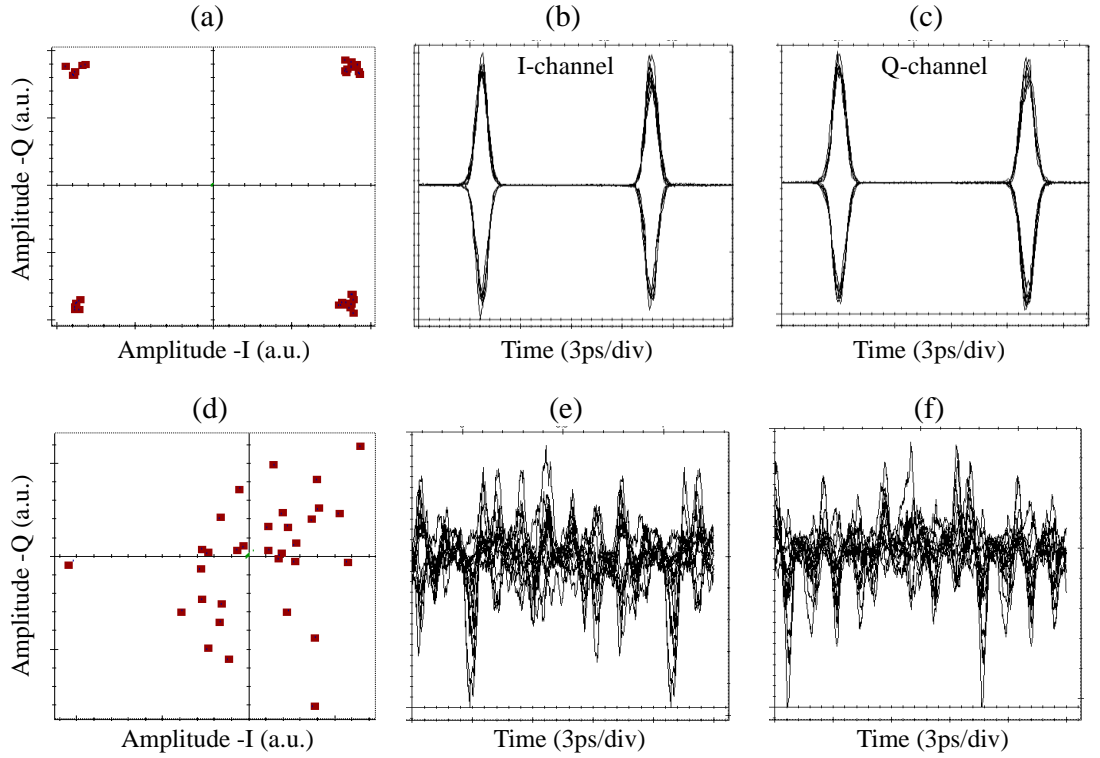


Figure 6.28 (a) Symbol constellation diagram, and demodulated I (b), Q (c) channels eye diagram for correctly decoding; (d) ~ (f) are the incorrectly decoded symbol constellation diagram, demodulated eye diagrams for I and Q channels, respectively.

138

without the proper OC. The proof-of-principle simulation indicates that the time domain bit-by- bit code shifting technique is potentially compatible with the four-level DQPSK data modulation, and even more advanced, spectrally efficient modulation formats such as D8PSK, QAM, for improving the security of time domain spectral phase en/decoding OCDMA system.

## 6.7   Summary

In this chapter, a novel time domain bit-by-bit code shifting technique using highly dispersive elements and phase modulator has been proposed for improving the data rate and enhancing the security of time domain spectral phase en/decoding OCDMA system. The proposed technique enables rapid programming the optical code that is code-length variable and has a large unprecedented code space. Based on this scheme, security enhancement of 10-Gb/s and 40-Gb/s time domain SPE/SPD-OCDMA systems with DPSK data modulation format with a high chip rate of 40Gchip/s and code length of up to 1024 chips are demonstrated. A novel approach based on symbol overlapping is further proposed to improve the OOK data security against eavesdropping using conventional energy detection attack and a 40Gb/s OOK-OCDMA system is demonstrated. In the OOK optical system, the data security mainly depends on the dispersion and chip rate. By increasing the two values, security enhancement in such an OOK system with various data rates could be achieved. Finally, the application of the bit-by-bit code shifting technique in advanced DQPSK data modulation systems for improving the data security is also investigated by simulation, which shows that this technique can be potentially used for advanced data modulation formats. It is also possible to upgrade this technique to higher data rate and longer code length to realize even one time pad for high speed optical code based secure communication.

# CHAPTER 7

# A novel tunable 2-D coherent optical en/decoder based on coupled micro-ring resonator optical waveguide

As one of the key devices in OCDMA system, various optical en/decoders have been previously developed for either 1-D or 2-D OCDMA en/decoding, such as fiber optical delay line, planar lightwave circuits, spatial light modulator and superstructured FBG *etc*, which has been discussed in Chapter 2. However, there has no report on 2-D coherent optical en/decoder until now [17, 36], although the 2-D OCDMA has larger code cardinality compared with the 1-D OCDMA and it can potentially enhance the capacity and security of OCDMA system. It is desirable to develop a type of 2-D coherent optical en/decoder for 2-D OCDMA applications. Moreover, it would be more attractive for future flexible and dynamic OCDMA networks that the 2-D coherent optical en/decoder can be fast reconfigured.

On the other hand, optical micro-ring resonator based integrated photonic devices have received great research attention in recent years as they can provide a useful platform for various signal processing in a ultra-small volume (with typical diameters in the order of micrometres). They are particularly attractive for large scale photonic integrations [133-136]. The optical micro-ring resonator is analogous to a traditional Fabry-Perot cavity consisting of two parallel mirrors, in which the optical field bounces back and forth between the two mirrors with increased effective optical paths, and thus it can be used for diverse applications such as optical channel add/drop filters [133], optical switches [136], optical delay lines [137-139], optical logic gates [140-141], optical modulator [142] and photonic biosensors [143], etc.

The optical micro-ring resonator is firstly suggested by *Marcatili* [144] in the early 1960's, but it was not until the 1990's that a large amount of researches began to emerge with the mature of fabrication technologies for the micro-ring resonators. Generally, the micro-ring can be fabricated in two coupling configurations: laterally coupling and vertically coupling [145-147]. When the ring and waveguide are fabricated in the same waveguide layer, the configuration is called 'laterally coupling', while if the ring and the waveguide are in different layers, it is called 'vertically coupling'. The vertical coupling configuration has the advantage that the coupling depends mainly on the thickness of the

layer in between, which can be controlled very accurately during deposition, and therefore it is widely used in the micro-ring fabrication. Various micro-rings have been fabricated in a wide range of materials such as silicon [142], III-IV semiconductors [136, 140-141], and polymer [148]. Besides the advances of fabrication technique, the micro-ring design method has also achieved great development, which mainly includes transfer matrix method [149], pole-zero method [150], characteristic matrix method [151]. As the transfer matrix method is easy to operate and can deal with complex structure, it is adopted in this chapter.

Previously, a micro-ring resonator based optical en/decoder has been proposed and demonstrated, which has the advantages of compact, programmable, ultrafine frequency resolution and accurate phase control, allowing the precise tailoring of the spectral-phase characteristics of a broadband coherent optical signal [69]. A six-user OCDMA system at data rate of 2.5Gb/s using this device with eight-chip optical codes has been reported [70]. The micro-ring resonator based optical en/decoder is suitable for high-level photonic integration with other photonic devices to enable ultrafast optical signal processing in a chip. However, this device can only perform spectral phase encoding in one dimension.

In this chapter, a novel 2-D coherent optical en/decoder based on coupled micro-ring reflectors is proposed for 2-D coherent OCDMA application. The proposed device is very flexible to generate and recognize the 2-D optical code, and can simultaneously reconfigure the wavelength hopping and spectral phase patterns using a single device.

## 7.1 Basics of coupled mode theory

Optical waveguide is the fundamental building block of the micro-ring resonators, and theoretical analysis of the waveguide coupling is one of the most important issues in understanding the transmission property of micro resonators. Optical coupled mode theory is a widely used method for analyzing the waveguide coupling. We will now establish the coupled mode equation from the wave equations that governs the electromagnetic field propagation [152-153]. The wave equation for the electrical field $E$ can be given as:

$$\nabla^2 \vec{E}(x,y,z) + k_0{}^2 n^2 \vec{E}(x,y,z) = 0 \tag{7.1}$$

Assuming there are two parallel straight waveguides along the $z$-direction, as illustrated in Figure 7.1. The electrical field $E$ for each of the waveguide can be expressed as:
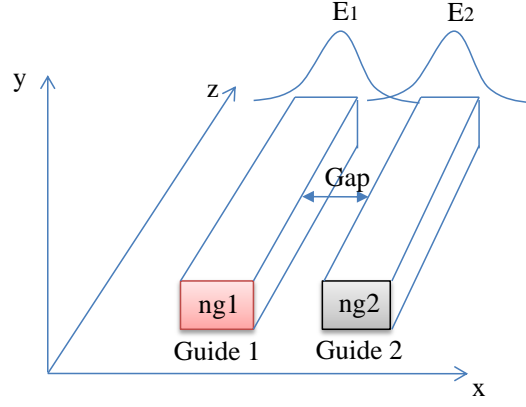
Figure 7.1 Schematic diagram of two parallel rectangular waveguides and the overlapped transverse fields.

$$E_i(x, y, z) = E_i(x, y)\exp(-i\beta_i z)\,(i{=}1,2) \tag{7.2}$$

Thus we can obtain the wave equation for each waveguide as:

$$\frac{\partial^2 E_i(x, y)}{\partial x^2} + \frac{\partial^2 E_i(x, y)}{\partial y^2} + (k_0^2 n^2_i - \beta^2_i)E_i(x, y) = 0 \tag{7.3}$$

When the two waveguides are closely placed with a small gap, the evanescent fields of both waveguides will overlap and thus coupling occurs between the waveguides, which can be described by the linear combination of the two fields as [152]:

$$E(x, y, z) = A(z)E_a(x, y)\exp(i\beta_a z) + B(z)E_b(x, y)\exp(i\beta_b z) \tag{7.4}$$

Here, the $A(z)$ and $B(z)$ are the mode amplitude as a result of coupling, and the $\beta_a$ and $\beta_b$ are the propagation constant. By inserting Eq. (7.4) into the wave equation and making use of the isolated wave equations for each waveguide using Eq.(7.3), the coupled mode equations can be obtained under the slowly varying field approximation,

$$\begin{aligned}\frac{dA}{dz} &= i\kappa B \exp(-i\Delta\beta z)\\[1mm]\frac{dB}{dz} &= i\kappa A \exp(i\Delta\beta z)\end{aligned} \tag{7.5}$$

where a new parameter $\kappa$ is introduced which is known as the coupling coefficient between waveguides, and $\Delta\beta$ is the mismatch of the propagation constant. For identical waveguides, the mismatch is negligible, and the solution of the coupled mode equations can be expressed as:

$$\begin{bmatrix} A(z) \\ B(z) \end{bmatrix} = \begin{bmatrix} \cos\kappa z & i\sin\kappa z \\ i\sin\kappa z & \cos\kappa z \end{bmatrix} \begin{bmatrix} A(0) \\ B(0) \end{bmatrix} \tag{7.6}$$

Assuming that $t = \cos\kappa z$, $k = \sin\kappa z$ which are called straight coupling and cross-coupling coefficient and $k^2 + t^2 = 1$ for losses coupling, the coupled mode equations can be

further simplified as:

$$\begin{bmatrix} A(z) \\ B(z) \end{bmatrix} = \begin{bmatrix} t & ik \\ ik & t \end{bmatrix} \begin{bmatrix} A(0) \\ B(0) \end{bmatrix} \tag{7.7}$$

One should note that the coupling introduces a phase shift of $\pi/2$ between the two output ports, as indicated by the factor $i$. The coupled mode equation (7.7) can be used to describe the coupling between the micro resonator and straight waveguide, and it constitutes as the foundation for analyzing the micro-resonator structures throughout this thesis.

## 7.2 Tunable 2-D coherent optical en/decoder based on coupled double micro-ring reflector

In this section, we will introduce the proposed tunable 2-D coherent optical en/decoder based on a coupled double micro-ring reflector. The operation principle of the proposed device is explained in Section 7.2.1, followed by a theoretical analysis using the coupled mode theory in Section 7.2.2; and then in section 7.2.3, we will optimize the coupling coefficient for achieving single peak reflection and investigate the reflection property by considering fabrication error and propagation loss. The resonant wavelength tuning is also analyzed in the last section.

### 7.2.1 Principle of coupled double micro-ring reflector based optical en/decoder

Figure 7.2 (a) shows the configuration of the proposed device, which consists of several pairs of identical coupled double micro-ring reflectors. In Fig.7.2 (a), five pairs are used as an example. Each pair is composed of two weakly coupled ring resonators that are both coupled to a bus optical waveguide [154]. A heater is laid over every single ring resonator to change the effective refractive index by using thermal-optic effect to tune the resonant wavelength. Carrier injection or electro-optic effect can also be applied under the p-i-n diode structure to enable high speed electrical tuning [142]. A phase shifter (PS) is placed on the bus waveguide between two adjacent pairs of coupled reflectors to adjust the relative phase shift of the reflected spectral component according to the optical code pattern: $\pi$ phase shift for symbol "-1", or 0 phase shift for symbol "1". The interval between every two reflectors is $L$ corresponding to time delay $T=2nL/c$,
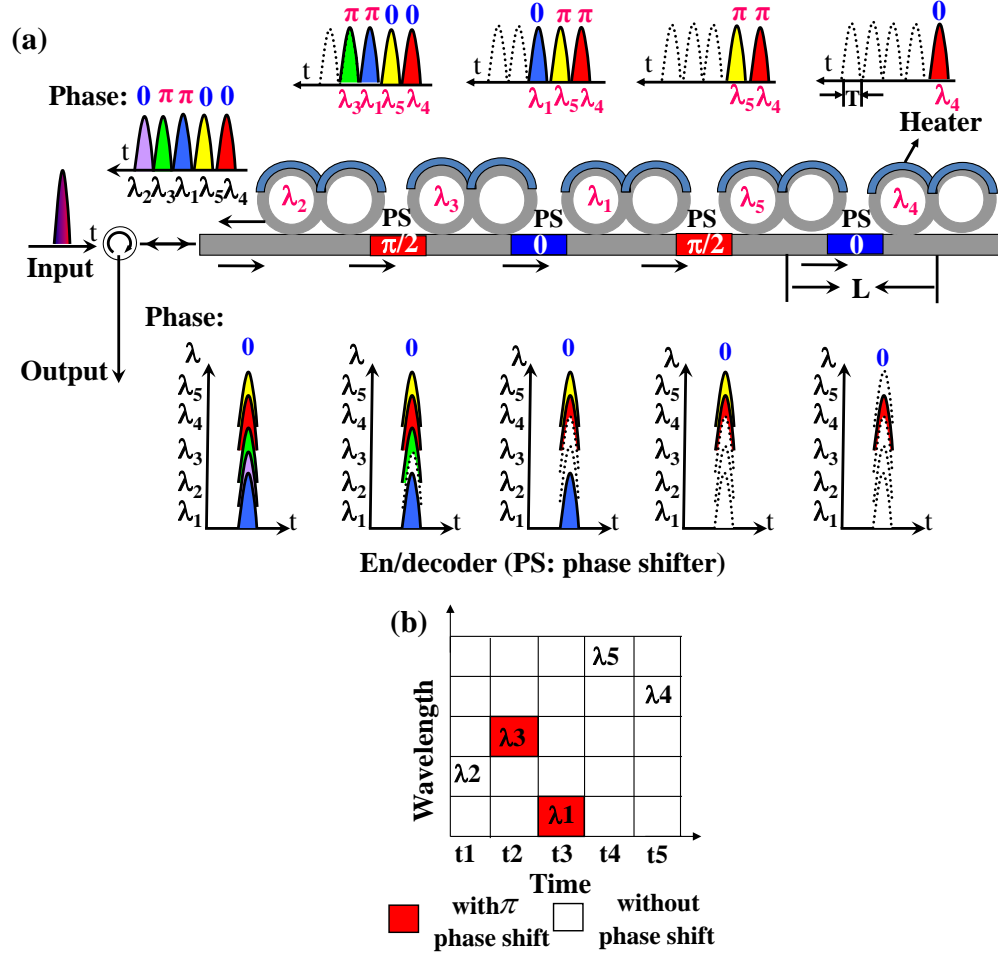
Figure 7.2 (a) Schematic diagram of proposed optical en/decoder and (b) the lookup map of the 2-D optical code to be generated.

where $c$ is the light velocity, $n$ is the effective refractive index. $T$ is chip duration of the optical code.

The working principle of this device is described as below. The 2-D coherent optical code to be generated in this example is shown in Fig.7.2 (b). The wavelength hopping code (WHC) is ($\lambda_2$, $\lambda_3$, $\lambda_1$, $\lambda_5$, $\lambda_4$) and the spectral phase code (SPC) is (0, $\pi$, $\pi$, 0, 0). An ultra-short optical pulse with a broadband spectrum is coupled into the bus waveguide via either an optical circular or coupler for integration with other photonic devices. By properly tuning the resonant wavelength of the first pair of coupled reflectors, the spectral component of $\lambda_2$ is on resonance. $\lambda_2$ is therefore reflected back and output from the waveguide, while the other wavelengths ($\lambda_1$, $\lambda_3$, $\lambda_4$, $\lambda_5$) will transmit through the structure. Similarly, the spectral component of $\lambda_3$ is reflected back from the second reflector after experiencing a relative time delay of $T$ and has $\pi$ relative phase shift adjusted by the first PS ($\pi/2$ phase shift as light pass through it twice). The remaining spectral components of $\lambda_1$, $\lambda_4$, $\lambda_5$...are operated in the same manner by the rest reflectors

144

and the output signal from the waveguide is encoded by the 2-D optical code. Both the WHC and SPC can be reconfigured simultaneously by the heaters and PSs, respectively. The decoder is exactly the same structure as the encoder but with the reverse wavelength and phase pattern.

## 7.2.2 Coupled mode theory for the coupled double micro-ring reflector

Figure 7.3 shows the detailed structure of the coupled double micro-ring resonator reflector, which is composed of two identical micro-rings coupled with other and then both coupled to a common bus waveguide [154]. It can be seen that when the input wavelength is tuned on resonance, the resonant wavelength will be reflected back and the non-resonant wavelength will transmit through the structure. Each coupled micro-ring reflector can generate one frequency bin which acts as a spectral chip. To realize fast wavelength hopping, single peak flat-top spectral response of each frequency bin is required which can be achieved by properly optimize the ring-bus and ring-ring coupling coefficient $k_{rb}$ and $k_{rr}$, respectively. In this structure, there are two propagation waves: the clockwise and counter-clock wise wave, which are coupled with each other through the two micro-rings. As there are multiple optical paths for both waves, complicated interference will happen at the input and output ports, and under certain conditions, reflection can be achieved.



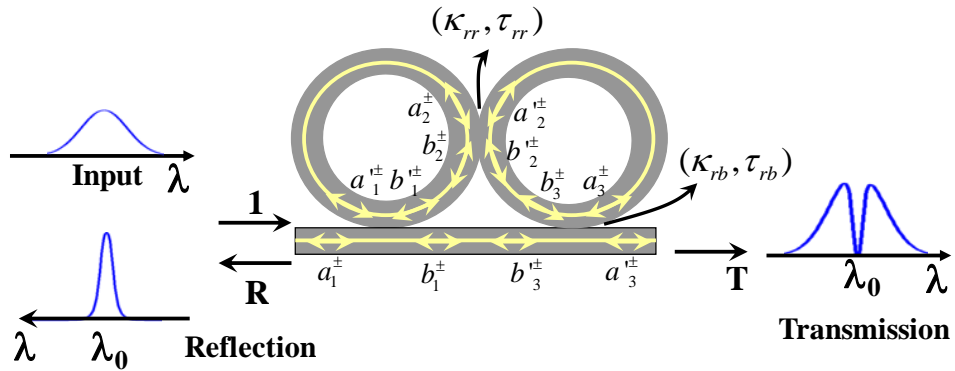Figure 7.3 Structure of the coupled double micro-ring reflector.

To analyze the reflection property of the coupled micro-ring reflector, coupled mode theory presented in Section 7.1 can be used [154]. For simplicity, the electric field in the rings is denoted as the matrix expression:

$$x_i = [a^+_i \quad b^+_i \quad a^-_i \quad b^-_i]^T$$
$$x'_i = [a'^+_i \quad b'^+_i \quad a'^-_i \quad b'^-_i]^T$$

$$(7.8)$$

($i$=1, 2, 3), where the $a^+_i$、 $b^+_i$、 $a^-_i$、 $b^-_i$ and $a'^+_i$、 $b'^+_i$、 $a'^-_i$、 $b'^-_i$ represents the corresponding electric fields in the coupler port, and "+" and "-" correspond to the clock-rise and anti-clock rise directions. The coupling of the electric field from the ring to the bus waveguide for the $i_{th}$ coupler can be represented by:

$$x'_i = P_i x_i \tag{7.9}$$

Where $P_i$ is the coupling matrix for each coupler, and is given by

$$P_i = \frac{1}{-ik_i} \begin{bmatrix} -t_i & 1 & 0 & 0 \\ -T_i & t_i^* & 0 & 0 \\ 0 & 0 & -t_i & 1 \\ 0 & 0 & -T_i & t_i^* \end{bmatrix} \tag{7.10}$$

The $k_i$ and $t_i$ are the cross-coupling and straight coupling coefficient for the $i_{th}$ coupler, $T_i = |k_i|^2 + |t_i|^2$ is the power transmission ($T_i$ =1 for losses coupler). For the ring-bus coupler, $k_i = \kappa_{rb}$, $t_i = \tau_{rb}$, while for the ring-ring coupler, $k_i = \kappa_{rr}$, $t_i = \tau_{rr}$. The electric field inside the rings can be related by the following equations:

$$x_{i+1} = Q_i x'_i \ (i=1, 2) \tag{7.11}$$

where $Q_i$ is the coupling matrix inside the ring and is given by

$$Q_i = \begin{bmatrix} 0 & 0 & 0 & e^{-j\beta_i R_i \theta_i} \\ 0 & 0 & e^{j\beta_i R_i (2\pi-\theta_i)} & 0 \\ 0 & e^{-j\beta_i R_i (2\pi-\theta_i)} & 0 & 0 \\ e^{j\beta_i R_i \theta_i} & 0 & 0 & 0 \end{bmatrix} \tag{7.12}$$

The $\beta_i = 2\pi n_i / \lambda$ is the propagation constant, $n_i$ is the refractive index, $R_i$ is the ring radius, and $\theta_i = \pi/2$. By combining the Eq. (7.9) and (7.11), we can get the electric fields in the output bus waveguide as:

$$x'_3 = P_3 x_3 = P_3 Q_2 x'_2 = P_3 Q_2 P_2 x_2 = P_3 Q_2 P_2 Q_1 x'_1 = P_3 Q_2 P_2 Q_1 P_1 x_1 \tag{7.13}$$

Let $P_3 Q_2 P_2 Q_1 P_1 = A$, the Eq. (7.13) can be simplified as

$$x'_3 = A x_1 \tag{7.14}$$

If there is no input optical signal in the output waveguide namely $a^+_1$=1 and $a^-_3$=0, the following matrix can be derived by Eq. (7.14),

$$\begin{bmatrix} b^-_1 \\ b^+_1 \\ a^-_1 \\ a'^+_3 \end{bmatrix} = \begin{bmatrix} A_{11} & A_{12} & A_{14}-e^{-j\beta l} & 0 \\ A_{21} & A_{22} & A_{24} & 1 \\ A_{31} & A_{32} & A_{34} & 0 \\ A_{41}-e^{j\beta l} & A_{42} & A_{44} & 0 \end{bmatrix}^{-1} \begin{bmatrix} -A_{13} \\ -A_{23} \\ -A_{33} \\ -A_{43} \end{bmatrix} \tag{7.15}$$

From the above the matrix equation, the reflection and transmission coefficient of the

coupled double micro-ring resonator can be given by:

$$R = \frac{a^-_1}{a^+_1}$$

$$T = \frac{a'^+_3}{a^+_1}$$

(7.16)

and therefore, the reflection spectrum can be eventually obtained by solving the Eq. (7.15) and (7.16).

## 7.2.3 Reflection characteristics of coupled double micro-ring resonator

In this section, the reflection characteristic of the coupled double micro-ring resonator is comprehensively analyzed. The optimization of the ring-bus and ring-ring coupling coefficients that mainly determine the reflection profile is discussed at first. Then, the effect of fabrication error and ring loss on the reflection spectrum and the tuning method of the resonant wavelength are also investigated.

**Coupling coefficient**

In the proposed 2-D en/decoder, each frequency bin is provided by one pair of coupled double micro-ring resonator that requires single peak and box-like reflection
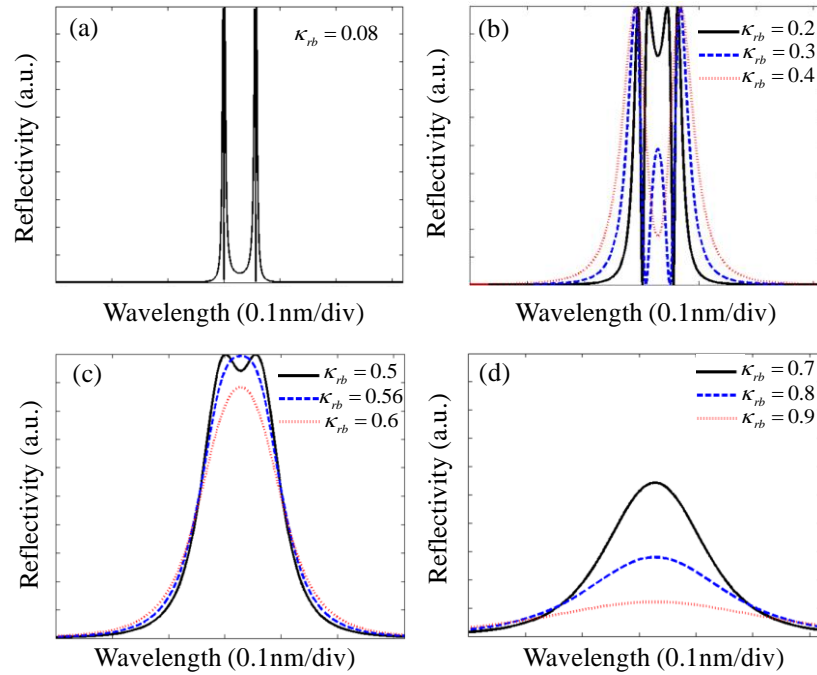


Figure 7.4 Reflection spectrum with different ring-bus coupling coefficients for $\kappa_{rr}$ =0.08.

spectrum, which can be achieved by optimizing the coupling coefficients. In the simulation, both of the two rings in each reflector are assumed identical and have a ring radius of 50μm. The effective refractive index related to the waveguide guiding and cladding materials is chosen as 3 to get the resonant wavelength around 1550nm. Figure 7.4 shows the simulated reflection spectrum for different ring-bus coupling coefficients when keeping the ring-ring coupling coefficient as a constant $\kappa_{rr}$=0.08. It can be seen from Fig.7.4 (a) that when $\kappa_{rb}$ is equal to $\kappa_{rr}$, there are two reflection peaks with splitting spectrum, and with the increase of the $\kappa_{rb}$, the split peaks gradually approach to each other as shown in Fig.7.4 (b), and then eventually evolve into a single peak when the $\kappa_{rb}$ approximate to 0.56 (c). In the process of spectrum evolution, a nearly flat-top filter response appears which indicates that it is possible to design a box-like reflection spectrum by properly choosing the ring-bus coupling coefficient for specific ring-ring coupling. Further increase of the ring-bus coupling will cause the peak reflectivity degradation, as is shown in Fig.7.4 (d). Figure 7.5 (a)~(b) shows the periodical optimized single peak reflection spectrum around 1550nm and its corresponding phase response, respectively. It can be seen that the free spectral range (FSR) of the reflection spectrum is about 2.5nm for the device and there is an abrupt phase shift when the ring is on resonance, which is determined by the resonant condition:

$$2\pi R n_{eff} = m\lambda \tag{7.17}$$

where $m$ is an integer, $n_{eff}$ is the effective refractive index, and the FSR can be derived as:

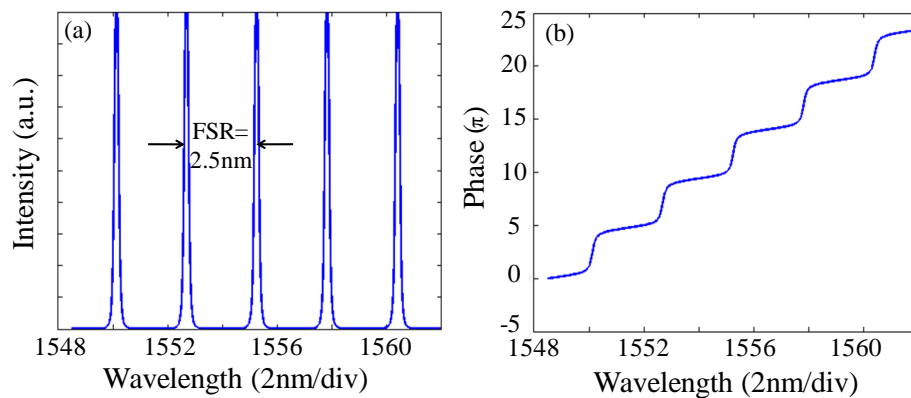$$FSR = \frac{\lambda^2}{2\pi R n_{eff}} \tag{7.18}$$



Figure 7.5 (a) Periodical reflection spectrum and (b) its corresponding phase response.

For silicon material with effective refractive index of around 3.48 [155], or III-V semi conductors like GaAs-Al$_x$Ga$_{1-x}$As that can be engineered via adjustment of the

composition $x$ to achieve a refractive index of 2.9~3.4 [156-157], the FSR is about 2.5nm for ring radius of 50um that allows the resonant wavelength tuning within 5nm spectral range which is enough for general purpose. Small radius can enlarge the FSR but may introduce high loss as the bend loss of the resonator is inversely proportional to the ring radius [158].

An optimization of various $\kappa_{rb}$ and $\kappa_{rr}$ to achieve single peak operation is further carried out, as shown in Figure 7.6 (a) represented by the solid line with circles, in which the optimized $\kappa_{rb}$ increases with the $\kappa_{rr}$. Because of the inevitable fabrication error in practice, the coupling coefficient may deviate from the ideal value, which induces either spectrum splitting when the $\kappa_{rb}$ is smaller than the optimized value, or reduced reflectivity if $\kappa_{rb}$ is larger than the target value as can be seen from the shadow and blank areas in Fig.7.6 (a). The evolution of the reflective spectrum for different $\kappa_{rb}$ errors ($\delta\kappa_{rb}$) is depicted in Fig. 7.6 (b), from which one can clearly see the spectral profile change with the deviation of $\kappa_{rb}$ and the single peak reflection with high reflectivity can only be achieved for an appropriate single vaule $\kappa_{rb}$.
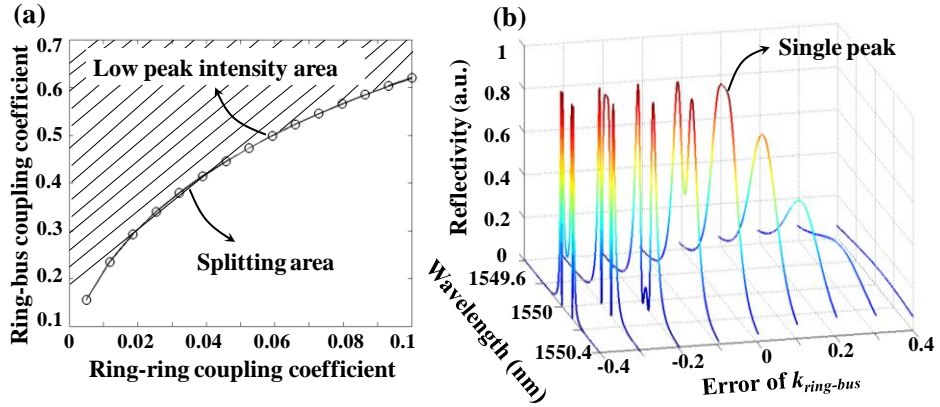


Figure 7.6 (a) Dependence of $\kappa_{rb}$ and $\kappa_{rr}$ to achieve single peak reflection; (b) Reflective spectrum evolution for different $\kappa_{rb}$ errors.

**Fabrication error and ring loss**

In practice, the coupling coefficient is rather difficult to be precisely controlled by changing the coupling distance and it's inevitable to introduce slight error during fabrication. To investigate the reflection performance in presence of fabrication error, Figure 7.7 plots the peak reflectivity (PR) and 3dB bandwidth (BW) versus $\kappa_{rr}$ for different $\delta\kappa_{rb}$. As can be seen from Fig.7.7, the PR decreases when the error $\delta\kappa_{rb}$=0.05 is introduced comparing with the ideal case of no error, while the BW is similar for both
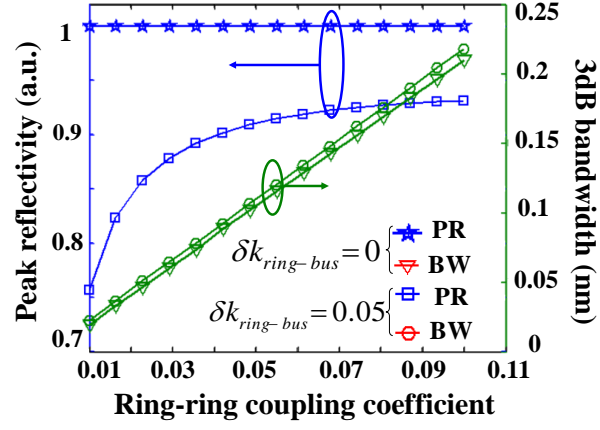
Figure 7.7 Peak reflectivity and 3dB bandwidth versus $\kappa_{rr}$ for different error of $\delta\kappa_{rb}$.

cases. Note that when the $\kappa_{rr}$ is very small ($< \sim 0.05$), the PR dramatically decreases if the error of $\delta\kappa_{rb}$ is introduced, which indicates that the small $\kappa_{rr}$ is more sensitive to the fabrication error. The loss from sidewall roughness, bending, and straight-to-bend junctions is another non-negligible parameter when designing the micro-ring resonator [156]. In this thesis, all the losses inside the micro-ring are treated together as ring loss. Figure 7.8 (a) shows the reflection spectrum for different ring losses, from which one can see that the peak reflectivity gradually decreases as the ring loss increases while its profile remains unchanged. The peak reflectivity versus the ring loss for different $\kappa_{rr}$ is also shown in Fig.7.8 (b). It's clear that the larger the $\kappa_{rr}$, the higher ring loss can be tolerated for a high reflectivity in the structure. For a ring loss of 2dB/cm, to achieve a tolerance of 3dB degradation of the reflectivity, the $\kappa_{rr}$ should be larger than $\sim 0.05$. On the other hand, large $\kappa_{rr}$ corresponds to large BW as shown in Fig.7.7, which may reduce the chip number for a given bandwidth-limited optical pulse. In addition, when the $\kappa_{rr}$ is greater than 0.1, the $\kappa_{rb}$ is approximately 1 to keep single peak operation, which makes it
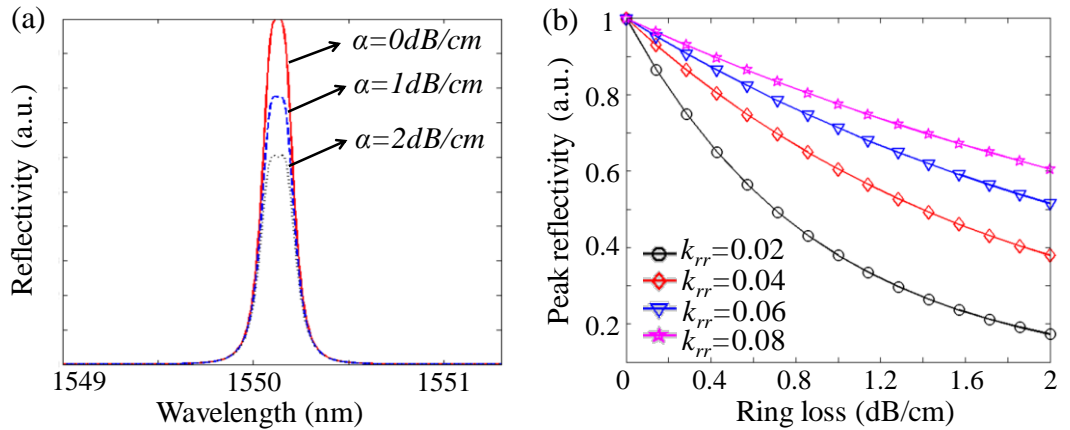


Figure 7.8 (a) Reflection spectrum for different losses; (b) Peak reflectivity versus ring loss for different $\kappa_{rr}$.

150

quite sensitive to the coupling distance error, indicating the tradeoff for choosing the $\kappa_{rr}$ and corresponding $\kappa_{rb}$. By considering the coupling coefficient fabrication error and ring loss effect, it's desirable to select the $\kappa_{rr}$ in the region of 0.05 and 0.1.

## Resonant wavelength tuning

In the proposed 2-D coherent optical en/decoder, each pair of the coupled micro-ring resonator is independent of each other and their resonant wavelengths should be able to be flexibly tuned to enable rapid wavelength hopping. Several approaches have been previously proposed for tuning purpose, such as thermo-optic effect by implanting a micro-heater above the micro-ring resonator [159-160], electro-optic effect by doping the intrinsic silicon to form a p-i-n structure [142], and free-carrier plasma dispersion effect [161]. Among them, the thermo-optic tuning is the easiest and most mature technique. The reported thermal tuning speed can reach up to several milliseconds [69], and thus it is assumed in the simulation for tuning purpose. Figure 7.9 (a) shows the reflective spectrum shifting by adjusting the temperature and consequently the effective refractive index of the optical waveguide, from which it can be seen that the resonant wavelength can be continuously red shifted by increasing the effective refractive index. The resonant wavelength detuning with the temperature is determined by the following formula [160]:

$$\frac{\Delta\lambda}{\Delta T} = \frac{\lambda_0}{n_{eff}}\left(\frac{\Delta n_{eff}}{\Delta T}\right) \tag{7.19}$$

where $\lambda_0$ is the resonant wavelength, $\Delta n_{eff}/\Delta T$ is the thermal-optic coefficient which is in the order of $10^{-4}$ for many materials. Fig.7.9 (b) shows the resonant wavelength detuning versus the temperature change for silicon material with a thermal-optic coefficient of $\sim 1.86\times10^{-4}$ $C^{-1}$ [162], from which one can see the temperature change
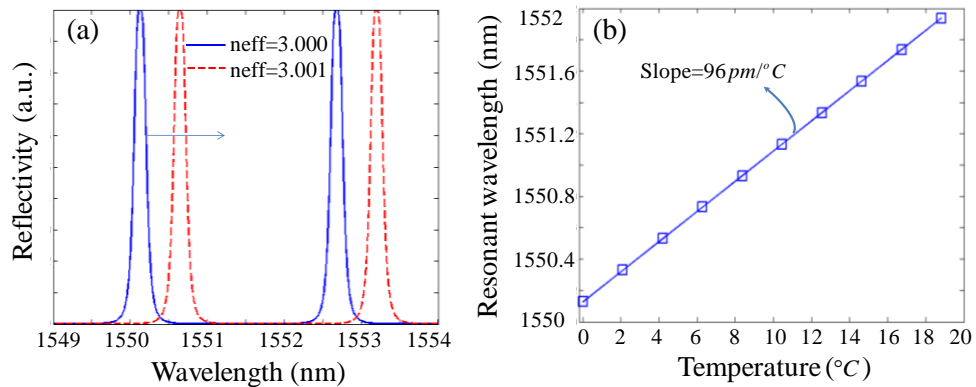


Figure 7.9 (a) Reflection spectrum for different effective refractive index; (b) Resonant wavelength detuning versus the temperature change.

induces the resonant wavelength linearly shifted and the sensitivity can be reach up to 96pm/$^o$C, which is suitable for the tuning of the proposed device. It is worthy to note that the tuning here refers to synchronously tune the temperature of the two micro-rings in each micro reflector, otherwise the reflective spectrum profile will be deteriorated, as is shown in Figure 7.10. It can be seen that although the resonant wavelength is shifted when the temperature difference ($\Delta T$) of the two rings increases, the reflectivity gradually decreases and the spectrum is broadened and split correspondingly. For a temperature difference of 4$^o$C, the peak reflectivity could be degraded from 1 to 0.1 and the bandwidth also increases accordingly, therefore, in the practical adjustment, the temperature of the two rings should be synchronously and finely tuned to avoid the resonance detuning induced spectrum splitting. To enable fast reconfiguring the 2-D codes up to picoseconds speed, electrical tuning can also be applied by using electro-optic effect but at the cost of the device complexity.
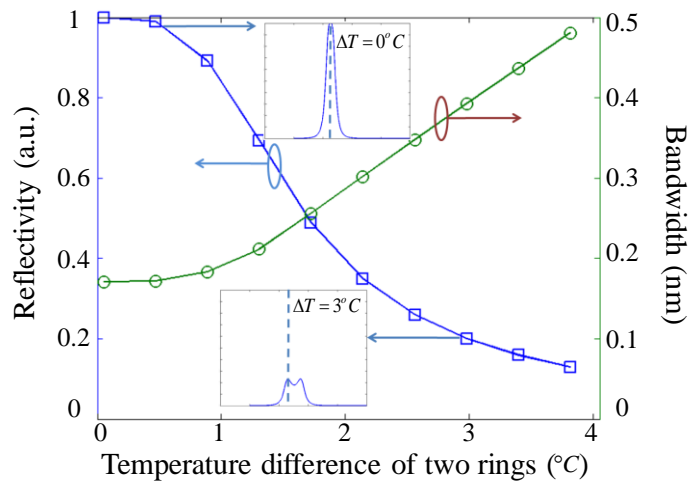


Figure 7.10 Reflection change versus temperature difference of two rings. Insets (i) and (ii) are reflective spectra for temperature difference of 0$^o$C and 3$^o$C.

## 7.3 En/decoding performance of 2-D optical en/decoder based on coupled double micro-ring reflector

### 7.3.1 Transfer matrix model of the 2-D optical en/decoder

Transfer matrix has been widely used in analyzing the light propagation through periodic structure in the literature, especially in calculating the reflection profile of fiber Bragg grating [163]. In the proposed 2-D optical en/decoder, each micro-ring reflector is placed along a straight waveguide, which is equivalent to a periodic structure, so similar

transfer matrix approach can also be used for analyzing the whole reflection spectrum of the proposed device.

Figure 7.11 shows the theoretical model of the cascaded structure, in which each unit cell represents each micro-ring reflector that is tuned on different resonant wavelength. The total transfer matrix of the whole structure can be derived by cascading the transfer matrix of each unit cell and the phase shifter as follows:
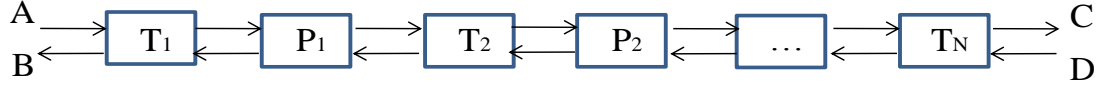


Figure 7.11 Theoretical model of cascaded coupled double micro-ring reflector.

$$\begin{bmatrix} A \\ B \end{bmatrix} = T \cdot \begin{bmatrix} C \\ D \end{bmatrix} = T_1 \cdot P_1 \cdot T_2 \cdot P_2 \cdots T_N \cdot \begin{bmatrix} C \\ D \end{bmatrix} = \begin{bmatrix} T_{11} & T_{12} \\ T_{21} & T_{22} \end{bmatrix} \cdot \begin{bmatrix} C \\ D \end{bmatrix} \tag{7.20}$$

where $T_i$ and $P_i$ ($i=1, 2 \ldots N$) is the transfer matrix of the $i_{th}$ micro reflector and phase shifter. Assuming the input from the first reflector is $A=1$ and there is no input from the last reflector ($D=0$), the total reflection coefficient can be given by:

$$R = \frac{T_{21}}{T_{11}} \tag{7.21}$$

For each unit cell, the elements of the transmission matrix $T_i$ ($i=1, 2, \ldots N$) can be derived from Eq. (7.13) as:

$$T_{11}^i = A_{23} + (A_{21} \cdot A_{44} \cdot A_{13} + (A_{21} \cdot A_{43} \cdot (e^{-(j\beta_i+\alpha)L} - A_{14}) + A_{24} \cdot A_{11} \cdot A_{43} + A_{24} \cdot A_{13} \cdot (e^{-(j\beta_i+\alpha)L} - A_{41}))/C$$

$$T_{12}^i = A_{22} + (A_{21} \cdot A_{44} \cdot A_{12} + (A_{21} \cdot A_{42} \cdot (e^{-(j\beta_i+\alpha)L} - A_{14}) + A_{24} \cdot A_{11} \cdot A_{42} + A_{24} \cdot A_{12} \cdot (e^{-(j\beta_i+\alpha)L} - A_{41}))/C \tag{7.22}$$

$$T_{21}^i = A_{33} + (A_{31} \cdot A_{44} \cdot A_{13} + (A_{31} \cdot A_{43} \cdot (e^{-(j\beta_i+\alpha)L} - A_{14}) + A_{34} \cdot A_{11} \cdot A_{43} + A_{34} \cdot A_{13} \cdot (e^{-(j\beta_i+\alpha)L} - A_{41}))/C$$

$$T_{21}^i = A_{22} + (A_{31} \cdot A_{44} \cdot A_{12} + (A_{31} \cdot A_{42} \cdot (e^{-(j\beta_i+\alpha)L} - A_{14}) + A_{34} \cdot A_{11} \cdot A_{42} + A_{34} \cdot A_{12} \cdot (e^{-(j\beta_i+\alpha)L} - A_{41}))/C$$

where $\alpha$ is the loss of the straight waveguide, and $C$ is given by

$$C = (e^{-(j\beta_i+\alpha)L} - A_{14})(e^{(j\beta_i+\alpha)L} - A_{41}) - A_{44} \cdot A_{11} \tag{7.23}$$

The transfer matrix of the phase shifter can be expressed as:

$$P_i = \begin{bmatrix} e^{-jC_{pi}\pi/2} \cdot e^{(jn_g w/c+\alpha)L} & 0 \\ 0 & e^{jC_{pi}\pi/2} \cdot e^{-(jn_g w/c+\alpha)L} \end{bmatrix} \tag{7.24}$$

where $C_{pi}$ (0 or 1) is the spectral phase pattern. The phase shift is assumed as a constant value of $\pi/2$ which could be achieved by using a wideband phase shifter or adjusting the relative phase shift for adjacent phase shifters. In the decoder side, the encoded wavelength hopping time spreading pulse should be recombined to generate the auto-correlation signal, so the time-reversed wavelength hopping code (WHC) should be applied, and the transfer matrix in the decoder becomes $T = T_N \cdot P_N \cdot T_{N-1} \cdot P_{N-1} \cdots T_1$. Note

that the spectral phase code (SPC) is not simply the reverse order of the original SPC as the phase shift is accumulated for the latter chip, and thus code translation is required in the decoder for correct decoding (e.g. SPC: 01011 in the encoder will correspond to SPC: 01101 in the decoder).

## 7.3.2 Investigation of en/decoding performance of coupled double micro-ring reflector

In this section, the en/decoding performance is investigated by injecting a Gaussian-shaped optical pulse with pulse width of ~3ps and center wavelength of 1550.64nm ($\lambda_3$) into the en/decoder, which has five pairs of coupled double micro-ring reflectors. Both the two rings in each reflector have a ring radius of 50μm, and the $\kappa_{rr}$ and $\kappa_{rb}$ are chosen as 0.08 and 0.56 to achieve a BW of 0.16 nm for each frequency bin. The chip rate is set as 15GHz/chip corresponding to $L$=3.3mm. The ring loss and straight waveguide propagation loss are assumed as 2 dB/cm and 0.5 dB/cm in the following simulation, respectively. The effective refractive index is assumed as 3, which can decrease the straight bus waveguide length $L$ to reduce the loss. By considering different WHC and SPC for the cascaded structure, the en/decoding performance can be studied using the transfer matrix approach.

Figure 7.12 (a) shows the encoded spectrum for WHC of {1, 2, 3, 4, 5} without
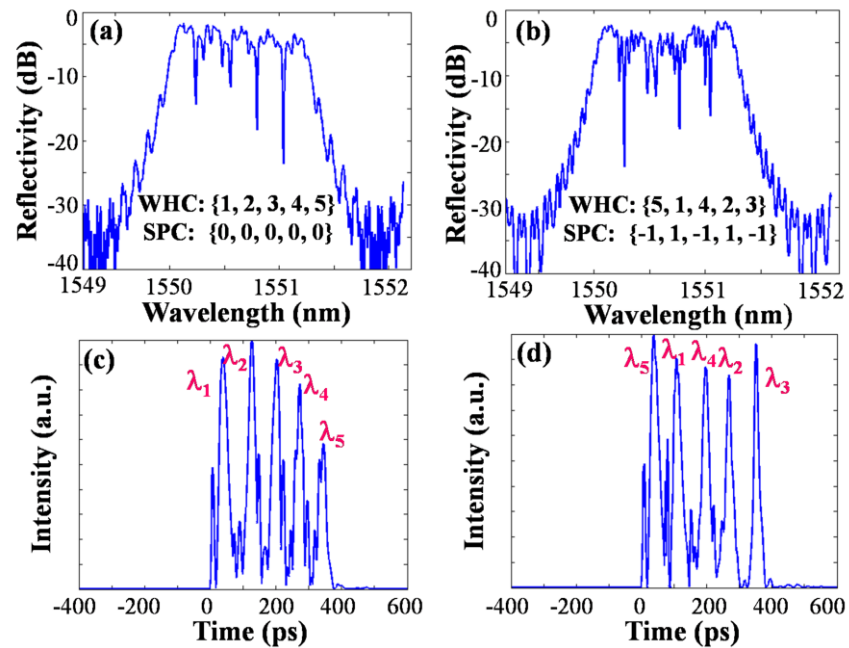


Figure 7.12 (a) ~ (b) are encoded spectrum for WHC {1, 2, 3, 4, 5} without SPC, and WHC {5, 1, 4, 2, 3} with SPC {-1, 1, -1, 1, -1}; (c) and (d) are corresponding encoded waveforms for (a) and (b), respectively.

spectral phase pattern, and the corresponding encoded waveform is shown in Fig. 7.12 (c), from which one can see clearly different wavelengths are temporally spread into different time positions. The reflectivity of the five frequency bins are decreased gradually because the final pulse experiences much more losses. A 2-D coherent code with WHC {5, 1, 4, 2, 3} and SPC {-1, 1, -1, 1, -1} are also applied to verify the capability of simultaneous fast wavelength hopping and spectral phase encoding, and the encoded spectrum and waveform are shown in Fig. 7.12 (b) and (d), respectively. The dip and ripple existing in the encoded spectrums indicate the applied phase pattern and the interferences between adjacent channels due to the crosstalk. To effectively recover the original pulse, both the WHC and SPC are indispensible for the decoder. Figure 7.13 (a-i) depicts the decoded auto-correlation signal with high peak and needle-like pulse, while for the case of incorrect SPC (ii), incorrect WHC (iii) and both the SPC and WHC are incorrect (iv), the decoded signal spread in time domain with low peak power, which verifies the feasibility of 2-D coherent en/decoding using the proposed device. It can be seen from Fig.7.13 that there are some small sidelobes in the auto-correlation signal due to the reflection, which are mainly associated with several factors: channel spacing and crosstalk between two adjacent frequency bins, chip rate, propagation loss and coupling coefficient error, as will be discussed as follows.
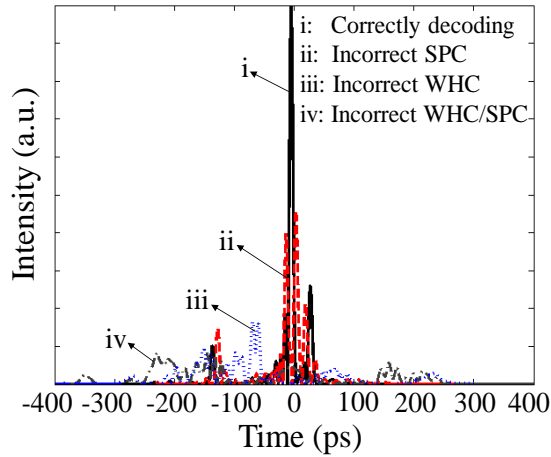


Figure 7.13 Auto-/cross-correlation signals with (i) correct WHC and SPC (i) and (ii-iv) incorrect WHC and SPC, respectively.

To investigate the effect of channel spacing on the en/decoding performance, we have simulated the encoded spectrum, waveform and decoded waveform for two channel spacing of 10GHz and 25GHz, as shown in Figure 7.14 (a)~(d) and (e)~(h), respectively. When the channel spacing is too small (10GHz), the crosstalk between each frequency bin arises inducing multi-layer reflection, and thus the encoded

spectrum and waveform have significant oscillations, which can be seen from Fig. 7.14 (b)~(c). The corresponding decoded waveform has rather poor performance with very high sidelobes and the temporal profile is no longer a short pulse, as shown in Fig.7.14 (d). However, when slightly increasing the channel spacing to 25GHz, the encoded spectrum is clearly separated and temporally spread to different time positions, as can be seen from Fig. 7.14 (f)~(g). The decoded waveform recovers as a short optical pulse with very low sidelobes (see Fig.7.14 (h)), showing that the decoding performance is dependent on the channel spacing.
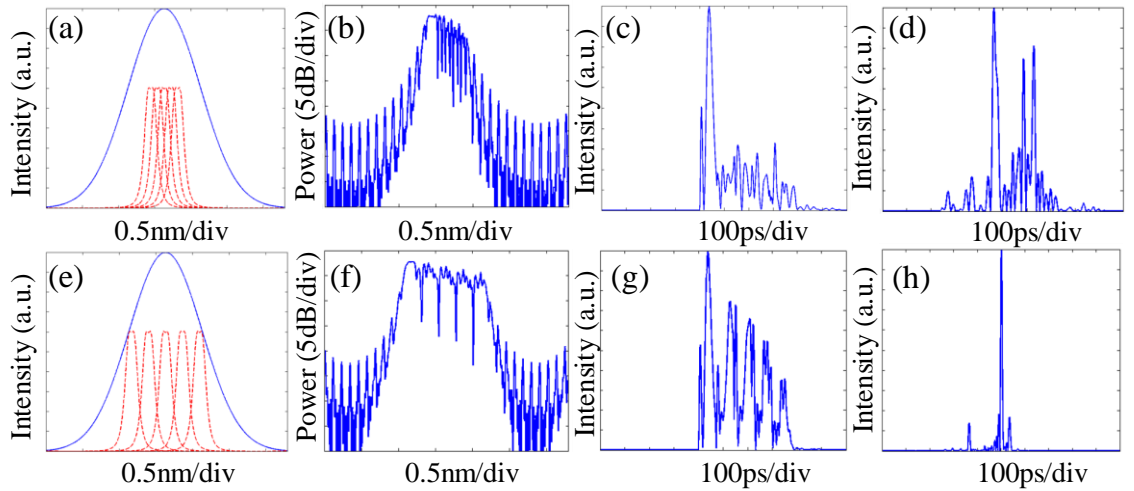


Figure 7.14 (a)~(d) and (e)~(h) are the frequency bins, encoded spectrum, waveform and decoded waveform for channel spacing of 10GHz and 25GHz, respectively.

Figure 7.15 illustrates the dependence of the autocorrelation peak to maximum wing ratio (P/W) and P/C with the channel spacing, from which one can see that both the P/W and P/C will be degraded for too large or too small channel spacing. When the channel spacing is extremely large, the spectrum between two adjacent channels will transmit
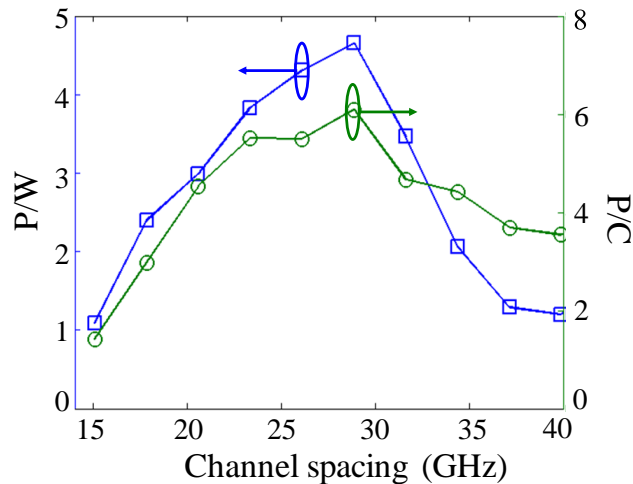


Figure 7.15 P/W and P/C versus the channel spacing.

through the structure and cannot be efficiently utilized resulting high sidelobes in the decoded waveforms, while for too small channel spacing, the interference between different channels will be strengthened and the effective code length will be decreased inducing the degradation of P/W and P/C. Since the P/C is of the main concern for multi-user OCDMA system, the channel spacing should be adjusted to a magnitude comparable to the bandwidth to guarantee the en/decoding performance.

Besides the channel spacing, the en/decoding performance is also associated with the chip rate and propagation loss. Figure 7.16 shows the relationship between the P/W and P/C with the chip rate, from which it can be seen that as the chip rate increases, the P/W roughly locates at 5 with slight fluctuation due to the coherent interference, while the P/C gradually decreases mainly caused by the encoded pulses overlapping induced decreasing of the effective WHC chip number. On the other hand, when the chip rate is too small, the waveguide length will be increased correspondingly, making the whole device more bulky and susceptible to propagation loss. In the proposed device, a chip rate of 15Gchip/s is used, which corresponds to a waveguide length of 3.3mm between two frequency bins and the whole device has a footprint of ~1.3cm. The waveguide propagation loss plays an important role in general design of micro-ring resonator and cannot be neglected. Figure 7.17 depicts the propagation loss effect on the P/W and P/C, from which one can see both the P/W and P/C decrease with the increase of the propagation loss. The insets (i) and (ii) in Fig.7.17 show the decoded auto-/cross-correlation signals for propagation loss of 0dB/cm and 3dB/cm, which clearly shows the degradation of the decoding performance due to the loss. As the latter encoded pulses will experience much more loss than the former one, causing the loss imbalance for
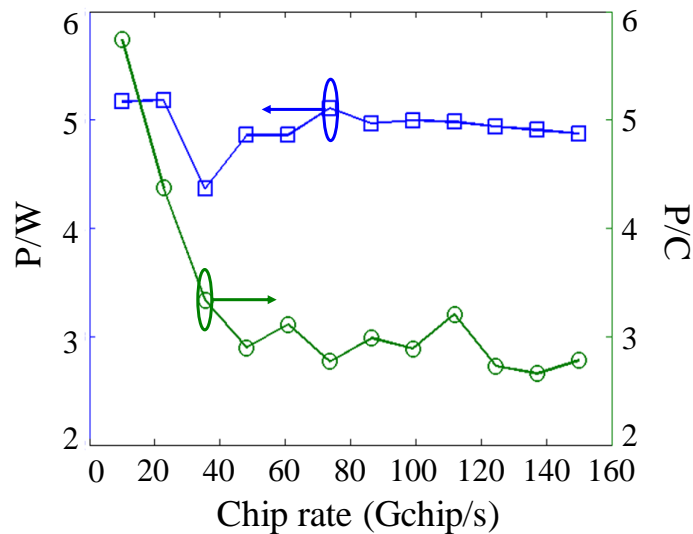


Figure 7.16 Relationship of P/W and P/C with the chip rate.
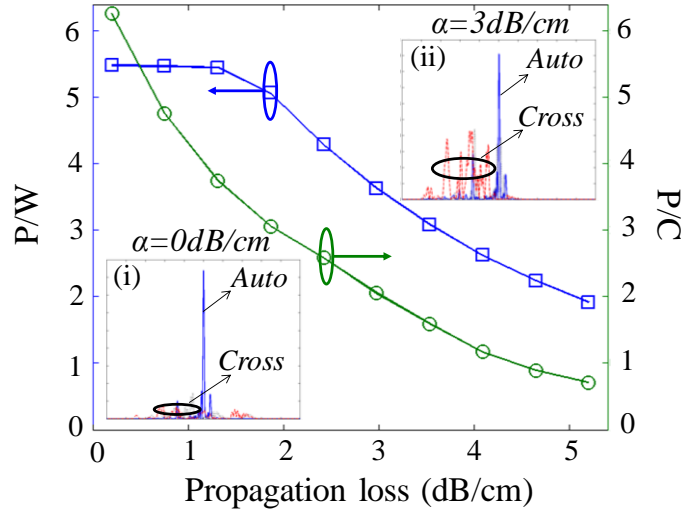
Figure 7.17 Relationship of P/W and P/C with the propagation loss.

each chip and thus the encoded waveform is not uniform, as shown in Fig. 7.14(g), which directly degrades the auto-correlation signal with pulse broadening and peak intensity reduction. In the simulation, a propagation loss of 0.5dB/cm has been used, which is acceptable for the functionality of the en/decoder. Remarkably, smaller straight waveguide loss close to 0.1dB/cm [68-69] and ring bend loss of 0.8dB/cm [164] for a 50um micro-ring by selective thermal oxidation has been recently reported, which could be used to significantly reduce the loss in the proposed device. Moreover, the ring loss can also be reduced by using high index contrast material system for strong optical confinement [69]. To achieve unity reflectance of each frequency bin to improve the performance, besides reducing the loss, one could also make the reflectivity slightly different for each reflector or non-uniformly allocate the spectrum by manipulating the coupling coefficient individually to compensate for the loss imbalance.

In addition, the fabrication error of the coupling coefficient is another factor that may affect the decoding performance. Figure 7.18 shows the simulated results when the $\kappa_{rb}$ and $\kappa_{rr}$ have a random deviation of 10% from the designed ideal value, from which one find that P/W is more sensitive to the error of the coupling coefficients than the P/C. For a random error of 10%, the P/W fluctuates between 3 and 6, while the P/C slight changes between 4 and 5. As the P/C mainly determines the multi-user system performance, the slight fabrication error of the coupling coefficients can be tolerated within at least ~10%.

In the previous simulation, we have used five frequency bins to show the operation principle of the proposed 2-D optical en/decoder. Intrinsically, it is capable of supporting more frequency bins by cascading more micro-reflectors. To show this
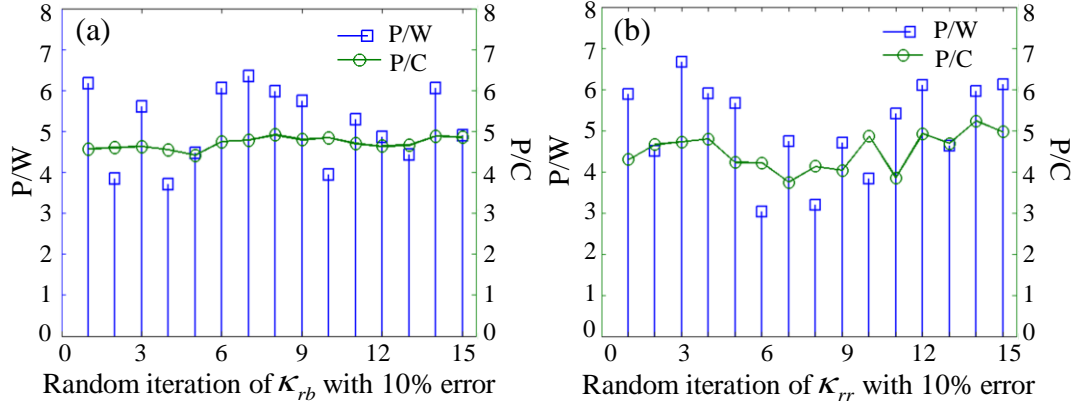
Figure 7.18 (a) and (b) are the P/W and P/C for a random $\kappa_{rb}$ and $\kappa_{rr}$ with error of 10%.

capability, Figure 7.19 illustrates the en/decoding performances for eight frequency bins with two WHC and SPC codes, respectively. As can be seen from Fig. 7.19 (d)~(e), after applying the wavelength hopping pattern {8, 1, 2, 7, 3, 6, 5, 4} and spectral phase pattern {0, 1, 1, 0, 1, 0, 0, 0}, the encoded spectrum and waveform are distinctly different from that of Fig.7.19 (a)~(b) with WHC of {1, 2, 3, 4, 5, 6, 7, 8 } and SPC all zeros, different spectral components have been temporally hopped to different time positions, showing the original short pulse has been encoded by the wavelength hopping and spectral phase pattern. As has been discussed before, the non-uniform encoded spectra and waveforms are owing to the existence of the propagation loss. Fig.7.19 (c) and (f) are the decoded signals for both codes, from which one can see that the auto-correlation signal with high peak power can be achieved, while the cross-correlation
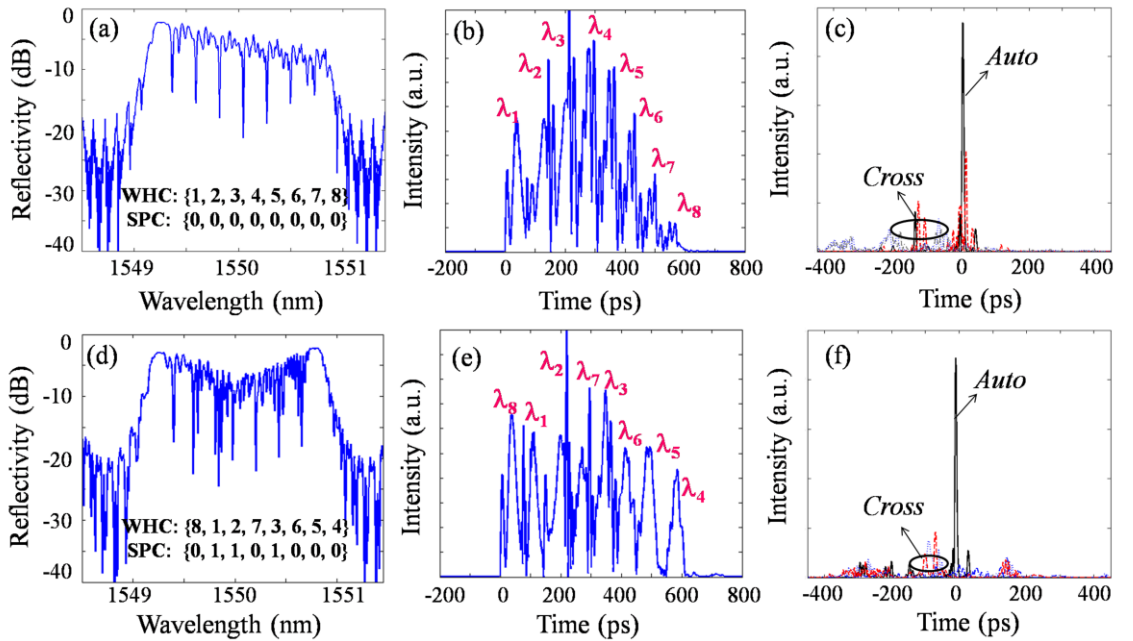


Figure 7.19 (a)~(c) and (d)~(f) are the encoded spectrum, waveform and decoded signals for two WHCs and SPCs, respectively.

159

signal exhibits like a noise with very low peak power. The distinguishment of the auto-/cross-correlations can be performed by using proper optical threshoding/time gating techniques [74-82]. As the 2-D optical codes can be generated simultaneously by the proposed device, the number of possible codes (or code cardinality) could reach up to $(8! \times 2^7)/2 = 2580480$. By further increasing the frequency bins, the code cardinality and decoding performance could be significantly improved, and thus it could support more active users comparing to that of a 1-D transmission device with only spectral phase pattern. In a practical OCDMA system with multi-user interferences, the usable code set may be reduced. To scale this technique by increasing the code length or frequency bins, reducing the ring radius at the expense of high loss could be a solution for achieving larger FSR and covering more frequency bins. Another possible solution to considerably expand the FSR is via Vernier effect [165] without decreasing the radius of the rings, and thereby avoiding large ring losses. If the radii of the two rings in the coupled double ring resonator are slightly different, the resonance wavelengths of the two rings are misaligned at all the resonance wavelengths, except at certain wavelengths are still on resonant condition which may greatly increase the FSR and change the reflection spectrum. Figure 7.20 compares the reflection spectrum of the coupled double micro-reflector with different ring sizes, from which it can be seen that the entire profile of the reflection spectrum changes for different ring radius, especially the resonant wavelength and the FSR. For the reflector with the same radius of 50um, the resonant
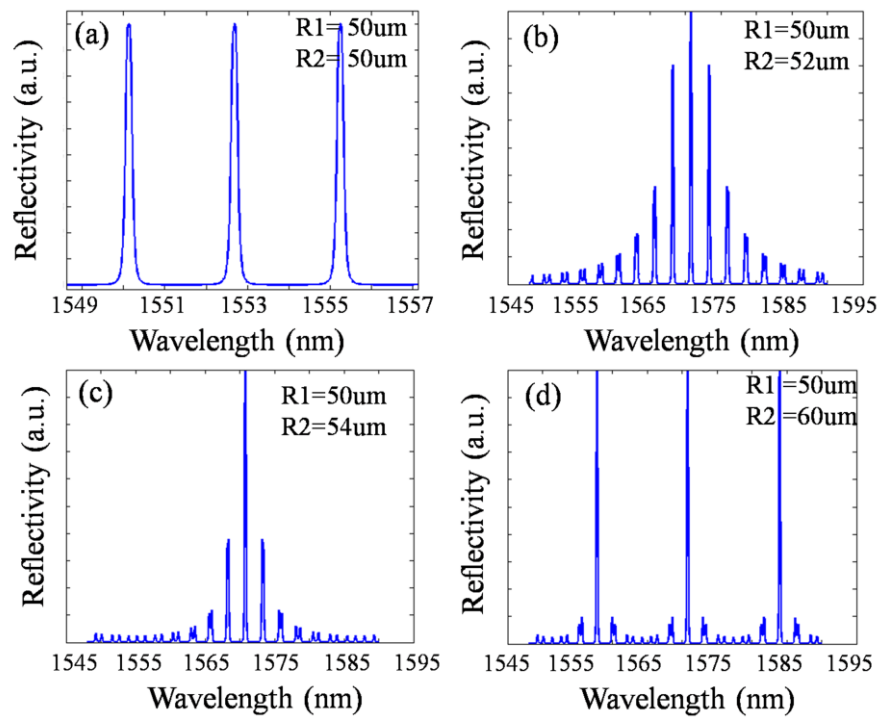


Figure 7.20 (a)~(d) are the reflection spectrum for different ring radius, respectively.

wavelength periodically changes with a FSR of ~2.5nm. As the radius of one ring is slightly changed to 52um or 54um, the side modes will be gradually suppressed as shown in Fig.7.20 (b)~(c), which is particularly obvious when the ring radius reach to 60um. The FSR for case (d) can be dramatically expanded to 20nm while keeping high side mode suppression, which can be potentially used for scaling of the proposed device.

## 7.4    Analysis of reflection properties of circular coupled micro-ring reflector

In addition to the coupled double micro-ring reflector, researchers have also proposed several other kinds of micro-ring reflector based on the coupled micro-resonator. In 2005, *G. T. Paloczi*, *et al* have proposed a compact wavelength selective in line reflector, which employed a micro-ring resonator and Mach-Zehnder interferometer (MZI) to realize Bragg Grating reflection [166]. This structure can deliver the desired reflection band profile by employing many cascaded ring resonators, but it is very complex since MZI have been introduced. Based on a circular array of coupled micro-ring resonators, *J. K. S. Poon*, *et al* proposed another wavelength selective reflector [167], which has been predicted to produce a narrow-band reflection peak. Here, in this section, we theoretically analyze the reflective properties of this wavelength selective reflector based on three circular coupled micro-ring resonators by considering the ring loss, and find the flat-top reflection profile reported in [167] have spectrum splitting when the ring loss is rather small and optical analogous to electromagnetic induced transparency (EIT) could be generated [168], which is a quantum interference effects but now occurs in a photonic resonator system due to the coherent interference between coupled resonators.

Figure 7.21 shows the structure of the circular coupled micro-ring reflector, which consists of three micro-rings that are circularly coupled with each other by coupling coefficients. All the ring-ring coupling coefficients are assumed identical as ($\kappa_{rr}$, $\tau_{rr}$) and different from the ring-bus coupling coefficient ($\kappa_{rb}$, $\tau_{rb}$). To analyze the reflection spectrum for the structure, transfer matrix method can also be used [167]. Figure 7.22 (a) and (b) shows the reflection spectrum and phase response for a lossless structure with $\kappa_{rb}$=0.53, $\kappa_0$=$\kappa_1$=$\kappa_2$=0.08, from which one can see that a flat-top reflection spectrum can also be formed but it exhibits two narrow splitting resonances with reflectivity of zero when the ring-ring are weakly coupled with each other. The phase response has
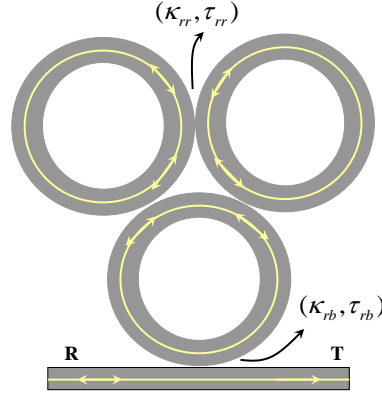
Figure 7.21 Schematic of circular coupled micro-ring reflector.

different profiles for both of the two narrow resonances, as can be seen from Fig.7.22
(b) and the inset. An input light with its wavelength falling into the two narrow splitting
resonant windows will transmit through the structure without any reflection, which is
particularly similar to the electromagnetic induced transparency (EIT) in an atomic
system where a narrow transparent window in the absorption spectra can be produced
by coherently driving the atom with an external laser [168]. In a two coupled resonators
system, it has also been observed and is regarded as coupled resonator induced
transparency (CRIT) [168]. The resonance splitting is strongly dependent on the
coupling co-efficients. When the ring-bus and ring-ring coupling coefficients are
increased, as shown in Fig.7.22 (c) for the transmission spectrum, the linewidth of two
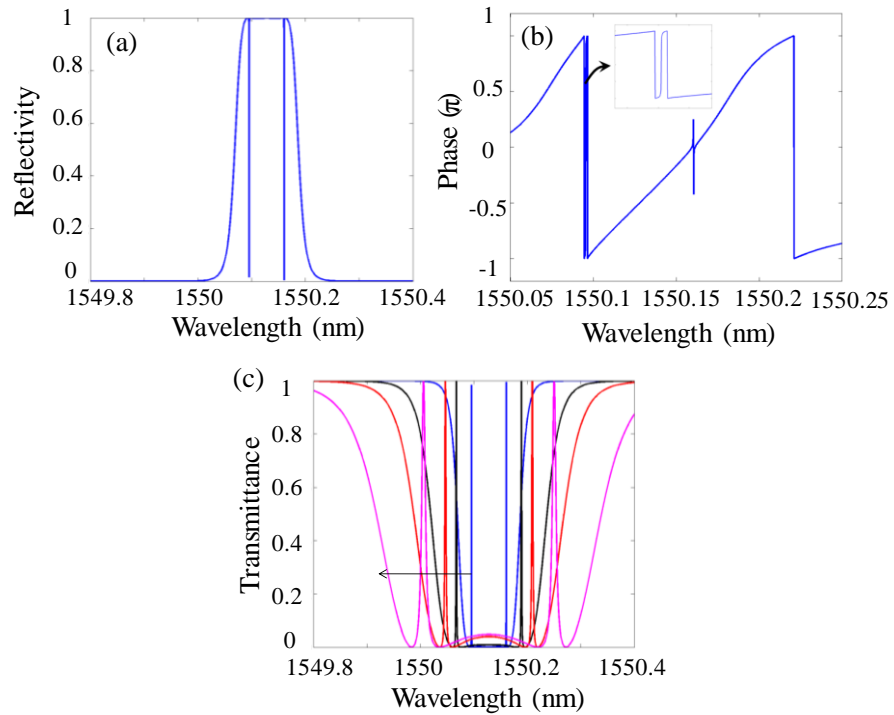


Figure 7.22 (a) Reflection spectrum and (b) phase response for $\kappa_{rb}$=0.53. (c) is the transmission
spectrum when increasing the $\kappa_{rb}$ from 0.53 to 0.7, 0.8, 0.9.

162

splitting resonances will be widened with the two resonant wavelengths moving toward the opposite directions. The capability for creating such transparency resonance using the resonator system, and for controlling the resonance linewidth through tuning the coupling coefficient, is important for on-chip optical interconnects and optical processing applications, such as switching, all-optical slowing and stopping of light, nonlinear optics, as well as tunable bandwidth filter without the use of atomic resonance [168].

In practical situation, the ring loss cannot be neglected in the micro-resonator system. Further investigation shows that the reflection spectrum is loss dependent, as shown in Figure 7.23 (a), from which we can see the two splitting resonances gradually disappear as the loss increases while the peak reflectivity is also decreased. A wideband reflection spectrum without resonance splitting will be generated as a result of the loss, which is the desired reflection profile for the application in the proposed 2-D optical en/decoder, though its peak reflectivity is no longer unity. For a fixed ring loss of 2dB/cm, the relationship between the peak reflectivity, 3dB bandwidth with the $\kappa_{rr}$ for $\kappa_{rb}$=0.7 is shown in Fig.7.23 (b). It can be seen as the ring-ring coupling coefficient $\kappa_{rr}$ decreases from 0.2, the peak reflectivity and 3dB bandwidth will also be decreased. Resonance splitting and the CRIT will occur for any further strengthen of the ring-ring coupling. It is also possible to get versatile reflection responses, such as single or multiple narrow/wide-band peaks by considering more complicated inter-resonator coupling such as symmetric coupling and asymmetric coupling, which can be referred in [169]. Since this circular coupled micro-ring reflector can also generate spectral reflection in presence of loss by properly optimizing the coupling coefficient, it could also be an alternative candidate to be used for the 2-D optical en/decoding. However, as the circular coupled micro-ring reflector requires precisely control three coupled resonators
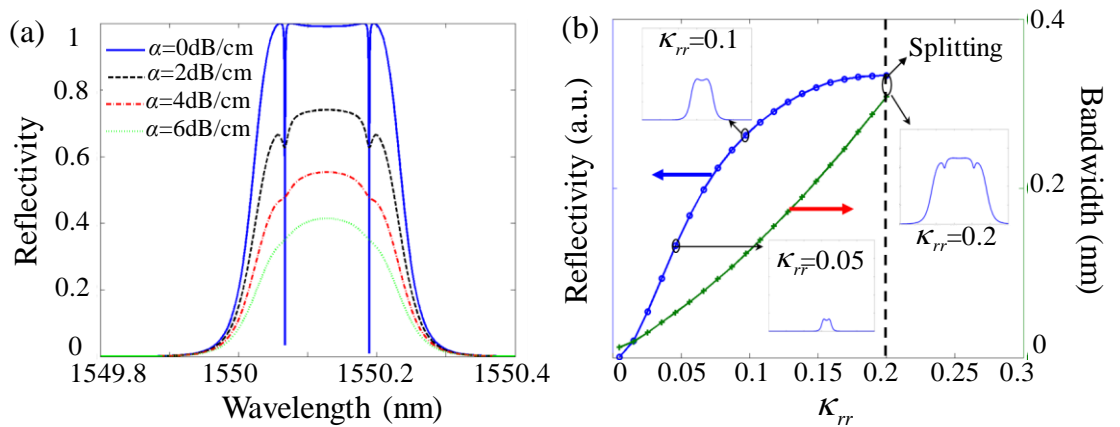


Figure 7.23 (a) Reflection spectrum with losses; (b) reflectivity and bandwidth versus $\kappa_{rr}$.

and the loss dependent reflection profile has CRIT effect, it is not particularly attractive for application in the proposed 2-D coherent optical en/decoder.

## 7.5 Parallel cascaded coupled micro-ring resonator array for 2-D optical en/decoder

As single ring resonator has a Lorentz shape transfer function, which may not provide adequate spectral response [156], there has been a growing research interest in exploring more sophisticated micro-ring device topologies consisting of multiple cascaded coupled micro-ring resonators to realize complex optical transfer functions for versatile applications such as add-drop filtering, slow light and other spectral engineering [170-171]. Although various micro-ring configurations have been proposed, they can be roughly classified as type I: parallel cascaded, type II: serially cascaded, and a hybrid of both configurations [170, 173]. In the parallel cascaded structure, the micro-rings are not mutually but are periodically coupled to two side waveguides, which is analogous to a Bragg grating, with each ring acting as a "tooth" or reflection element in the grating that is frequency dependent and has high reflectivity at resonance [173]. While the serially coupled ring resonators, which are referred to coupled-resonator optical waveguides (CROW), require the rings mutually coupled in a linear cascade and each ring forms a F-P cavity. The input signal must pass all the ring resonators, and thus the output signal is very sensitive to the coupling condition of each ring, but the type II configuration has well out-of-band sidelobe suppression [173].

In this section, a parallel cascaded coupled micro-ring resonator array is proposed to be used for the 2-D coherent optical en/decoder, as shown in Figure 7.24. In this configuration, multiple micro-rings are serially coupled with each other and form an array of resonators. Then the array is coupled to an input and output bus straight waveguide. The resonant wavelength of each array can be adjusted by changing the temperature of all the rings in the array synchronously. An interesting characteristic of this configuration is that the output signal from the drop port transmits toward opposite directions depending on the mutually cascaded ring number. For an even number of rings, the dropped signal will transmit in the same direction as the input signal, while for an odd number of rings, it propagates in the opposite direction. Therefore, by parallel cascading several serially coupled micro-ring resonator arrays with odd number of micro-rings to form several frequency bins, and inserting the phase shifter between
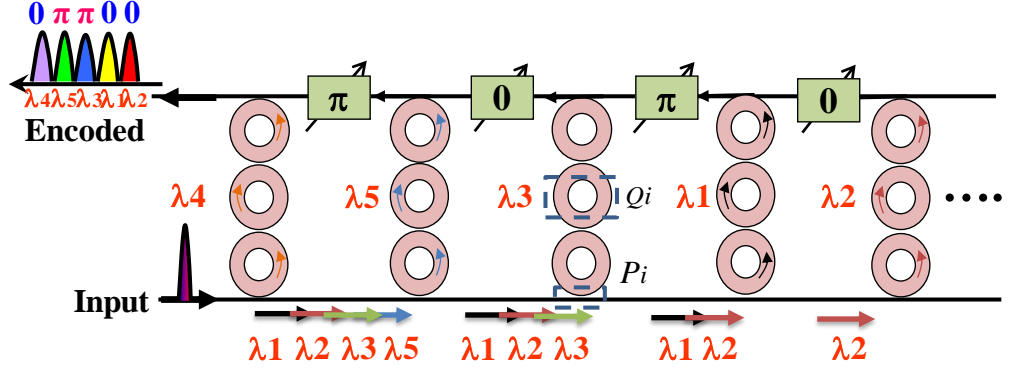
Figure 7.24 Schematic of parallel cascaded coupled micro-ring resonators array.

adjacent frequency bins, this structure could also realize 2-D wavelength hopping and spectral phase encoding, as illustrated in Fig. 7.24 with a third-order serially cascaded array as a frequency bin. Unlike the coupled double micro-ring and circular coupled micro-ring reflectors based en/decoder, the original signal and encoded signal output from different bus waveguides in this structure, and hence it is unnecessary to use additional optical circulator, which seems very attractive for practical application.

The reflection property of each array of serially coupled micro-ring resonators in Fig.7.24 can be analyzed by using the transfer matrix method. The inter-ring and ring-bus coupling transfer matrix $P_i$ can be derived from the coupled mode equations as

$$P_i = \frac{1}{-ik_i}\begin{bmatrix} -t_i & 1 \\ -1 & t_i \end{bmatrix} (i=rb,\ rr) \tag{7.25}$$

while the transfer matrix inside of the rings $Q_i$ can be expressed as

$$Q_i = \begin{bmatrix} 0 & e^{-i\pi R\beta_i} \\ e^{i\pi R\beta_i} & 0 \end{bmatrix} \tag{7.26}$$

where $k_i$ and $t_i$ are the coupling coefficients, $\beta_i$ is the propagation constant. By cascading the inter-ring and ring-bus coupling matrix, the output electrical field for each serially cascaded array can be derived as

$$E_{out} = P_{rb}Q_{rr}P_{rr}Q_{rr}P_{rr}Q_{rb}P_{rb}E_{in} = BE_{in} \tag{7.27}$$

from which one can get the transfer matrix for each frequency bin as follow:

$$T_j = \begin{bmatrix} \dfrac{-B_{12}}{B_{11}} & \dfrac{1}{B_{11}} \\ B_{22} - \dfrac{B_{12}B_{21}}{B_{11}} & \dfrac{B_{21}}{B_{11}} \end{bmatrix} (j=1,\ 2\ldots N) \tag{7.28}$$

Finally, the whole transfer matrix of the structure can be derived by cascading Eq. (7.28) with the transfer matrix of the phase shifter as below:

$$T = T_1 \cdot P_1 \cdot T_2 \cdot P_2 \cdots T_N \tag{7.29}$$

and the transfer matrix of the phase shifter is given as:

$$P_i = \begin{bmatrix} e^{-j\{\pi,0\}} \cdot e^{(jn_g w/c + \alpha)L} & 0 \\ 0 & e^{j\{\pi,0\}} \cdot e^{-(jn_g w/c + \alpha)L} \end{bmatrix} \tag{7.30}$$

Note the phase shift is no longer $\pi/2$ but $\pi$ here. The reflectance can be finally obtained by using the Eq. (7.21) and Eq. (7.29). Figure 7.25 (a) shows the reflective spectrum and corresponding phase response of the serially cascaded micro-resonators with a ring radius of 50um for $\kappa_{rb}=0.65$ and $\kappa_{rr}=0.17$ without loss and with the presence of 2dB/cm loss. By appropriately optimizing the coupling coefficient, a box-like reflection spectrum can be obtained accompanied with an abrupt phase shift in the vicinity of the resonance. The structure is more tolerable to the ring loss with a peak reflectivity reduction of 20% for 2dB/cm ring loss, which is much lower than the 40% of the coupled double micro-reflector. For a fixed $\kappa_{rb}$ of 0.65, the evolution of the reflective spectrum with the $\kappa_{rr}$ is depicted in Fig.7.25 (b), from which one can see that as the $\kappa_{rr}$ increases, the profile of the reflective spectrum is gradually changed into a box-like spectrum from an ultra-narrow reflection and then split into multi-peaks with great ripples in the pass band, showing the $\kappa_{rr}$ should be optimized to achieve single peak reflection. Fig. 7.25 (c) shows the dependence of $\kappa_{rb}$ and its optimized $\kappa_{rr}$. As can be seen, the weakly coupled $\kappa_{rr}$ monotonically increases with the $\kappa_{rb}$, and the corresponding bandwidth also increase as well, which indicates that the reflective spectrum can be synthesized by changing the $\kappa_{rb}$ and $\kappa_{rr}$.
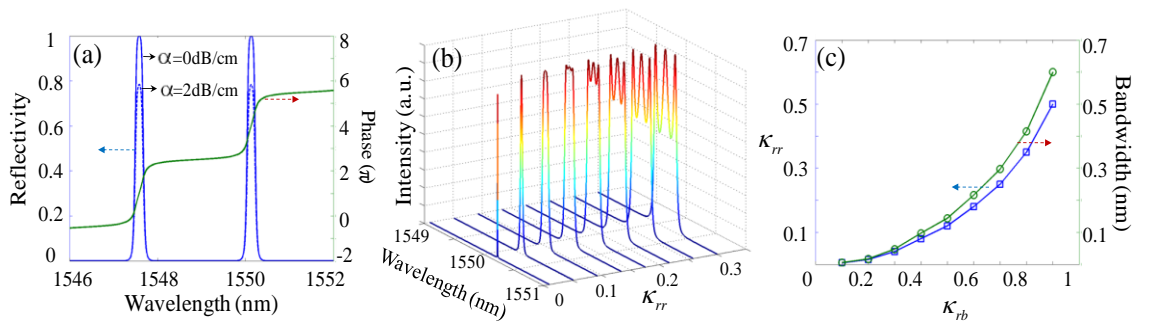


Figure 7.25 (a) Reflective spectrum and phase response; (b) spectrum evolution with the ring-ring coupling coefficient; (c) optimized $\kappa_{rr}$ and bandwidth with $\kappa_{rb}$.

The en/decoding performance has also been investigated based on the parallel coupled micro-ring resonator array and compared with the coupled double micro-ring reflector with the same 3dB bandwidth. Figure 7.26 (a) shows the reflective spectrum for both structures, from which it can be seen that the parallel cascaded coupled

resonators has a high extinction ratio of up to 60dB and much sharper roll-off than the coupled double micro-reflector, which can mitigate the channel crosstalk more efficiently. The corresponding en/decoding waveform and spectrum for the two structures with the same 8-chip WHC {8, 1, 2, 7, 3, 6, 5, 4} and SPC {0, 1, 1, 0, 1, 0, 0, 0} are shown in Fig.7.26 (b) and (c), respectively. It can be seen that the encoded spectrum and waveform for the parallel cascaded coupled resonators have very smooth response and much little out-of-band ripples. Compared with the coupled double micro-rings, the parallel cascaded structure exhibits superior decoding performance with a P/W and P/C improvement from 4.2 to 5.6 and 5.5 to 9.1, which can be ascribed to the sharp spectral response. As has been previously discussed in section 7.3, the en/decoding performance of the 2-D coherent optical en/decoder is associated with the channel crosstalk between adjacent frequency bins. When different frequency bins are tuned to close with each other, their reflective spectrum will partially overlap inducing the channel crosstalk that will be out of phase with all the frequency bins after decoding, and thus the decoding performance will be degraded. This implies us that the coding performance of the proposed 2-D coherent optical en/decoder can be potentially enhanced by improving the sharpness of the reflection spectrum, which could be a further research direction.
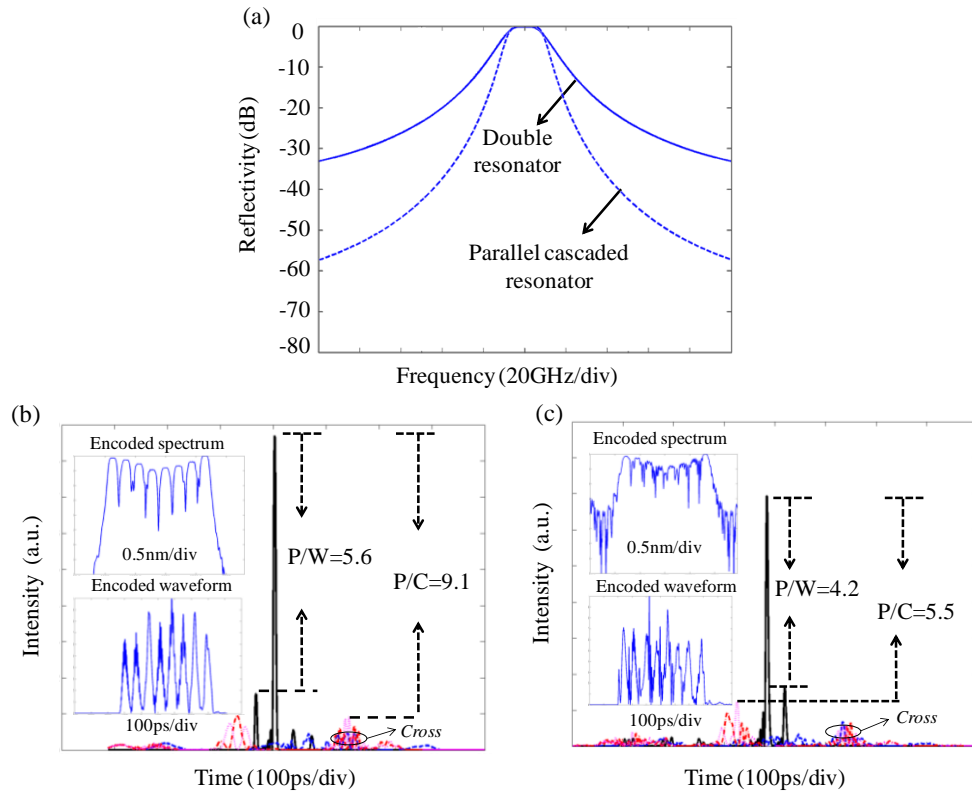


Figure 7.26 (a) Reflective spectrum for coupled double resonator and parallel cascaded resonator; (b) and (c) are the en/decoding performances for the parallel cascaded coupled and double micro-ring resonators, respectively.

167

## 7.6  Summary

In this chapter, a novel 2-D coherent optical en/decoder based on coupled micro-ring reflector for two-dimensional coherent OCDMA application is proposed, which enables fast reconfiguring the wavelength hopping and spectral phase patterns simultaneously using only a single device.

A mathematical transfer matrix model for analyzing the en/decoding performance of the 2-D optical en/decoder is established. Based on the transfer matrix model, a comprehensive study of the reflective property and en/decoding performance for a coupled double micro-ring reflector is then presented. It has been found that a single peak reflective spectral response can be formed for the micro-ring reflector by optimizing the rings-bus and ring-ring coupling coefficients. The effects of ring loss, chip rate and fabrication error on the en/decoding performance have been studied. Two other kinds of micro-ring reflector based on circular coupled resonator and parallel coupled cascaded micro-ring array are also investigated for the 2-D optical en/decoder application. Simulation shows that the circular coupled micro-rings reflector has coupled resonator induced transparency and loss dependent reflection property, which makes it less attractive. While the parallel coupled cascaded micro-ring array can provide sharp reflective spectral response and relatively good en/decoding performance, though it needs additional bus waveguide and more complex coupling. This structure could be an alternative candidate for the 2-D coherent optical en/decoder. The analysis and design guideline presented in this chapter allow one to fabricate practical 2-D optical en/decoder based on the coupled micro-ring reflectors. It should be noted that the proposed device also exhibits the potential to perform simultaneous DPSK data modulation and optical code generation even bit-by-bit for improving the security and simplifying the OCDMA system if the wavelength hopping and spectral phase patterns can be rapidly reconfigured. The proposed micro-ring reflector based 2-D optical en/decoder can be integrated with other photonic devices, and enable a compact, flexible and programmable 2-D coherent OCDMA system. It may also find its applications in other research areas such as pulse shaping, microwave signal synthesizing, and so on.

# Chapter 8

# Conclusions and Future Work

As an emerging research field for optical access network and a potential candidate for secure optical communication, the OCDMA technique has attracted great research attention in recent years. The work presented in this thesis has focused on the development of advanced optical modulation and fast reconfiguring optical en/decoding techniques for improving the code reconfigurability and data security, which are crucial for future flexible and dynamically reconfigurable OCDMA systems. In this chapter, the key results and findings from the research will be summarized with more details described as below. After the conclusions, an outlook will be given with some recommendations for future work.

## 8.1 Summary of Results

### A. Time domain spectral phase encoding scheme

A novel time domain spectral phase encoding scheme that can rapidly reconfigure the optical code and is compatible with conventional spectral phase decoding has been proposed and experimentally demonstrated for OCDMA application. This scheme has a simple configuration which consists of only a pair of dispersive elements and a high speed phase modulator to perform the spectral phase encoding. Based on this scheme, a novel advanced modulation format that can simultaneously generate DPSK data modulation and optical encoding using a single phase modulator has been demonstrated to simplify the OCDMA system and reduce the cost. A 2.5Gb/s two-user OCDMA system using the proposed time domain spectral phase encoding technique was also presented, which verified the capability of this technique for multiple access applications.

### B. Bit-by-bit time domain spectral phase encoding and decoding for security improvement

Based on the time domain spectral phase encoding scheme, a symmetric time domain spectral phase encoding and decoding scheme that uses a similar setup for both the transmitter and receiver was proposed to simplify the OCDMA system architecture as well as enhancing the security. Simultaneous generation and decoding of 2.5Gb/s DPSK data modulation and 40-Gchip/s, 16-chip optical code patterns has been demonstrated. Using this symmetric scheme, the first bit-by-bit optical code scrambling technique was proposed to significantly improve the DPSK data security by performing bit-by-bit optical encoding and data modulation. 2.5Gb/s DPSK data has been encoded bit-by-bit by scrambling five 20Gchip/s, 8-chip optical code patterns, decoded and successfully transmitted over 34km fiber. The analysis of the security showed that the bit-by-bit optical code scrambling technique can provide a high security level, and exhibits the potential to provide unconditional transmission security and realize the "one time pad". The use of this technique is also expected to improve the security for even CSK data modulation format.

## C. Time domain spectral phase encoded OCDMA signal overlay WDM network architecture

A novel approach by overlaying time domain spectral phase encoded OCDMA signals over public WDM networks has been proposed for improving the security of OCDMA signal and channel capacity. By employing group velocity dispersion, the time domain spectral phase encoded OCDMA signal can be hidden into the public WDM network and makes the eavesdropper unaware of its existence. Meanwhile, because of the introduction optical encoding technique, the difficulty to extract the OCDMA signal for the eavesdropper is significantly increased, which can further enhance the OCDMA signal security. A transparent optical network architecture of overlaying time domain spectral phase encoded OCDMA signals with not only OOK data modulation but also advanced DPSK data modulation onto public DWDM networks enabled by a spectral notch filter for excluding the optical thresholding/time gating detection has also been proposed and experimentally demonstrated. Bit-by-bit time domain spectral phase encoding/decoding technique has also been applied into the proposed network architecture. Transparent transmission and detection of a secure 2.5-Gb/s time domain spectral phase encoded DPSK-OCDMA signal spectrally overlaid on a two-channel 10-Gb/s DWDM network using a fiber Bragg grating based spectral notch filter has been

demonstrated. The proposed transparent network architecture provides an attractive approach for improving the channel security and spectral efficiency.

## D. Rapid programmable, code-length variable bit-by-bit code shifting for high speed secure optical communication

In order to improve the data rate of the time domain spectral phase encoding scheme, a novel bit-by-bit code shifting technique was proposed in chapter 6, which has the advantages of enabling high speed operation, rapid programming the code-length variable, ultra-long optical code pattern that has a large code space. Significant security improvement for 10-Gb/s and even 40-Gb/s DPSK data with chip rate of 40Gchip/s and an ultra-long code length of up to 1024-chip has been successfully demonstrated. Based on this technique, a novel approach based on symbol overlapping for both the encoded and incorrectly decoded signal was further proposed for improving the security of OOK data that has been conventionally predicted to be vulnerable to an eavesdropper's energy detection attack. A 40Gb/s secure optical communication system with OOK data modulation format has been demonstrated and compared with a 10Gb/s OOK system. It has been shown that the security improvement for OOK data modulation depends on the chromatic dispersion and chip rate. The proposed technique also has the potential of applying longer code lengths and supporting advanced optical modulation formats to enable high speed optical code based secure optical communication.

## E. Tunable 2-D coherent optical en/decoder based on coupled micro-ring reflector

A novel 2-D coherent optical en/decoder based on coupled micro-ring reflector has been proposed and numerically studied in Chapter 7. This device is capable of fast reconfiguring the wavelength hopping and spectral phase pattern simultaneously, which is promising to improve the code cardinality and flexibility of 2-D OCDMA system. By optimizing the ring-bus and ring-ring coupling coefficient, a single peak reflection spectrum for a coupled double micro-ring resonator can be achieved. The proof-of-principle 2-D optical en/decoding based on the coupled double micro-ring resonator has been verified in the simulation using a cascaded transfer matrix model. The en/decoding performance of the coupled double micro-ring resonator based 2-D optical en/decoder has been investigated with various parameters such as propagation loss, chip rate as

well as fabrication error taken into account. The reflection properties of two other candidates of micro-ring reflectors namely circular coupled resonator and parallel cascaded coupled micro resonator array were also investigated. It has been found that the circular coupled resonator has coupled resonator induced transparency and loss dependent reflection profile, which makes it not very attractive than the other structures. While although it requires complex coupling, the parallel cascaded coupled micro-resonator array could be an alternative candidate for the 2-D coherent optical en/decoder. The proposed 2-D coherent optical en/decoder has the potential to perform bit-by-bit optical en/decoding and data modulation by fast reconfiguring the applied wavelength hopping and spectral phase code patterns for improving the security and OCDMA network flexibility.

## 8.2   Future Research Directions

In this section, an outlook and some suggestions for future research work are briefly discussed. Some of them deserve more thorough investigations and are outlined below:

1.  Achieving information security by the OCDMA technique is a rather attractive approach for secure optical communication, especially when the optical code can be rapidly reconfigured. We believe that the demonstration of 2.5Gb/s bit-by-bit simultaneous DPSK data modulation and optical encoding using only single phase modulator based on the time domain spectral phase en/decoding scheme in Chapter 4 has confirmed this point. However, in the demonstration, the generation of the DPSK data and optical code is realized by manually editing the pulse pattern generator which greatly limits the programming speed and achievable code scrambling length. A future research effort can be made on designing a digital electronic circuit to automatically generate the DPSK data and optical code according to a code look up table that could be changed in real time.

2.  As this thesis focuses on improving the reconfigurability and security of OCDMA system using advanced optical modulation and en/decoding techniques, most of our demonstrations on security improvement are based on the comparison of the eye diagrams assuming the eavesdropper has no code information. Currently, there has no general parameter on measuring the security

level for various OCDMA systems. A future work could be quantitatively analyzing the security level of various systems using a widely acceptable parameter. Moreover, besides the security improvement, the multi-user capability of the time domain spectral phase encoding technique could be further explored. To support more active users in the systems with DPSK data format, optical thresholding/time gating techniques should be used. Unfortunately, there is no suitable optical thresholder for DPSK data up to now, which could be a challenging future research work.

3.  In the proposed transparent time domain spectral phase encoded OCDMA signal overlay public WDM network, a 2.5Gb/s OCDMA signal overlaid onto a two-channel 10Gb/s DWDM channels have been demonstrated in this thesis. To further improve the security and channel capacity, a future work could be on demonstration of multi-user OCDMA signal spectrally overlaid onto multi-channel DWDM channels, which would be particularly attractive for high security and high capacity optical network.

4.  In the bit-by-bit code shifting work described in chapter 6, the security improvement for a high date rate of up to 40Gb/s with 1024-chip optical code for both OOK and DPSK data modulation formats have been demonstrated. As the bit-by-bit code shifting technique exhibits the capability to enable high data rate operation and is compatible with advanced data modulation, a future research work would be focused on demonstration of higher speed secure optical communication with ultra-long optical code and various modulation formats (DQPSK, D8PSK, etc).

5.  For the proposed 2-D coherent optical en/decoder based on coupled micro-ring reflector described in chapter 7, further research work could be on designing novel micro-ring reflector with box-like spectral response to improve the en/decoding performance as well as special optical code for the 2-D coherent optical en/decoder. Meanwhile, based on the theoretical guideline presented in this thesis, efforts should also be made on the fabrication and characterization of this device in future. An investigation of the 2-D wavelength hopping and spectral phase coding performance in a practical OCDMA system would also be desired.

# References

[1] C. Decusatis, *Handbook of Fiber Optic Data Communication: A Practical Guide to Optical Networking*, (Third Edition), pp. 6-10, 2008.

[2] K. C. Kao and G. A. Hockham, "Dielectric-fiber surface waveguide for optical frequencies", *Proceeding IEE*, vol. 113, pp. 1151-1158, 1966.

[3] G. P. Agrawal, *Fiber-Optic Communications Systems*. (Third Edition). New York, US: John Wiley & Sons, Inc., pp. 1-19, 2002.

[4] R. J. Mears, L. Reekie, I. M. Jauncey, D. N. Payne, "Low-noise erbium-doped fibre amplifier operating at 1.54 um", *IEE Electronics Letters*, vol.23, no.19, pp.1026 -1028, 1987.

[5] L. G. Kazovsky, N. Cheng, W. Shaw, D. Gutierrez, and S. Wong, *Broadband Optical Access Networks*, First Edition. John Wiley & Sons, Inc. pp. 1-5, 2011.

[6] D. Qian, M, Huang, E. Ip, Y. Huang, Y. Shao, J. Hu and T. Wang, "101.7-Tb/s (370×294-Gb/s) PDM-128 QAM-OFDM transmission over 3×55-km SSMF using pilot-based phase noise mitigation", in OFC 2011, Los Angeles, PDPB5.

[7] J. Sakaguchi, Y. Awaji, N. Wada, A. Kanno, T. Kawanishi, T. Hayashi, T. Taru, T. Kobayashi, and M. Watanabe, "109-Tb/s (7×97×172-Gb/s SDM/ WDM/PDM) QPSK transmission through 16.8-km homogeneous multi-core fiber", in OFC 2011, Los Angeles, PDPB6.

[8] G. Kramer and G. Pesavento, "Ethernet passive optical network (EPON): building a next-generation optical access network", *IEEE Communications Magazine*, pp.66-73, Feb. 2002.

[9] D. Breuer, F. Geilhardt, R. Hülsermann, M. Kind, C. Lange, T. Monath, and E. Weis, "Opportunities for next-generation optical access", *IEEE Communications Magazine,* pp.16-24, 2011.

[10] H. Shinohara, "Broadband access in Japan: rapidly growing FTTH market", *IEEE Communications Magazine*, pp.72-78, 2005.

[11] J. Kani, "Challenges for next generation optical access networks-an operator's view", in next generation optical access networks: architectures, technology and systems workshop, Torino, ECOC 2010.

[12] C. Lee, W. V. Sorin, and B. Y. Kim, "Fiber to the home using a PON infrastructure", *Journal of lightwave technology*, vol. 24, no. 12, pp. 4568-4583, 2006.

[13] K. Kitayama, X. Wang, and N. Wada, "OCDMA over WDM PON-solution path to gigabit-symmetric FTTH", *Journal of lightwave technology*, vol. 24, no. 4, pp. 1654-1662, April. 2006.

[14] K. Kitayama, H. Sotobayashi and N. Wada, "Optical code division multiplexing (OCDM) and its applications in photonic networks", *IEICE Trans. Fundamentals*, vol. E82-A, no. 12, 1999.

[15] A. Stock and E. H. Sargent, "The role of optical CDMA in access networks", *IEEE Communication Magazine,* vol. 40, pp. 83-87, 2002.

[16] P. R. Prucnal, M. A. Santoro, and T. R. Fan, "Spread spectrum fiber-optic local area network using optical processing," *Journal of lightwave technology*, vol. LT-4, no. 5, pp. 547-554, May. 1986.

[17] X. Wang, N. Wada and K. Kitayama, "Enabling techniques for asynchronous coherent OCDMA", *Proc. of SPIE,* vol. 6021, 60212Z, 2005.

[18] K. Fouli and M. Maier, "OCDMA and optical coding: principles, applications, and challenges", *IEEE Communications Magazine,* pp. 27-34, August. 2007.

[19] A. Stock and E. H. Sargent, "Lighting the local area: optical code-division multiple access and quality of service provisioning", *IEEE Communication Magazine,* pp. 42-46, 2000.

[20] X. Wang and K. Kitayama, "Analysis of the beat noise in coherent and incoherent time-spreading OCDMA network", *Journal of lightwave technology*, vol.22, no.10, pp.2226-2235, 2004.

[21] X. Wang, N. Wada, T. Miyazaki, G. Cincotti and K. Kitayama, "Field trial of 3-WDM×10-OCDMA×10.71-Gb/s asynchronous WDM/DPSK-OCDMA using hybrid E/D without FEC and optical thresholding," *Journal of lightwave technology*, vol. 25, no. 1, pp. 207-215, 2007.

[22] P. C. Teh, P. Petropoulos, M. Ibsen, and D. J. Richardson, "A comparative study of the performance of seven- and 63-chip optical code-division multiple-access encoders and decoders based on superstructured fiber Bragg gratings," *Journal of lightwave technology*, vol. 19, no. 9, pp. 1352–1365, Sep. 2001.

[23] X. Wang, K. Matsushima, A. Nishiki, N. Wada, F. Kubota, and K. Kitayama, "High-performance optical code generation and recognition by use of a 511-chip, 640-Gchip/s phase-shifted superstructured fiber Bragg grating," *Optics Letters*, vol. 30, no.4, pp. 355–357, Feb. 2005.

[24] Y. Dai, X. Chen, Y. Zhang, J. Sun, and S. Xie, "Phase-error-free, 1023-chip OCDMA En/de-coders based on reconstruction-equivalent-chirp Technology and error-correction method", in *OFC* 2007, Anaheim, USA, Paper JWA28.

[25] M. E. Marhic, "Coherent optical CDMA networks," *Journal of lightwave technology*, vol. 11, no.5, pp. 854-863, 1993.

[26] N. Wada, K. Kitayama, "A 10 Gb/s optical code division multiplexing using 8-Chip optical bipolar code and coherent detection", *Journal of lightwave technology*, vol.17, no.10, pp. 1758-1765, Oct. 1999.

[27] C. Ji, R. G. Broeke, Y. Du, Jing Cao, N. Chubun, P. Bjeletich, F. Olsson, S. Lourdudoss, R. Welty, C. Reinhardt, P. L. Stephan, and S. J. B. Yoo, "Monolithically Integrated InP-Based Photonic Chip Development for O-CDMA Systems", *IEEE Journal of Selected*

*Topics in Quantum Electronics,* vol. 11, no. 1, pp. 66-77, 2005.

[28] M. R. Mokhtar, M. Ibsen, P. C. Teh, and D. J. Richardson, "Reconfigurable multilevel phase-shift keying encoder-decoder for all-optical networks," *IEEE Photon. Technol. Lett.,* vol. 15, no. 3, pp. 431-433, 2003.

[29] Z. Zhang, C. Tian, M. R. Mokhtar, P. Petropoulos, D. J. Richardson and M. Ibsen, "Rapidly reconfigurable optical phase encoder-decoders based on fiber Bragg gratings", *IEEE Photon. Technol. Lett.,* vol. 18, no. 11, pp. 1216-1218, 2006.

[30] Z. Jiang, D. E. Leaird and A. M. Weiner, "Experimental investigation of security issues in O-CDMA," *Journal of lightwave technology*, vol. 24, no.11, pp. 4228-4234, 2006.

[31] Z. Si, F. Yin, M. Xin, H. Chen, M. Chen, and S. Xie, "Code extraction from encoded signal in time-spreading optical code division multiple access," *Optics Letters*, vol. 35, no.2, pp. 229-231, 2010.

[32] Z. Jiang, D. S. Seo, S.-D. Yang, D. E. Leaird, R. V. Roussev , C. Langrock M. M. Fejer, and A. M. Weiner, "Four user, 2.5 Gb/s, spectrally coded OCDMA system demonstration using low-power nonlinear processing," *Journal of lightwave technology,* vol. 23, no.1, pp. 143-158, 2005.

[33] D. E. Leaird, Z. jiang, and A. M. Weiner, "Experimental investigation of security issues in OCDMA: a code-switching scheme," *Electronics Letters*, vol. 41, no. 14, pp. 817-819, 2005.

[34] E. Marcom and O. G. Ramer, "Encoding-decoding optical fibre network," *Electronics Letters,* vol. 14, no. 3, pp. 48-49, 1978.

[35] A. M. Weiner, J. P. Heritage, and J. A. Salehi, "Encoding and decoding of femtosecond pulses," *Optics Letters*, vol. 13, no. 4, pp. 300-302, 1988.

[36] H. Yin, D. J. Richardson, *Optical Code Division Multiple Access Communication Networks: Theory and Applications*, Springer and Tsinghua University Press, 2007.

[37] X. Wang, "Keys towards practical OCDMA networks", in *7th IEEE Int. Conf. on Optoelectronics, Fiber optics and Photonics*, paper NET2.2 (invited), December 2004, Kochi, India.

[38] K. Kitayama, "Code division multiplexing lightwave networks based upon optical code conversion," *IEEE J. Sel. Areas Commun.,* vol. 16, no. 7, pp. 1309-1319, Sep. 1998.

[39] M. Kavehrad and D. Zaccarina, "Optical code-division-multiplexed system based on spectral encoding of noncoherent sources," *Journal of lightwave technology*, vol. 13, no. 3, pp. 534-545, Mar. 1995.

[40] Z. Wei, H. G. Shiraz, and H. M. H. Shalaby, "Performance analysis of optical spectral-amplitude-coding CDMA systems using a super-fluorescent fiber source", *IEEE Photonics Technology letters*, vol.13, no.8, pp.887-889, Aug. 2001.

[41] A. T. Pham, Hiroyuki Yashima, "Performance enhancement of the 2-D wavelength-hopping/time spreading synchronous OCDM system using a heterodyne detection

receiver and PPM signaling", *Journal of optical networking*, vol. 6, no. 6, pp. 789-800, 2007.

[42] L. Tanceski and I. Andonovic, "Wavelength hopping/time spreading code division multiple access systems," *Electronics Letters*, vol. 30, no. 9, pp. 721-723, 1994.

[43] V. Baby, I. Glesk, R. J. Runser, R. Fischer Y. Huang, C.-S. Bres, W. C. Kwong, T. H. Curtis, P. R. Prucnal, "Experimental demonstration and scalability analysis of a four-node 102-Gchip/s fast frequency-hopping time-spreading optical CDMA network," *IEEE Photonics Technology letters*, vol. 17, no. 1, pp. 253-255, Jan. 2005.

[44] C.-S. Bres, I. Glesk, and P. R. Prucnal, "Demonstration of an eight-user 115-Gchip/s incoherent OCDMA system using supercontinuum generation and optical time gating", *IEEE Photonics Technology letters*, vol. 18, no. 7, pp. 889-891, Apr. 2006.

[45] J. A. Salehi, "Emerging OCDMA communication systems and data networks", *Journal of optical networking*, vol. 6, no.9, pp.1138-1178, 2007.

[46] D. Zaccarin, and M. Kavehrad, "An optical CDMA system based on spectral encoding of LED", *IEEE Photonics Technology letters*, vol.4, no.4, pp. 479-428, 1993.

[47] C.-S. Bres, Y. Huang, I. Glesk, and P. R. Prucnal, "Scalable asynchronous incoherent optical CDMA", *Journal of optical networking*, vol. 6, no. 6, pp. 599-615, 2007.

[48] X. Wang, K. Matsushima, A. Nishiki, N. Wada, and K. Kitayama, "High reflectivity superstructured FBG for coherent optical code generation and recognition," *Opt. Express*, vol. 12, no.22, pp. 5457-5468, 2004.

[49] X. Wang, and N. Wada, "Spectral phase encoding of ultra-short optical pulse in time domain for OCDMA application," *Opt. Express*, vol. 15, no. 12, pp. 7319-7326, 2007.

[50] X. Wang, K. T. Chan, "A sequentially self-seeded Fabry-Perot laser for two-dimensional encoding/decoding of optical pulses", *Journal of Quantum Electronics,* vol. 39, no. 1, pp. 83-89, Jan. 2003.

[51] Le Nguyen Binh and Nam Quec Ngo, *Ultrafast Fiber Lasers, Principles and Application with Matlab Models*, CRC press, 2011.

[52] K. Kitayama and M. Murata, "Versatile optical code-based MPLS for circuit,burst, and packet switchings," *Journal of lightwave technology*, vol. 21, no. 11, pp. 2753-2764, 2003.

[53] X. Wang, and N. Wada, "Experimental demonstration of OCDMA traffic over optical packet switching network with hybrid PLC and SSFBG en/decoders", *Journal of lightwave technology*, vol. 24, no. 8, pp. 3012-3020, 2006.

[54] N. Wada and K. Kitayama, "10Gbit/s, 8-chip coherent optical code division multiplexing using all-optical dncoder/decoder", in the *Pacific Rim Conference on Lasers and Electro-Optics (CLEO/PacificRim'97)*, PD2-14, 1997.

[55] Naoya Wada, "Code processing system, device, and its application", *Journal of networks*, vol. 5, no. 2, pp. 242-250, 2010.

[56] B. J. Eggleton, P. A. Krug, L. Poladian, and F. Ouellette, "Long periodic superstructure Bragg gratings in optical fibers," *Electronics Letters*, vol. 30, no. 19, pp. 1620-1622, 1994.

[57] P. Petropoulos, M. Ibsen, A. D. Ellis, and D. J. Richardson, "Rectangular pulse generation based on pulse reshaping using superstructured fiber Bragg grating," *Journal of lightwave technology*, vol. 19, no. 5, pp. 746-752, 2001.

[58] P. Petropoulos, M. Ibsen, M. N. Zervas, and D. J. Richardson, "Generation of a 40-GHz pulse stream by pulse multiplication with a sampled fiber Bragg grating," *Optics Letters*, vol. 25, no. 8, pp. 521-523, Apr. 2000.

[59] P. C. Teh, M. Ibsen, J. H. Lee, P. Petropoulos and D. J. Richardson, "Demonstration of a four-channel WDM/OCDMA system using 255-chip 320-Gchip/s quarternary phase coding grating," *IEEE Photonics Technology letters,* vol. 14, no. 2, pp. 227-229, 2002.

[60] T. Hamanaka, X.Wang, N.Wada, A. Nishiki, and K. Kitayama, "Ten-user truly asynchronous gigabit OCDMA transmission experiment with a 511-chip SSFBG en/decoder," *Journal of lightwave technology*, vol. 24, no. 1, pp. 95-102, Jan. 2006.

[61] A. M. Weiner, Z. Jiang, and D. E. Leaird, "Spectrally phase-coded O-CDMA", *Journal of optical networking*, vol. 6, no. 6, pp. 728-755, 2007.

[62] Z. Jiang, D. Seo, S. Yang, D. E. Leaird, R. V. Roussev, C. Langrock, M. M. Fejer, and A. M. Weiner, "Four-user 10-Gb/s spectrally phase-coded O-CDMA system operating at ~ 30 fJ/bit," *IEEE Photonics Technology letters,* vol. 17, no. 3, pp. 705-707, 2005.

[63] R. P. Scott, W. Cong, V. J. Hernandez, K. Li, B. H. Kolner, J. P. Heritage, S. J. B. Yoo "An eight-user time-slotted SPECTS O-CDMA testbed: demonstration and simulations", *Journal of lightwave technology*, vol. 23, no. 10, pp. 3232–3240, 2005.

[64] S. J. B. Yoo, J. P. Heritage, V. J. Hernandez, *et al*., "Spectral phase encoded time spread optical code division multiple access technology for next generation communication networks", *Journal of optical networking*, vol. 6, no. 10, pp. 1210-1227, 2007.

[65] B. E. Little, S. T. Chu, H. A. Haus, J. Foresi, and J. P. Laine, "Microring resonator channel dropping filters," *Journal of lightwave technology*, vol. 15, no. 6, pp. 998–1005, Jun. 1997.

[66] C. K. Madsen, "Subband all-pass filter architectures with applications to dispersion and dispersion-slope compensation and continuously variable delay lines," *Journal of lightwave technology*, vol. 21, no. 10, pp. 2412-2420, Oct. 2003.

[67] J. E. Heebner and R. W. Boyd, "Enhanced all-optical switching by use of nonlinear fiber ring resonator," *Optics Letters*, vol. 24, no. 12, pp. 847-849, Jun. 1999.

[68] A. Agarwal, P. Toliver, R. P. Menendez, S. Etemad, J. Jackel, *et al.,* "Fully Programmable Ring-Resonator-Based Integrated Photonic Circuit for Phase Coherent Applications", in *OFC*, Paper PDP6, 2005.

[69] A. Agarwal, P. Toliver, R. P. Menendez, S. Etemad, J. Jackel, *et al.,* "Fully

Programmable Ring-Resonator- Based Integrated Photonic Circuit for Phase Coherent Applications", *Journal of lightwave technology*, vol. 24, no. 1, Jan. 2006.

[70] A. Agarwal, P. Toliver, R. P. Menendez, T. Banwell, J. Jackel, S. Etemad, "Spectrally efficient six-user coherent OCDMA system using reconfigurable integrated ring resonator circuits", *IEEE Photonic Technology Letters*, vol. 18, no. 18, pp. 1952-1954, Sep. 2006.

[71] G. Cincotti, "Design of optical full encoders/decoders for code-based photonic routers", *Journal of lightwave technology*, vol. 22, no. 7, pp. 1642-1650, 2004.

[72] N. Wada, G. Cincotti, S. Yoshima, N. Kataoka, and K. Kitayama, "Characterization of a full encoder/decoder in the AWG configuration for code-based photonic routers—Part II: experiments and applications", *Journal of lightwave technology*, vol. 24, no.1, pp. 113-121, 2006.

[73] X. Wang, N. Wada, N. Kataoka, T. Miyazaki, G. Cincotti and K. Kitayama, "100 km field trial of 1.24 Tbit/s, spectral efficient asynchronous 5 WDM×25 DPSK-OCDMA using one set of 50×50 ports large scale en/decoder", in *OFC'07 post-deadline*, PDP 14, Anaheim, CA., USA, Mar., 2007.

[74] X. Wang, T. Hamanaka, N. Wada, K. Kitayama. "Dispersion-flattened-fiber based optical thresholder for multiple-access-interference suppression in OCDMA system", *Opt. Express*, vol. 13, no. 14, pp. 5499-5505, 2005.

[75] T. Hamanaka, X. Wang, N. Wada and K. Kitayama, "Compound data rate and data-rate-flexible 622 Mb/s–10 Gb/s OCDMA experiments using 511-chip SSFBG and sascaded SHG-DFG-based PPLN waveguide optical thresholder", *IEEE Journal of selected topics in Quantum Electronics*, vol. 13, no. 5, pp. 1516-1521, Sep. 2007.

[76] H. Sotobayashi and K. Kitayama, "All-optical code and wavelength conversion of 10Gb/s BPSK codes by four-wave mixing in semiconductor optical amplifier for optical code division multiplexing," *Optical Amplifiers and their Applications (OAA) '99*, FA-3, Nara, 1999.

[77] X. Wang, N. Wada, K. Kitayama, "Demonstration of 3-λ×8×10Gbps WDM/DPSK-OCDMA using 31-chip, 640 Gchip/s SSFBG en/decoder for 10G flexible access network", *in 33rd European Conference and Exhibition on Optical Communication (ECOC 2007)*, pp. 543, Sep. 2007.

[78] J. H. Lee, P. C. Teh, Z. Yusoff, M. Ibsen, W. Belardi, T. M. Monro, and D. J. Richardson, "A holey fiber-based nonlinear thresholding device for optical CDMA receiver performance enhancement", *IEEE Photonic Technology Letters*, vol. 14, no. 6, pp. 876-878, 2002.

[79] Z. Zheng, A. M. Weiner, J. H. Marsh and M. M. Karkhanehchi, "Ultrafast optical thresholding based on two-photon absorption GaAs waveguide photodetectors," *IEEE Photonic Technology Letters*, vol. 9, no. 4, pp. 493-495, 1997.

[80] K. J. Dexter, D. A. Reid, P. J. Maguire, L. P. Barry, C. Tian, M. Ibsen, P. Petropoulos and

D. J. Richardson, "Multiple access interference rejection in OCDMA using a two-photon absorption based semiconductor device", *Optics Communications*, vol. 282, no. 7, pp. 1281-1286, 2009.

[81] J. H. Lee, P. C. Teh, P. Petropoulos, M. Ibsen, and D. J. Richardson, "A grating-based OCDMA encoding-decoding system incorporating a nonlinear optical loop mirror for improved code recognition and noise reduction," *Journal of lightwave technology*, vol. 20, no. 1, pp. 36-46, Jan. 2002.

[82] K. Kravtsov, Paul R. Prucnal and M. M. Bubnov, "Simple nonlinear interferometer-based all-optical thresholder and its applications for optical CDMA", *Optics Express*, vol. 15, no. 20, pp. 13114-13122, Oct. 2007.

[83] Q. T. Le, L. Bramerie, H. T. Nguyen, M. Gay, S. Lobo, M. Joindot, J.-L. Oudar, and J.-C. Simon, "Saturable-absorber-based phase-preserving amplitude regeneration of RZ DPSK signals", *IEEE Photonic Technology Letters,* vol. 22, no. 12, pp. 887-889, 2010.

[84] P. J. Winzer, R. J. Essiambre, "Advanced optical modulation formats", *Proceedings of the IEEE*, vol. 94, no. 5, pp. 952-985, 2006.

[85] P. J. Winzer, R. J. Essiambre, "Advanced modulation formats for high-capacity optical transport networks", *Journal of lightwave technology*, vol. 24, no. 12, pp. 4711-4728, 2006.

[86] R. Ramaswami and K. N. Sivarajan, *Optical Networks, A Pactical Perspective*, 2nd ed. San Francisco: Morgan Kaufmann Publishers, 2002.

[87] X. Wang, N. Wada, T. Miyazaki and K. Kitayama, "Coherent OCDMA system Uusing DPSK data format with balanced detection", *IEEE Photonic Technology Letters,* vol. 18, no. 7, pp. 826-828, 2006.

[88] G. Manzacca, F. Benedetto, V. Sacchieri , G. Giunta, G. Cincotti, "Advanced modulation formats in optical code division multiple access networks", in *ICTON*, Tu.A1.4, pp. 91-94, 2007.

[89] C. Xu, X. Liu, and X. Wei, "Differential phase-shift keying for high spectral efficiency optical transmissions," *IEEE Journal of selected topics in Quantum Electronics,* vol. 10, no. 2, pp. 281-293, 2004.

[90] N. Tadano, N. Wada, F. Kubota, and M. Yokoyama, "A novel 10 Gb/s optical CDMA system based on code shift keying data modulation and balanced detection," in *Proc. Photonics Switching* 2003 (PS 2003), pp. 53-55, PS.Mo.B5.

[91] B. Dai, Z. Gao, X. Wang, N. Kataoka and N. Wada, "A novel optical orthogonal modulation format based on differential phase shift keying and code-shift keying", *IEEE Photonic Technology Letters*, vol. 23, no. 17, pp. 1210-1212, 2011.

[92] G. S. Kanter, "Secure optical communication", in *CLEO/QELS*, 2010, Paper. CFC3.

[93] N. boudriga, W. Abdallah, M. Hamdi, "Physical layer cryptography in optical network: a lattice-based approach", in *ICTON* 2010, Paper We.A.1.6.

[94] P. R. Prucnal, M. P. Fok, Y. Deng, and Z. Wang, "Physical layer security in data networks using optical signal processing", in *OSA/ACP*, 2009, Paper FK1.

[95] V. Scarani, H. B. Pasquinucci, N. J. Cerf, M. Dusek, N. Lutkenhaus, M. Peev, "The security of practical quantum distribution", *Rev. Mod. Phys.*, vol. 81, no. 3, pp. 1301-1350, 2009.

[96] T. E. Chapuran, P. Toliver, N. A. Peters, J. Jackel, M. S. Goodman, *et al.*, "Optical networking for quantum key distribution and quantum communication", *New. J. Phys.,* vol. 11, pp. 105001, 2009.

[97] G. D. Van Wiggeren and R. Roy, "Communication with Chaotic Lasers", *Science,* vol. 279, no. 5354, pp. 1198-1200, 1998.

[98] A. Argyris, D. Syvridis, L. Larger, V. A. -Lodi, P. Colet, I. Fischer, J. G. -Ojalvo, C. R. Mirasso, L. Pesquera and K. A. Shore, "Chaos-based communications at high bit rates using commercial fibre-optic links", *Nature,* vol. 438, pp. 343-346, 2005.

[99] J. Hizanidis, S. Deligiannidis, A. Bogris and D. Syvridis, "Enhancement of chaos encryption potential by combining all-optical and electro-optical chaos generators", *IEEE Journal of Quantum Electronics*, vol. 46, No. 11, pp. 1642-1649, 2010.

[100] T. H. Shake, "Confidentiality performance of spectral-phase-encoded optical CDMA," *Journal of lightwave technology,* vol. 23, no. 4, pp. 1652-1663, 2005.

[101] T. H. Shake, "Security performance of optical CDMA against eavesdropping", *Journal of lightwave technology*, vol. 23. no. 2, pp. 655-670, 2005.

[102] B. Dai, Z. Gao, X. Wang, N. Kataoka and N. Wada, "Performance comparison of 0/$\pi$- and $\pm\pi/2$-phase-shifted superstructured fiber Bragg grating en/decoder", *Optics Express*, vol. 19, no. 13, pp.12248-12260, 2011.

[103] C.-B. Huang, Z. Jiang, D. E. Leaird , J. Caraquitena, and A. M. Weiner, "Spectral line-by-line shaping for optical and microwave arbitrary waveform generations", *Laser & Photon. Rev.,* vol. 2, no. 4, pp. 227-248, 2008.

[104] S. Anzai, M. Mieno, T. Komai, N. Wada, T. Yoda, T. Miyazaki, and K. Kodate, "Amplitude, phase, and bandwidth tunable high-resolution optical spectrum shaper and its application for optical communication systems," in *OFC 2008*, San Diego, CA, Feb. 2008, Paper JThA25.

[105] M. Mieno, Y. Komai, N. Wada, S. Shinada, T. Yoda, T. Miyazaki, and K. Kodate, "Ultrafast time-spread optical BPSK code label generation and processing based on variable-bandwidth spectrum shaper," *IEEE Photonic Technology Letters*, vol. 21, no. 13, pp. 860-862, 2009.

[106] X. Wang, Z. Gao, N. Kataoka and N. Wada, "Time domain spectral phase encoding/DPSK data modulation using single phase modulator for OCDMA application", *Optics Express,* vol. 18, no. 10, pp. 9879-9890, 2010.

[107] Z. Gao, X. Wang, N. Kataoka and N. Wada, "Demonstration of time-domain spectral

phase encoding/DPSK data modulation using single phase modulator", *IEEE LEOS Summer Topical* 2009, New port, CA, USA, 2009, Paper TuA3.1.

[108] Z. Gao, X. Wang, N. Kataoka and N. Wada, "2.5Gbps two-user OCDMA transmission based on time domain spectral phase encoding and variable-bandwidth spectrum shaper", *Microwave and Optical Technology Letter,* vol. 53, no. 8, pp. 1879-1882, 2011.

[109] X. Wang, Z. Gao, X.-H.Wang, N. Kataoka and N. Wada, "Bit-by-bit optical code scrambling technique for secure optical communication", *Optics Express,* vol. 19, no. 4, pp. 3503-3512, 2011.

[110] Bruce Schneier, "Applied cryptograhpy", Second edition, Chapter 7, John Wiley & Sons, 1996.

[111] Z. Wang, A. Chowdhury and P. R. Prucnal, "Optical CDMA code wavelength conversion using PPLN to improve transmission security", *IEEE Photonic Technology Letters*, vol. 21, no. 6, pp. 383-385, 2009.

[112] B. Dai, Z. Gao, X. Wang, N. Kataoka and N. Wada, "Demonstration of differential detection on attacking code-shift-keying OCDMA system", *Electronics Letter,* vol. 46, no. 25, pp. 1680-1682, 2010.

[113] J. M. Castro, I. B. Djordjevic and D. F. Geraghty, "Novel super structured Bragg gratings for optical encryption," *Journal of lightwave technology,* 24, 1875 (2006).

[114] P. Torres, L. C. G. Valente, and M. C. R. Carvalho, "Security system for optical communication signals with fiber Bragg gratings", *IEEE Trans. Microwave Theory and Technol.,* vol. 50, no. 1, pp. 13-16, 2002.

[115] M. P. Fok, and P. R. Prucnal, "Low-latency nonlinear fiber-based approach for data encryption and anti-jamming in optical network", 2008 *IEEE/LEOS Annual Meet.,* Newport Beach, CA, USA, 2008, Paper ThG 3.

[116] K. Vahala, R. Paiella, and G. Hunziker, "Ultrafast WDM logic", *IEEE Journal of selected topics in Quantum Electronics,* vol. 3, no. 2, pp. 698-701, 1997.

[117] B. B. Wu and E. E. Narimanov, "A method for secure communications over a public fiber- optical network," *Optics Express*, vol. 14, no. 9, pp. 3738-3751, May 2006.

[118] M. P. Fok and P. R. Prucnal, "A compact and low-latency scheme for optical steganography using chirped fiber bragg gratings", *Electronics Letter,* vol. 45, no. 3, pp. 179-180, 2009.

[119] K. Kravtsov, B. Wu, I. Glysk, P. R. Prucnal, E. Narimanov, "Stealth transmission over a WDM network with detection based on an all-optical thresholder", *Proc. LEOS annual meeting*, Oct. 2007, Paper WH2.

[120] P. R. Prucnal, M. P. Fok, Y. Deng and Z. Wang, "Physical layer security in fiber-optic networks using optical signal processing," in *Asia Communications and Photonics Conference* (*ACP*), invited paper, 7632, 76321M, 2009.

[121] S. Galli, R. Menendez, P. Tolive, T. Banwell, J. Jackel, J. Young and S. Etemad,

"Experimental results on the simultaneous transmission of two 2.5 Gbps optical-CDMA channels and a 10 Gbps OOK channel within the same WDM window," in *Proc. OFC*, vol. 3, pp. 29-31, 2005.

[122] S. Galli, R. Menendez, P. Toliver, T. Banwell, J. Jackel, J. Young, S. Etemad, "DWDM-compatible spectrally phase encoded O-CDMA," *IEEE Globecom Conference,* Dallas, Texas, USA, 2004.

[123] S. Galli, R. Menendez, P. Toliver, T. Banwell, J. Jackel, J. Young, S. Etemad, "Novel results on the coexistence of spectrally phase encoded OCDMA and DWDM", *IEEE International Conference on Communications*, ICC'05, Seoul, Korea, May 16-20, 2005.

[124] M. Yoshino, N. Miki, N. Yoshimoto, M. Tsubokawa, "Simultaneous OCDM signal transmission over multiple WDM channels using Mach-Zehnder interferometric selector", *Electronics Letter*, vol. 44, no. 22, pp. 1319-1320, 2008.

[125] X. Hong, D. Wang, L. Xu, and S. He, "Demonstration of optical steganography transmission using temporal phase coded optical signals with spectral notch filtering," *Optics Express*, vol. 18, no. 12, pp. 12415-12420, 2010.

[126] Z. Wang, and P. R. Prucnal, "Optical steganography over public DPSK channel with asynchronous detection," *IEEE Photonic Technology Letters* vol. 23, no. 1, pp. 48-50, 2011.

[127] H. Sotobayashi, W. Chujo and K. Kitayama, "Transparent virtual optical code/wavelength path network," *IEEE J. Select Areas in Commun.,* vol. 8, no. 3, pp. 99-704, May. 2002.

[128] J. P. Heritage and A. M. Weiner, "Advances in spectral optical code- division multiple-access," *IEEE Journal of Quantum Electronics*, vol. 13, no. 5, pp. 1351-1369, 2007.

[129] Y. J. Wen, J. Mo, Y. Wang, C. Lu, "Advanced data modulation techniques for WDM transmission", *IEEE Communications Magazine*, pp. 58-65, Aug. 2006.

[130] A. H. Gnauck and P. J. Winzer, "Optical phase-shift-keyed transmission", *Journal of lightwave technology*, vol. 23, no. 1, pp. 115-130, 2005.

[131] R. A. Griffin, R. I. Johnstone, R. G. Walker, J. Hall, S. D. Wadsworth, K. Berry, A. C. Carter, M. J. Wale, J. Hughes, P. A. Jerram, and N. J. Parsons, "10Gb/s optical differential quadrature phase shift key (DQPSK) transmission using GaAs/AlGaAs integration", in *OFC*, 2002, Paper FD6.

[132] H. Kim, R.-J. Essiambre, "Transmission of 8×20Gb/s DQPSK signals over 310-km SMF with 0.8-b/s/Hz spectral efficiency", *IEEE Photonic Technology Letters*, vol. 15, no. 5, pp. 769-771, 2003.

[133] B. E. Little, S. T. Chu, H. A. Haus, J. Foresi, and J.-P. Laine, "Microring resonator channel dropping filters", *Journal of lightwave technology*, vol. 15, no. 6, pp. 998-1005, 1997.

[134] A. Yariv, Y. Xu, R. K. Lee, A. Scherer, "Coupled-resonator optical waveguide: a

proposal and analysis", *Optics Letters*, vol. 24, no. 11, pp. 711-713, 1999.

[135] B. E. Little, S. T. Chu, W. Pan, and Y. Kokubun, "Microring resonator arrays for VLSI photonics," *IEEE Photonic Technology Letters*, vol. 12, no. 3, pp. 323-325, 2000.

[136] V. Van, T. A. Ibrahim, K. Ritter, P. P. Absil, F. G. Johnson, R. Grover, J. Goldhar, and P.-T. Ho, "All-optical nonlinear switching in GaAs-AlGaAs microring resonators," *IEEE Photonic Technology Letters*, vol. 14, no. 1, pp. 74-76, 2002.

[137] J. E. Heebner, R. W. Boyd, Q. H. Park, "Slow light, induced dispersion, enhanced nonlinearity, and optical solitons in a resonator array waveguide", *Physical Review E*, vol. 65, 036619: 1-4, 2002.

[138] F. Xia, L. Sekaric, Y. Vlasov, "Ultracompact optical buffers on a silicon chip", *Nature Photonics*, vol. 1, no. 1, pp. 65-71, 2007.

[139] J. K. S. Poon, J. Scheuer, Y. Xu, A. Yariv, "Designing coupled-resonator optical waveguide delay lines", *Journal of the Optical Society of America B*, vol. 21, no. 9, pp. 1665-1673, 2004.

[140] T. A. Ibrahim, R. Grover, L. C. Kuo, S. Kanakaraju, L. C. Calhoun, P.-T. Ho, "All-optical AND/NAND logic gates using semiconductor microresonators", *IEEE Photonic Technology Letters*, vol. 15, no. 10, pp. 1422-1424, 2003.

[141] T. A. Ibrahim, K. Amarnath, L. C. Kuo, R. Grover, V. Van, P.-T. Ho, "Photonic logic NOR gate based on two symmetric microring resonators", *Optics Letters*, vol. 29, no. 23, pp. 2779-2781, 2004.

[142] Q. Xu, B. Schmidt, S. Pradhan, M. Lipson, "Micrometre-scale silicon electro-optic modulator", *Nature,* vol. 435, no. 7040, pp. 325-327, 2005.

[143] A.Schweinsberg, S. Hocde, N. N. Lepeshkin, R. W. Boyd, *et al.,* "An environmental sensor based on an integrated optical whispering gallery mode disk resonator", *Sensors and Actuators B: Chemical*, vol. 123, no. 12, pp. 727-732, 2007.

[144] E. A. J. Marcatili, "Bends in optical dielectric guides", *Bell Labs Technical Journal*, vol. 48, pp. 48: 2103-2132, 1969.

[145] T. A. Ibrahim, W. Cao, Y. Kim, *et al.,* "All-optical switching in a laterally coupled microring resonator by carrier injection", *IEEE Photonic Technology Letters*, vol. 15, no. 1, pp. 36-38, 2003.

[146] B. E. Little, S. T. Chu, W. Pan, et al., "Vertically coupled glass microring resonator channel dropping filters", *IEEE Photonic Technology Letters*, vol. 11, no. 2, pp. 215-217, 1999.

[147] P. P. Absil, J. V. Hryniewicz, B. E. Little, *et al.,* "Vertically coupled microring resonators using polymer wafer bonding", *IEEE Photonic Technology Letters*, vol. 13, no. 1, pp. 49-51, 2001.

[148] P. Rabiei, W. H. Steier, "Tunable polymer double micro-ring filters", *IEEE Photonic Technology Letters,* vol. 15, no. 9, pp. 1255-1257, 2003.

[149] A. Yariv, "Universal relations for coupling of optical power between microresonators and dielectric waveguides", *Electronics Letters,* vol. 36, no. 4, pp. 321-322, 2000.

[150] C. J. Kaalund, G.-D. Peng, "Pole-zero diagram approach to the design of ring resonator-based filters for photonic applications", *Journal of lightwave technology*, vol. 22, no. 6, pp. 1548-1559, 2004.

[151] W. Chen, Z. Wang, W. L. Chen, Y. Chen, "General ring-resonator analysis and characterization by characteristic matrix", *Journal of lightwave technology*, vol. 23, no. 2, pp. 915-922, 2005.

[152] C. K. Madsen, J. H. Zhao, *Optical Filter Design and Analysis*, New York, US: John Wiley & Sons, Inc., pp. 19-93, 2001.

[153] A. Yariv, "Coupled-Mode theory for guided wave optics", *IEEE Journal of Quantum Electronics*, vol. 9, no. 9, pp. 914-933, 1973.

[154] Y. Chung, D.-G. Kim, and N. Dagli, "Reflection properties of coupled-ring reflectors," *Journal of lightwave technology*, vol. 24, no. 4, pp. 1865-1874, Apr. 2006.

[155] R. Baets, W. Bogaerts, D. Taillaert, P. Dumon, P. Bienstman, D. Van Thourhout, J. Van Campenhout, V. Wiaux, J. Wouters, S. Beckx, "Low loss nanophotonic waveguides and ring resonators in silicon-on-insulator", *Proceedings of the International School of Quantum Electronics*, Erice (Italy), vol. 709, pp. 308-327, 2003.

[156] R. Grover, P. P. Absil, T. A. Ibrahim, P.-T. Ho, "III-V semiconductor optical micro-ring resonators," in *Proceedings of the International School of Quantum Electronics*, Erice (Italy), vol. 709, pp. 110-129, 2003.

[157] G. Wicks and M. C. Gupta, *Handbook of Photonics*, CRC Press, New York, 1997.

[158] Q. Xu, D. Fattal, and R. G. Beausoleil, "Silicon microring resonators with 1.5um radius", *Optics Express*, vol. 16, no. 6, pp. 4309-4315, 2008.

[159] M. S. Nawrocka, T. Liu, X. Wang, R. R. Panepucci, "Tunable silicon microring resonator with wide free spectral range", *Appl. Phys. Lett.*, vol. 89, pp. 071110-071112, 2006.

[160] D. H. Geuzebroek, E. J. Klein, H. Kelderman, and A. Driessen, "Wavelength tuning and switching of a thermo-optic microring resonator," *Proc. ECIO*, pp. 395-398, 2003.

[161] V. R. Almeida, Q. Xu and M. Lipson, "Ultrafast integrated semiconductor optical modulator based on the plasma-dispersion effect", *Optics Letters*, vol. 30, no. 18, pp. 2403-2405, 2005.

[162] B. Guha, B. B. C. Kyotoku, and M. Lipson, "CMOS-compatible athermal silicon microring resonators", *Optics Express*, vol. 18, no. 4, pp. 3487-3493, 2010.

[163] T. Erdogan, "Fiber grating spectra", *Journal of lightwave technology*, vol. 15, no. 8, pp. 1277-1294, 1997.

[164] L. Luo, G. S. Wiederhecker, J. Cardenas, C. Poitras, and M. Lipson, "High quality factor etchless silicon photonic ring resonators", vol. 19, no. 7, pp. 6284-6289, 2011.

[165] S. J. Choi, Z. Peng, Q. Yang, Sang. J. Choi and P. D. Dapkus, "Tunable narrow linewidth all-buried heterostructure ring resonator filters using vernier effects", *IEEE Photonic Technology Letters*, vol. 17, no. 1, pp. 106-108, 2005.

[166] G. T. Paloczi, J. Scheuer, and A. Yariv, "Compact microring-based wavelength-selective inline optical reflector", *IEEE Photonic Technology Letters*., vol.17, no.2, pp. 390-392, Feb. 2005.

[167] J. K. S. Poon, J. Scheuer, and A. Yariv, "Wavelength-selective reflector based on a circular array of coupled microring resonators", *IEEE Photonic Technology Letters,* vol. 16, no. 5, pp. 1331-1333, 2004.

[168] Q. Xu, S. Sandhu, M.L. Povinelli, J. Shakya, S. Fan, and M. Lipson, "Experimental realization of an on-chip all-optical analogue to electromagnetically induced transparency", *Physical Review Letter*, vol. 96, no. 12, pp. 123901: 1-4, 2006.

[169] Z. Gao, X. Wang, "Analysis of Optical Reflector Based on Circular Coupled Microring Resonators", *in ICTON 2009,* Island of São Miguel, Azores, Portugal, July, 2009.

[170] R. Grover, V. Van, T. A. Ibrahim, P. P. Absil, L. C. Calhoun, F. G. Johnson, J. V. Hryniewicz and P.-T. Ho, "Parallel-cascaded semiconductor microring resonators for high-order and wide-FSR filters," *Journal of lightwave technology*, vol. 20, no. 5, pp. 900-905, 2002.

[171] D. G. Rabus, M. Hamacher, U. Troppenz, and H. Heidrich, "Optical filters based on ring resonators with integrated semiconductor optical amplifiers in GaInAsP/InP," *IEEE Journal of selected topics in Quantum Electronics,* vol. 8, no. 6, pp. 1405-1411, 2002.

[172] B. E. Little, S. T. Chu, P. P. Absil, *et al*., "Very high-order microring resonator filters the WDM applications", *IEEE Photonic Technology Letters*, vol. 16, no. 10, pp. 2263-2265, 2004.

[173] Y. M. Landobasa, S. Darmawan, and M.-K. Chin, "Matrix analysis of 2-D microresonator lattice optical filters", *IEEE Journal of Quantum Electronics*, vol. 41, no. 11, pp. 1410-1418, 2005.